United States Department of Commerce
Technology Administration
National Institute of Standards and Technology

NIST Special Publication 864

Technical Digest Symposium on Optical Fiber Measurements, 1994

Sponsored by the National Institute of Standards and Technology
in cooperation with the IEEE Lasers and Electro-Optics Society
and the Optical Society of America

NIST Technical Publications

Periodical

Journal of Research of the National Institute of Standards and Technology—Reports NIST research and development in those disciplines of the physical and engineering sciences in which the Institute is active. These include physics, chemistry, engineering, mathematics, and computer sciences. Papers cover a broad range of subjects, with major emphasis on measurement methodology and the basic technology underlying standardization. Also included from time to time are survey articles on topics closely related to the Institute's technical and scientific programs. Issued six times a year.

Nonperiodicals

Monographs—Major contributions to the technical literature on various subjects related to the Institute's scientific and technical activities.

Handbooks—Recommended codes of engineering and industrial practice (including safety codes) developed in cooperation with interested industries, professional organizations, and regulatory bodies.

Special Publications—Include proceedings of conferences sponsored by NIST, NIST annual reports, and other special publications appropriate to this grouping such as wall charts, pocket cards, and bibliographies.

Applied Mathematics Series—Mathematical tables, manuals, and studies of special interest to physicists, engineers, chemists, biologists, mathematicians, computer programmers, and others engaged in scientific and technical work.

National Standard Reference Data Series—Provides quantitative data on the physical and chemical properties of materials, compiled from the world's literature and critically evaluated. Developed under a worldwide program coordinated by NIST under the authority of the National Standard Data Act (Public Law 90-396). NOTE: The Journal of Physical and Chemical Reference Data (JPCRD) is published bi-monthly for NIST by the American Chemical Society (ACS) and the American Institute of Physics (AIP). Subscriptions, reprints, and supplements are available from ACS, 1155 Sixteenth St., NW, Washington, DC 20056.

Building Science Series—Disseminates technical information developed at the Institute on building materials, components, systems, and whole structures. The series presents research results, test methods, and performance criteria related to the structural and environmental functions and the durability and safety characteristics of building elements and systems.

Technical Notes—Studies or reports which are complete in themselves but restrictive in their treatment of a subject. Analogous to monographs but not so comprehensive in scope or definitive in treatment of the subject area. Often serve as a vehicle for final reports of work performed at NIST under the sponsorship of other government agencies.

Voluntary Product Standards—Developed under procedures published by the Department of Commerce in Part 10, Title 15, of the Code of Federal Regulations. The standards establish nationally recognized requirements for products, and provide all concerned interests with a basis for common understanding of the characteristics of the products. NIST administers this program in support of the efforts of private-sector standardizing organizations.

Consumer Information Series—Practical information, based on NIST research and experience, covering areas of interest to the consumer. Easily understandable language and illustrations provide useful background knowledge for shopping in today's technological marketplace.

Order the **above** *NIST publications from: Superintendent of Documents, Government Printing Office, Washington, DC 20402.*

Order the **following** *NIST publications—FIPS and NISTIRs—from the National Technical Information Service, Springfield, VA 22161.*

Federal Information Processing Standards Publications (FIPS PUB)—Publications in this series collectively constitute the Federal Information Processing Standards Register. The Register serves as the official source of information in the Federal Government regarding standards issued by NIST pursuant to the Federal Property and Administrative Services Act of 1949 as amended, Public Law 89-306 (79 Stat. 1127), and as implemented by Executive Order 11717 (38 FR 12315, dated May 11, 1973) and Part 6 of Title 15 CFR (Code of Federal Regulations).

NIST Interagency Reports (NISTIR)—A special series of interim or final reports on work performed by NIST for outside sponsors (both government and non-government). In general, initial distribution is handled by the sponsor; public distribution is by the National Technical Information Service, Springfield, VA 22161, in paper copy or microfiche form.

NIST Special Publication 864

Technical Digest—Symposium on Optical Fiber Measurements, 1994

Digest of a symposium sponsored by the
National Institute of Standards and Technology
in cooperation with the
IEEE Lasers and Electro-Optics Society
and the Optical Society of America

September 13-15, 1994
National Institute of Standards and Technology
Boulder, Colorado 80303-3328

Edited by
G.W. Day
D.L. Franzen
R.K. Hickernell

September 1994

U.S. DEPARTMENT OF COMMERCE, Ronald H. Brown, Secretary
TECHNOLOGY ADMINISTRATION, Mary L. Good, Under Secretary for Technology
NATIONAL INSTITUTE OF STANDARDS AND TECHNOLOGY, Arati Prabhakar, Director

National Institute of Standards and Technology Special Publication 839
Natl. Inst. Stand. Technol., Spec. Publ. 864, 225 pages (Sept. 1994)
CODEN:NSPUE2

U.S. GOVERNMENT PRINTING OFFICE
WASHINGTON: 1994

For sale by the Superintendent of Documents, U.S. Government Printing Office, Washington, DC 20402-9325

PREFACE

This Digest contains the manuscripts of 50 papers, 10 invited and 40 contributed, presented at the eighth Symposium on Optical Fiber Measurements, September 13-15, 1994, in Boulder, Colorado.

The invited papers were selected from about 50 nominations. The contributed papers were selected from 57 submitted.

The most significant theme of the Symposium is the present importance of polarization measurements. More than 20 percent of the papers are concerned either with polarization measurements, especially polarization mode dispersion and polarization dependent loss, or with the characterization of fibers and components with special polarization properties. Optical time-domain reflectometry (OTDR) measurements are another important theme, as they have been since the first Symposium in 1980, and the characterization of optical fiber amplifiers continues to be important. Nonlinear processes in fiber seem to be a growing interest.

Approximately two thirds of the papers come from outside the United States, up from about half at the seventh Symposium. Ten countries are represented in the program.

G.W. Day
D.L. Franzen
R.K. Hickernell
Boulder, Colorado
September 1994

SYMPOSIUM COMMITTEE

D.L. Franzen, NIST, General Chair

G.W. Day, NIST Program Chair

N. Channon, York

P. Di Vita, CSELT

R.K. Hickernell, NIST

M. Jinno, NTT

W.T. Kane, Corning

A.D. Kersey, NRL

R.B. Kummer, AT&T Bell Laboratories

P.S. Lovely, Photon Kinetics

S.A. Newton, Hewlett-Packard

S. Pollitt, NPL

S.B. Poole, University of Sydney

W.A. Reed, AT&T Bell Laboratories

P.R. Reitz, AMP

C. Saravanos, Siecor Canadian Cable

H.H. Yuce, Bellcore

CONTENTS

Noise Figure Measurement in Optical Fibre Amplifiers

Simon Poole
Optical Fibre Technology Centre, University of Sydney, NSW 2006, Australia

1 Introduction

Since the first reports of erbium-doped optical fibre amplifiers (EDFAs)[1,2] the key measurements required have been those of amplifier gain, output power and noise. The first two are relatively easily measured using a tunable source, attenuator and a spectrum analyser, with only minor compensation for the effects of Amplified Spontaneous Emission (ASE) at low input signal powers being required. Amplifier noise measurements are, however, more difficult due to the interaction of the signal with the ASE.

Amplifier noise is a critical parameter for in-line and pre-amplifiers. In the former, it is the cumulative effect of the noise which can limit system performance whilst in the latter additional noise leads to a decrease in receiver sensitivity. Noise contributions from power amplifiers are generally less critical, except for AM-TV distribution systems. Nevertheless, accurate measurements of noise figure are essential to both amplifier manufacturers and users to ensure optimum system performance.

In this paper, the origins of noise in fibre amplifiers are reviewed and the Noise Figure of an amplifier defined (Section 3.) Section 4 describes a range of techniques which have been developed for noise figure measurement in a production/test environment whilst Section 5 looks at the rapidly-developing area of in-service noise figure monitoring. The relative strengths and weaknesses of the various techniques are compared in Section 6. Throughout this paper, reference will be made primarily to the Erbium-doped Fibre Amplifier (EDFA) for operation at around 1.55μm although the techniques outlined can also be used, with minor modifications to account for the different excited-state lifetime, for noise measurements in Praseodymium-doped Fluoride Fibre Amplifiers (PDFFAs) around 1.3μm.

2 Origin of Noise in Amplifiers

Gain in an EDFA is obtained by optically pumping the electrons in erbium ions from the $^4I_{15/2}$ ground-state to the $^4I_{13/2}$ metastable, followed by ***stimulated emission*** when a signal photon is incident on the excited atom. This inversion can be achieved by pumping directly into the metastable level with light at 1.48μm[3] or indirectly through light at 980nm[4] Energy transfer mechanisms involving Er/Yb ions[5] can also be used and, for the purposes of the consideration of amplifier noise, can be considered to have the same performance as 980nm pumping.

However, if stimulated emission does not occur, the excited erbium ions will eventually decay spontaneously to the ground state with the emission of a photon which has random phase and direction and with a wavelength anywhere within the fluorescence spectrum of the amplifier. The photon may be captured by the fibre and amplified, leading to amplified spontaneous emission, which is unpolarised and the major contributor to noise in EDFAs.

The amplifier design (co- or counter-propagating pumps, single or double pumps, etc) and the choice of pump wavelength can significantly affect the amplifier noise figure. Generally, amplifiers pumped at 980nm have a lower noise figure[6] (theoretical minimum =3dB but typically around 3 - 4 dB in practical amplifiers) than those pumped at 1480nm (typically 5-7dB) since the former achieve a higher inversion of the erbium ion population than the latter.

The noise sources in a receiver for a signal that has been amplified by an optical amplifier can be summarised as:

Signal shot noise due to the intrinsic thermal noise of the source. This is usually small although for accurate definition of the amplifier *Noise Figure* (see below) this term must be included.

Spontaneous shot noise from the amplifier spontaneous emission. Again, this is usually negligible.

Signal-spontaneous beat noise caused by the mixing of the signal and amplified spontaneous emission which falls within the detector bandwidth. In a well-designed amplifier, this is the dominant term.

Spontaneous-spontaneous beat noise due to mixing of the amplified spontaneous emission with itself on a detector. This is the dominant noise term at very low signal powers but for a well-designed amplifier this contribution can generally be ignored.

Signal excess noise caused by multiple reflections from components inside the amplifier. This is primarily a problem for systems which employ narrow line-width sources of the type commonly found in AM TV distribution systems.

The noise figure *(NF)* of an amplifier is defined in terms of the signal to noise ratios measured with an ideal optoelectronic receiver as the optical bandwidth (and hence the contribution from spontaneous-spontaneous beat noise) is reduced to an infinitesimally small value and is defined as $NF = \lim_{B_0 \to 0} \frac{SNR_{input}}{SNR_{output}}$ where B_0 is the optical bandwidth of the receiver. For optical measurement techniques, it is generally necessary to simplify this definition by setting the measurement conditions such that signal spontaneous beat-noise is the dominant factor, giving a simplified noise figure of $NF \approx \frac{2\rho_{ASE}}{(G-1)h\nu}$ where ρ_{ASE} is the ASE power density with the same polarisation and wavelength as the signal, G is the optical gain and $h\upsilon$ is the photon energy. In practice, the receiver optical bandwidth is finite and the effect of spontaneous-spontaneous beat noise should be included. However, this contribution is typically less than the signal-spontaneous noise for optical bandwidths of around 5nm.

The exact definition of amplifier noise figure, including which minor terms need to be included, is still under discussion in various standards groups worldwide[7]. However, for the purposes of comparing the various measurement techniques, the exact definition is of secondary importance.

3 Noise Figure Measurement Techniques

Optical measurement techniques for amplifier noise measurement all require a measurement or estimation of the ASE noise component within the signal band. This measurement can be made optically through techniques such as spectral subtraction and interpolation (Section 3.1), polarisation nulling (Section 3.2), and pulse recovery techniques (Section 3.3) or electrically through RIN subtraction (Section 3.4) A number of points are common to all of the techniques. In particular, the effects of reflections and connections losses from the measurement or stimulus instrumentation need to be minimised to ensure accurate, repeatable measurements. In practise this is often achieved by splicing the amplifier under test to the measurement instrumentation to minimise any reflections[8].

3.1 Spectral Interpolation

Spectral interpolation is probably the simplest measurement technique for ASE estimation and uses an optical spectrum analyser to measure the ASE noise either side of the signal, with the ASE at the signal wavelength being interpolated either linearly or through a curve using *a priori* knowledge of the shape of the noise spectrum around the wavelength of interest (Fig 1). The simplicity of the technique allows measurements to be made rapidly but it is highly sensitive to source spontaneous emission, particularly in highly-saturated amplifiers. Furthermore, it cannot be used to characterise amplifiers (eg line or pre-amplifiers) which contain any form of narrow-band output filter. Spectral hole burning also limits the technique

to amplifiers which are homogeneously broadened, although this is not a problem for current generation EDFA and PDFFAs.

3.2 Polarisation Nulling

The polarisation-nulling technique[9] uses a linearly polarised input signal and the spectra at the amplifier output measured for both the polarisation of the transmitted polarised light and for the orthogonal polarisation. Since the ASE is randomly polarised, whilst the input signal is linearly polarised, measure the in-band ASE power on the orthogonal polarisation to that of the input signal can be measured. The experimental apparatus for this measurement is shown schematically in Figure 2.

Residual source laser sidebands can introduce significant error into the measurement and care must be taken to ensure maximum suppression of the sidebands using an in-line bandpass filter[10]. It should also be noted that, as for all of the techniques outlined, the source power should be varied through an external attenuator rather than through a varying drive current. This ensures that the ratio of source power to sideband noise is constant throughout the measurement.

Polarisation dependent gain or loss and polarisation mode dispersion can introduce errors into the polarisation nulling technique, particularly for measurements in highly saturated amplifiers. The first two create a polarisation-dependence of the ASE spectrum, whilst the latter can limit the degree of nulling of the amplified signal.

3.3 Pulse Recovery

In the pulse recovery technique[11] the principle of measurement is very simple; The input signal is chopped at a low frequency (typically 2-300Hz) but with a fast (<1 μSec) fall-time. Immediately after the signal is blocked, the ASE at the output of the amplifier is measured using a on opto-electronic converter and a digitising oscilloscope. A typical trace is shown in Fig 3. Since the ASE is measured when the signal source is blocked, there is effectively infinite rejection of the signal and any associated sidebands. Furthermore, the ASE is measured at the signal wavelength, thus obviating the need for any interpolation of measured values either side of the measurement wavelength. The technique has recently[12] been extended to provide accurate measurement of noise figure in the saturated regime. Measurements have been made with up to 15dB of gain compression with an accuracy of +/-0.5dB.

3.4 RIN Subtraction

Electrical measurement techniques use a comparison of the measured of the relative intensity noise (RIN) of a laser before and after amplification to provide a ***direct*** measurement of the noise contributed to a signal by the optical amplifier. This should be contrasted with optical technques which use an indirect measurement, with the measured parameters related to the actual amplifier noise, generally through some approximate expression. RIN is measured on an electrical spectrum analyser and is the noise measured electrical power per unit bandwidth normalised to the detected dc electrical power. For amplifier characterisation, it is udsual to choose a region of the laser noise spectrum away from any spectral features and the amplifier noise can then be determined by simply subtracting the noise of the source as measured without the amplifier from that measured when the amplifer is present. To obtain accurate measurements, a well characterised, very high quality optical receiver is required and considerable care must be taken to achieve repeatable results.

4 In-service noise-figure measurement

In service measurement of amplifier noise is a relatively recent development and hence measurement techniques for this are somewhat less developed than for laboratory or production measurements. Forward propagating ASE at wavelengths away from the signal wavelength using the technique shown schematically in Figure 4 has been demonstrated[13]. Here a small proportion of the ASE is tapped off and passed through a narrow band filter before measuring on a photodiode. To prevent cumulative errors due to ASE amplification in multiple amplifiers in the chain a band reject filter is placed in the signal line to reject the wavelengths used for monitoring. Despite the approximations required a measurement accuracy of +/- 0.05dB with a reproducibility of +/- 0.03dB was achieved for a wide range of input signal powers at a carefully controlled wavelength. The technique is extendable to other wavelengths but at a reduced level of accuracy due to the approximations used.

A second configuration uses a circulator to monitor the backward propagating ASE[14,15] (Fig 5). This has the advantage in that the ASE can be measured at the signal wavelength although the technique as described suffers from the need to assume uniform inversion along the amplifier. Since this is unlikely to be achieved in practice, there is a potentially significant error due to this assumption. The authors report that noise figures accurate to within 1dB of the measured forward propagated noise figure were achieved for input powers below -6dBm. The system is advantageous in that the measured power levels are significantly higher than for the previous example but suffers form the need to use a circulator, a device which is not yet available in commercial quantities or specifications.

A third alternative is the use of a shaped slit/integrating photodiode combination[16] which relies on the detection of side-scattered spontaneous emission along the fibre length, with the effective capture angle for the detector weighted as a function of position along the fibre. This technique is shown schematically in Figure 6. Calculations indicate an absolute accuracy of +/-0.08dB, although this was difficult to establish experimentally due to scatter in the measured results to which it was being compared.

5 Discussion

A number of techniques for amplifier noise figure measurement have been developed which can be broadly broken down into optical domain and electrical (RF) domain measurements. Whilst the latter are able to take into account all aspects of amplifier noise, including internal reflections, and provide a direct measurement of the amplifier noise figure, the former are more generally used due to their simplicity, ease of implementation and reduced measurement times. Table 1 below summarises the relative advantages and disadvantages of the techniques discussed above.

Technique	Advantages	Disadvantages
Signal Interpolation	Quick, easily implemented	Lack of traceability
Polarisation Nulling	Quick, accurate	Polarisation dependent loss/gain introduces errors
Pulse Recovery	Good in saturation	More complex technique
RIN Subtraction	Direct measurement of amp noise	Complex, can be operator dependent
In-service measurements	Real-time	Cost, complexity, are they necessary?

Table 1 Comparison of amplifier noise figure measurement techniques

There is still some discussion as to the need for in-service measurements of noise figure, since degradation of the pump laser (the most likely reason for amplifier performance degradation) is most easily detected by monitoring the amplifier output power, rather than the noise figure.

Despite the number of techniques which have been developed, there is no one procedure which has gained universal acceptance. This is due in part to the lack of direct, objective comparisons between the different techniques. To the authors' knowledge, only two studies have been reported[17,18] which have attempted to directly compare results obtained by both optical and electrical measurement techniques. This is clearly an area requiring further investigation and where the efforts of standards working parties can be of immense value to both the amplifier manufacturer and the amplifier users. Further agreement on the definition of amplifier noise figure may also be required before a definitive set of test methods can be develcped.

6 Acknowledgments

The author would like to thank many colleagues world-wide for assistance in the preparation of the manuscript. Particular thanks go to Steve Newton of Hewlett Packard, Paul Morkel of STC Alcatel and Richard Laming of the ORC, Southampton University for the supply of background information and to Ralph Betts and Steve Frisken of Photonic Technologies Pty Ltd for useful discussions.

7 References

1 R.J.Mears, I.M.Jauncey, L.Reekie, D.N.Payne, *"High-gain rare-earth doped fiber amplifiers at 1.54 μm"*, Proc OFC/IOOC87, paper WI2

2 E.Desurvire, J.R.Simpson, P.C.Becker *"High-gain erbium-doped travelling-wave fiber amplifier"* Opt.Lett., **11**, 1987, pp.888-890.

3 E.Snitzer, H.Po, F.Hakimi, R.Tuminelli, B.C.McCollum, *"Erbium fibre laser amplifier at 1.55μm with pump at 1.49μm and Yb-sensitised oscillator"* Proc OFC'88 paper PD-2.

4 R.I.Laming, S.B.Poole, E.J.Tarbox *"Pump excited-sate absorption in erbium-doped fibres"* Optics Lett., **13**, p.1084, 1988

5 S.G.Grubb *et al* Proc OFC'91 paper PD7.

6 R.Olshansky *"Noise figure for erbium-doped optical fibre amplifiers"*, Electron.Lett., **24**, 1988, p1363

7 eg WG6 of IEC-T686 on Optical Fibre Amplifiers

8 D.Baney, C.Hentschell, J.Dupre *"Optical fiber amplifiers - Measurement of gain and noise figure"* 1993 HP Lightwave Symposium,

9 J.Aspell, J.Federice, B.Nyman, D.Wilson, D.Schenk *"Accurate noise figure measurements or erbium-doped fibre amplifiers in saturation conditions"* Proc OFC'92, paper ThA4, 1992

10 T.Kashiwada, M.Shigematsu, M.Nishimura *"Accuracy of noise figure measurement for erbium-doped fiber amplifiers by the optical method"* Tech Dig Symposium on Optical Fibre Measurements 1992, pp209-212

11 D.M.Baney, J.Dupre *"Pulsed source technique for optical amplifier noise figure measurement"* Proc ECOC'92, paper We P2.11pp 509-512

12 K.Bertilsson, P.A.Andrekson, B.E.Olsson *"Noise figure of Erbium Doped Fibre Amplifiers in the Saturated Regime"* IEEE Photon. Technol. Lett.,vol 6, pp.199-201, 1994.

13 H.Masuda, K.Aida, K.Nakagawa *"Noise figure monitoring of a cascaded in-line erbium-doped fiber amplifier"* IEEE Photonics Tech. Lett., **5** 1993, pp.1436 - 1438.

14 Y.Sato, Y.Yamabayashi, K.Aida *"Monitoring the noise figure of EDFAs with circulators via backward amplified spontaneous emission"* Proc Topical Mtg on Optical Amplifiers and their Applications, Yokohama, Japan, 1993, paper MD-14

15 Y.Sato, Y.Yamabayashi, K.Aida *"Noise figure monitoring of optical amplifiers via backward amplified spontaneous emission"* IEEE Photonics Technol Lett, 6, 1994, pp. 203-204.

16 H.Masuda, K.Aida *"A novel noise figure measuring and monitoring method for erbium-doped fiber amplifiers with high resolution (0.01db) and short response time (50μS)"* Proc Topical Mtg on Optical Amplifiers and their Applications, Yokohama, Japan, 1993, paper MD-17

17 S.Nishi, M.Saruwatari *"Comparison of noise figure measurement methods for erbium-doped fiber amplifiers"* Proc ECOC '93, paper Tu3

18 F.W.Willems *et al "Comparison of saturated EDFA NF determination with the ESA and OSA methods"* Proc OFMC, Turino, paper 5.2, 1993.

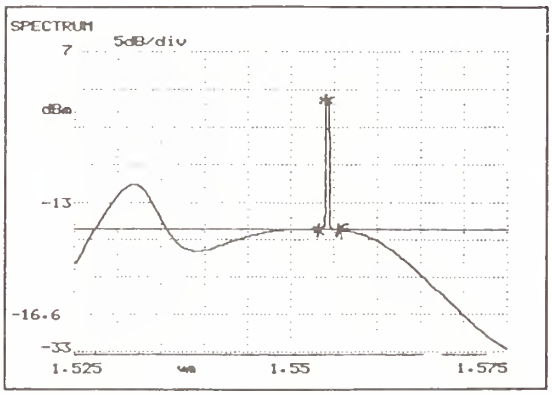

Figure 1 Spectrum Analyser trace of amplifier ASE and signal showing interpolation markers

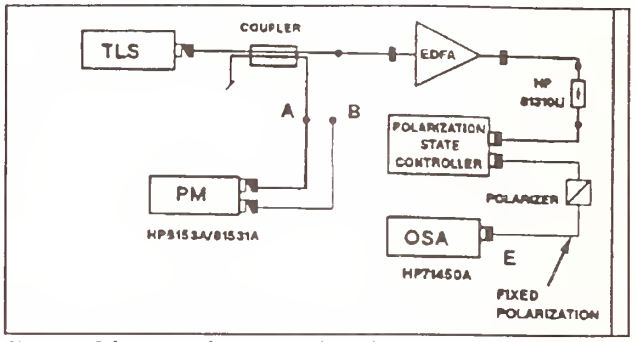

Figure 2 Schematic of apparatus for polarisation nulling technique (from [8])

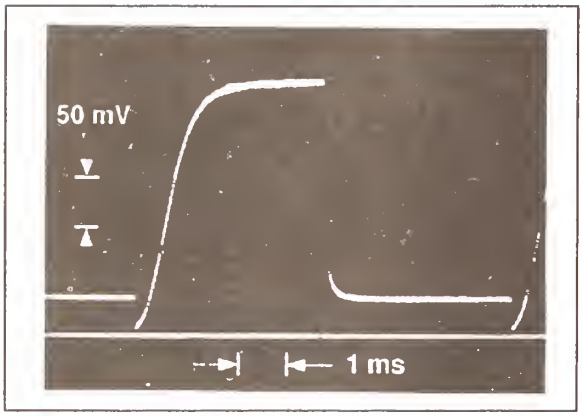

Figure 3 Typical measurement trace for pulse recovery technique (from ref 12)

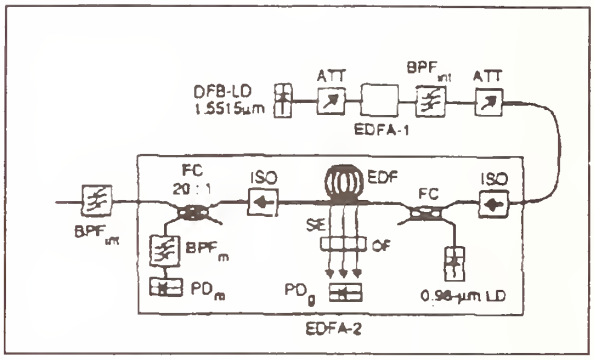

Figure 4 In-service noise-figure measurement technique due to Masuda [13]

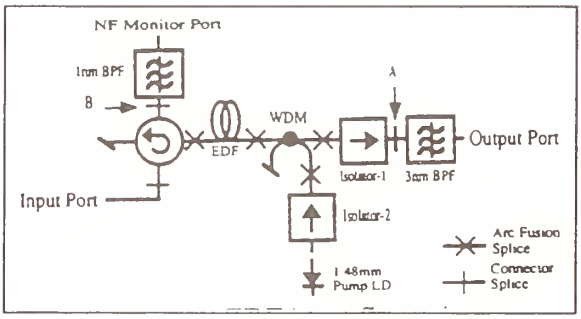

Figure 5 Circulator-based in-service noise figure measurement [14]

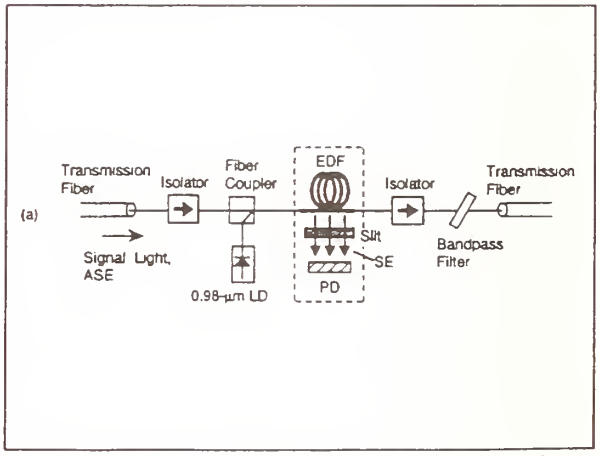

Figure 6 Schematic of integrating photodiodetechnique for in-service noise figure monitoring [16]

Optical Amplifier Noise Figure Determination by Signal RIN Subtraction

F.W. Willems and J.C. van der Plaats
AT&T Network Systems Nederland B.V.
P.O. Box 18, 1270 AA Huizen, The Netherlands

C. Hentschel and E. Leckel
Hewlett-Packard GmbH
Herrenberger Strasse 130, Böblingen, Germany

Abstract: A novel way to determine the noise figure of a saturated optical amplifier is presented, based on subtracting the EDFA input and output Relative Intensity Noise. The resulting noise figure is baseband frequency resolved and includes the contribution of interferometric effects caused by multiple reflections and Rayleigh scattering in the amplifier.

1 Introduction

The Noise Figure (NF) of an optical amplifier can, in principle, be determined using an Optical Spectrum Analyzer (OSA) by measuring the DC Amplified Spontaneous Emission (ASE) power and applying a theoretical relationship between this power and the noise figure [1]. Wavelength dependence is easily obtained with a tunable external cavity laser. Noise from Multiple Path Interference (MPI) at the signal wavelength [2] can be added if the reflectivities in the amplifier are known; however, this requires access to the EDFA internal components.

Alternatively, an Electrical Spectrum Analyzer (ESA) can be used to measure input and output Signal-to-Noise Ratios (SNR); subtracting the SNRs leads to the NF by definition. In this case, noise from MPI is automatically included. However measurement of the SNR at several electrical baseband frequencies is time consuming. In this paper we present a measurement method that has none of these disadvantages: the RIN subtraction (RINS) method. It combines high measurement speed, full automation potential and complete noise figure characterization.

2 Theory

The noise terms in a system using saturated optical amplifiers, taking into account all coupling losses are [3] signal shot noise, relative intensity noise caused by interferometric effects in the EDFA and signal spontaneous beatnoise, assuming a shot noise limited source (i.e. no signal laser RIN) and negligible receiver thermal noise.

$$N_{shot,signal} = 2e\eta_i G^* \eta_o L \rho P_o B_e \quad (1)$$

$$N_{s-sp} = \frac{4h\nu n_{sp}}{\eta_i P_o}\frac{G^*-1}{G^*}(\eta_i G^* \eta_o L \rho P_o)^2 B_e \quad (2)$$

$$= RIN_{s-sp}(\eta_i G^* \eta_o L \rho P_o)^2 B_e$$

$$N_{mpi}(f) = RIN_{mpi}(f)(\eta_i G^* \eta_o L \rho P_o)^2 B_e \quad (3)$$

with B_e the electrical noise measurement bandwidth, n_{sp} the spontaneous emission coefficient ($n_{sp} \geq 1$), e the electron charge, h Plancks constant, ν the optical signal frequency, η_i the input coupling efficiency of the EDFA, η_o the output coupling efficiency of the EDFA, L the coupling efficiency between the EDFA output and the receiver, G^* the internal optical gain of the EDFA, P_o the optical power just in front of the EDFA, $\rho = \frac{\eta e}{h\nu}$ the receiver responsivity (η being the detector quantum efficiency, including the coupling efficiency), $RIN_{mpi}(f)$ the relative intensity noise caused by incoherent interferometric effects in the EDFA.

The noise figure is defined by

$$NF = \frac{SNR_{in}}{SNR_{out}} \quad (4)$$

If we assume by definition that the detector is ideal, i.e. $\eta = 1$ and $L = 1$, and if we define

$G = \eta_i G^* \eta_o$ we arrive at

$$NF(f) = (RIN_{mpi}(f) + RIN_{s-sp}) \frac{P_o}{2h\nu} + \frac{1}{G} \quad (5)$$

The spectrum analyzer measures the total noise RIN_{total}, including the signal laser diodes noise $RIN_{LD}(f)$ which has to be subtracted and thus:

$$NF(f) = (RIN_{total}(f) - RIN_{LD}(f)) \frac{P_o}{2h\nu} + \frac{1}{G} \quad (6)$$

A detailed error analysis for the OSA method used in the HP 81600 EDFA test system shows that the total measurement uncertainty of the EDFA noise figure is 0.4 dB, which can be reduced to 0.25 dB if fusion splicing of the EDFA to the test system is applied [4]. The accuracy of the RIN subtraction method is limited by the amplitude accuracy of the modulated power trace, which is 2 dB electrical.

3 Experiment

The NF of a specially prepared EDFA, see figure 1, has been measured with the OSA and the RIN-subtraction method respectively. For the OSA method the HP 81600 Series 200 EDFA test system was used, incorporating a tunable external cavity laser (TECL), polarization insensitive optical spectrum analyzer and polarization nulling capabilities. The input power was -2 dBm, leading to a saturated condition in which ASE power is much smaller than the signal output power; that is important because the optical power measurement during the RIN procedure does not distinguish between signal power and ASE and secondly the RIN subtraction method presumes that spontaneous-spontaneous beat-noise is absent. For the RIN subtraction method a 1556 nm DFB laser with a linewidth of 1.5 MHz and a RIN below -160 dB/Hz were used. An HP 71400 lightwave signal analyzer set with RIN measurement software was employed.

Figure 1 shows the noise figure of the EDFA as a function of electrical baseband frequency for two settings of the Variable Optical Back-Reflector (VOBR): $R = -68$ dB and $R = -15$ dB. If $R = -68$ dB, the cavity reflectance is small enough to avoid interferometric noise and

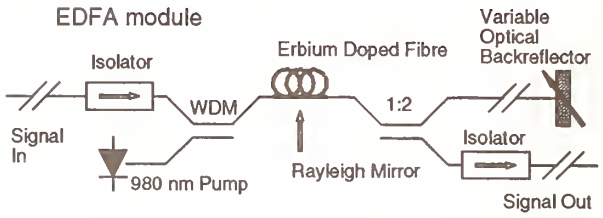

Figure 1: EDFA with internal Rayleigh Mirror and external Variable Optical Backreflector.

the noise figure is more or less independent of the electrical frequency. The data from the RIN subtraction method for R=-15 dB follow the curve as predicted in [5], indicating that the cause of the noise figure increase at lower frequencies is phase to intensity noise conversion due to optical cavities in the EDFA and that the length of the cavity is smaller than the coherence length of the laser. In this case the cavity is formed by the effective Rayleigh Mirror of the EDFA and an external Variable Optical Backreflector.

A simplified model for the interferometric noise assuming only incoherent mixing, is given by

$$NF = \left(RIN_{s-sp} + \frac{4}{\pi} R_{eff}^2 \frac{\Delta\nu}{f^2 + \Delta\nu^2} \right) \frac{P_0}{2h\nu} + \frac{1}{G} \quad (7)$$

With R_{eff} the effective cavity reflectance from, in this case, amplified Rayleigh scattering and the discrete mirror, including polarization alignment, $\Delta\nu$ the FWHM of the source linewidth (Lorentzian model). With an amplified Rayleigh scattering of -41 dB, we find, assuming perfect polarization matching of the direct and doubly reflected signals that $R_{eff} \approx -28$ dB; using this value in equation 7 gives the solid curve plotted in figure 2. The data from the OSA method are on a straight line by definition and approach the tail of the RIN subtraction data.

4 Conclusions

An EDFA noise figure measurement method has been described that is able to resolve Interferometric phase to intensity noise conversion due to the presence of optical cavities in a saturated EDFA. It is based on the subtraction of input

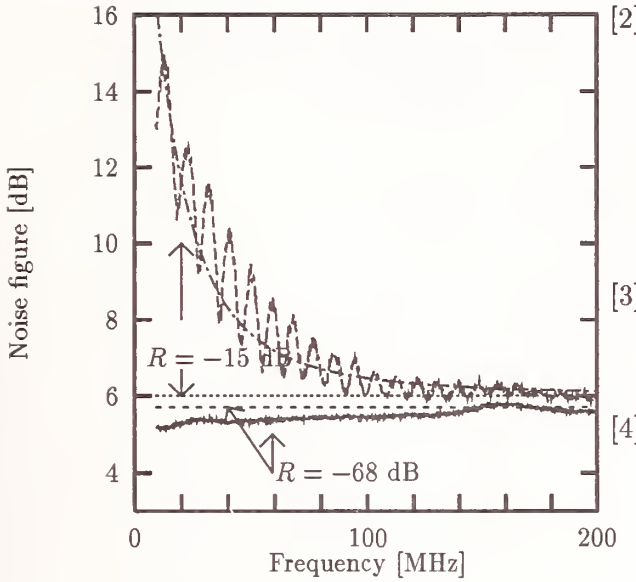

Figure 2: Noise figure as a function of electrical baseband frequency using the OSA method (straight lines) and the RIN subtraction method at a signal input power of -2 dBm at 1556 nm; the solid curve was obtained from modeling the reflections with equation 7.

and output Relative Intensity Noise that can be measured with a calibrated spectrum analyzer and thus gives at once the NF frequency resolved. The method gives results that are comparable with the OSA method when the influence of MPI is negligible.

Acknowledgement

This work was partly supported by the Commission of the European Union under the RACE II program, project R2062, "Components for Fibre to the Home (COMFORT)".

References

[1] J. Aspell, J. F. Federici, B. M. Nyman, D. L. Wilson, and D. S. Shenk, "Accurate noise figure measurements of erbium doped fiber amplifiers in saturation conditions," in *Digest of Conference on Optical Fiber Communications '92, San Jose*, pp. 189–190, Feb. 1992. paper ThA4.

[2] W. I. Way, C. Lin, C. E. Zah, L. Curtis, R. Spicer, and W. C. Young, "Multiple-Reflection-Induced intensity noise studies in a lightwave system for a multichannel AM-VSB television signal distribution," *IEEE Photonics Technology Letters*, vol. 2, pp. 360–362, May 1990.

[3] N. A. Olsson, "Lightwave systems with optical amplifiers," *IEEE Journal of Lightwave Technology*, vol. 7, pp. 1071–1082, July 1989.

[4] D. Baney, C. Hentschel, and J. Dupre, "Optical fiber amplifiers - measurement of gain and noise figure," Lightwave symposium, Hewlett-Packard, 1993.

[5] J. C. van der Plaats and F. W. Willems, "Relative intensity noise increase caused by amplified signal redirected Rayleigh Scattering in Erbium doped fibers," in *Digest of Conference on Optical Fiber Communications '94, San Jose*, pp. 158–160, Feb. 1994. Paper WM6.

The intricacies of an EDFA Round-Robin: First observations from COST-241 and RACE "COMFORT"

F.W. Willems
AT&T Network Systems Nederland B.V.
P.O. Box 18, 1270 AA Huizen, The Netherlands

Abstract: Fundamental differences between the ESA and OSA noise figure measurement method and the more "trivial" problems of measuring an EDFA's NF, such as calibration and definitions are discussed, based on observations made during a "mini" round-robin along five European laboratories. The differences between results can be attributed to calibration of the optical resolution bandwidth and absolute optical power as far as OSA is concerned. Major problems with the ESA method are in the proper handling of source noise levels.

1 Introduction

COST 241 "Characterization of Advanced Fibres for the new Photonic Networks" working group 3, study group 2 is currently performing an EDFA round-robin among the participants of this group.

The RACE R2062 "COMFORT", "Components for fibre to the home" project is developing EDFAs for analog applications. One task is to identify the measurement procedure for noise behavior taking into account all effects that can influence the system operation.

The common task of both COST 241-WG3-SG2 and COMFORT is to make a well defined measurement protocol. This requires a good knowledge of all the problems that are encountered in doing the measurement and those are often not foreseeable. Therefore we choose as a first approach to accompany the round-robin EDFA (RREDFA) with a person that could monitor how the measurements were performed and where the difficulties arose. We will report first observations and point out the pitfalls we discovered so far in the round-robin.

2 Noise Figure measurement Methods: OSA and ESA

In terms of input and output signal-to-noise ratio, the noise figure of an optical amplifier as measured by an electrical spectrum analyzer, is defined by

$$NF_{ESA} = \frac{SNR_{in}}{SNR_{out}} \qquad (1)$$

The signal-to-noise ratio at the EDFA input is determined by three noise sources: signal laser RIN, receiver shot noise and thermal noise; to make a comparison with the optical measurements possible, we require shot noise limited operation of the system, i.e. low intrinsic RIN of the laser and high input powers in the photodetector.

It can be shown [1] that the ASE level is related to equation 1 by

$$NF_{ESA} = \frac{P_{ASE}}{h\nu G B_o} + \frac{1}{G} \qquad (2)$$

assuming that the signal spontaneous beatnoise dominates (i.e. we use an optical filter in front of the system's detector or we operate the EDFA in saturation).

3 Fundamental differences between OSA and ESA

It has been pointed out previously [2] that differences in noise figure measurements by the ESA and OSA method are often caused by different definitions. However by identifying the proper relationships between the parameters that are measured by both methods, one can usually end up with comparable noise figures (see section 2). Unfortunately two fundamental differences in the ESA and OSA method have been identified. The first is related to the fact that it is impossible with the OSA method to measure the noise at the optical carrier frequency, whereas this is exactly what one does with the ESA method. The second is even more intricate and plays a role in saturated amplifiers only; it is related to the fact that the photon statistics of a saturated, non-linear EDFA differs from the statistics in the linear regime. (i) Interferometric noise caused by incoherent multi path interference is always present in EDFAs even when the utmost care is taken to prevent discrete reflections. Its source is Rayleigh scattering in the Erbium Doped Fibre itself. This kind of noise can only be detected by the ESA method and can influence the noise figure significantly [3]. (ii) The equations that relate the ASE power level to a signal-to-noise ration degradation have been derived in the regime where the EDFA

is not saturated [1]. It is show that when the real photon statistics in a saturated EDFA is taken into account by calculating the photon master equation, the noise figure can be significantly higher than the one calculated from the DC ASE power level [4][5]. Differences in noise figures from optical measurements that are converted to the CNR degradations by the conventional rules (see section 2) are mostly attributed to measurement errors, but could well be caused by phenomenon just described.

Both fundamental observations imply that the optical measurement method can not, from first principles, give a correct noise figure in all cases.

4 Measurement results

Since for the ESA method, knowledge of the exact gain is not required, some labs did not implement the gain measurement at this time. Therefore we will restrict ourselves in this paper to presentation of the noise figure measurement results. To compare the ESA and OSA values, we made use of the conversion equations mentioned in section 2 realizing that these are in principle wrong according to the observations in section 3.

The device used for the round-robin was a double 1430 nm pumped, temperature and pump current stabilized EDFA with input and output isolators to ensure that operation of the device is *not dependent on the residual reflection* in the measurement system. Further requirements are *long term stability* and *independence of temperature*. We measured the noise figure of the device over a period of six months and the values stayed in a 0.2 dB range. In doing the measurement we took care to use each time the same calibration procedure. The noise figure of the RREDFA is also hardly dependent on temperature as can be seen in figure 1.

First we will show the influence of two successive procedure changes we implemented. Refer to figure 2. Curve A was our first measurement using an optical spectrum analyzer with polarization nulling [6]. The ASE power was measured in an optical resolution bandwidth of ORBW=1 nm according to the OSA. When this bandwidth was calibrated using a tunable external cavity laser over a wavelength range it turned out that the "real" bandwidth varied between 0.965 at 1520 nm to 0.92 nm at 1560 nm. At a resolution bandwidth of 0.5 nm the situation was much better, since the variation was now between 0.505 and 0.485 nm which has hardly any influence on the noise figure anymore: for this particular spectrum analyzer the best ORBW is 0.5 nm. The influence of the change of ORBW from 1 nm to

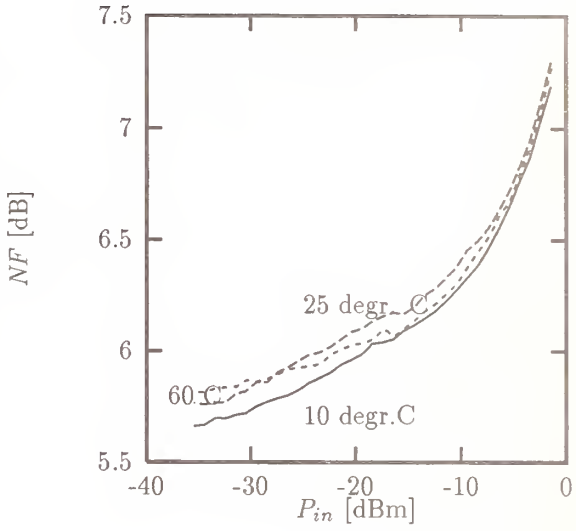

Figure 1: Noise figure as function of input power for 10, 25 and 60 degr. C

0.5 nm on the noise figure can be seen in trace B in figure 2. This trace is positioned around 0.4 dB higher than trace A as expected from the decrease in ORBW. Trace A and B were measured both using input power measured after the source connector and the EDFA output connector in open air. The power calibration was done by a power meter using a lensed photodetector. Changing to the definition of input power to fibre guided power and using a large area detector without any lenses led to trace C in figure 2. Trace C in figure 2 will be used as a reference line in the discussion that follows.

Five different labs up to now have measured the RREDFAs noise figure at a wavelength closely around 1555 nm. One lab used both the OSA (I) and ESA method (IA), three only the OSA method (II,III and V) and one merely the ESA method (IV). We have plotted the results in figure 3. Two following observations can be made from figure 3:

- Labs I and III use identical procedures in calibration and definitions. The noise figures they get are within a range of 0.3 dB, which is quite good.
- Lab II, the manufacturer, obviously is rather optimistic on its noise figure, this is most probably caused by a bad ORBW and absolute optical power calibration
- Lab V makes a large error in its optical bandwidth calibration which results in a large deviation from the rest of the data.

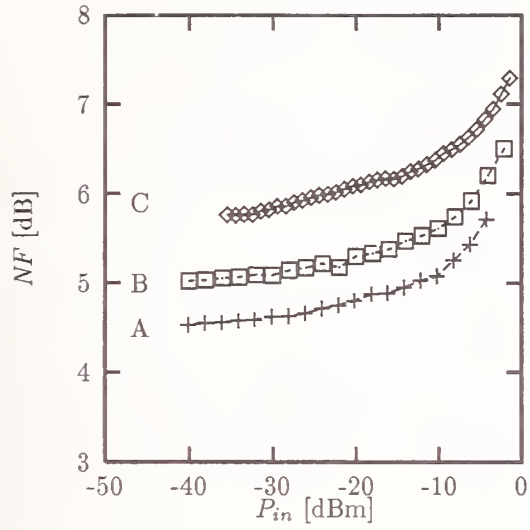

Figure 2: Noise figure measured by OSA method as a function of input power. Trace A first measurement; Trace B: second measurement after calibration of ORBW; trace C: third measurement after changing definitions of input and output power and using a large area detector for calibration of absolute optical power.

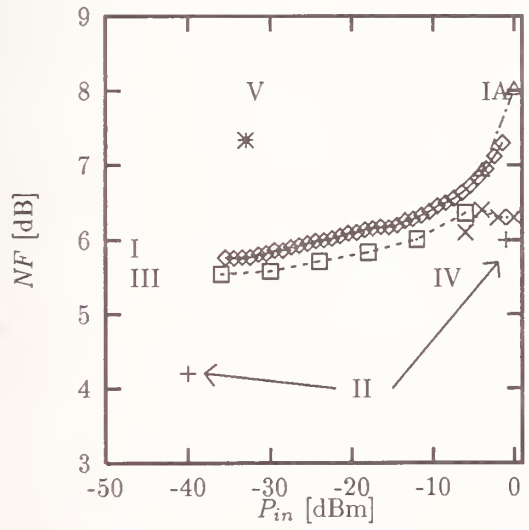

Figure 3: Noise figure as a function of input power as measured in five different labs. See text for explanation of legend.

- Lab IV uses the measurement of the carrier to noise ratio with an analog transmission system. The RIN of the laser is not low enough to be discarded, and input and output shot noise levels are different. This means that complicated corrections must be made resulting in data that are near the traces from labs I and II for the lower input powers, but deviate significantly for higher input powers, showing that conversion of the electrical data to the "right definition" is intricate.

- The measurement at lab I with the electrical method (IA), shows good agreement with the values obtained by its OSA measurement (trace I) for an input power of -5 dB. However for higher input powers the noise figure increases steeper. Whether this is caused by the fact that "inversion noise" start to play a role, as claimed in section 3 or simply by measurement error, remains to be investigated.

5 Items to be specified in the measurement protocol

The accuracy of the measurement depends of course on the accuracy of the equipment that is used. This accuracy is in turn is determined by proper calibration by the user itself, and the "intrinsic" accuracy of the system. The latter is related e.g. to scale fidelity, dynamic range of the equipment and cannot be controlled by the user in most cases. Next we will discuss the items that can and should be influenced by the operator of the measurement setup.

- *Connector:* The best way to avoid problems with connector losses is to avoid connectors by fusion splicing. However this requires a fusion splicer at every lab. Therefore the second best option is the use of a low-reflection connector. These can not be handled by every lab either. The approach we choose is that the coordinating lab receives the RREDFA back after each measurement, and supplies it by fusion splicing with the connector appropriate for the next round-robin candidate. The coordinating lab can characterize the connectors and thus track possible measurement differences caused by connector losses.

- *Input and output power location:* The power measured by a power meter is not the fiber guided power, but the fraction that leaves the fiber after the glass-air surface. The power entering the EDFA however is the fibre guided

power, minus connector losses of course. The differences between those two power levels are around 0.16 dB and influence directly the outcome of a noise figure measurement.

- *For ESA method: minimum input power:* To ensure that the signal spontaneous beatnoise dominates. If the input power in the EDFA drops below a certain level, sp-sp beatnoise starts to influence the total noise level. Although it is in principle possible to include this effect in the conversion equations, it adds an error source and should therefore be omitted for a round-robin.

- *For ESA method: RIN of the transmitter laser:* If the noise of the transmitter laser is not shot noise limited, which is usually the case when the laser's intrinsic RIN exceeds -155 dB/Hz, we need to know this RIN to correct for it in the calculations.

- *Optical Bandwidth Calibration:* The optical bandwidth directly enters the conversion equation 2. The bandwidth readout at the optical spectrum analyzer can not be trusted and is usually not the same over the whole wavelength range. Often there is one optimum bandwidth, where the calibration is optimal. It is prefered to do a careful calibration using a very narrow linewidth tunable laser.

- *Absolute power calibration:* The measured ASE level enters directly the conversion equation 2 and depends on the absolute power level calibration, which is usually done by a calibrated optical power meter. Differences can be caused by using a large area detector i.s.o. a lens coupled small area device.

- *Subtraction of source noise:* The amplified source noise can not be distinguished from the ASE noise power and should be subtracted from the measured ASE, either by calculation or by making use of the polarization properties of the source light.

6 Conclusions

Besides the fundamental differences between the ESA and OSA noise figure measurement method caused by the fact that photon noise statistics at high input powers differs from the assumed statistics and caused by the inability of the OSA method to measure interferometric noise, the more "trivial" problems of measuring an EDFA's NF properly have been discussed. This discussion was based on observations made during a "mini" round-robin along five European laboratories up to now. Most of the differences between the results can be attributed to using calibration of the optical resolution bandwidth and absolute optical power as far as OSA is concerned. Major problems with the ESA method are in the proper subtraction of source noise and handling different shot noise levels. Both the ESA and OSA method require clear definition of the positions where the optical power is measured.

Acknowledgements

The following individuals provided measurements: Chris van der Plaats, AT&T Network Systems Netherlands; Martin Kowatsch, Alcatel-SEL, Andreas Klar, Universität Kaiserslautern; Edgar Leckel, Hewlett-Packard Boeblingen. The discussions with Christian Hentschel and Edgar Leckel from HP were highly appreciated. This work was partly supported by the Commission of the European Union under the RACE II program, project R2062, "Components for Fibre to the Home (COMFORT)".

References

[1] E. Desurvire, "Analysis of noise figure spectral distribution in Erbium doped fiber amplifiers near 980 and 1480 nm.," *Appl. Opt.*, vol. 29, pp. 3118–3125, July 1990.

[2] F. W. Willems, J. C. van der Plaats, M. A. Jutte, and M. Babeliowsky, "Comparison of saturated EDFA noise figure determination with ESA and OSA method," in *Proc. of. Optical Fibre Measurement Conference, OFMC'93, Turin*, Sept. 1993.

[3] F. W. Willems, J. C. van der Plaats, and D. J. DiGiovanni, "EDFA noise figure degradation caused by amplified signal double Rayleigh scattering in Erbium doped fibres," *IEE Electronics Letters*, vol. 30, pp. 645–646, Apr. 1994.

[4] E. Jaunart, P. Crahay, and M. Blondel, "EDFA noise figure compuatation for small and large signals regime.," in *Digest of COST 94 Workshop Optical Telecommunicationsm, Nice, April 1994.*, pp. 264–267, Apr. 1994.

[5] E. Desurvire, *Erbium-doped fiber amplifiers.* John Wiley & Sons, 1994.

[6] J. Aspell, J. F. Federici, B. M. Nyman, D. L. Wilson, and D. S. Shenk, "Accurate noise figure measurements of erbium doped fiber amplifiers in saturation conditions," in *Digest of Conference on Optical Fiber Communications '92, San Jose*, pp. 189–190, Feb. 1992. paper ThA4.

Crosstalk in 1.3μm. Praseodymium Fluoride Fibre Amplifiers

S.C.Fleming

Optical Fibre Technology Centre, University of Sydney, Australia[1]

Abstract

Praseodymium doped fluoride fibre amplifiers have been demonstrated to be practical components for 1.3μm. telecommunications systems. This paper presents the first experimental measurement of the crosstalk performance of a Pr^{3+}:fluoride fibre amplifier. An experimental setup is described in detail. Measurement results are presented and compared with the results of a theoretical analysis. Good agreement between measurement and theory is demonstrated. Conclusions are presented concerning the implications of the measured crosstalk performance of these amplifiers for real systems. Furthermore, the first experimental evaluation of the lower state lifetime of the Pr^{3+}:fluoride system is derived from these measurements.

Introduction

Recently there has been much interest in praseodymium doped fluoride fibre amplifiers for use in the second telecommunications window. Gains of over 30dB [1] and saturated output powers over 200mW [2] have been demonstrated. More recently Nd:YLF lasers have been demonstrated as practical pump sources for efficient Pr^{3+}:fluoride amplifiers [3]. With excellent levels of gain and saturated output power demonstrated using practical pump sources there is now a need to examine other characteristics of these amplifiers, of importance to their application in real telecommunications systems.

Crosstalk is the transfer of modulation or information between two signals. This paper addresses crosstalk between two such signals, both within the gain band of the amplifier. This is an important parameter for amplifiers where there will be more than one signal within the gain band. Given the broad and relatively flat gain band of Pr^{3+}:fluoride fibre amplifiers they will be especially attractive for use in wavelength division multiplex systems where potentially many signals at slightly different wavelengths around 1.3μm. will be used simultaneously.

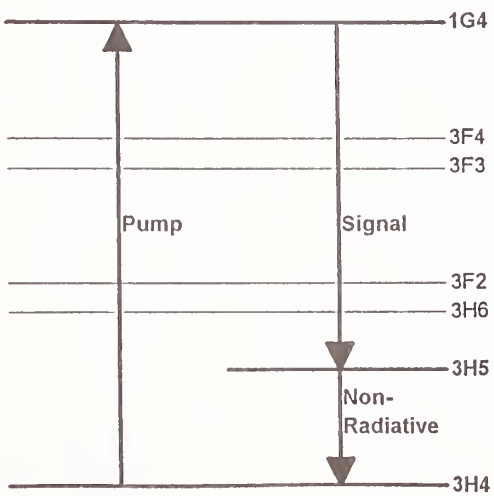

Figure 1 - Pr^{3+} Energy Levels

Figure 1 shows the energy level diagram for Pr^{3+}. Pumping at around 1μm. creates an inversion between levels $^1G_4$ and $^3H_5$ producing gain for signals around 1.3μm. Crosstalk involves the modulation of the inversion and hence the gain. A large signal around 1.3μm. in the amplifier will tend to reduce the inversion and hence the gain available to any other signals. If the large signal is modulated, the inversion and gain will pick up this modulation, approximately in anti-phase. Any other signals around 1.3μm. will thus experience a time varying gain and be modulated correspondingly.

---

[1] This work was carried whilst the author was with the Networks Research Division, BT Labs, Ipswich, UK.

Experiment

Figure 2 shows a schematic diagram of the experimental setup used in this work. An amplifier fibre consisting of 7m of ~0.2 NA, 500ppm Pr^{3+}:fluoride fibre was pumped with around 1W at 1010nm from a Ti:Sapphire laser through a wavelength division multiplexer (WDM). 7m is not the optimum length for such an amplifier and hence the pumped/unpumped change in transmission was around 22dB (giving an input/output gain of around 18dB). Unabsorbed pump light was blocked by a silicon filter in a beam expander. A pump block is essential since this high level (compared with the signals) of remnant pump has also picked up modulation since the pump absorption increases when the large signal pulls down the inversion. This pump block was later replaced with a high concentration ytterbium doped silica fibre which was found to be a better absorber for the remnant pump with lower losses at the signal wavelengths.

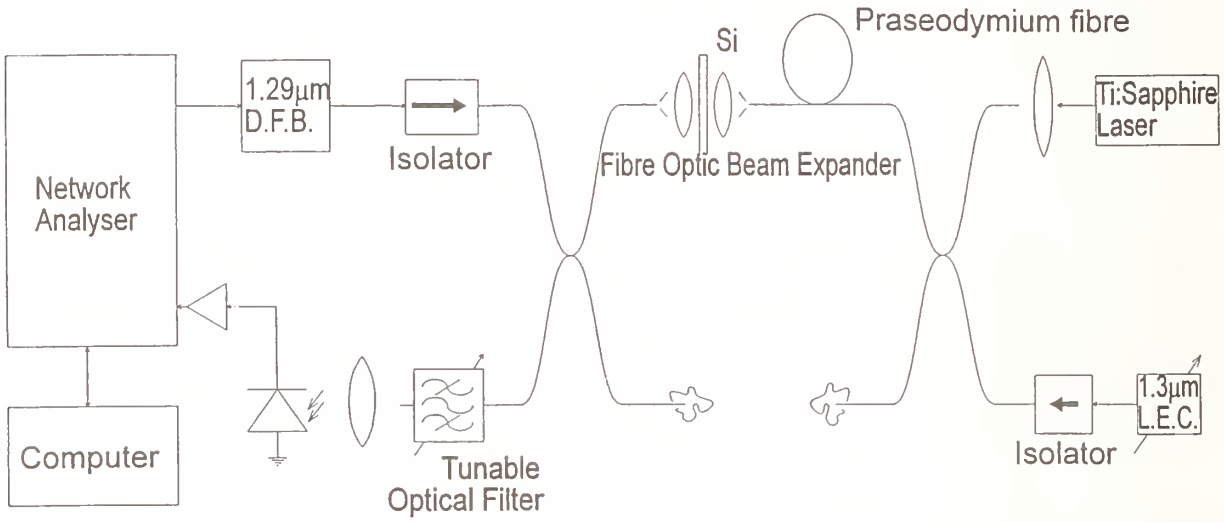

Figure 2 - Experiment for Measuring Crosstalk

A ~100µW, 1.31µm probe signal, from a tunable long external cavity laser, was launched, co-propagating with the pump, through the WDM. A 2mW, 1.29µm distributed feedback laser was modulated, from 5Hz to 200MHz, by a network analyser. The signal from this laser diode was launched via a coupler into the amplifier, counter-propagating with respect to the other two signals. Having the probe and perturbing signals counter-propagating significantly complicates the analysis of the transfer of modulation. However it also significantly simplifies the experiment in that it is much easier to separate these two signals (which are at very similar wavelengths and carrying the same frequency modulation) if they are not propagating in the same direction. It was necessary to use a very unbalanced coupler (~95/5%) in order to maintain a sufficiently high level of modulated signal within the amplifier to perturb the gain.

This large modulated signal reduced the gain, by around 1dB at the peak, resulting in a modulation transfer to the amplified probe signal. After passing through the pump-block filter, ~5% of the amplified probe signal is coupled off and passes through a tunable optical filter and onto a detector. Any back-reflected perturbing signal, amplifier ASE and remnant pump is blocked by the tunable optical filter. By tuning the optical filter and the probe laser, the spectral separation of the probe and perturbing signal could be varied and, in principle, any variation in crosstalk with spectral separation, due to inhomogenous broadening, could be measured.

A network analyser was used to process the amplified detector signal to give the amplitude and phase of the transfer of modulation from output to input. To calibrate the measurement system it was necessary also to measure the transfer functions of the electrical and electro-optical components and the finite length of fibre between the modulated laser diode, the detector and the amplifier input. This was performed by breaking the connection between the pump-block output and the amplifier input and tuning the optical filter to the perturbing signal wavelength. The ~4% reflection from the bare end of the pump block pigtail fibre could then be used to measure the response of these other components and hence to calibrate a crosstalk measurement.

Results and Conclusions

To analyse the measurement results it was necessary to develop a model for the crosstalk performance of a Pr^{3+}:fluoride fibre amplifier. Development of an exact analytic description of this is almost certainly an intractable problem. However, a perturbation analysis [4] of the rate equations yielded a set of approximate analytic equations describing the transfer of modulation to the inversion from a small modulated signal. A range of parameters were used in the evaluation of these equations and the results compared with those of an exact dynamic rate equation model. It was found that the perturbation analysis gives simple approximate analytic equations which agree well with the exact solution.

A full propagation model was written incorporating these perturbation equations. Using this model the steady state solutions for a pump and the mean levels of a perturbing signal and a non-perturbing probe signal throughout a fibre amplifier were calculated. Typical cross-section and lifetime values were used (τ_{21}=100nS, τ_{32}=110μS, σ_P=4.00×10^{-26}m^2, σ_S=3.48×10^{-25}m^2). Exact field shapes were taken into account but not amplified spontaneous emission. Steady state values of the pump and signal rates and the inversion at each point in the fibre were calculated and used to evaluate the analytic equations derived from the perturbation analysis. From this evaluation of the amplitude and phase of the crosstalk at each point in the fibre the overall crosstalk of the amplifier was calculated, taking into account whether the probe and perturbing signal were co- or counter-propagating with respect to each other.

Figure 3 shows a comparison of the measured and calculated results. Parameters matching those of the experiment were used to run the model. As can be seen there is excellent agreement, in both amplitude and phase, between the two data sets from low frequency to around 4MHz. This upper frequency limit was set by the measurement noise floor; at this frequency the crosstalk had decreased to a level where it could no longer be extracted from the noise. Extension of the measurement range to higher frequencies could be simply achieved by either increasing the perturbing signal level or the amplifier gain.

The general trends are as expected with the crosstalk amplitude essentially constant at low frequencies, rolling off at a frequency in the region of the inverse of the upper state lifetime (the exact position of this breakpoint is a strong function of the pump rate) and decreasing at 10dB/decade at higher frequencies. The crosstalk phase response starts in exact anti-phase at low frequencies moving to a $\pi/2$ phase lead at higher frequencies.

Some specific features of this response are of interest. At high frequencies on the phase plot the roll-off is due to the probe and perturbing signal counter-propagating. In contrast, it is found that in the co-propagating case the high frequency phase response tends to a $\pi/2$ phase lead. Despite this significant difference in the phase response, there is negligible difference in the amplitude response between the co- and counter-propagating cases.

At around 1MHz there is a distinct feature in the theoretical responses which is due to the lower state lifetime but occurs a decade lower in frequency than the inverse lifetime. Inspection of the measured response shows that this feature is not present for frequencies below 1MHz and is not apparent, above the noise, at higher frequencies. Hence an upper limit of around 50nS can be placed on this, previously unmeasured, lifetime.

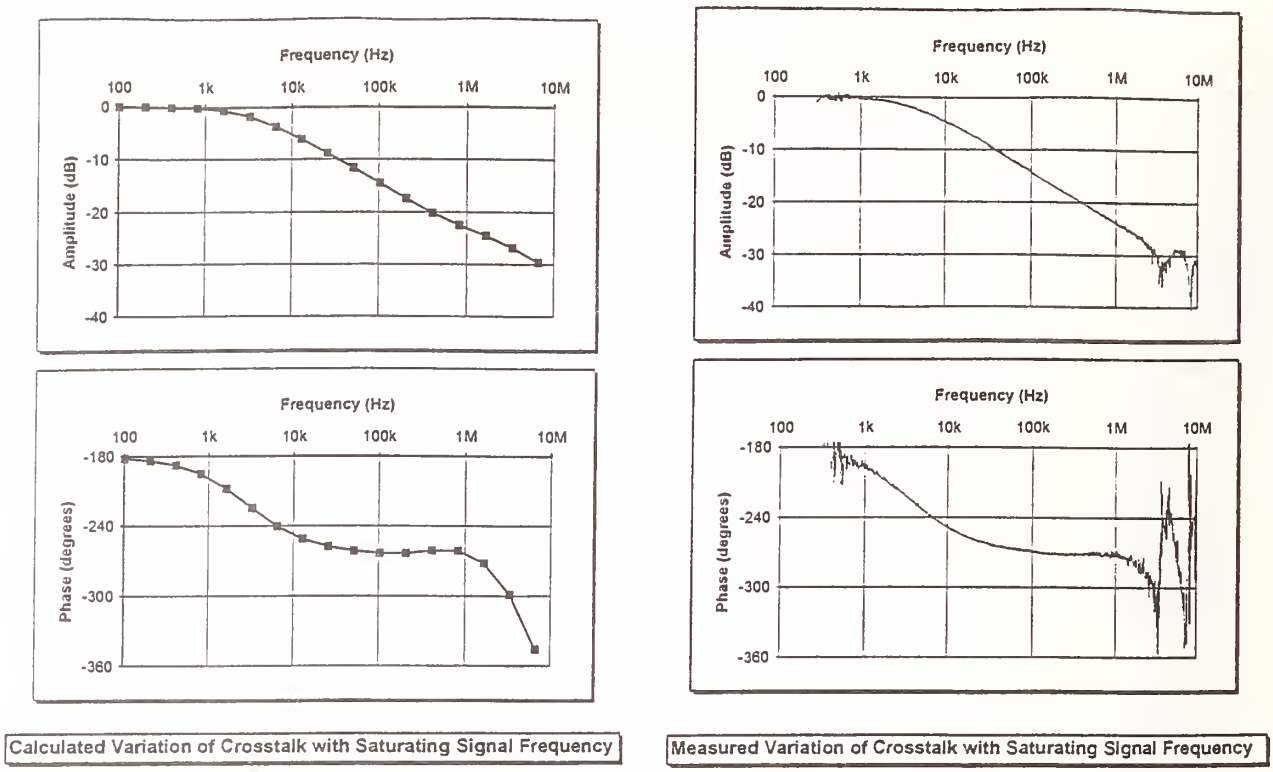

Figure 3 - Calculated and Measured Crosstalk

Conclusion

The general form of the crosstalk is very similar to that of an erbium doped fibre amplifier [5]. Hence, probably the most important conclusion of this work is that there are unlikely to be any new problems encountered with crosstalk in Pr^{3+}:fluoride amplifiers. Specifically, for digital systems operating at hundreds of MHz or more the crosstalk will be negligible. However as for erbium amplifiers problems may be encountered with low frequency supervisory signals or with analog systems.

It is also of significance that the lower state lifetime has been found to be at least four orders of magnitude smaller than the upper state lifetime. This indicates that there will be no significant problems with Pr^{3+}:fluoride fibre amplifiers due to "bottlenecking" [6] and that the effect that this level has on the crosstalk performance is negligible. This lifetime has not been previously measured since it is a non-radiative transition and not measurable by fluorescence decay.

Acknowledgments

The author gratefully acknowledges Richard Wyatt and Tim Whitley for many useful discussions. This work was funded in part by the Commission of the European Community, Project R2018.

References

1 - Y.Ohishi et al, IEEE Photonics Tech. Lett., 3, 8, pp.715-717 (Aug. '91)
2 - T.J.Whitley, OSA OAA'92, p8 (1992)
3 - T.J.Whitley et al, IEEE Photonics Tech. Lett., 4, 4, pp. 399-401 (Apr. '93)
4 - T.J.Whitley, private communication (Oct. '91)
5 - E.Desurvire, IEEE Photonics Tech. Lett., 1, 8, pp.196-199 (Aug. '89)
6 - W.P.Urquhart, IEEE J. Quantum Elect., 28, 10, pp.1962-1965 (Oct. '92)

MEASUREMENT AND COMPENSATION OF GAIN-PEAKING IN MULTI-AMPLIFIER LINKS

Evan L. Goldstein
Bellcore, Red Bank, NJ

ABSTRACT

The emergence of practical fiber-amplifier chains has raised the prospect of transparent lightwave networks, in which signals travel from source to destination through a sequence of intermediate nodes without optoelectronic conversion. When such networks employ multiple wavelengths, however, some of the most substantial new research challenges are those posed by the amplifier chains themselves. Such networks suffer from accumulating inter-channel power-spread, from sensitivity to inter-amplifier loss variations, and from transient cross-saturation, as the network undergoes reconfiguration. We here describe two different approaches to address these problems.

I. Introduction

Due to the superior noise performance, erbium-doped fiber-amplifiers (EDFAs) have demonstrated in single-wavelength point-to-point communications links, there is growing interest in employing EDFA cascades in reconfigurable multiwavelength networks that can be scaled to large size [1]. The chief obstacle facing such cascades arises from amplifier gain nonuniformities. Each amplifier provides gain, in dB, given by $G_{\mathrm{dB}}(\lambda) \sim \int_0^l [\sigma_e(\lambda) n_2(z) - \sigma_a(\lambda) n_1(z)] dz$, referred to below as the spectral gain equation. Here $\sigma_e(\lambda)$ and $\sigma_a(\lambda)$ are the emission and absorption cross-sections of the erbium ions, $n_1(z)$ and $n_2(z)$ are their lower- and upper-state linear population densities at position z along the amplifying fiber, and l is the amplifier's length [2]. The integrand of the spectral gain equation exhibits a wavelength-dependence imposed by $\sigma_e(\lambda)$ and $\sigma_a(\lambda)$, which are in turn determined by the spectroscopic properties of erbium atoms in silicate glass. While this wavelength-dependence can be modified, via $n_1(z)$ and $n_2(z)$, by adjusting pump power, input signal power, erbium-ion density, and fiber length, it cannot be eliminated. This implies that wavelength-multiplexed channels traversing a chain of nominally identical amplifiers will develop an inter-channel power spread that grows exponentially along the chain. This effect is illustrated in Fig. 1, showing the output spectrum after the first and last amplifier in a six-amplifier cascade. The five channels are equalized at the input of the cascade. After one amplifier a power spread of $\sim$ 3 dB is seen. The spread grows exponentially along the cascade and has reached

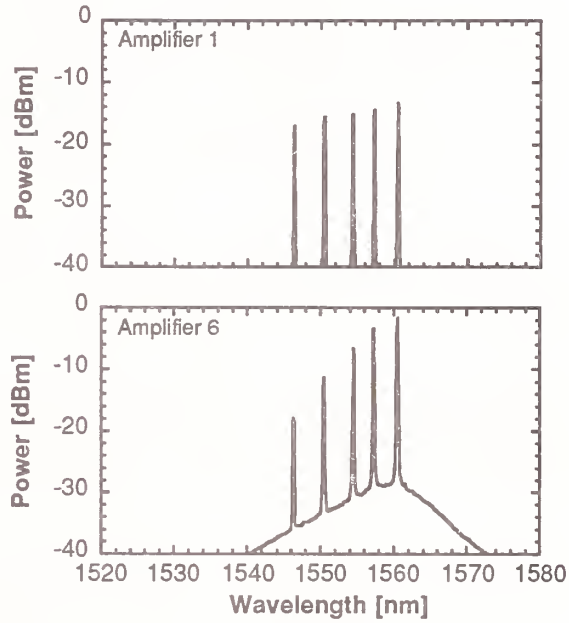

Figure 1: Inter-channel power spread accumulates through amplifier cascades.

$\sim$ 16 dB after the sixth amplifier. Thus, as a multiwavelength network is scaled up in size, channels residing off the gain peak will fall toward power levels that are undetectable in the presence of receiver noise or amplifier-induced beat noise or both.

Furthermore, there are significant additional challenges. In order to build amplifier chains that will suffice for large wavelength-division-multiplexed (WDM) communications networks, two additional problems must be surmounted. Like the problem of accumulating inter-channel power-spread articulated above, both of these are inherent in the spectral gain equation, and are thus more or less fundamental. The first problem is that variations in inter-amplifier loss result, via saturation, in variations of $n_1(z)$ and $n_2(z)$ in the system's amplifiers and consequently in the gain spectra $G_{\mathrm{dB}}(\lambda)$ of the individual amplifiers. These in turn accumulate to produce variations in the accumulated gain spectrum of the chain. Thus, WDM amplifier chains are not in general particularly robust in the presence of inter-amplifier loss-variations [3]. In single-wavelength cascades, this problem is elegantly addressed by operating the amplifiers at moderate-to-high levels

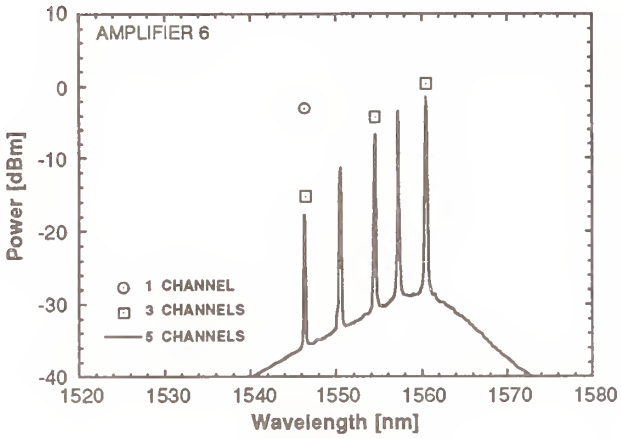

Figure 2: Dynamic cross-saturation arises when WDM channels are turned on or rerouted in optical networks with amplifiers.

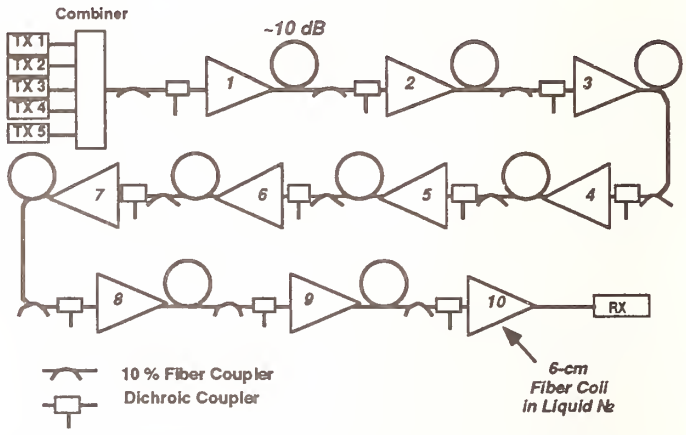

Figure 3: Experimental setup for investigating inhomogeneously broadened amplifiers.

of gain-compression, which provides automatic compensation for inter-amplifier loss-variations [4][5]. However, in multi-wavelength cascades, this tactic loses all of its effectiveness, since it serves to regulate only total optical power, not per-channel power.

The second problem is that when a transparent WDM communications system undergoes network reconfiguration, e.g. by adding or rerouting just one channel, the added power in this channel will stimulate emission and absorption in the first amplifier it encounters, altering $n_1(z)$ and $n_2(z)$ and thus, through (1), the amplifier's gain spectrum. Once again, these perturbations will accumulate along the chain of amplifiers. The result is that by adding or rerouting one channel in a reconfiguring WDM network, one perturbs other channels sharing all or part of the route. This is illustrated in Fig. 2 where the peak power levels of the individual channels are shown at the output of the six-amplifier cascade with one, three or five channels present at the input. The output power variation of the 1546 nm channel is 16 dB when the loading changes from just one channel to all five channels.

In the following sections, we discuss two different approaches to address these problems: cooled inhomogeneously broadened amplifiers and pump-shared amplifiers in parallel.

II. Accumulating inter-channel power-variations

When wavelength-multiplexed signals traverse a single fiber amplifier, the channels experience spectral gain variations that are generally modest. The serious problem, however, is that these variations accumulate from stage to stage, rapidly growing far too large to allow adequate noise performance at the less-favored signal wavelengths. Efforts to solve this problem have thus far centered on two approaches. In moderate-sized point-to-point systems, boosting the transmitter power for channels with low gain [6] is quite effective. However, this will not generally suffice in multipoint-to-multipoint lightwave networks (e.g. [7]) with dynamically varying signal paths, or in ultra-long-haul point-to-point links. One can also use various optical-filtering schemes to selectively attenuate high-gain channels [8][9]. However, in such schemes, inter-channel power variations still accumulate from stage to stage unless a separate active servo-loop is used for each wavelength.

We here show that when cooled, gain-saturated fiber amplifiers are placed in cascade, their gain is effectively clamped on a channel-by-channel basis by the propagating signals themselves, without the use of feedback arrangements or servo-loops [10]. The system thus behaves as a parallel overlay of independent amplifiers for the various channels. Furthermore, we show the effectiveness of using physically separated pump-shared amplifiers in parallel as a room-temperature implementation of per-channel amplification.

II.A Cooled inhomogeneously broadened amplifiers

Experiment. The experimental arrangement, shown in Fig. 3, consists of a cascade of ten erbium-doped aluminosilicate fiber amplifiers. Each is codirectionally pumped with ~11 dBm of light at 1480 nm giving a small-signal gain of ~ 14 dB. The 20-m-long doped fibers were wound into coils of 6-cm diameter, so they could be immersed in liquid nitrogen at ~77 K. Each fiber amplifier is separated from its successor by a transmission fiber with about 10 dB of loss. The transmission path contains neither optical filters nor, apart from the inhomogeneous amplifiers themselves, any special channel-power-equalizing components.

Results and Discussion. Five wavelength-multiplexed channels ranging from 1546 nm to 1560 nm, at −15 dBm per

channel, were coupled into the first amplifier. Inter-channel wavelength separations were about 4 nm, which is considerably larger than the measured ~1-nm homogeneous linewidth of the amplifiers at 77 K [11]. We measured the optical power spectra emerging from each amplifier stage under two conditions: with all amplifiers at room temperature (293 K), and with all at 77 K.

The plots in Fig. 1 show the output power of amplifiers 1 and 6 operating at room temperature. After amplifier 1, the signals vary in power by about 3 dB. However, after amplifier 6 the variation has accumulated to about 16 dB, with the weakest channel, at 1546 nm, transporting only about -18 dBm. Most importantly, the inter-channel power variations are accumulating rapidly as the signals pass amplifiers 1 through 6.

The trends are more clearly seen in Fig. 4, which plots the output power of the five wavelength-multiplexed signals versus amplifier number for the full 10-amplifier cascade. At room temperature (Fig. 4a), the inter-channel power spread accumulates at the rate of about 3 dB per stage, and totals 27 dB after amplifier 10. At 77 K (Fig. 4b), the signal powers spread out slightly in the first few amplifiers to about 5 dB by amplifier 4, after which the accumulation slows greatly. The accumulation is completely arrested, up to uncertainties imposed by experimental error, in amplifiers 7, 8, 9, and 10. It is worth noting that the cooled, inhomogeneous amplifier's saturation-output power is remarkably high, in view of the fact that each channel is coupled to only a subset of the fiber's erbium ions. Indeed, after the sixth amplifier, the weakest channel (1560 nm) still transports -5 dBm of power. Thus, in the inhomogeneous chain the signal powers not only converge toward a fixed or nearly fixed interchannel power spread; they also propagate at readily detectable power levels. In conventional, homogeneously broadened amplifier chains, whether saturated or not, the inter-channel power-spread monotonically accumulates from stage to stage, thus limiting system scalability. In a saturated, gain-decoupled chain, however, e.g. the above inhomogeneously broadened system, the per-channel powers asymptotically approach spatially fixed values. This provides automatic per-channel power-regulation, and prevents the spatially accumulating inter-channel power spread that prevents transparent WDM lightwave-communications networks from being scaled up in size.

II.B Pump-shared parallel amplifiers

We here show that the uncomplicated approach of placing pump-shared parallel amplifiers between a multiplexer pair

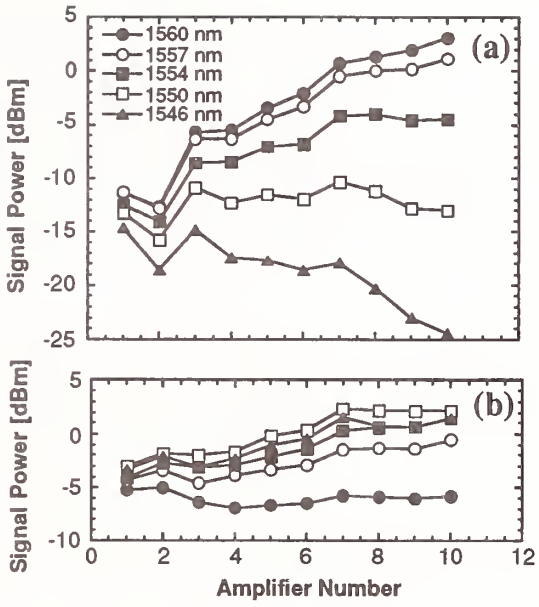

Figure 4: Per-channel output power vs. amplifier number for: a) Room temperature (293K) homogeneously broadened and b) cooled (77K) inhomogeneously broadened amplifiers.

stops the accumulating power-spread, so long as the amplifiers are properly configured. Moreover, if properly configured, no per-channel attenuators or servo-loops are required. Systems constructed from such modules self-adjust for transparency at each signal wavelength without servo-loops since the channels effectively have been gain-decoupled in the amplifier chain. Given a large inter-channel power spread, they will compress the spread in each amplifier module, rather than accentuating it. Although it is not widely appreciated that properly configured systems have these properties, the approach itself is based on well-known saturation phenomena. What is novel is the relative simplicity with which a fundamental problem, inherent in the gain dynamics of fiber amplifiers, can be addressed.

Experiment. To demonstrate the properties summarized above, we have performed measurements on the amplifier module shown in Fig. 5. Four twenty-meter lengths of erbium-doped fiber share a 70-mW 1480-nm pump laser, with each fiber receiving ~ 13 mW of pump light, and providing ~ 14 dB of small-signal gain at 1550 nm. The fibers were placed between interference-filter-based wavelength multiplexers having nearly flat, 1.5 nm passbands at the signal locations of 1546, 1550, 1554, and 1558 nm. Each multiplexer imposed 1.5 dB of insertion loss on each channel, and 27 dB of isolation between any pair of channels. Each dichroic coupler added ~1 dB of insertion loss at 1550 nm. Thus, when the assembled amplifier module was operated single-stage (i.e. without

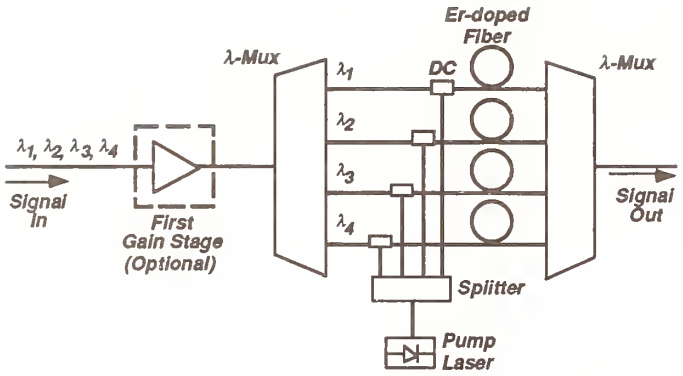

Figure 5: Experimental setup. DC: dichroic coupler. λ-Mux: interference-filter-based wavelength-multiplexer.

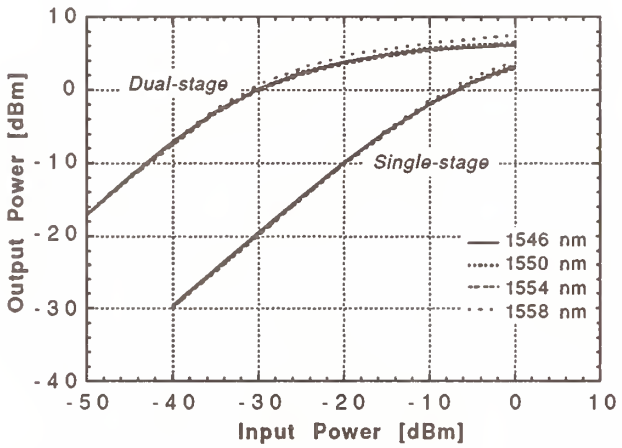

Figure 6: Per-channel input power versus per-channel output power for the single-stage and dual-stage amplifier modules, measured with all per-channel powers varied in unison.

the first gain stage), it provided each channel with a small-signal gain of 10.0 ± 0.2 dB. The optional first gain stage in Fig. 5 consisted of a conventional, bidirectionally pumped, single-stage fiber amplifier employing 40-mW, 1480-nm pump lasers and operated at a relatively strong inversion level of $n_2/n_1 \sim 3$ [12]. Its small-signal gain at 1550 nm was 25 dB.

Results and Discussion. Figure 6 shows the measured output power versus input power at each of the four channel locations for the single-stage amplifier module, and for the dual-stage module employing the optional first gain stage. Power levels were measured at the positions marked 'signal in' and 'signal out' in Fig. 5. At low input-power levels, little inter-channel power-spread is seen in Fig. 6. At high input power, the output-power spread approaches 0.8 dB in the single-stage module, and 1.5 dB in the dual-stage module. Power spreads of this magnitude are readily tolerated in communications systems. The question we wish to focus on, however, is that of 'scalability': does the inter-channel power spread accumulate from stage to stage?

The chief virtue of this system is that inter-channel power-spread does not accumulate from stage to stage, so long as the system is operated in gain-compression. On the contrary, when illuminated with signals at widely divergent per-channel powers, the system will tend to compress the inter-channel power-spread to a small, fixed value. We show this through measurements on a single amplifier module, since we were unable to perform measurements on cascades of them.

The performance of a cascade of single-stage modules is easily predicted to reasonable accuracy by using the fact that the per-channel gains are decoupled. One need only choose a value of the per-channel power P_{in} incident on each amplifier; this design choice will in turn be constrained by the accumulation of degradations due to spontaneous-emission noise and fiber nonlinearity. The target loss L between amplifier modules is then given implicitly by the expression

$$LG_0 \exp\left[(1 - L^{-1})(P_{\text{in}}/P_{\text{sat}})\right] = 1, \qquad (1)$$

obtained from Ref. [4] by setting the saturated gains of the modules equal to the losses between them. Here G_0 is the amplifier module's small-signal gain and P_{sat} is its saturation power, with all quantities in linear units and $L < 1$. Eq. (1) has a nonzero solution for P_{in}, provided that $G_0 > L^{-1}$; thus, the amplifiers must be operated in gain-compression. If L varies along the chain, P_{in} will also show variations, though these will be partly compensated by the compressed amplifiers' self-adjusting gains [4].

The single-stage curve of Fig. 6 in fact represents a measurement of the relations implicit in (2) if one sets $L = P_{\text{in}}/P_{\text{out}}$. Thus, choosing a reasonable input-power level of -10 dBm, Fig. 6 shows that an inter-amplifier loss of 8 dB ($= -2\text{dBm} + 10\text{dBm}$) should be selected. Given a set of per-channel powers incident on a cascade of such modules, their evolution along it can then be computed through iterative use of Fig. 6. An example is plotted in Fig. 7, where we have taken $[P^{\text{in}}_{1546}, P^{\text{in}}_{1550}, P^{\text{in}}_{1554}, P^{\text{in}}_{1558}] = [-20, -15, -5, 0]$ dBm, with 8 dB of loss between amplifiers. Although the amplifiers are gain-compressed by only ~ 2 dB, it is seen from Fig. 7 that the system rapidly power-equalizes. The inter-channel power spread, initially 20-dB, drops to ~ 10 dB at the input to the third module, thereafter approaching an equilibrium value of ~ 1 dB. The spread then remains fixed from stage to stage.

III. Transient cross-saturation

The last problem we address, transient cross-saturation, is unique to transparent amplified WDM networks that undergo physical network reconfiguration during normal system operation. It does not arise in point-to-point links. Although

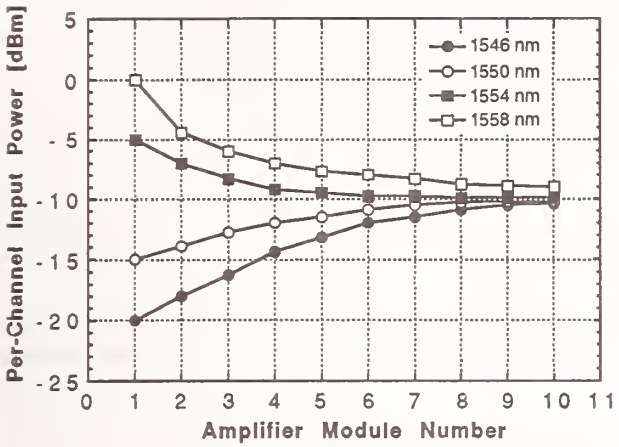

Figure 7: Calculated evolution of the per-channel power-levels along a cascade of single-stage modules.

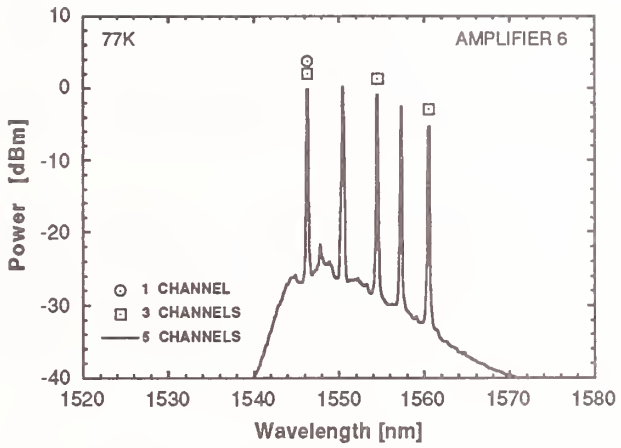

Figure 8: Transient cross-saturation in a cascade of six inhomogeneously broadened amplifiers.

transient cross-saturation in fiber amplifiers is a well-known phenomenon [13], it is widely believed that WDM systems employing fiber amplifiers are, in practice, immune from it due to the device's slow saturation dynamics. As has long been known [13], the saturation process in fiber amplifiers is characterized by a time constant of $\sim 300\mu s$; consequently, there is effectively no transient cross-saturation at frequency components higher than $\sim$ 5 kHz. This does indeed imply that amplified point-to-point high-speed WDM transmission links suffer no ill-effects from transient cross-saturation. However, amplified WDM lightwave networks are not immune if they undergo reconfiguration with Fourier components at kHz frequencies and below. This is in practice precisely where those Fourier components are likely to be, due to the slow, computation-intensive process of determining and broadcasting the network switch settings required for a given network reconfiguration. Thus, one must build into amplified multi-wavelength networks some mechanism which confers immunity to transient cross-saturation.

Clearly, inhomogeneous broadening, or more generally the decoupling of per-channel gain dynamics, provides such a mechanism. It is because of the homogeneous broadening of conventional fiber amplifiers that cross-saturation will arise in networks. If the amplifiers are instead inhomogeneously broadened, they will saturate on a channel-by-channel basis, leaving their signals unperturbed by turn-ons and reroutings at other wavelengths. Thus, inhomogeneous amplifiers not only help power-equalize a wavelength-multiplexed network; they also suppress the dynamic inter-channel cross-saturation that occurs during network reconfigurations [14].

This beneficial crosstalk suppression was again experimentally measured using the set-up of Fig. 3. Signal light from five wavelength-multiplexed lasers, transporting -15 dBm per channel, was sent into the first amplifier. Various signal channels were then switched on and off, simulating multi-access network reconfigurations. The signal spectrum was monitored at the output of each amplifier in the chain using the 10% probe couplers of Fig. 3. Figure 2 plots data taken for three system configurations: single-channel (1546 nm only), three-channel (1546, 1554, 1560 nm), and five-channel (1546, 1550, 1554, 1557, 1560 nm).

Figure 2 shows that when the homogeneous system is operated single-channel, reconfiguring to three channels results in a 12-dB drop in signal power at 1546 nm. Reconfiguring to five channels produces a 15-dB drop. This is due to homogeneous inter-channel cross-saturation in the cascaded amplifiers. The perturbations are enhanced by the fact that the 1546-nm channel lies well off the gain peak of the room-temperature amplifiers.

In the cooled, inhomogeneous system, by contrast, a power drop of only 2 dB occurs when reconfiguring to three channels, as shown in Fig. 8. A drop of 4 dB occurs when reconfiguring to five channels. Thus, when moving from single-channel to five-channel operation, the inhomogeneous amplifiers suppress inter-channel cross-saturation by about 11 dB. The improvement results from the decoupling of wavelengths in saturated, inhomogeneous, cascades. However, some homogeneous broadening is evident in the cooled system too; as a result, the single-channel and three-channel points in Fig. 8 do not lie precisely at the peaks of the five-channel spectrum.

As for the pump-shared parallel amplifiers, the single-stage amplifier showed complete decoupling of saturation dynamics for the various channels, as one would expect given

the multiplexer parameters stated above; its per-channel gain and output-power levels thus showed no measurable sensitivity to the number of channels incident on the module. The dual-stage module showed slight coupling, as one would also expect, due to gain-competition in the first stage.

IV. Summary

To summarize, we have seen that fiber-amplifier chains for reconfiguring WDM communications networks pose not simply the problem of the non-flat gain-spectrum, difficult though that problem in fact is. They instead pose a set of related challenges, all of which result from the non-flat gain-spectrum of erbium atoms in silicate glass, together with the homogeneous saturation properties inherent in the spectral gain equation of section 1. Transparent amplified WDM networks using conventional fiber amplifiers exhibit spatially accumulating inter-channel power-spread and sensitivity to changes in inter-amplifier loss. Moreover, when such systems undergo dynamic reconfiguration, they are vulnerable to transient inter-channel cross-saturation. These properties are inherent in the spectroscopy of the gain medium, and are thus reasonably thought of as fundamental.

Nonetheless, we have also seen that all three challenges can be addressed in one stroke if the per-channel gain dynamics of the amplifier modules can be decoupled, e.g. by employing an inhomogeneously broadened gain medium or by amplifying each channel in a physically separate amplifier. Saturation can then be employed to yield a system that power-regulates on a per-channel basis, rather than on a total-power basis. The result is an automatically equalizing system that not only arrests the inter-channel power-spread but also provides tolerance to inter-amplifier loss variations as well as reduces the transient cross-saturation present in transparent reconfigurable optical networks.

Acknowledgement. This work was partially funded by the Advanced Research Projects Agency (ARPA) under the Optical Networks Technology Consortium.

REFERENCES

[1] M. J. Karol, G. Hill, C. Lin, and K. Nosu, eds., Special Issue on Broadband Optical Networks, *IEEE J. Lightwave Technology*, vol. 11, May 1993.

[2] C. R. Giles and E. Desurvire, "Modeling erbium-doped fiber amplifiers," *IEEE J. Lightwave Technology*, vol. 9, pp. 271-283, 1991.

[3] E. L. Goldstein, L. Eskildsen, C. Lin, and R. E. Tench, "Multiwavelength propagation in lightwave systems with strongly inverted fiber amplifiers," *IEEE Photon. Technol. Lett.*, vol. 6, 1994.

[4] C. R. Giles and E. Desurvire, "Propagation of signal and noise in concatenated erbium-doped fiber optical amplifiers," *IEEE J. Lightwave Technol.*, vol. 9, pp. 147-154, 1991.

[5] N. S. Bergano, J. Aspell, C. R. Davidson, P. R. Triscitta, B. M. Nyman, and F. W. Kerfoot, "A 9,000 km 5 Gb/s and 21,000 km 2.4 Gb/s feasibility demonstration of transoceanic EDFA systems using a circulating loop," *Proc. Conf. Optical Fiber Commun.*, 1991, paper PDP-13.

[6] A. R. Chraplyvy, J. A. Nagel, and R. W. Tkach, "Equalization in amplified WDM lightwave transmission systems," *IEEE Photon. Technol. Lett.*, pp.920–922, 1992.

[7] C. A. Brackett, "The principles of scalability and modularity in multiwavelength optical networks," *Proc. Conf. Optical Fiber Commun.*, paper TuJ2, 1993.

[8] K. Inoue, T. Kominato, and H. Toba, "Tunable gain-equalization using a Mach-Zehnder optical filter in multistage amplifiers," *IEEE Photon. Technol. Lett.*, pp. 718–720, 1991.

[9] S. F. Su, R. Olshansky, G. Joyce, D. A. Smith, and J. E. Baran, "Gain-equalization in multiwavelength lightwave systems using acoutooptical tunable filters," *IEEE Photon. Technol. Lett.*, pp.269–271, 1992.

[10] E. L. Goldstein, V. da Silva, L. Eskildsen, M. Andrejco, and Y. Silberberg, "Inhomogeneously broadened fiber-amplifier cascade for wavelength-multiplexed systems," *IEEE Photon. Technol. Letts.*, vol. 5, pp. 543-545, 1993.

[11] E. Desurvire, J. L. Zyskind, and J. R. Simpson,, *IEEE Photon. Technol. Lett.*, pp. 246–248, 1990.

[12] E. L. Goldstein, L. Eskildsen, C. Lin, and R. E. Tench, "Multiwavelength propagation in lightwave systems with strongly inverted fiber amplifiers," *IEEE Photon. Technol. Lett.*, vol. 6, 1994.

[13] C. R. Giles, E. Desurvire, and J. R. Simpson,, "Transient gain and crosstalk in erbium-doped fiber amplifiers," *Optics Lett.*, vol. 14, pp. 880–882, 1989.

[14] E. L. Goldstein, V. da Silva, L. Eskildsen, M. Andrejco, and Y. Silberberg, "Suppression of dynamic cross-saturation in multiwavelength lightwave networks with inhomogeneously broadened amplifiers," *IEEE Photon. Technol. Letts.*, vol. 5, pp. 937-939, 1993.

OUT-OF-BAND ON-LINE MONITORING OF THE OPTICAL NETWORK

E. Cottino (*), M. Artiglia (**)

(*) AET Telecomunicazioni - Via Sestriere 130, Rivoli - Cascine Vica, Torino (Italy)
(**) CSELT - Via G. Reiss Romoli 274, Torino (Italy)

Abstract

The state of the art of monitoring systems for the external optical plant is reviewed. The various approaches proposed in the literature are discussed emphasizing the role of in-service non-intrusive monitoring systems, whereby the important function of preventive maintenance is accomplished. Existing systems and equipment are described with particular emphasis on the first out-of-band on-line monitoring system ever realised developed in Italy .

1. Introduction

A substantial improvement in the quality of telecommunication services is expected because of the superior performance of fibre optic cables. However, the huge amount of information that can be carried by systems based on optical fibre is setting requirements on system reliability which are much more stringent than usually encountered in traditional systems based on copper wire, particularly in view of the introduction of new broadband services.

In today's optical telecommunication systems, surveillance is made only on the received signal by measuring the Bit Error Ratio of the transmission, according to ITU-T (former CCITT) recommendations. No supervision of the physical carrier is considered, contrary to what happens with copper cables. As a consequence, repair is time consuming, costly and involves long service interruptions. Such situation, which can hardly be tolerated in inter-office trunks maintenance, may become intolerable for subscriber loop maintenance, where typically a very large number of fibres is involved and maintenance made while the system is in-service is preferable.

Supervision of the optical carrier offers a very promising solution to these problems [1-7], allowing to recognise immediately whether the fault is to be ascribed to the optical carrier and permitting the supervisor to localise promptly the damage with an efficient exploitation of field work. Another important advantage is that by a suitable choice of the maintenance wavelength window a continuous monitoring of the performance of the installed fibres is possible, which enables the supervisor to prevent degradation of the optical properties of the link and repair them before faults occur.

Scope of the paper is to review the state of the art of in-service non-intrusive monitoring techniques, with particular emphasis on an original technique developed in Italy, called *VDO* (*Valutazione del Degrado Ottico* , Testing of the Optical Degradation of the fibre plant). Advantages and drawbacks of the various techniques will be discussed; results of the first field trials will also be presented and commented.

2. Basic principles

The primary scope of remote monitoring of the external plant is that of detecting quickly from the central office a trouble or a critical situation which could lead to a fault, thus reducing the time in which the system is out of order. The general structure of an external plant maintenance system is comprised of three main parts: the testing system, the diagnostic system and the data base system. The testing system should be able to access automatically the fibres of a given cable and remotely measure their characteristics. The testing systems are distributed along the optical network. In principle, all the fibres of a link should be taken under surveillance, without affecting service, for as much time as possible in order to detect anomalies as soon as they occur. The testing equipment may be for example an OTDR machine or a power meter plus suitable optical sources for measuring fibre attenuation and/or other type of equipment (such as sensors for strain, temperature or humidity). Then, the detected anomalies are signalled to the diagnostic system, placed in the office, which processes the information and automatically requires, if necessary, further measurements on the damaged fibre(s) in order to understand nature and location of the fault. In this way network operators are able to analyse promptly the

trouble and initiate maintenance and administrative activities to accomplish repair and return to service in an efficient manner. Besides these corrective tasks, another important possibility opened by in-service surveillance systems is that of preventive maintenance. By means of a real-time evaluation of the parameters of in-service and not-yet-in-service links, early degradation of the optical properties of the fibre line can be promptly detected and removed, before the occurrence of service interruptions. This task can be accomplished very well by monitoring the fibre in the 1600-1650 spectral region as discussed below [6]. Advantages of out-of band monitoring versus traditional methods are summarised in Table 1. Then, information about faults is transmitted to a storage centre so as to create a data base containing all data pertaining to the network configuration. Automated and prompt input of this extremely voluminous and constantly changing data is mandatory. Manual update of the data base, besides requiring an enormous amount of manpower, is much risky, because of possible errors and delays which may cause the data base fail to reflect the actual status of the system. Finally the system must fit into the Telecommunication Management Network (TMN) and thus comply to existing TMN recommendations and standards.

The actual configuration and philosophy of the monitoring system will depend on many factors, such as the network characteristics and architecture, transmission equipment and operation windows.

3. Proposed approaches to remote optical plant monitoring

Various approaches to remote monitoring of the optical network have been proposed in the literature [2-6].

In a first approach, the aim is to detect only macroscopic damages of the optical cable, which could impair the proper operation of a large number of lines, as shown in Fig. 1a. To this end, the monitoring system make use of one or more fibres of the cable (one fibre per cable groove, for example) dedicated to the transmission of the monitor signal (dark-fibre approach). These systems cannot detect troubles of in-service fibres supporting the traffic, but only catastrophic damages of the cable itself. A drawback of the method is that a fraction of the fibres of the cable cannot be used for data transmission, thus reducing the transmission capacity of the cable itself. If the whole cable is to be put in-service, monitoring becomes impossible.

To overcome the limitations of the dark-fibre approach, different approaches have been devised which make use of in-service fibres to transport the monitor signal (see Fig. 1b). To avoid disturbing the transmission, the monitor signal must propagate in the fibre at a wavelength different from that used for the traffic. Therefore, suitable Wavelength Division Multiplexers (WDM) are to be used for monitor signal injection into each fibre. At the end of the line the monitor signal is demultiplexed and detected. In this way all fibres in the cable are kept under control. In this approach, the crucial element is the WDM, which must feature low crosstalk, low loss and low cost. As far as the allocation of the monitoring wavelength is concerned, the monitor signal can be transmitted at 1310 if the cable only supports systems operating at 1550 nm and viceversa if the supported systems operate in the second window. Problems may occur when the the cable supports mixed systems; in this case, information about the transmission wavelength on a given fibre should be available to the monitoring system, which should implement two optical sources and a double set of WDMs for switching on the right wavelength. Further problems may occur for WDM systems where, for example, telephony is transmitted at 1310 nm and CATV is distributed at 1550 nm. Allocation of a monitoring window outside the two spectral regions commonly used for transmission would solve all these problems, allowing the monitoring of full cables irrespective of the system characteristics.

Various transmission and detection techniques can be used for the monitor signal. A first class of approaches use point-to point transmission, with transmitter separated from the receiver (Fig. 1.c). The second is based on Optical Time Domain Reflectometry (OTDR) which allows for one-end access to the fibre (Fig. 1d). In this case, very low crosstalk WDMs are mandatory, since OTDR pulses are strong and may disturb the transmission.

The use of point-to-point transmission of the monitor signal makes it possible to have a continuous monitoring of the global attenuation of the fibre link under test. The

measured attenuation, may, for example, be compared with some stored reference values corresponding to proper system operation, so as to detect line interruptions or degradation of attenuation characteristics with respect to reference. This method is well suited for the maintenance of trunk network links, where the transmitter and the receiver are located in the exchange offices at the ends of the line to be monitored. To reduce the costs, the same receiver and/or transmitter can be shared by many fibres by using, for example, a suitable mechanical optical switch. In this way the fibres of a cable can be monitored cyclically by means of a fully automated equipment. As far as the distribution network is concerned, this method is practical only in a ring architecture; in fact, the dispersion of the many remote terminals in tree-structures distribution networks (such as PONs) makes the implementation of point-to-point monitoring quite difficult. On the other hand, in a tree architecture, surveillance by monitoring a dark-fibre may be applied to the feeder cable, from the office to the first distribution point.

Monitoring of the fibre line by means of OTDR equipment has the advantage of providing information about possible reflections and behaviour of the attenuation along the line, thus enabling possible critical points to be localised. Moreover, OTDR equipment requires access to only one fibre end and therefore may be used for monitoring tree-structured networks, even though special care must be exercised in analysing the OTDR trace when passive branching points are present. On the other side, the equipment is rather complex and costly. An effective way of reducing costs is using a mechanical switch to select periodically the fibre to be monitored; this allows a single OTDR equipment to be shared by large number of fibres. Some OTDR issues are still under study in view of their application in monitoring systems, such as improvement of spatial resolution, for subscriber loop applications, extension of dynamically range, for long distance, faster speed of operation and availability of optical sources if out-of-band surveillance windows are allocated.

Also the possibility of monitoring installed fibre stress by means of Brillouin Optical Time Domain Analysis has been proposed and is under study [7].

4. Equipment and field trials

The first generation of remote fibre test systems is already on the market, having been introduced in the early 90's by fibre optic test and measurement equipment suppliers. This equipment are likely to be deployed first in inter-office and feeder plant and only later on in high-density fibre areas such as the subscriber loop. Telephone network operators in USA, Europe and Japan are either deploying these machines or conducting field trials. The leading country today is Japan, where since 1990 nearly 300 monitoring systems have been installed, mostly for long-haul trunk routes [11].

The OTDR technique is the one most frequently used in the surveillance systems already developed or under study. This is the case of AURORA (Automatic Optical Fibre Operations and Support System) realised by NTT [8,9], the first optical plant maintenance system ever developed and deployed. AURORA provides automatic continuous monitoring of fibre attenuation of in-service fibres from the value of suitable reflections from the line terminals. AURORA, already deployed in Japan, is operating at 1310 nm for long-haul systems, where third window fibres are installed, and at 1550 nm in the subscriber loop, where distribution is performed in the second window.

A general approach similar to this is applied in equipments developed by USA suppliers, using dark or in-service fibres, although at a lower level of complexity.

Interesting advantages are offered by the OTDR based surveillance system, called VDO, developed in Italy by AET [12]. VDO has been devised to fit the Operation and Maintenance System of the Italian telephone operating company. In particular VDO is able to detect variations of the attenuation of fibre, connectors and splices which could affect the service. The main structure of the system is shown in Fig. 2. As can be seen the system is modular in order to gain flexibility and fit already existing office infrastructures. The main feature of VDO is that it is the first surveillance system which allocates an out-of-band monitoring window, placed in the long wavelength spectral region beyond 1600 nm. The reason for this choice is twofold. In the first place, the Italian optical network is based on two types of optical fibre, standard dispersion unshifted fibres operating around 1310 nm and dispersion shifted fibres operating around 1550 nm. Secondly, in the spectral region around 1600 nm fibres are more sensitive to

bending and stresses, so anomalies in transmission properties can be more easily detected. A wavelength of 1625 nm has been chosen, in order to measure fibre attenuation values very close to those around 1550 nm and guarantee a good isolation at the data transmission wavelength. To support these statements, a comparison of attenuation and splice loss measurements at 1550 nm and 1625 over a wide sample of installed optical fibres is given in Fig. 3 and 4. As can be seen, the differences are very small.

The system features an originally developed 240 fibre high-stability mechanical switch; an OTDR equipment implementing also a laser source at 1625 nm; WDMs able to multiplex or demux 1310 nm, 1550 nm and 1625 nm signals with very high isolation. The VDO operates on in-service fibres and spare fibres and gives periodically the behaviour of the total attenuation of the monitored link signalling occurring anomalies. A number of VDO machines has been deployed in Italy on the long distance network and field trials are in run. Transparent to data transmission has been demonstrated by field measurement of the system BER. BER curves of a 2.5 Gbit/s system measured in the field before and after the installation of the monitoring systems are given in Fig. 5, showing no significant degradation of the quality of the transmission after deployment. The possibility of preventive maintenance, thanks to monitoring at 1625 nm, has also been demonstrated in practice. Figure 6 shows the OTDR traces of a fibre placed in an installed cable which was accidentally damaged during operation. Trace 1) is the OTDR reference trace at 1625 nm before damaging. Traces 2) and 3) are the OTDR traces at 1625 nm and 1550 nm respectively, taken after damage occurred. As can be seen the 1550 nm trace doesn't show any degradation, while the 1625 nm trace shows a sudden drop of attenuation at the damage location. The attenuation drop is well inside the system margin, so no service interruption occurred. However, the fibres of the cable have been and still are subjected to an anomalous stress which could favour fibre breaks with consequent risk of service interruptions. This situation could not be detected by monitoring the cable at 1310 nm or 1550 nm, as AURORA or other proposed systems do.

5. Conclusions

The widespread use of optical fibre in long distance and inter-office network and the progressive introduction of optical fibre in the subscriber loop originated an ever increasing interest in test facilities of the fibre plant which guarantee a continuous monitoring of the fibre lines and operate when the system is live. Various solutions have been proposed. The most promising approach seems to be the continuous monitoring of in-service fibres by means of OTDR equipment operating in the 1600-1650 nm window. In this way, non intrusive preventive maintenance of the optical plant is possible. The first out-of-band in-service monitoring system, developed in Italy, has been presented. This area is rather new and much work is still to be done. Also other fibre properties besides attenuation, such as fibre strain, may be monitored, permitting on-line prediction of fibre reliability, and, last but not least, proper standards for the massive introduction of remote system monitoring in the telecom network are to be studied and issued.

References

[1] F.A. Huzarik et al, Proceedings of IW&CS pp. 158-162 (1988)
[2] H. Hornung et al., Proceedings of ICC 90, p. 341.5 (1990)
[3] Y. Koyamada et al., Proceedings of ICC 90, p. 341.1.1 (1990)
[4] H. Koga et al., Proceedings of ICC 91, paper 11A.3 (1991)
[5] P. Keeble et al, Proceedings of ICC 91, paper 11A.2(1991)
[6] I. Sankawa et al., Proceedings of IW&CS 92, pp. 81-87 (1992)
[7] T. Horiguchi et al., J. Lightwave Technol., vol. 7, pp.1170-1176 (1989)
[8] H. Matsumoto et al., Proceedings of IW&CS 91, pp.787-791 (1991)
[9] N. Tomita et al., Proceedings of EFOC 91, London, pp 130-134 (1991)
[10] H. Takasugi et al., Proceedings of IW&CS 90, pp.623-628 (1990)
[11] Marketing Intelligence, Fiberoptic, April 25, 1194
[12] E. Cottino et al. , Proceedings of IW&CS 93, pp. 799-804 (1993)

	MAINTENANCE PURPOSE	TRADITIONAL METHOD	OUT-OF-BAND MONITORING
PREVENTIVE	EVALUATION OF IN-SERVICE LINK PARAMETERS (FIBRES, SPLICES, CONNECTORS)	NO	YES (FROM MAINTENANCE CENTRE)
	EVALUATION OF NOT-IN-SERVICE LINK PARAMETERS	YES (MEASUREMENT IN LOCO)	YES (FROM MAINTENANCE CENTRE)
	EARLY DEGRADATION DETECTION	NO (MAY BE)	YES
	TIMELY DEGRADATION REMOVAL	NO	YES
CORRECTIVE	DETECTION OF DAMAGE (MAN/NATURE, TYPE, LOCATION)	NOT PRECISE	YES
	DETECTION TIME	HOURS	MINUTE
	AFTER REPAIR TEST AND RECORDING	MANUAL	AUTOMATIC (FROM MAINTENANCE CENTRE)

Table 1

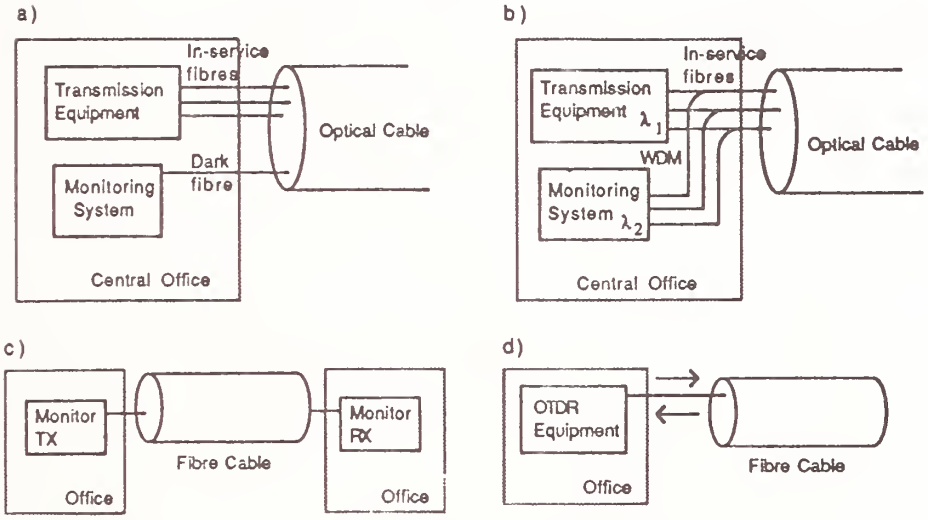

Fig. 1 - Review of monitoring techniques. See Section 3.

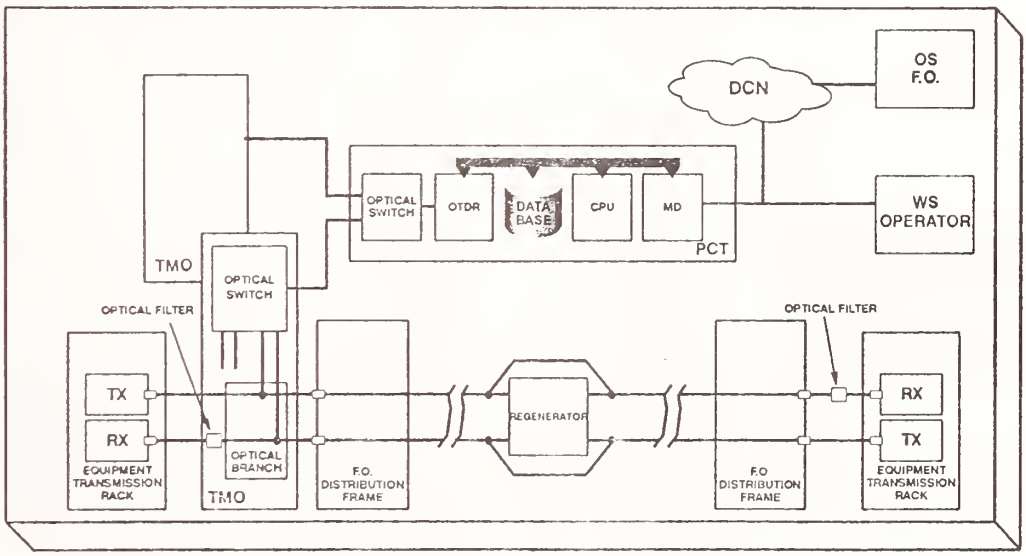

Fig. 2 - Schematic of the VDO system. PCT: local system controller; TMO: Optical Monitoring Rack Components; DCN: Data Communication Network; MD: Mediation Device.

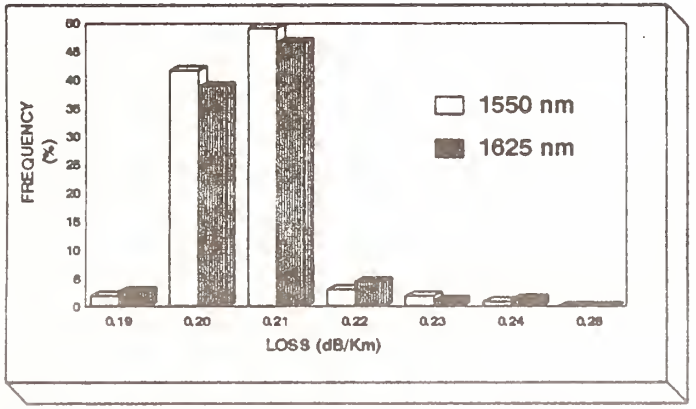

SAMPLES = 800	1550 nm	1625 nm	Δ(1625-1550)
AV. (dB/Km)	0.206	0.217	0.011
ST. DEV. (dB/Km)	0.007	0.008	0.001

Fig. 3 - DS fibre loss comparison at 1550 nm and 1625 nm.

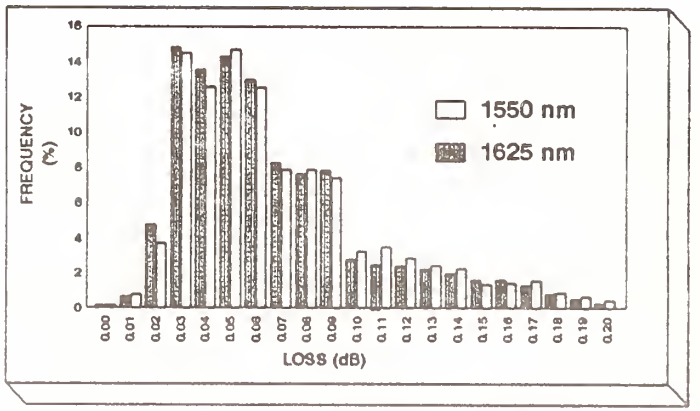

SAMPLES = 1740	1550 nm	1625 nm	Δ(1625-1550)
AV. (dB)	0.067	0.064	0.003
ST. DEV. (dB)	0.036	0.034	0.002

Fig. 4 - DS fibre splice loss comparison at 1550 nm and 1625 nm

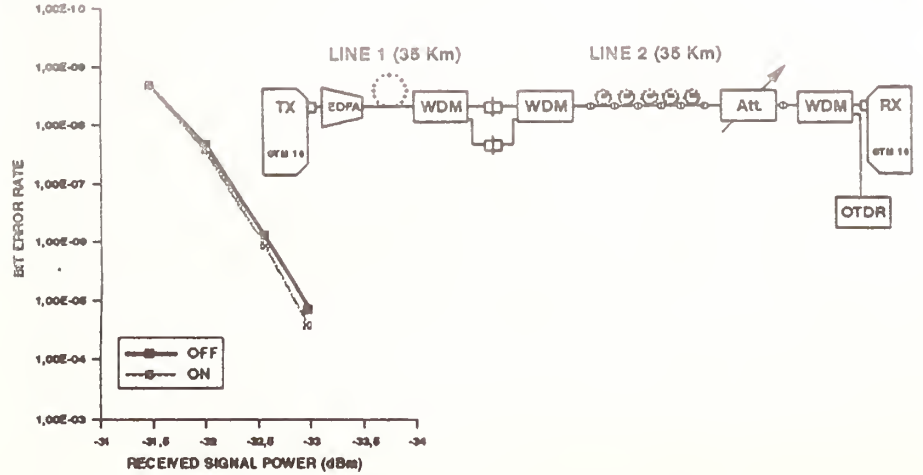

Fig. 5 - BER measurement on a monitored SDH fibre link operating at 2.5 Gbit/s with a booster EDFA. The repeater has been by-passed

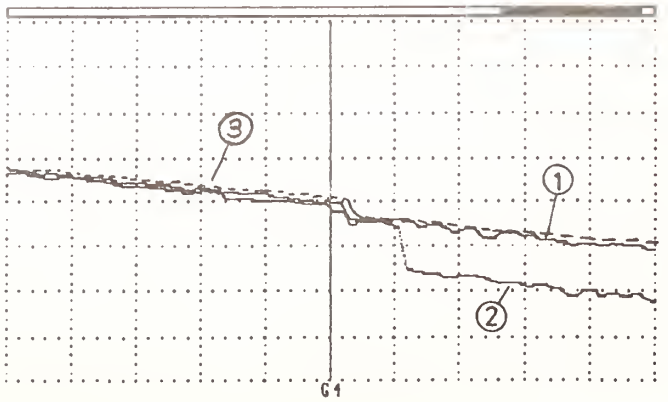

Fig. 6 - Monitored OTDR traces of a damaged fibre link: 1) reference trace at 1625 nm before cable damaging; traces after damage occurred: 2) 1625 nm, 3) 1550 nm (HSC: 400 m/div; VSC: 0.05 dB/div).

Multi-100 Gbit/s optical waveform measurement using sum-frequency-generation optical sampling with subpicosecond supercontinuum pulses

H. Takara, S. Kawanishi, T. Morioka, K. Mori and M. Saruwatari
NTT Transmission Systems Laboratories
1-2356 Take, Yokosuka, Kanagawa, 238-03 Japan

Introduction

Ultrahigh-speed optical waveform measurement becomes the key to evaluating ultrahigh-speed/long-distance optical fiber transmission characteristics [1]. Optical sampling based on optical nonlinearity is expected to realize the waveform measurement with subpicosecond temporal resolution. To date, several optical sampling methods have been reported based on sum-frequency-generation (SFG) [2][3], nonlinear optical loop mirror (cross-phase-modulation) [4] and four-wave mixing [5]. However, the temporal resolution was limited to 6~150 ps by the sampling pulse sources such as mode-locked external cavity laser-diodes, gain-switched laser-diodes and Nd:YAG lasers. Recently, we reported 0.63 ps resolution 100 Gbit/s optical waveform measurement using SFG optical sampling with subpicosecond (0.55 ps) sampling pulses by supercontinuum (SC) generated in an optical fiber [6].

In this report, we demonstrate the successful waveform measurement of a 400 Gbit/s optical signal with the improved resolution of 0.44 ps by shortening the pulse duration of the SC sampling pulses down to 0.30 ps. This optical sampling system can measure, with good linearity, optical signal waveforms over wavelength ranges of more than 25 nm around 1.55 μm. Also discussed is the S/N characteristics of the proposed method.

Experiments

Figure 1 shows the experimental setup, which is based on that of the previous report [6]. Summarizing the configuration of the previous setup, 3.0 ps, 0.9 nm bandwidth optical pulses from a mode-locked Er-doped fiber (ML-EDF) laser were converted into SC pulses in an SC fiber [7]. 1559 nm-wavelength subpicosecond sampling pulses were obtained by filtering the SC pulses. The signal pulses were also generated by the same SC technique. The repetition rates of the signal and sampling pulses were set to 6.3 GHz and 6.3 GHz minus the frequency offset of 50 Hz, respectively. The 6.3 Gbit/s signal was multiplexed to the 100 Gbit/s signal with a planar-lightwave-circuit multiplexer (PLC-MUX) [8]. The sampling and signal pulses were combined by a polarization beam splitter (PBS) and injected into a $KTiOPO_4$ (KTP) crystal. Type II phase-matching SFG was used to eliminate the unwanted second harmonic light generated from the sampling or signal light because two orthogonal polarization lights are needed for phase-matching [3]. The crosscorrelation signals (the SF light) at 777 nm were detected with a photomultiplier tube and the sampled waveform at a repetition frequency of 50 Hz was displayed on an oscilloscope. The details are described in the previous report.

To upgrade this basic setup, we shortened the sampling pulse duration to improve the temporal resolution; the goal was measurement at 400 Gbit/s. Shorter sampling pulses were obtained by compensating the chirping of the SC pulses with a 190 m, 1.3 μm zero-dispersion fiber (Comp. fiber) and by filtering these pulses with a 3nm Lorentzian shape bandpass filter (BPF) [9]. An autocorrelation trace and the optical spectrum of the sampling pulses are shown in Fig. 2. The calibrated pulse duration t_{sam} and spectral bandwidth were 0.30 ps and 3.1 nm, respectively. The time-bandwidth product $\Delta t \cdot \Delta \nu$ was calculated to be 0.12, close to that of the single sided exponential decay shape transform-limited pulses ($\Delta t \cdot \Delta \nu = 0.11$). The peak power of the sampling pulse P_{sam} was amplified to 1.06 W by an Er-doped fiber amplifier (EDFA).

In order to generate the 400 Gbit/s optical signal from the 100 Gbit/s optical signal, two polarization maintaining fibers (PM1 and PM2) with polarization dispersions of 15 ps and 7.5 ps, respectively, were used as an additional 4:1 multiplexer. At the connecting points (A, B and C in Fig. 1), the principal axis offsets were set to 45 deg. in order to make the single polarization state 400 Gbit/s signal. The original signal pulse duration t_{sig} of 0.45 ps was increased to 1.4 ps by the 6.3 Gbit/s to 400 Gbit/s multiplexing. This is mainly attributed to the influence of filtering with a 10 nm BPF to eliminate the amplified spontaneous emission of EDFA at the polarizer output. The amplified peak power P_{sig} was 40 mW.

Results and discussion

Figures 3 shows the measured waveform of the 400 Gbit/s optical signal. This optical sampling system well measured the data pattern "0100101101101l0" with the measured pulse duration t_{meas} of 1.5 ps. The temporal resolution t_{res} of the measurement system was given by,

$$t_{res} = (t_{meas}^{\ 2} - t_{sig}^{\ 2} - j_{sig}^{\ 2})^{1/2} \qquad (1)$$

where j_{sig} is the timing jitter of the signal pulses. From the measured j_{sig} of 0.31 ps, t_{res} was estimated to be 0.44 ps. This value well agrees with the calculated value considering the pulse duration (t_{sam} = 0.30 ps) and the timing jitter (j_{sam} = 0.30 ps) of the sampling pulse (0.42 ps = $((t_{sam})^2 + (j_{sam})^2)^{1/2}$).

As seen in Fig. 3, background-free detection was realized because of type II phase-matching. Please note that no optical filter was used for extracting the SF light in this experiment. This means that this method can measure the optical signal waveform at any wavelength, even the same wavelength as that of the sampling light. The signal wavelength dependency of the SF light level is shown in Fig. 4. The change of the SF light level was less than ±5 % for the wavelength range from 1535 nm to 1560 nm. This result shows that this optical sampling method has a wide signal wavelength tolerance of more than 25 nm around 1.55 μm. Fig. 5 shows the relationship between the crosscorrelation signal (SF light) levels and the input signal peak powers. The crosscorrelation signal levels were proportional to the signal peak power up to 400 mW. It is clear that this scheme realizes optical waveform measurement with good linearity.

The SN ratio of type II phase-matching SFG optical sampling is given by [3]

$$\frac{S}{N} = A\ \eta_{sfg} P_{sam} P_{sig}$$

$$A = \frac{K\eta_q}{2} \cdot \left(\frac{\lambda}{hc}\right)\left[B^2 + 2\left(\frac{ln2}{\pi\tau}\right)^2\right]^{-\frac{1}{2}} \qquad (2)$$

where η_{sfg} is the SFG conversion efficiency, K is the averaging number, η_q is the quantum efficiency, λ is the wavelength of the SF light, h is Plank's constant, c is the velocity of light, B is the bandwidth of the photomultiplier, and τ is the pulse duration of the SF light. Here, we assume that shot noise is much larger than any other noise, such as thermal noise in the photodetector. η_{sfg} of the KTP crystal was measured to be 6 x 10^{-5} W^{-1}. λ, B and τ were 777 nm, 1 kHz and 0.30 ps, respectively. The calculated SN ratio of one shot (K = 1) is 0.3 and this value is too small to measure optical signal waveforms. In this experiment, the SN ratio was improved by the averaging performed in the photomultiplier. Accordingly, the averaging number K was the ratio between the SF light repetition frequency f_{rep} of 6.3 GHz and the photomultiplier bandwidth B of 1 kHz ($K = f_{rep}/B$ = 6 x 10^6), so the high SN ratio of 2 x 10^6 was realized.

Conclusion

We have demonstrated the successful measurement of a 400 Gbit/s optical signal waveform by using type II phase-matching SFG optical sampling with SC pulses. The temporal resolution was improved to 0.44 ps by utilizing 0.30 ps chirp-compensated SC sampling pulses. This optical sampling system can measure, with good linearity, optical signal waveforms over wavelength ranges of more than 25 nm around 1.55 μm.

Acknowledgment

The authors would like to thank Dr. Hideki Ishio for his encouragement.

References

[1] S. Kawanishi, T. Morioka, O. Kamatani, H. Takara and M. Saruwatari, Tech. Dig. OFC'94, PD-23 (1994)

[2]. T. Kanada and D. L. Franzen, Opt. Lett., **11**, pp. 4-6 (1986)

[3]. H. Takara, S. Kawanishi, Y. Yamabayashi and M. Saruwatari, Transactions of IEICE (B-1), **J75-B-1**, pp.372-380 (1992) (in Japanese)

[4]. B. P. Nelson and N. J. Doran, Electron. Lett., **27**, pp.204-205 (1991)

[5]. P. A. Andrekson, Electron. Lett., **27**, pp. 1440-1441 (1991)

[6].H. Takara, S. Kawanishi, T. Morioka, K. Mori and M. Saruwatari, CLEO'94, CPD10 (1994)

[7].T. Morioka, S. Kawanishi, K. Mori and M. Saruwatari, OFC'94, PD-21 (1994)

[8].K. Uchiyama, H. Takara, S. Kawanishi, T. Morioka, M. Saruwatari and T. Kitoh, Electron. Lett., **29**, pp.1870-1871 (1993)

[9].T. Morioka, S. Kawanishi, K. Mori and M. Saruwatari, submitted to Electron. Lett.

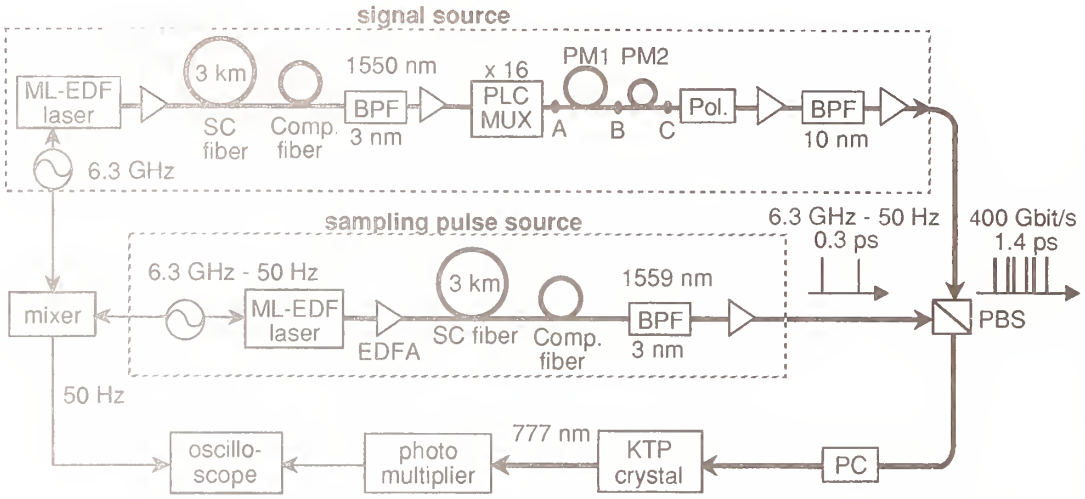

Fig. 1 Configuration for SFG optical sampling

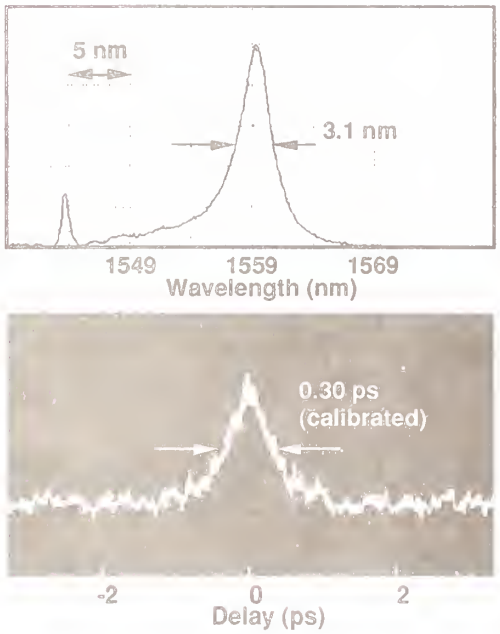

Fig. 2 Optical spectrum and autocorrelation trace of the sampling pulses

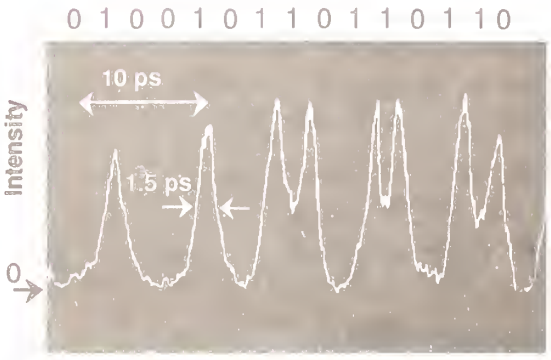

Fig. 3 Sampled waveform of the 400 Gbit/s optical signal

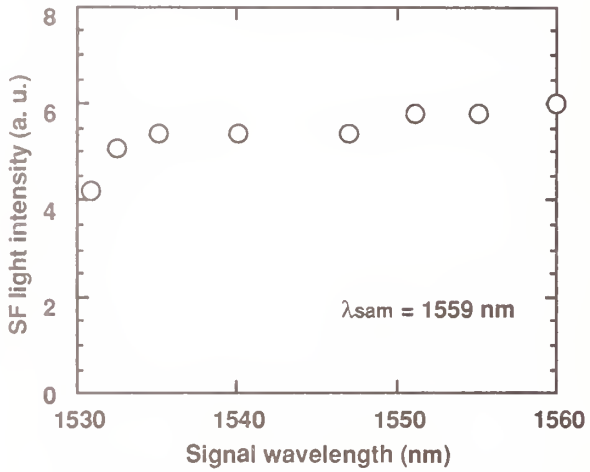

Fig. 4 Signal wavelength dependency of the SF light intensity

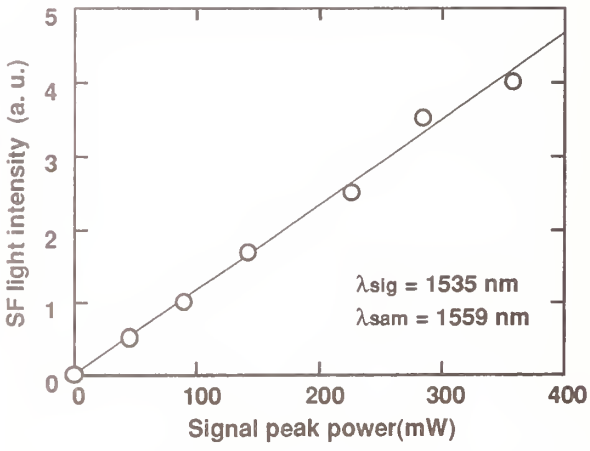

Fig. 5 Relationship between intensity of the SF light and signal peak power

Characterizing Modal Interference in Field Installable Single-Mode Fiber Connectors Incorporating Short Fiber Stubs

D. O. Harris and R. A. Throckmorton
SIECOR CORPORATION
489 Siecor Park – HE, Hickory, NC, 28603-0489

1. Introduction

In many fiber-optic applications, elimination of excess cable lengths or emergency repairs necessitate installation of connectors onto deployed optical fibers. Because conventional connectors designed for factory installation must be cured at high temperatures and meticulously polished, they are not practical for field installation. As an alternative, field installable fiber-optic connectors have been developed that consist of a short (≤ 2 cm) fiber stub preinstalled into a connector housing [1]; the connector is installed in the field by mechanically splicing the stub to a deployed fiber. The proximity of single-mode fiber joints in such connectors can produce modal interference which may cause a significant dependence of static connection loss on both source coherence and operating wavelength.

In order to understand the field operation of these connectors and subsequently establish accurate test procedures indicative of their field performance, we must first understand the mechanisms which cause modal interference. The theory conventionally used to describe modal interference in single-mode fiber joint pairs was developed to explain modal noise in applications where the operating wavelength is slightly below cutoff and the distance between joints is greater than 0.5 meters [2]–[4]; in this case, initially orthogonal LP_{11} modes generated at the first joint may couple within the intermediate fiber so that the energy they carry is redistributed upon arrival at the second joint. This same theory has since been used for applications where the distance between joints is of the order of centimeters [5]–[7]. In the latter case, modal interference can affect the loss of the joint pair, but no modal noise is present [5], [6]; moreover, there is minimal mode coupling or polarization conversion within the short intermediate stub fiber, so modes which are orthogonal just beyond the first joint tend to maintain their independence throughout the entire length of the stub. Given these subtle differences, we have modified the theory for the aggregate transmission efficiency of a closely spaced single-mode fiber joint pair operating slightly below cutoff. This revised theory shows that the LP_{01} to LP_{11} dominated modal interference is dependent on the azimuthal angle between the lateral offsets at the two joints. The azimuthal effect is verified experimentally

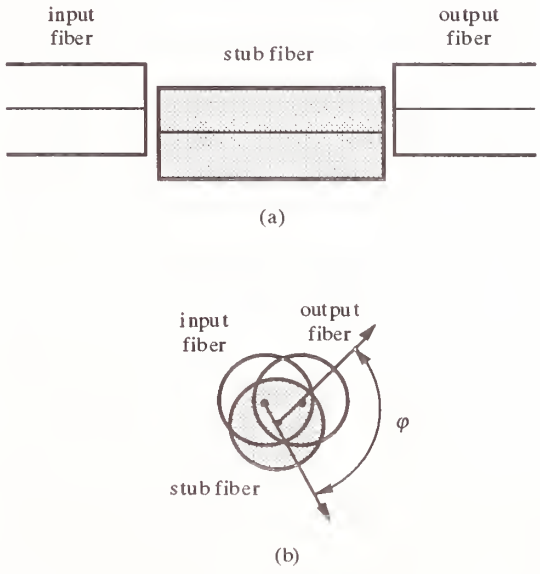

Figure 1. (a) Longitudinal and (b) transverse cross section of a two-joint single-mode fiber system which generates modal interference. For a field installable connector incorporating a short fiber stub, the joint separation is on the order of a centimeter.

not only for operation below LP_{11} cutoff wavelength, but also at wavelengths above cutoff where interference occurs between the LP_{01} and radiation modes [7].

From our revised theory, we derive an approximate formula for the "modulation index," which expresses the uncertainty of connector insertion loss due to modal interference as a percentage of the expected loss when no modal interference is present [8]. We further implement a method for measuring this parameter, and use results of such measurements to characterize modal interference for a sample population of stub connector assemblies.

2. Transmission Efficiency

We analyze the case of two closely spaced single-mode fiber joints with lateral misalignment as shown in Figure 1 for the condition where the operating wavelength is below cutoff. Using the Gaussian approximation for both LP_{01} and LP_{11} mode amplitudes [2], [9], overlap integrals yield the following analytical results for coupling efficiencies at the first joint:

$LP_{01} \rightarrow LP_{01}$: η_1

$LP_{01} \rightarrow LP_{11}$: $-\eta_1 \ln \eta_1$

$LP_{01} \rightarrow$ higher order modes: $1 - \eta_1 + \eta_1 \ln \eta_1$.

(1)

The LP_{01} to LP_{11} coupling efficiency given in equation (1) agrees with previously published empirical results [10] to better than 1% when $\eta_1 > 0.8$ (< 1 dB single-mode joint loss, which encompasses the range of practical interest). Equation (1) also indicates that for $\eta_1 > 0.8$, the LP_{11} mode power just beyond the first joint is at least an order of magnitude greater than the total power contained in the higher order modes; this suggests, as does conventional theory, that intermodal interference beyond the second joint will be dominated by interaction between the LP_{01} and LP_{11} modes of the stub fiber.

Given the above result, we consider only coupling between the LP_{01} and LP_{11} modes to approximate the aggregate transmission efficiency of a closely spaced, low-loss joint pair at wavelengths below cutoff. We first calculate the normalized LP_{01} mode amplitude beyond the second joint through analytical evaluation of correlation integrals between modes at the joints, while also accounting for mode attenuation and optical path differences in the stub fiber; for this calculation, we assume that no mode coupling or polarization conversion occurs within the stub. The square modulus of our normalized amplitude then yields the following expression for LP_{01} transmission efficiency through the low-loss joint pair:

$$\eta = \eta_1 \eta_2 \left\{ 1 + \ln \eta_1 \ln \eta_2 \, 10^{-\frac{\alpha_{11} l}{10}} \cos^2 \varphi \right.$$

$$\left. -2 r(\Delta n l) \sqrt{\ln \eta_1 \ln \eta_2} \, 10^{-\frac{\alpha_{11} l}{20}} \cos \varphi \cos\left[\frac{2\pi \Delta n l}{\lambda} \right] \right\}, \quad (2)$$

where η_1 and η_2 are the LP_{01} to LP_{01} efficiencies at the first and second joints, respectively, α_{11} is the LP_{11} mode attenuation in the stub fiber, l is the length of the stub fiber, φ is the azimuthal angle between the lateral offsets at the first and second joints , $r(\Delta n l)$ is a source autocorrelation for the optical path length difference between the LP_{01} and LP_{11} modes in the stub which ranges from 0 for incoherent illumination to 1 for completely coherent illumination, Δn is the refractive index difference between the LP_{01} and LP_{11} modes in the stub fiber, and λ is the free-space operating wavelength.

As stated in the introduction, a significant difference between this equation and the theory conventionally applied to modal interference is the dependence of the second and third terms on the azimuthal angle φ; this dependence arises from the assumption that polarization alignment and mode structure are maintained in the stub, which is the expected behavior for a short stub with no bends.

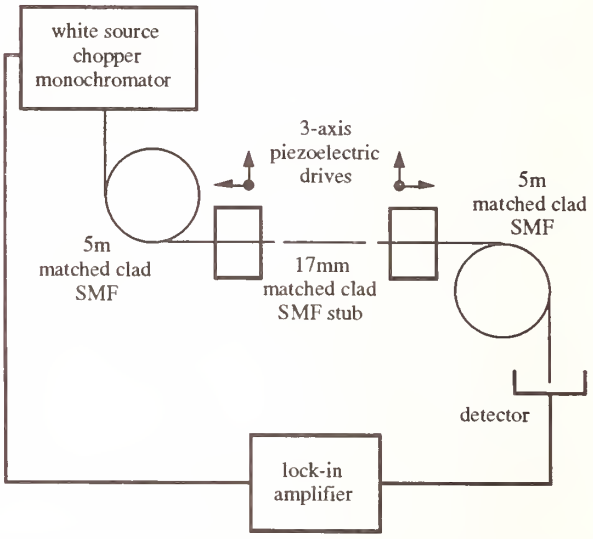

Figure 2. Apparatus for demonstrating the azimuthal dependence of modal interference.

To verify the azimuthal dependence, we used the apparatus in Figure 2 to measure spectral loss for one joint pair in the region below the LP_{11} cutoff wavelength of its the stub and for another joint pair in the spectral region above stub cutoff; both joint pairs are index matched and separated by approximately 17 mm of matched cladding fiber. The cutoff wavelength for the stub fiber of the first joint pair as measured by the EIA method [11] is 1289 nm, while the EIA cutoff for the second stub is 1209 nm; the respective cutoff wavelengths of these stub fibers in their deployed condition are estimated to be 1435 nm and 1295 nm as determined by the interference method described in Ref. 12. For both pairs, we introduce approximately 0.2 dB of loss due to lateral offset at each joint for the three cases where $\varphi = 0°$, 90°, and 180°.

Spectral loss from 1260 nm to 1360 nm is shown in Figure 3(a) for the first joint pair; as equation (2) predicts for operation below cutoff wavelength, spectral loss for the two parallel offset cases ($\varphi = 0°$ and $\varphi = 180°$) have approximately the same high levels of modal interference but nearly opposite polarity, while modal interference practically vanishes when the offsets are orthogonal ($\varphi = 90°$). Figure 3(b) contains a plot of spectral loss over the 1500 nm to 1600 nm region for the second joint pair, representing operation above cutoff wavelength. In this case, interference occurs

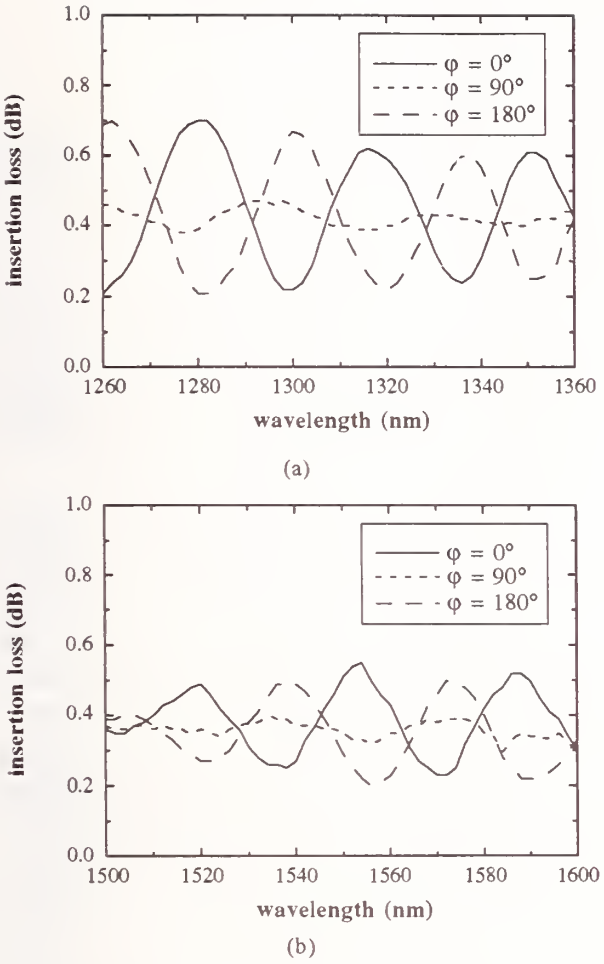

Figure 3. Measured spectral loss (a) below and (b) above cutoff wavelength for closely spaced, single-mode fiber joint pairs with approximately 0.2 dB of lateral offset induced loss at each joint and offset azimuthal angles of 0°, 90°, and 180°.

between the LP_{01} and radiation modes, but the azimuthal effect still exists; this is consistent with the notion that lateral offset causes light to be coupled primarily to radiation modes having amplitudes with odd symmetry about the fiber axis.

3. Modulation Index

When individual joints are reasonably efficient (η_1, $\eta_2 \geq 0.8$), the product $\eta_1\eta_2$ in equation (2) is very nearly the aggregate transmission efficiency of the joint pair under incoherent illumination. If we designate $\eta_1\eta_2$ as η_{inc}, then we may also write $\eta_1 = (\eta_{inc})^g$ and $\eta_2 = (\eta_{inc})^{(1-g)}$, where g ranges from 0 to 1. Further, $L_1 = gL_{inc}$, and $L_2 = (1-g)L_{inc}$, where L_1 and L_2 are the losses at the first and second joints, respectively, and L_{inc} is the approximate aggregate incoherent loss of the joint pair (i.e., loss under incoherent illumination). Hence, the parameter g represents the incoherent loss allocation between the two joints.

The extreme values of aggregate insertion loss over the spectral range of interest can be represented as $L_{max} \approx L_{inc}(1+m)$ and $L_{min} \approx L_{inc}(1-m)$ [8], where m is called the "modulation index;" accordingly,

$$L_{inc} \approx \frac{L_{max} + L_{min}}{2} \quad \text{(dB)} \tag{3}$$

is the approximate incoherent loss for the spectral range of interest and

$$m = \frac{L_{max} - L_{min}}{L_{max} + L_{min}} \quad . \tag{4}$$

For a low-loss single-mode joint pair ($L_{inc} < 1$ dB), we can derive the following approximation for modulation index based on equation (2):

$$m \approx 2r(\Delta nl)\sqrt{g(1-g)}\,10^{-\frac{\alpha_{11}l}{20}}\cos\varphi \quad . \tag{5}$$

From this expression, we see that modulation index is dependent on the source coherence, loss allocation between the joints, LP_{11} mode loss in the stub, and the azimuthal angle between the offsets. Since the modulation index represents the loss uncertainty from modal interference relative to incoherent loss and is, in theory, independent of incoherent losses < 1 dB, it is a good candidate for characterizing modal interference.

To demonstrate the application of modulation index in characterizing modal interference, we fabricated 28 field installable connectors having 17 mm matched cladding stubs with EIA cutoff wavelengths of 1203 nm; the estimated cutoff wavelength for these stubs in their deployed state is near 1300 nm. Spectral loss was measured by the cutback method for matings of each of these connectors to a factory installed connector using the transmitter and receiver configuration shown in Figure 2.

Modulation indices for the 1260 nm to 1360 nm spectral range were calculated for the 28 connectors using equation (4); Figure 4 contains a histogram of the modulation indices for these sample connectors. Since modulation index is basically independent of incoherent loss, histograms such as this can be can be used to describe connector insertion loss uncertainty due to modal interference in much the same way histograms of connector insertion loss are presently used. For the current example, the average modulation

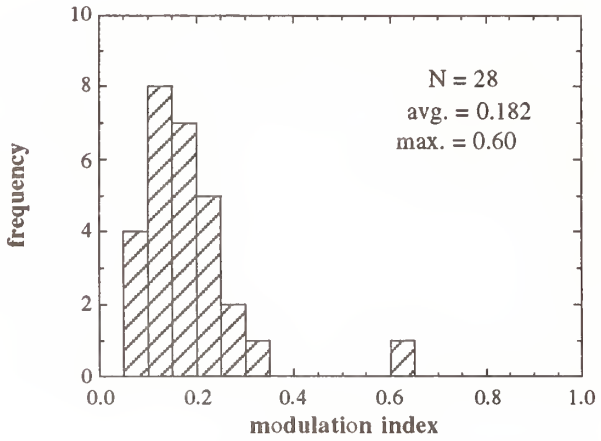

Figure 4. Histogram of modulation index over the 1260 nm to 1360 nm spectral range for 28 stub connectors. Since modulation index is essentially independent of incoherent loss, its distribution and sample statistics can be used to characterize modal interference in much the same way insertion loss distributions are currently used.

index is approximately 0.18 while the maximum is 0.60; therefore, we would assert that the coherent insertion loss uncertainty due to modal interference for connectors from this population will be about ±18% on average, with a worst-case of ±60%.

4. Conclusion

We have have provided a theoretical basis and demonstrated that modal interference in a closely spaced single-mode fiber joint pair is dependent on the azimuthal angle between the lateral offsets at the two joints — an effect which is not predicted by conventional theory. Using our revised theory, we deduce a parameter called the modulation index that can be used to characterize modal interference. A measurement technique for determining the modulation index of stub connectors is implemented, and the modulation index distribution obtained from measurements on a set of connectors is used to characterize modal interference for the set.

The authors wish to acknowledge technical discussions with C. K. Eoll, W. S. Jackman, C. Saravanos, and O. I. Szentesi, as well as assistance with experiments from S. C. Grant and her staff.

References

[1] M. deJong, "Cleave and crimp fiber optic connector for field installation," *Tech. Digest Conf. on Optical Fiber Commun.*, paper ThA1, p. 139, 1990.

[2] S. Heckmann, "Modal noise in single-mode fibres operated slightly above cutoff," *Electron. Lett.*, vol. 17, pp. 499-500, 1981.

[3] D. G. Duff, F. T. Stone, and J. Wu, "Measurements of modal noise in single-mode lightwave systems," *Tech. Dig. Conf. on Optical Fiber Commun.*, paper Tu01, pp. 52-53, 1985.

[4] M. Brandtner, D. Schicketanz, and C. Eoll, "Modal noise due to second mode interference in singlemode fiber systems," *Proc. 36th IWCS*, pp.622-628, 1987.

[5] G. A. Olson and R. M. Fortenberry, "Modal noise in single-mode fiber-optic systems with closely spaced splices," *Fiber and Integr. Opt.*, vol. 9, pp. 237-244, 1990.

[6] J. C. Goodwin and P. J. Vella, "Modal noise in short fiber sections," *J. Lightwave Technol.*, vol. 9, pp. 954-958, 1991.

[7] K. Abe, Y. Lacroix, L. Bonnell, and Z. Jakubczyk, "Modal interference in a short fiber section: fiber length, splice loss, cutoff, and wavelength dependences,"*J. Lightwave Technol.*, vol. 10, pp. 401-406, 1992.

[8] W. W. Wood, unpublished work, 1993.

[9] A. W. Snyder and J. D. Love, *Optical Waveguide Theory*, New York: Chapman and Hall, p. 307, 1983.

[10] L. Wei, R. S. Lowe, and C. Saravanos, "Practical upper limits to cutoff wavelength for different single-mode fiber designs," *J. Lightwave Technol.*, vol. 5, pp. 1147-1155, 1987.

[11] Electronic Industries Association, "Cutoff wavelength of uncabled single-mode fiber by transmitted power," EIA-455, FOTP-80, 1988.

[12] K. Abe, Y. Lacroix, Y. Cai, and L. Bonnell, "Determination of LP_{11} mode cutoff wavelength from the modal interference pattern," *Symp. on Optical Fiber Measurements*, NIST Special Publication 839, pp. 221-224, 1992.

Performance limits of coherent OTDR due to optical nonlinear effects

Hisashi Izumita, Yahei Koyamada, Shin-ichi Furukawa, and Izumi Sankawa
NTT Telecommunication Field Systems R&D Center,
Tokai, Ibaraki-ken 319-11, Japan.

Abstract

This paper clarifies the limit of incident optical pulse power in coherent optical time-domain reflectometry (C-OTDR) enhanced with optical fiber amplifiers. The critical pulse power, at which the performance of C-OTDR is degraded by the effect of optical nonlinear phenomena in a single-mode optical fiber, depends on the amplified optical pulse waveform, the pulse width and the effective length of the fiber. This paper also demonstrates the high performance of C-OTDR enhanced with EDFAs with 48 dB, 39 dB, and 29 dB single-way dynamic ranges after 2^{18} integrations for pulse widths of 10 μs, 1 μs and 100 ns, respectively, limited by the effect of SPM or FWM.

1. Introduction

Optical time-domain reflectometry (OTDR) is a commonly used technique for characterization and fault location in optical fiber transmission systems. Many studies have been undertaken to extend the dynamic range of OTDR [1], [2]. The use of erbium-doped fiber amplifiers (EDFAs) combined with a coherent detection technique is very effective in enhancing the performance of OTDR [3]-[6]. EDFAs have the potential for high gain and high saturation output power. An optical pulse can be amplified to more than 1 W by using EDFAs. However, a high-power optical pulse with the narrow linewidth needed for coherent detection stimulates optical nonlinear phenomena in a single-mode optical fiber [7]. These phenomena significantly degrade the performance of coherent OTDR (C-OTDR). It is therefore important to clarify the critical power of these phenomena, which are the origin of the single-way dynamic range (SWDR) limit of C-OTDR combined with EDFAs.

This paper describes theoretical and experimental studies on optical nonlinear phenomena stimulated by a high-power coherent pulse in a single-mode optical fiber, and clarifies the critical power for the degradation in performance of C-OTDR due to these phenomena. It shows the high performance of C-OTDR combined with EDFAs for 10 μs, 1 μs, and 100 ns pulse widths.

2. Experiments

Experiments were performed to clarify the critical conditions of the incident optical pulse for degrading the performance of C-OTDR due to optical nonlinear effects in the optical fiber.

2.1 Experimental set-up.

Figure 1 shows the experimental set-up for C-OTDR with EDFAs. A DFB-LD was coupled to a 1-km fiber to reduce the linewidth to less than 10 kHz. The continuous-wave (CW) light from the DFB-LD was divided into two paths by a 3-dB fused-fiber directional coupler (FC1): a signal path and a local oscillator (LO) path. The signal pulses were produced by an optical waveguide switch made of $LiNbO_3$ (EO-SW) operating in pulsed mode. The pulse period was 2 ms. The signal pulses were amplified by two post-amplifiers (EDFA1 and EDFA2) and an in-line amplifier (EDFA3). An acousto-optic switch (AO-SW), operating in pulse mode synchronized with the EO-SW, eliminated the amplified spontaneous emission (ASE) from EDFA1. The optical frequency of the signal pulses was shifted by 120 MHz at the AO-SW. The amplified signal pulses were launched into a 100-km test fiber. The Rayleigh backscattered signals from the test fiber were mixed with the LO by FC2 and detected with a double-balanced p-i-n-FET receiver.

2.2 Experimental results.

Figure 2 shows the C-OTDR traces measured for a 1 μs pulse width. In trace (a), the incident pulse power was 21 dBm. The total loss of the test fiber was found to be 22 dB from the C-OTDR trace, which agrees with the total loss measured with the optical power meter. In trace (b), the incident pulse power was 24 dBm. Compared with trace

(a), the attenuation curve of the optical fiber on the C-OTDR trace gradually became distorted from 10 to 100 km. The total measured loss of the optical fiber was 24 dB, which is 2 dB larger than that of (a).

Figure 3(1) shows incident optical pulse waveforms with a pulse width of 1 μs and an average pulse power over the pulse width of (a) 21 dBm and (b) 24 dBm. The power of the optical pulse amplified by EDFAs in the saturation regime gradually decreased from the head of the pulse to its tail, due to a reduction in the inversion population in the erbium-doped fiber. The power gradient within the pulse width increased in proportion to the pulse power. In these experiments, the power gradient within the pulse width was approximately constant, and the power gradient k with the pulse width of τ was given by

$$k = \frac{p(0) - p(\tau)}{\tau}, \qquad (1)$$

where p(t) is the optical pulse power at time t. From Fig. 3(1), the measured power gradient k for (a) was 2.9×10^4 W/s and for (b) was 6.6×10^4 W/s.

Figure 3(2) shows the spectra of the beat signal between the transmitted optical pulse and the LO. These spectra were measured with a conventional spectrum analyzer. In (a), the optical spectrum was in the form of the square of a SINC function with a center frequency of 120.4 MHz and a period of 1 MHz. The center optical frequency was shifted by 0.4 MHz in comparison with the optical frequency shift of 120 MHz at the AO-SW. In (b), the center optical frequency was shifted by 1 MHz.

Figure 3(3) shows the optical spectra in the wavelength domain of the transmitted optical pulse. In (a), the center wavelength of the transmitted pulse was 1.5513 μm. No Stokes or anti-Stokes light was generated. In (b), two side-bands were generated, one on each side of the center wavelength, as a result of four-wave mixing (FWM).

These experiments show that the critical condition for degrading the performance of C-OTDR combined with EDFAs is given by the optical frequency shift of the Rayleigh backscattered signals caused by the effect of SPM (discussed in next section). The critical power gradient of the incident pulse amplified using the EDFAs was 2.9×10^4 W/s and the pulse power for this critical condition was lower than the critical power for the other nonlinear phenomena.

Experiments were also performed for a 100 ns pulse width. Figure 4 shows the C-OTDR traces. In trace (a), the incident pulse power was 24 dBm. The total loss of the test fiber was 22 dB, which agrees with the experimental results shown in Fig. 2(a). In trace (b), the incident pulse power was 25 dBm. The C-OTDR trace was distorted and at 20 km it was shifted down by about 2 dB. The total measured loss of the test fiber was 2.5 dB greater than that of (a).

Figure 5(1) shows the incident optical pulse waveforms. The power gradient of the pulse was negligible for both (a) and (b). Figure 5(2) shows the spectra of the beat signal between the transmitted signal and the LO. They had the form of the square of a SINC function with a center frequency of 120 MHz and a period of 10 MHz. The optical frequency shift of the transmitted optical pulse was also negligible in both cases.

Figure 5(3) shows the optical spectra in the optical wavelength domain. In (a), the side-bands were very small. In (b), Stokes and anti-Stokes lights was generated on either side of the center wavelength as a result of FWM. This caused the incident optical pulse to interact parametrically with the amplified spontaneous emission (ASE). The power levels of the Stokes and anti-Stokes light were 15 dB higher than the ASE level. The optical wavelength shift (the optical frequency shift) between the signal and the Stokes or anti-Stokes light was about 0.5 nm (62 GHz) and the Stokes bandwidth was about 0.25 nm (32 GHz).

The test fiber consisted of several 5-20 km dispersion-shifted single-mode fibers with typical dispersion D of -1.50 ps/(km·nm). From Eq. (10.3.10) in Ref. [8], the calculated frequency shift and the Stokes bandwidth at the incident pulse power of 316 mW (25 dBm) were 147 GHz and 74 GHz, respectively. The reasons for the difference

between the measured value and the calculated one were some fluctuation of the dispersion in the test fiber and the parametric gain suppression of FWM caused by polarization mismatch between the signal pulse and the ASE.

These experiments show that the critical condition for a pulse width of 100 ns is given by FWM, which leads to the generation of the Stokes and anti-Stokes light. The FWM critical power for the incident pulse amplified with the EDFAs was lower than the critical power for the other nonlinear phenomena.

3. Discussion

When an optical pulse with a power gradient within the pulse width is incident to the optical fiber, the optical frequency of the transmitted optical pulse passing through the optical fiber is shifted by self-phase modulation (SPM) [9]. The Rayleigh backscattered signals have the same optical frequency shift as the optical pulse propagating in the optical fiber. Since a stable frequency difference between the Rayleigh backscattered signal and the local oscillator is needed for coherent detection, the optical frequency shift degrades the sensitivity of C-OTDR because the center frequency of the signal moves outside the receiver band.

When the critical frequency shift $\delta\nu_c$ is defined to make the sensitivity degradation less than 0.05 dB, $\delta\nu_c/B$ is 0.4 [6], thus the critical power gradient of the incident optical pulse is [6]

$$\left.\frac{\partial p(t)}{\partial t}\right|_c = \frac{\lambda A}{n_2 L_{eff}} \delta\nu_c = \frac{\lambda A}{n_2 L_{eff}} 0.4\, B , \qquad (2)$$

where

$$L_{eff} = \frac{1-\exp(-\alpha L)}{\alpha} , \qquad (3)$$

A is the effective cross section area, B is the receiver bandwidth, p(t) is the optical pulse power at time t, n_2 is the nonlinear refractive index of the optical fiber, λ is the wavelength of the incident optical pulse, L_{eff} is the effective length, L is the length of the optical fiber, and α is its attenuation coefficient. Equation (2) shows that the critical power gradient is proportional to the receiver bandwidth and the inverse of the effective length. For a receiver bandwidth B of 1 MHz (i.e., 1 μs pulse width), the critical power gradient is 4.7×10^4 W/s, assuming that an optical pulse with a wavelength of 1.55 μm is incident to a standard single-mode optical fiber with an effective cross section area of 50 μm^2, an optical fiber length of 100 km, and the nonlinear refractive index of 3.2×10^{-20} m^2/W [7]. The calculated critical power gradient roughly agrees with the experimental results for the 1 μs pulse width shown in Fig. 3(2).

Equation (2) shows that the critical condition for the effect of SPM is more severe for a narrow bandwidth (i.e., a long pulse width). Therefore, the critical conditions for pulse widths of 10 μs (i.e., 100 kHz receiver bandwidth) were also measured. The measured critical power gradient k was 2.1×10^3 W/s and the pulse power of the critical incident pulse amplified with EDFAs was 16.7 dBm.

Figure 6 shows the calculated critical power for stimulated Brillouin scattering (SBS), that for stimulated Raman scattering (SRS) using Eq. (12) in Ref.[10] and Eq. (14) in Ref. [11], assuming the test fiber to be a standard single-mode optical fiber with a Brillouin gain coefficient of 4.5×10^{-11} m/W and a Raman gain coefficient of 6.5×10^{-14} m/W, as a function of the receiver bandwidth. The experimental critical pulse powers for SPM and FWM are also plotted in Fig. 6. For a 1 μs or longer pulse width (i.e., a 1 MHz or narrower receiver bandwidth), the critical pulse power for SPM was lower than those for SBS or SRS. For a 100 ns pulse width (i.e., a 10 MHz bandwidth), the critical pulse power for FWM was also lower than those for SBS or SRS.

We also demonstrated the high performance of C-OTDR enhanced with EDFAs after 2^{18} integrations for 10 μs, 1 μs and 100 ns pulse widths, limited by the effect of SPM and FWM.

Figure 7 shows the C-OTDR traces for a 1 μs pulse width. The SWDR was found to be 39 dB. The incident pulse had a pulse power of 20.7 dBm and a power gradient of 2.9×10^4 W/s, which was the critical condition for the

effect of SPM. The minimum power detectable by the receiver was about -85 dBm for 1 MHz bandwidth.

Figure 8 shows the C-OTDR trace for a 100 ns pulse width. The incident pulse power was 24 dBm, which was limited by the effect of FWM. The minimum power detectable by the receiver for 10 MHz bandwidth was about -72 dBm. The SWDR was found to be about 29 dB.

Figure 9 shows the C-OTDR trace for a 10 μs pulse width. The critical power gradient of the incident pulse was 2.1×10^3 W/s, at which the incident pulse power was 16.7 dBm in this experiment. The SWDR was found to be 48 dB and the degradation by SPM was negligible in this case.

4. Conclusion

We have shown that the critical conditions at which the performance of C-OTDR combined with EDFAs is degraded by the effects of optical nonlinear phenomena in a single-mode optical fiber are given by the effect of SPM and FWM. For 1 μs or longer pulse widths, the incident pulse powers were limited by the optical frequency shift of the backscattered signal by SPM due to the optical power gradient of the incident optical pulse. For a 100 ns pulse width, it was limited by FWM, which caused the incident optical pulse to interact with ASE and caused the incident optical pulse to be converted to Stokes and anti-Stokes light. These critical powers were lower than those of SBS and SRS.

We also demonstrated the high performance of C-OTDR enhanced with EDFAs with 48 dB, 39 dB, and 29 dB SWDRs after 2^{18} integrations for pulse widths of 10 μs, 1 μs and 100 ns, respectively, limited by the effect of SPM or FWM.

Acknowledgements

We thank Y. Wakui and K. Ishihara for their continuous encouragement.

References.

[1] M. Tateda and T. Horiguchi, "Advances in Optical Time-Domain Reflectometry," J. Lightwave Technol., Vol. 7, No. 8, pp. 1217-1224, 1989.

[2] P. Healey, "Review of Long Wavelength Single-Mode Optical Fiber Reflectometry Techniques," J. Lightwave Technol., Vol. LT3, No. 4, pp. 876-886, 1985.

[3] Y. Koyamada and H. Nakamoto, "High performance single mode OTDR using coherent detection and fiber amplifiers," Electron. Lett., Vol. 26, No. 9, pp. 573-574, 1990.

[4] S. Furukawa, H. Izumita, I. Sankawa, and Y. Koyamada, "High dynamic range, low fading noise coherent OTDR using erbium fiber amplifier and LD temperature changing techniques," Proc. ECOC'91/IOOC'91, Mo.C1-3, pp. 81-84, 1991.

[5] H. Izumita, Y. Koyamada, I. Sankawa, and S. Furukawa, "Coherent optical time-domain reflectometer with a 40-dB dynamic range enhanced with erbium-doped fiber amplifiers," Proc. OFC'92, WK6. pp.147, 1992.

[6] H. Izumita, Y. Koyamada, S. Furukawa, and I. Sankawa, "The performance limit of coherent OTDR enhanced with optical fiber amplifiers due to optical nonlinear phenomena," to be published in J. Lightwave Technol., 1994.

[7] R. H. Stolen, "Nonlinearity in Fiber Transmission," Proc. IEEE, Vol. 68, No. 10, pp.1232-1236, 1980.

[8] G. P. Agrawal, *Nonlinear Fiber Optics.*, Academic Press, 1989.

[9] R. H. Stolen and Lin Chinlon, "Self-phase-modulation in silica optical fibers," Phys. Rev. A, Vol. 17, No. 4, pp. 1448-1453, 1978.

[10] R. G. Smith, "Optical Power Handling Capacity of Low Loss Optical Fiber as Determined by Stimulated Raman and Brillouin Scattering, " Appl. Opt. Vol. 11, No. 11, pp. 2489-2499, 1972.

[11] Y. Koyamada, H. Nakamoto, and N. Ohta, "High Performance Coherent OTDR Enhanced with Erbium Doped Fiber Amplifiers," J .Opt. Commun., Vol. 13, No. 4, pp.127-133, 1992.

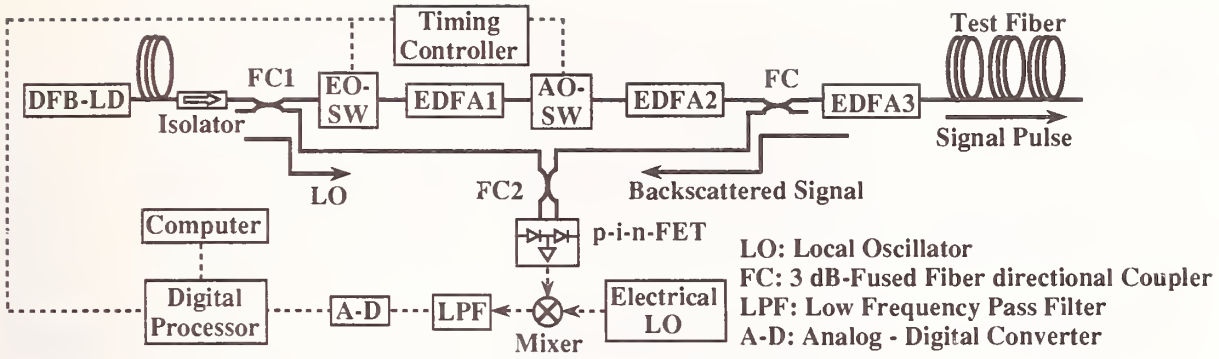

Fig. 1 Experimental set-up

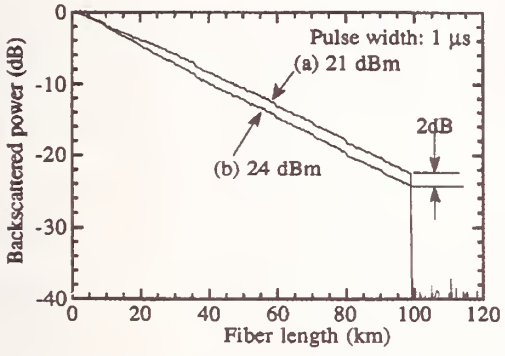

Fig. 2 C-OTDR traces with 1 μs pulse width for incident pulse power of (a) 21 dBm and (b) 24 dBm.

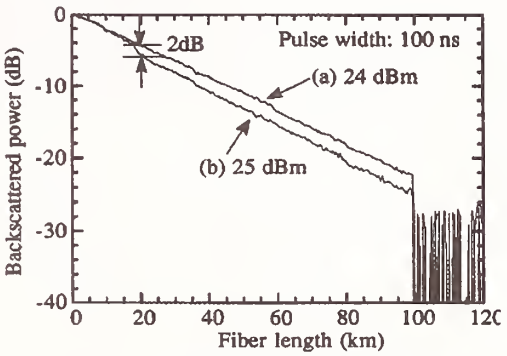

Fig. 4 C-OTDR traces with 100 ns pulse width for incident pulse power of (a) 24 dBm and (b) 25 dBm.

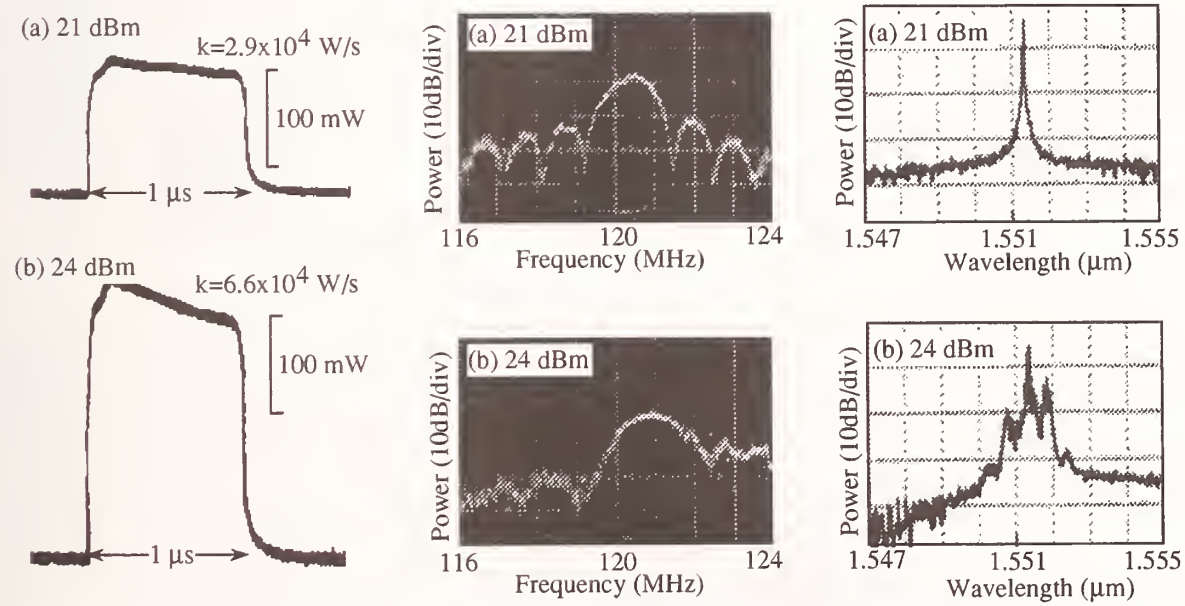

(1) incident optical pulse waveforms

(2) optical spectra in the frequency domain

(3) optical spectra in the wavelength domain

Fig. 3 Experimental results for 1 μs pulse width at (a) 21 dBm and (b) 24 dBm.
(1) incident optical pulse waveforms,
(2) optical spectra in the frequency domain of the transmitted optical pulse,
(3) optical spectra in the wavelength domain of the transmitted optical pulse.

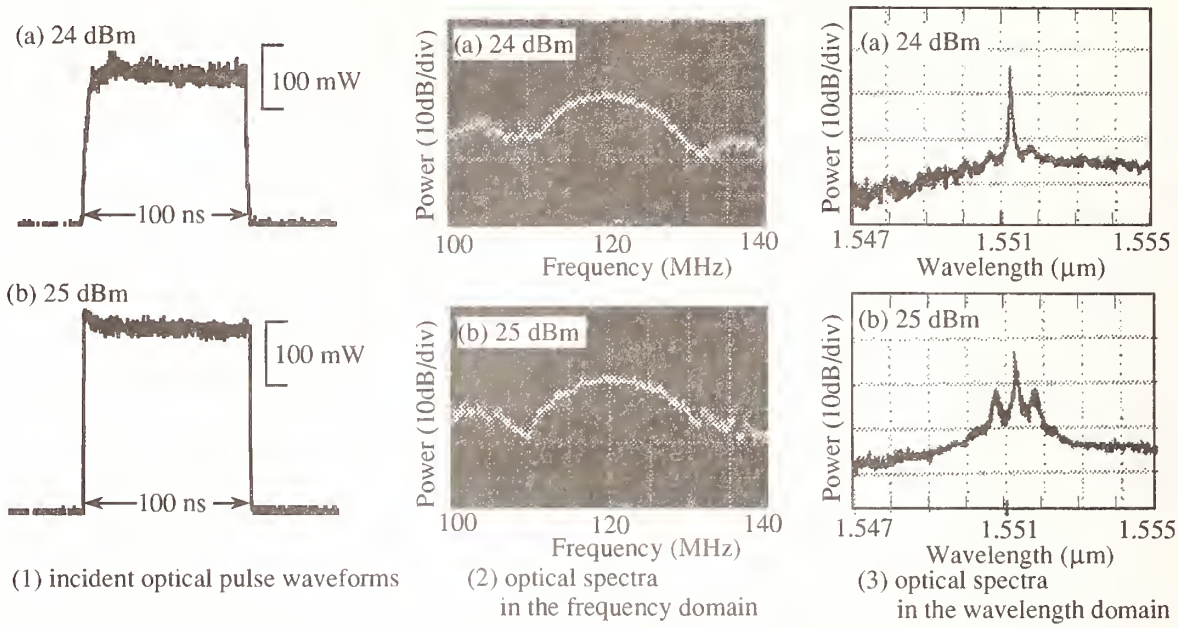

(1) incident optical pulse waveforms

(2) optical spectra in the frequency domain

(3) optical spectra in the wavelength domain

Fig. 5 Experimental results for 100 ns pulse width at (a) 24 dBm and (b) 25 dBm.
(1) incident optical pulse waveforms,
(2) optical spectra in the frequency domain of the transmitted optical pulse,
(3) optical spectra in the wavelength domain of the transmitted optical pulse.

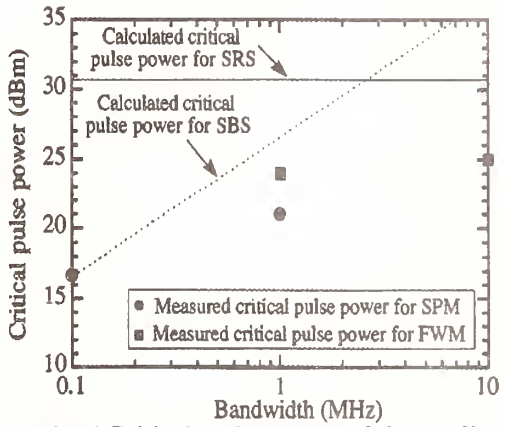

Fig. 6 Critical pulse power of the nonlinear phenomena as a function of bandwidth.

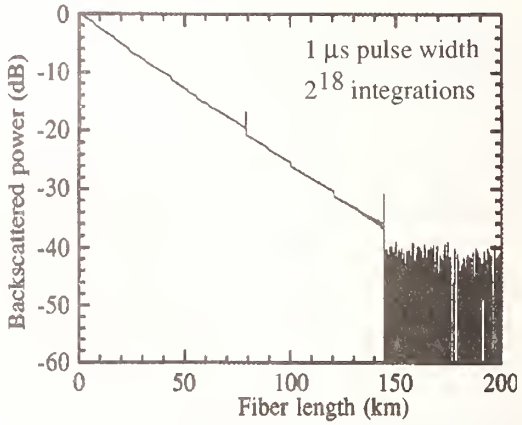

Fig. 7 C-OTDR trace for 1 μs pulse width at 21 dBm.

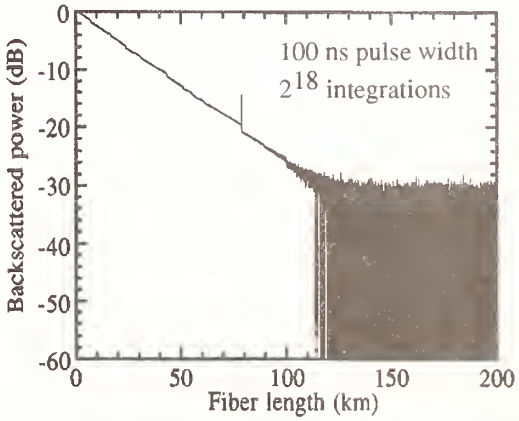

Fig. 8 C-OTDR trace for 100 ns pulse width at 24 dBm.

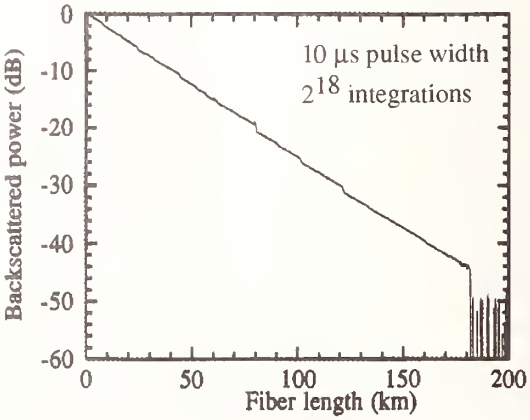

Fig. 9 C-OTDR trace for 10 μs pulse width.

WINDOWING TECHNIQUE FOR ACCURATE MEASUREMENT OF LOW REFLECTANCES BY OTDR

L. DUCOS* and P. FACQ**
* LCIE - 33, avenue du général Leclerc - 92260 FONTENAY AUX ROSES - FRANCE
** IRCOM - 123, avenue Albert Thomas - 87060 LIMOGES Cedex - FRANCE

INTRODUCTION

Accurate measurement of low reflectances by OTDR is essentially a matter of
1) correct discrimination between two contributions overlapping over the whole deadzone length on the OTDR display: the power R(t) returned by the reflective element under measurement and the power S(t) backscattered by the fiber portion corresponding to the deadzone length.
2) appropriate signal analysis in order to reduce the final uncertainty on the measured reflectance.

On the basis of the discrimination-integration method reported by Blanchard *et al* [1], we propose an improved signal processing technique leading to a better accuracy on measured reflectance values.

REFLECTANCE MEASUREMENT BY OTDR

The reflectance R(dB) corresponding to a reflective element can be written as [1]

$$R(dB) = 10 \log_{10}\{K \; E_r/P_s\}$$

where E_r is the reflected pulse energy, and P_s is the backscattered power value at the reflective element abscissa. The backscatter parameter K, with the dimensions of frequency, can be reached with the help of reflectometric measurements [2]. Blanchard *et al* have already shown in reference [1] that when an OTDR is used to measure the reflectance of a refractive index discontinuity (connector, coupler, splice,..) on an optical fiber link, the reflection coefficient can be written as

$$R = \frac{K}{S(t_0)} \int_{t_0}^{t_1} [B(t) - S(t)] \, dt = K \frac{E_r}{P_s} \qquad (1)$$

where B(t) and S(t) are, respectively, the total backward signal and the backscattered contribution. t_0 is time corresponding to the reflective element abscissa and t_1 is time depending upon the OTDR dead zone. We set $T = t_1 - t_0$. The determination of the signal S(t) has been shown in reference [1].

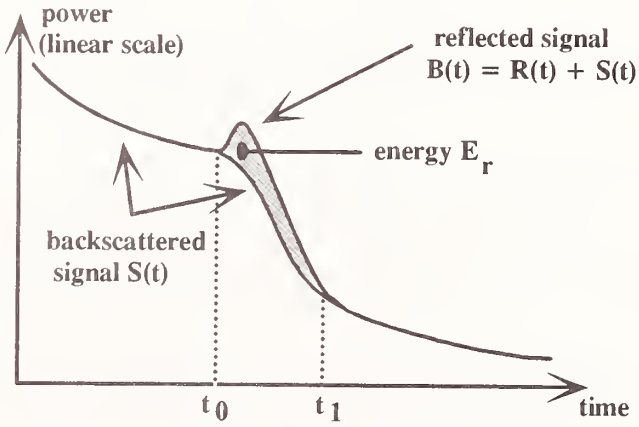

Figure 1: evaluation of the reflected energy

DEFINITION OF THE REFLECTION COEFFICIENT

The reflection coefficient expressed by relation (1) can be expressed as the ratio of the reflected pulse energy E_r to the incident pulse energy E_i in relation with the considered reflective event:

$$R = \frac{\int_{t_0}^{t_1} [B(t) - S(t)]\ dt}{S(t_0)/K} = \frac{\int_{t_0}^{t_1} R_r(t)\ dt}{\int_{t_0}^{t_1} R_i(t)\ dt} = \frac{E_r}{E_i} \qquad (2)$$

where $R_r(t)$ and $R_i(t)$ are, respectively, the reflected and the incident signals in relation with the reflecting event. $R_i(t)$ can be determined with knowing the pulse shape of the used OTDR and the energy $S(t_0)/K$. It is possible to express relation (2) with the help of convolution products, considering that a limited integral on $[t_0,t_1]$ acts on $R_r(t)$ and $R_i(t)$ as a low pass filter H with a rectangular impulse response h(t).

$$R = \frac{\int_{t_0}^{t_1} R_r(t)\ dt}{\int_{t_0}^{t_1} R_i(t)\ dt} = \frac{R_r(\theta) * h(\theta)}{R_i(\theta) * h(\theta)} \qquad (3)$$

The uncertainty on R depends on the amount of noise n(t) added to the signals $R_r(t)$ and $R_i(t)$. This uncertainty is directly related to the signal-over-noise ratio at the output of the filter H. Denoting x(t) the input signal and assuming an additive centered noise n(t) with power spectral density $N_0/2$, one can show that the SNR at the output of filter H is:

$$SNR = \frac{2\ F\ E_x}{N_0} \qquad (4)$$

where $E_x = \int_{-\infty}^{+\infty} x^2(t)\ dt$ is the input signal energy and

$$F = \frac{1}{T\ E_x} \left[\int_{-\infty}^{+\infty} x(\theta)\ d\theta\right]^2 \qquad (5)$$

is a positive factor depending on the shape of the signal x(t). With the help of Schwarz inequality, it can be shown that $0 \leq F \leq 1$. F reaches its maximum value $F=1$ when x(t) is rectangular.

THE WINDOWING TECHNIQUE

The OTDR impulse response (here denoted x(t)) generally departs from the rectangular shape on [0,T]. The leading and trailing edges of x(t) take more and more relative importance with high resolution OTDRs. So, F can fall to low values.

The noise spectral density $N_0/2$ being fixed in relation (4), one can see that SNR is directly proportional to the product FE_x.

A numerical study of the usual signal x(t) shows that starting to restrict this signal by right-side windowing into a smaller interval $[0,T'] \subset [0,T]$ leads to an increase of F not compensated by the correlative decrease of E_x. A resulting increase of FE_x is observed as the restriction begins. FE_x grows as long as $d(FE_x)/dT'$ remains negative. Consequently, the windowing process is stopped when the product F'E' of the truncated signal $\zeta(t) = x(t)\, rect_{[0,T']}(t)$ satisfies $d(F'T')/dT' = 0$. That is

$$\frac{2T'\left[\int_0^{T'} \zeta(t)\, dt\right] \zeta(T') - \left[\int_0^{T'} \zeta(t)\, dt\right]^2}{T'^2} = 0 \qquad (6)$$

finally reduced in $\zeta(T') = \frac{1}{2T'} \int_0^{T'} \zeta(t)\, dt = \frac{\langle \zeta_1 \rangle}{2}$. (7)

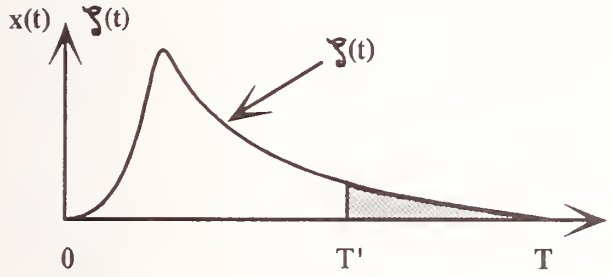

Figure 2: right-side windowing

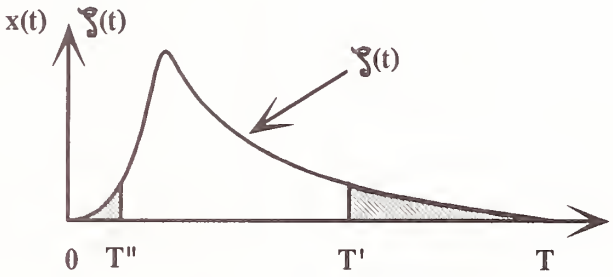

Figure 3: right and left sides windowing

The right-side windowing (Figure 2) is temporarily stopped when the sample $\zeta(T')$ reaches half the mean-value of $\zeta(t)$ on the interval $[0,T']$. Then, we compare the sample $\zeta(0)$ with half the mean-value. If $\zeta(0) \geq \langle \zeta_1 \rangle /2$ there is no hope of amelioration of the SNR by making a left-side windowing. On the other way, if $\zeta(0) \leq \langle \zeta_1 \rangle /2$, we must restrict $\zeta(t)$ to $[T'',T']$ (Figure 3) until

$$\zeta(T'') = \frac{1}{2(T' - T'')} \left[\int_{T''}^{T'} \zeta(t)\, dt\right] = \frac{\langle \zeta_2 \rangle}{2} \quad . \qquad (8)$$

The new mean-value of $\zeta(t)$ is then increased on its definition interval $[T'',T']$ in comparison with the precedent value on $[0,T']$: $\langle \zeta_2 \rangle > \langle \zeta_1 \rangle$. Then it is necessary to reconsider the stopping criteria for the right-side windowing in relation with $\langle \zeta_2 \rangle$ the new mean-value of $\zeta(t)$ and, eventually, to continue to decrease T'. This iterative process is pursued until

$$\zeta(T'') = \zeta(T') = \langle \zeta \rangle /2 \qquad (9)$$

where $\langle \zeta \rangle$ is the mean-value of $\zeta(t)$ on the domain $[T'',T']$. Criteria of relation (9) is called optimal windowing criteria. The corresponding amelioration on SNR, called SNA, can be expressed by:

$$SNA = \frac{T}{(T'-T'')} \frac{\left[\int_{T''}^{T'} x(t)\, dt\right]^2}{\left[\int_0^{T} x(t)\, dt\right]^2} . \qquad (10)$$

APPLICATION OF THE OPTIMAL WINDOWING CRITERIA

The optimal windowing criteria has been applied on theoritical and experimental signals to determine the SNA. Indicative values of SNA obtained for a triangular signal, a 20 ns pulse duration (OTDR A) and a 100 ns pulse duration (OTDR B) are 0.73 dB, 1.61 dB and 2.50 dB respectively. Then, the optimal windowing criteria has been applied in accordance to relation (3) to determine the reflectance R(dB) corresponding to 10 $\log_{10}$(R). Different selected values of R(dB) from -60 dB to -71 dB have been tested and were achieved with the help of a reflectance simulator [3]. Table 1 shows results of these measurements and associated repeatability uncertainty for the Blanchard technique (relation(2)) and the windowing technique applied to the same measured signals, ones referring to OTDR A and the others to OTDR B.

Blanchard technique (dB)	- 60.15 ± 0.54	- 62.21 ± 0.46	- 63.91 ± 0.64	- 66.32 ± 0.60	- 67.65 ± 0.81	- 69.23 ± 0.85	- 71.06 ± 1.32
	- 59.66 ± 0.13	*- 62.19 ± 0.16*	*- 64.09 ± 0.15*	*- 66.02 ± 0.21*	*- 68.10 ± 0.27*	*- 70.38 ± 0.45*	*- 72.80 ± 0.64*
optimal windowing technique (dB)	- 60.28 ± 0.51	- 62.35 ± 0.44	- 64.12 ± 0.58	- 66.61 ± 0.55	- 68.12 ± 0.73	- 69.87 ± 0.84	- 71.86 ± 1.17
	- 59.51 ± 0.10	*- 61.99 ± 0.10*	*- 63.90 ± 0.09*	*- 65.82 ± 0.12*	*- 67.90 ± 0.17*	*- 70.21 ± 0.27*	*- 73.04 ± 0.57*

Table 1: reflectance and associated repeatability uncertainty (± 1σ) on 20 measurements for OTDR A (pulse duration = 20 ns) and *OTDR B (pulse duration = 100 ns)* at λ = 1310 nm

DISCUSSION AND CONCLUSION

With the application of the optimal windowing technique in reflectance measurements, the uncertainty due to noise and random errors is reduced by an amount which corresponds to the correlative increase of the signal processing SNR. In the authors' knowledge, the accuracy of these measurements is the best yet reported in the low reflectance range.

A comparison made with the matched filtering technique (optimal in the presence of additive stationary noise) has shown that, due to the actual nature of noise, the accuracy of the experimental results is not better.

The optimal windowing is an efficient simple-to-implement technique. It can be quickly and easily set to work into an OTDR software.

REFERENCES

[1] P.Blanchard, P.H.Zongo, P.Facq, J.Rochereau.
Technical digest. Symposium on optical fiber measurement. Boulder 1990.

[2] P.Blanchard, P.H.Zongo, P.Facq. Electronics letters, Vol. 26, N° 25, pp. 2060-2061, dec. 1990.

[3] P.Blanchard, L.Ducos, P.Fournier, J.Dubard, F.Gauthier.
Technical digest. ESI Publications, OPTO 93, Paris, pp. 255-258.

NOISE ERROR IN OTDR SPLICE LOSS MEASUREMENT

Francesco CAVIGLIA, Piergiorgio RICALDONE
CSELT, via G. Reiss Romoli 274, 10148 Turin (Italy)

Abstract - The noise induced error in OTDR splice loss measurements is discussed for the classical loss evaluation procedures and for an alternative method, the last one giving occasionally the best results.

1 - Introduction

The OTDR (backscattering) technique is very often used to measure the losses of splices (or any other localized loss) in an optical link. The noise on the OTDR trace induces a random error on the measured losses; this error is usually reduced by increasing the averaging time and using procedures that approximate the noisy trace by a straight line, as discussed in the following. (The noise on the trace induces on the measured losses a systematic error as well, its magnitude too is considered below).

In this paper, the relationships between the noise observed on the trace and the error on the measured losses are analyzed for the classical loss evaluation procedures and for an alternative method. These relationships help in choosing the best procedure for the different conditions and to evaluate the possible error by observing the noise on the trace.

2 - Loss evaluation procedures

The most basic method to estimate a splice loss is the *two point method*. The splice loss is calculated starting from the level difference between two points taken on the trace at the two sides of the splice, corrected for the presumed fiber loss between the two points. Using this method, the noise induced error is quite high. Therefore, the splice loss is usually evaluated by measuring the level difference between two straight lines approximating the trace (Figure 1). Two different methods can be used for obtaining the parameters of the approximating lines.

2.2 - Variable slope fitting

Using the classical way (*variable slope method*) the position and the slope of the approximating lines are determined by the least square method, with reference to two fibre spans (D_1 and D_2) at the two sides of the splice, selected by the instrument operator. This method is implemented on almost all the commercial OTDR

The position of point P, that is the position where the distance between the two line is evaluated, should in theory be at the center of the step identifying the splice on the OTDR trace. In the practice, point P is often located to the left of the step (at the end of D_1) as its position has usually a negligible influence on the measured loss (the error on the loss is equal to the product of the misplacement of P for the difference between the attenuation coefficients of the two fibres).

2.3 - Fixed slope fitting

The alternative fitting method herein considered (*fixed slope method*) is similar to the previous one, but the slope of the two lines (fibre attenuation coefficient) is fixed and stated by the user,

while just the line vertical positions are calculated by the least square method. (When D_1 and D_2 approach to zero, this method becomes equivalent to the two point method).

This alternative method is attractive when fibre spans D_1 and D_2 are quite short and the horizontal separation between the two line segments (d_1 plus d_2) is large. This can occasionally happen in measuring splices between short fibre sections or because of the deadzone following the splice reflection. Under this conditions the noise induced error on the estimated fibre attenuation coefficients (line slopes) can be noticeable (see point 3.1) strongly affecting the loss measured with the previous method. On the other hand, the fibre attenuation coefficient is very often known with a good precision. Consequently this alternative method can offer better performances than the classical one, as discussed further in section 3.

The fixed slope method is not included within the functions offered by the commercial OTDR instruments, however it can be easily applied when useful. In fact, OTDR instruments, when using the variable slope fitting method, indicate not just the calculated loss (A_v), but also the calculated slopes: before the splice (α_1) and after the splice (α_2). Moreover the positions of the markers identifying the fitting zones and the point P are known. The loss (A_f) given by the fixed slope method can thus be calculated as:

$$A_f = A_v + (\alpha_1 - \alpha_a)\left(\frac{D_1}{2} + d_1\right) + (\alpha_2 - \alpha_a)\left(\frac{D_2}{2} + d_2\right)$$

where α_a is the fixed slope (fibre attenuation coefficient) assumed for the lines.

For: $D_1 = D_2 = D$ and $d_1 = d_2 = d$ the above equation reduces to:

$$A_f = A_v + \left(\frac{\alpha_1 + \alpha_2}{2} - \alpha_a\right)(D + 2\,d)$$

The above computations (or directly those for deriving the fitting line parameters) can be easily performed if the OTDR is connected to a portable computer.

3 - Noise induced error

3.1 - Random error

Table 1 reports expressions to calculate the amount of the r.m.s loss error from the trace amplitude, for the different loss evaluation methods. Expression in Table 1 are derived assuming that the line fitting on each segment D_i is done on N uncorrelated samples (being $N = (D_i + S)/S$). In the practice, the distance S between uncorrelated samples is either the OTDR sampling distance or the OTDR receiver rise-width, whichever is greater. (The latter can be easily observed on the trace, at the front of a non-saturating reflection).

Parameter σ_a is the r.m.s. value of the possible deviation, from the assumed α_a ,of the fibre attenuation coefficients (as indicated by the OTDR, that is including any OTDR loss scale error).

On the graph in Figure 2, an example is given for the dependence of the error from the fitting zone length. On the same graph some data obtained experimentally are reported. The data in Figure 2 confirm the advantage of the fixed slope method when the fibre spans at the splice sides are short. In the example this advantage is evident for spans under 500 m , while for lengths over 1 km, the possible error on the assumed attenuation coefficient impairs the result.

Incidentally, the error (σ_α) in the fibre attenuation coefficient evaluated using the least square method fitting on a fibre span (D) is given by (σ being the r.m.s. noise on the trace):

$$\sigma_\alpha^2 = (\sigma / D)^2 \frac{12\, D\, S}{(D + S)(D + 2\, S)}$$

for $D >> S$:

$$\sigma_\alpha^2 = 12\, (S / D)\, (\sigma / D)^2$$

while a two point evaluation trough the extreme points of the segment would give:

$$\sigma_\alpha^2 = 2\, (\sigma / D)^2$$

3.2 - Systematic error

The noise voltage is assumed to have a symmetrical distribution around the receiver backscattering power. However, on the logarithmic trace displayed on the OTDR screen this distribution is no longer symmetric and, as a consequence, the mean value on the trace does not coincide with the trace position in absence of noise, but it is shifted toward lower levels. As the noise (and the level shift) increases along the trace, this effect can influence the fibre and splice loss measurements when the least square method fitting is used.

The analysis shows that the downward shift (in dB) of the mean value of the trace is nearly equal to $0.45\ \sigma^2$, where σ is the r.m.s. noise (in dB) on the trace. Moreover it can be shown that the relative error in evaluating the loss (A) of a splice (or a fibre section) is again nearly proportional to σ^2 and given by: $\Delta A/A \cong 0.45\ \sigma^2$. This means that the error remains below 2% for σ below 0.2 dB (more than 1 dB peak to peak on the trace). The error always acts in increasing the measured loss.

When the noise is high, this effect can be avoided using fitting algorithms better than the simple straight line one, e. g. that presented in [1].

4 - Conclusions

The reported equations allow to estimate the noise induced by the noise on the trace on splice (and fibre section) losses measured by OTDR instruments. and evaluate the advantages of the methods based on the straight line fitting. Moreover they indicate the influence of the receiving system rise time on the noise induced error under similar r.m.s. noise condition.

The examined alternative loss evaluation method appears to be convenient in respect to the classical one in a range of conditions that can be again deduced from the equations in Table 1.

Discussion at point 3.2 allows to estimate the systematic error induced by the noise asymmetry.

References

[1] - D. Messing, A. Luthra, "Estimating the power and decay rate of noisy optical reflectometer return signals", Technical Digest of OFC "90, San Francisco (USA), 1990.

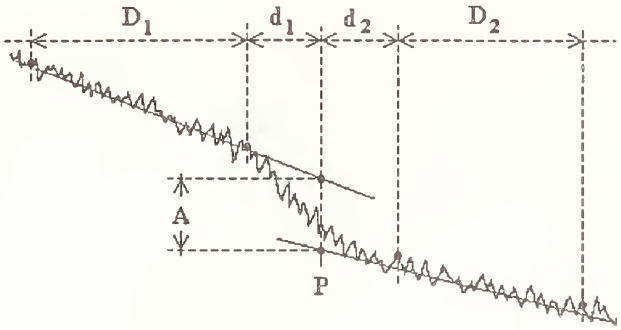

Figure 1 - Splice loss evaluation using straight lines fitted to the trace

Loss evaluation method	General expression for the noise induced error	Special cases
Two points	$\sigma_m^2 = \sum_{i=1}^{2} \sigma_i^2 + \sigma_a^2 \sum_{i=1}^{2} d_i^2$ (P at the center of the step)	For: $\sigma_1 = \sigma_2 = \sigma \quad d_1 = d_2 = d$ $\sigma_m^2 = 2\sigma^2 + 2\sigma_a^2 d^2$
Variable slope fitting	$\sigma_m^2 = \sum_{i=1}^{2} \sigma_i^2 \left(\frac{S}{D_i + S} \left(1 + \frac{12 \left(\frac{D_i}{2} + d_i \right)^2}{D_i (D_i + 2S)} \right) \right)$ (P at the location actually used for loss evaluation)	For: $\begin{cases} \sigma_1 = \sigma_2 = \sigma \\ D_1 = D_2 = D \\ d_1 , d_2 , S \ll D \end{cases}$ $\sigma_m^2 = 8\sigma^2 \frac{S}{D}$
Fixed slope fitting	$\sigma_m^2 = \sum_{i=1}^{2} \sigma_i^2 \frac{S}{D_i + S} + \sigma_a^2 \sum_{i=1}^{2} \left(\frac{D_i}{2} + d_i \right)^2$ (P at the center of the step)	For: $\begin{cases} \sigma_1 = \sigma_2 = \sigma \\ D_1 = D_2 = D \\ d_1 , d_2 , S \ll D \end{cases}$ $\sigma_m^2 = 2\sigma^2 \frac{S}{D} + \sigma_a^2 \frac{D^2}{2}$

σ_i = r.m.s. noise (in dB) on the trace in the D zone
σ_a = r.m.s. noise (in dB/km) between the assumed and the actual fibre attenuation coefficients
σ_m = r.m.s. error (in dB) on the measured splice loss
S = distance between uncorrelated samples
It is assumed that $(d_1 + d_2)$, D_1 and D_2 are always greater than S

Table 1 - Noise induced error for the different loss evaluation methods

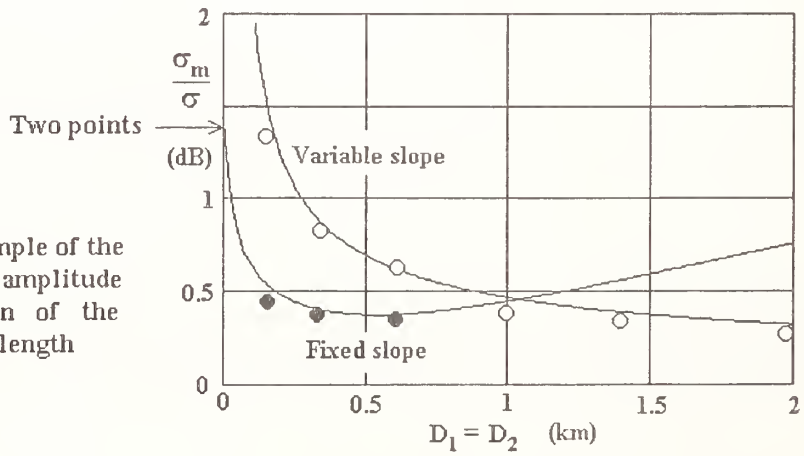

Figure 2 - Example of the error r.m.s. amplitude as a function of the fitting zone length

Effects of Fiber Parameter Mismatch on Uni-Directional OTDR Splice Loss Measurement

James Warder, Ming-Jun Li, Paul Townley-Smith, and Costas Saravanos
Siecor Canadian Cable Plant
1370 Fletcher Road, Saskatoon, SK., S7K 3L7

I. Introduction

Optical time-domain reflectometry (OTDR) is an effective tool for measuring fiber attenuation, locating faults, and determining splice loss. It is well known that bi-directional OTDR measurement is required to obtain accurate results [1]. This is especially true when measuring fiber splice loss. However, in the field, it is not always practical or economical to have access to both ends of the two spliced fibers, and uni-directional OTDR measurement is used to estimate the splice loss. In uni-directional OTDR measurement, the accuracy is affected by the direction-dependent backscatter change due to the parameter mismatch of the two spliced fibers. The OTDR signal level depends on the scattering coefficient, the group velocity which is inversely proportional to the group refractive index, and the capture fraction which varies as a function of the mode field diameter (MFD) and the effective refractive index of the fiber [2]. Thus, any differences in the scattering coefficient, the refractive index profile, or the MFD of the two fibers will introduce errors in the uni-directional OTDR measurement. To date, the fiber industry has developed "rules of thumb" to correct errors caused by the MFD mismatch only [3-4], while the contributions of all other components are ignored. When we splice the same fiber type, their scattering coefficients and refractive indices are similar. As a result, the contributions of these parameters to the backscatter change are small. But, they can be significant if different fiber types are spliced to each other.

In this paper, we examine the effect of fiber parameter mismatch on the backscatter change. As is shown, changes in fiber parameters such as scattering coefficient and refractive indices, should be considered to develop accurate rules of thumb.

II. Theory

In an OTDR, the backscattered power $P_{bS}(t)$ received at the launch end at time t, from an input pulse of power P_0 and width W is [2]

$$P_{bs}(t) = P_0 W \eta(z) \exp(-2\alpha z) \tag{1}$$

where α is the attenuation coefficient, and η the backscatter factor. This backscatter factor is propertional to:

- the scattering coefficient α_S,
- the group velocity v_g,
- the backscatter capture fraction $B(z)$.

For weakly guiding single mode fiber, using Gaussian approximation, η is given by [2]

$$\eta = 0.5\alpha_s B(z) V_g = \frac{12 c \alpha_s}{(k_0 MFD)^2 n_{eff}^2 n_g} \tag{2}$$

where n_{eff} is the effective refractive index, n_g is the group refractive index, and c and k_0 are the light velocity and wavenumber in free space, respectively. When two fibers are spliced, the splice loss determined by uni-directional measurement is

$$\alpha_{sp} = |\Delta S| + \Delta BS \tag{3}$$

where ΔS is the difference in OTDR signature reading (defined as $5logP_{bS}$) at the splice point for the two fibers, and ΔBS is the error introduced by the backscatter change due to the fiber parameter mismatch:

$$\begin{aligned} \Delta BS &= 5(\log \eta_1 - \log \eta_2) \\ &= 10\log\left[\frac{MFD_2}{MFD_1}\right] + 5\log\left[\frac{\alpha_{s1}}{\alpha_{s2}}\right] + 10\log\left[\frac{n_{eff\,2}}{n_{eff\,1}}\right] + 5\log\left[\frac{n_{g2}}{n_{g1}}\right] \end{aligned} \tag{4}$$

This error can be positive or negative depending on the direction of measurement. Eq. (4) shows that the error is caused by the mismatch in MFD, scattering coefficient, effective refractive index, and group index. These four parameters depend on the fiber type and manufacturing process. For the same fiber type, the contributions of the scattering coefficient and the refractive index profile are very small compared to that of the MFD and can be ignored. But for different fiber types, these two contributions are no longer negligible. They must be considered in the error correction.

III. Experimental

To examine the effects of fiber parameter mismatch on the backscatter change, we used three types of commercially available fibers in our experiments: Dispersion unshifted fiber A (DUA) and fiber B (DUB) and dispersion shifted fiber (DSF). We performed bi-directional OTDR measurements on three groups of fiber splices: DUA-DUA, DUA-DUB, and DUA-DSF. From the OTDR signatures obtained in the two directions, the backscatter change due to fiber parameter mismatch is separated from the splice loss as:

$$\Delta BS = \frac{\Delta S_1 - \Delta S_2}{2} \tag{5}$$

where ΔS_1 and ΔS_2 are the differences in OTDR signature reading at the splice point between the two fibers measured from both directions respectively.

Figure 1 shows the measured backscatter change for the DUA-DUA and DUA-DUB splices. In the same figure, we have also plotted a theoretical line of backscatter change due to MFD only (solid line) and a theoretical line simulating the DUA-DUB splice using Eq. (4) (dashed line). In the simulation, we used Marcuse's relationship between mode field radius and cutoff wavelength [5]. We also assumed that the scattering coefficient is proportional to the GeO_2 concentration in the core, and the ratios of refractive indices are approximately equal to that of the core refractive index. From this figure, we see that for the same fiber type , the backscatter change is mainly due to the MFD mismatch, with the contribution of the other parameters being negligible. But for different fiber types, the backscatter change due to the scattering coefficient and refractive index differences becomes significant. It is worthwhile to realize that fiber with higher backscatter does

not imply higher propagation loss, as the later is not only determined by the scattering coefficient, but also many other factors such as stresses, defects, and geometric imperfections in the fiber.

For the DUA-DSF splice, the results are plotted in Fig. 2. In this case, since the GeO_2 concentration is much higher in the dispersion shifted than in the dispersion unshifted fiber, the differences in scattering coefficient and refractive indices between the two fiber types are larger, causing the backscatter change due to these parameters to be more pronounced. The theoretical line using Eq. (4) has a small offset of 0.07 dB from the measured points. This difference may be due to the non-Gaussian shape of the mode field distribution and the non-step-index profile of dispersion shifted fiber [6]. Nevertheless, the theoretical and experimental results agree well qualitatively.

IV. Conclusion

We have studied theoretically and experimentally the effects of fiber parameter mismatch on OTDR backscatter change. It has been shown that, for different fiber types, the backscatter change due to differences in scattering coefficient and refractive indices, as well as MFD must be considered. This implies that, to correct the error in uni-directional OTDR splice loss measurements, rules of thumb that take these factors into account need to be developed by the fiber industry. Because fiber parameters, which depend on the shape of the refractive index profile, dopant types and concentrations, vary from manufacturer to manufacturer, and are not easily determined for each fiber type, an accurate and simple model is difficult to develop theoretically. Therefore, an experimental approach is recommended to establish the rules of thumb.

References:

[1] P. DiVita, and U. Rossi, "Backscattering measurements in optical fibers: Separation of power decay from imperfection contribution", *Elect. Lett.*, vol. 15, pp. 467-469, 1979.

[2] A. H. Hartog, and M. P. Gold, "On the theory of backscattering in single-mode optical fibers", *J. Lightwave Technol.*, vol. LT-2, pp. 76-82, 1984.

[3] F. Kapron, C. Kozikowski, and T. Olson, "Novel OTDR effects in determining losses of single-mode fibers and splices", *Proceedings of 35th IWCS*, pp. 338-343, 1986.

[4] S. C. Mettler, "Monte-Carlo analysis of the effects of mode field diameter mismatch on single-mode fiber splices", *8th Annual National Fiber Optic Engineers Conference*, Washington, D.C., pp. 647-663, April 21-24, 1992.

[5] D. Marcuse, "Loss analysis of single-mode fiber splices", *Bell Syst. Tech. J.*, vol. 56, pp. 703-718, 1977.

[6] B. J. Ainslie, and C. R. Day, "A review of single-mode fibers with modified dispersion characteristics", *J. Lightwave Technol.*, vol. LT-4, pp. 967-979, 1986.

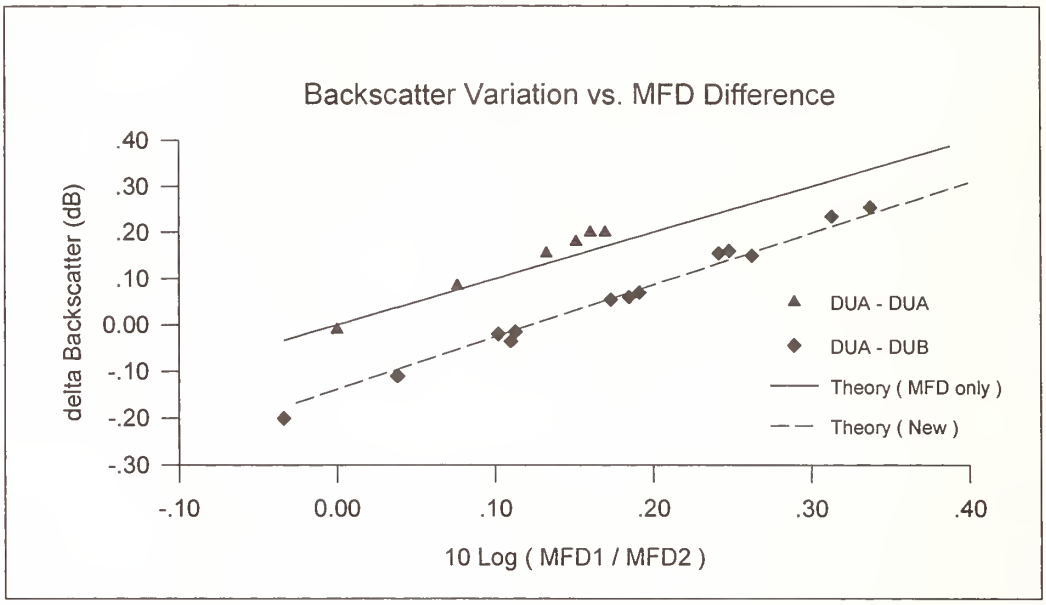

Figure 1 - Backscatter variation for dispersion unshifted fiber A spliced to dispersion unshifted fibers A and B. For the same fiber type (DUA-DUA), the backscatter change is due to the MFD mismatch only, while for different fiber type (DUA-DUB), the contribution of scattering coefficient and refractive index mismatch must be considered as well.

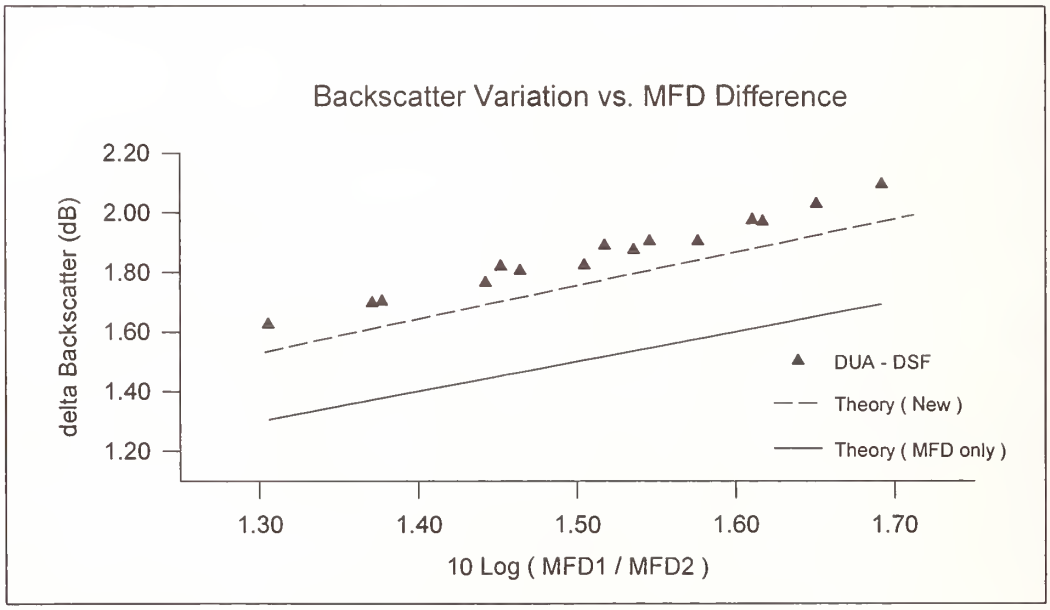

Figure 2 - Backscatter variation for dispersion unshifted fiber A spliced to dispersion shifted fiber. The backscatter change caused by scattering coefficient and refractive index mismatch is more pronounced due to the large dissimilarity of the two fiber types.

Practical Improved Splice Loss Estimation for Single-Mode Optical Fibers

Hisashi TANJI, Seiichi ITO

Submarine Cable Engineering Department
International Digital Communications Inc.

Abstract

An accurate splice loss in single-mode fibers can be estimated in the field based on a unidirectional OTDR measurement combined with a splicer prediction by direct core monitoring (DCM) technique.

1. Introduction

In the estimation of splice losses in single-mode fibers by a fusion splicer with DCM system, a large mismatch of mode field diameters (MFDs), whose effect is omitted from the estimation [1], might induce an erroneous prediction. On the other hand, a unidirectional OTDR measurement shows a splice loss with a rather large deviation from true one due to even a small MFD mismatch [2]. Bidirectional OTDR measurement, which may not always be done in the field, has been needed to obtain an actual splice loss correctly. This paper offers an improved estimation formula taking MFD effect into account in addition to a splicer indicated loss.

2. Theory

A splice loss α in single-mode fibers may be expressed as [3]

$$\alpha = \alpha_f + \alpha_d + \alpha_t \quad \text{[dB]} \tag{1}$$

$$\alpha_f = -20\log(2w_1w_2 / (w_1^2+w_2^2)) \tag{2}$$

where α_f, α_d and α_t are the splice losses due to MFD mismatch, core misalignment and core tilt, respectively, and $2w_1$ and $2w_2$ are the MFDs of the spliced fibers 1 and 2, respectively.
A fusion splicer with DCM system indicates the estimated loss [1]:

$$\alpha_S = \alpha_d + \alpha_t \tag{3}$$

A splice loss as seen by OTDR from fiber 1 to fiber 2 is [2]

$$L(1\text{-}2) = \alpha - 10\log(w_1/w_2) \tag{4}$$

The real splice loss α_R is obtained as a bidirectional average of OTDR apparent losses:

$$\alpha_R = (L(1\text{-}2) + L(2\text{-}1)) / 2 \tag{5}$$

Fig.1 presents the true splice loss α_f and OTDR apparent loss L_f caused by MFD mismatch in the function of MFD ratio a (= $2w_1/2w_2$). From [2], α_f can be calculated from L_f without knowing MFDs. By taking splicer indicated loss α_S into consideration in the calculation, the total splice loss can be estimated as

$$\alpha_E = 2.1715 + L - [\, 2.1715^2 + 4.343(L - \alpha_S)]^{1/2} \qquad (6)$$

where L means L(1-2) or L(2-1). Fig.2 gives the relationships between α_S, L and α_E in (6) with broken lines of MFD ratio a = 1 ($\alpha_E = \alpha_S$), 0.9 and 1/0.9. For example, if MFDs of spliced fibers are limited from 9 to 10 μm, the splice losses are expected to lie within the area between the two lines of a = 0.9 and 1/0.9.

3. Measurements

Splice losses at 1310 nm in the field cable joints were measured by OTDR in both directions. Fig.3 shows the measured and calculated splice losses in some fibers as an example. The deviation of α_E from α_S (y = α_S) in Fig.3 implies α_f, which is negligible if $|L-\alpha_S| \lesssim 0.1$ dB or a = 0.98 to 1.02. The estimation error appears to be attributed mainly to an error in splicer indicated loss, which could differ from actual loss with no MFD mismatch by 0.1 dB at the maximum (average 0.00 dB, σ = 0.03 dB) [1], while an OTDR reading error (usually less than 0.01 dB) may have negligible effect on the estimation due to the significant reduction in the result.

Fig.4 demonstrates measured and estimated losses in comparison with real losses in actual 50 splices with relatively large MFD mismatches. It is obvious that the splice losses estimated by (6) are, on the whole, more accurate than the splicer indications, in which the underestimated loss contribution of average 0.023 dB (Fig.4 (c)) is considered the effect of mixed MFD mismatches that are expected to be a = 0.9 to 0.97 (or 1.03 to 1.11) from the calculation.

4. Conclusion

The improved splice loss estimation with a useful chart of Fig.2 is applicable to practical cable joints, where only unidirectional OTDR measurement can be conducted during cable installation. Care should be taken that the OTDR reading as "splice loss" contains no excess loss factors such as micro/macrobend in the vicinity of the splice. Visual inspection on the display of fusion splicer is also important to eliminate unanalyzable losses due to any anomaly at the splice.

References

[1] N. Hakamata, *et al.*, "Development of a Compact Fusion Splicer with Direct Core Monitoring System SUMIOFCAS® TYPE 34", Sumitomo Electric Tech. Review, No.27, pp. 37 - 41, 1988.

[2] F. Kapron, *et al.*, "Novel OTDR Effects in Determining Losses of Single-Mode Fibers and Splices", 35th IWCS, pp. 338 - 343, 1986.

[3] D. Marcuse, "Loss Analysis of Single-Mode Fiber Splices", B.S.T.J., Vol.56, No.5, pp. 703 - 718, 1977.

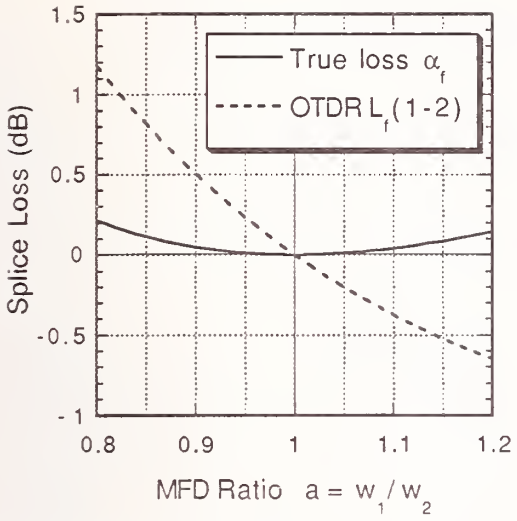

Fig.1 Splice Loss Due to MFD Mismatch
(Assuming $\alpha_d = \alpha_t = 0$ dB)

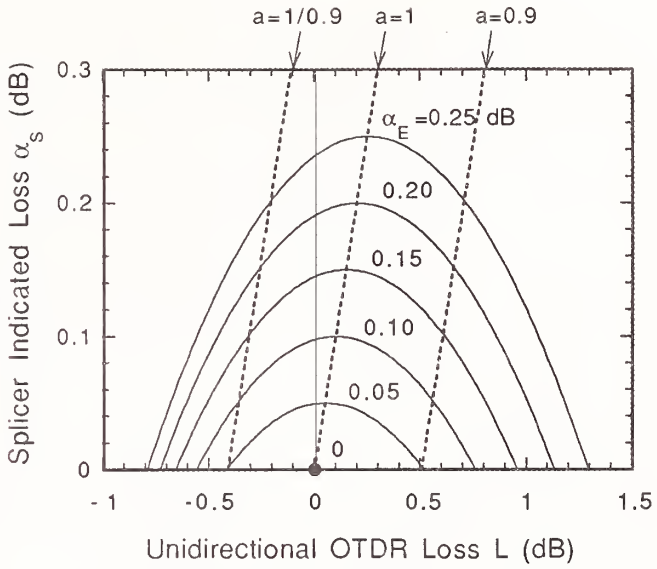

Fig.2 Splice Loss Estimation Chart

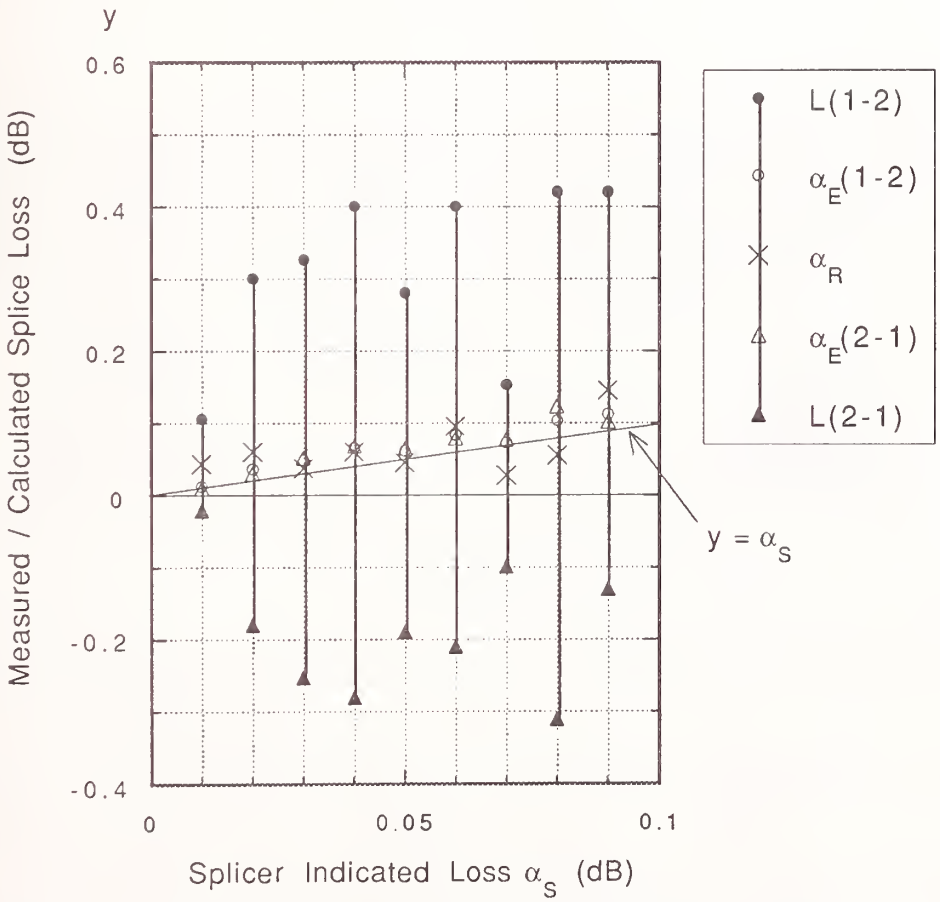

Fig.3 Example of Measured and Calculated Splice Losses

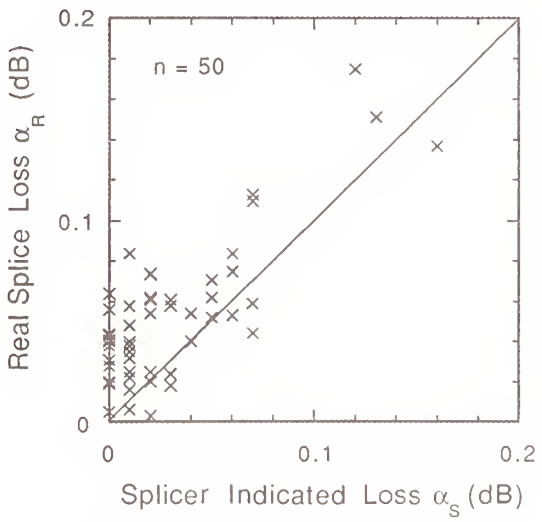

(a) Correlation Between Splicer Indicated Loss and Real Loss

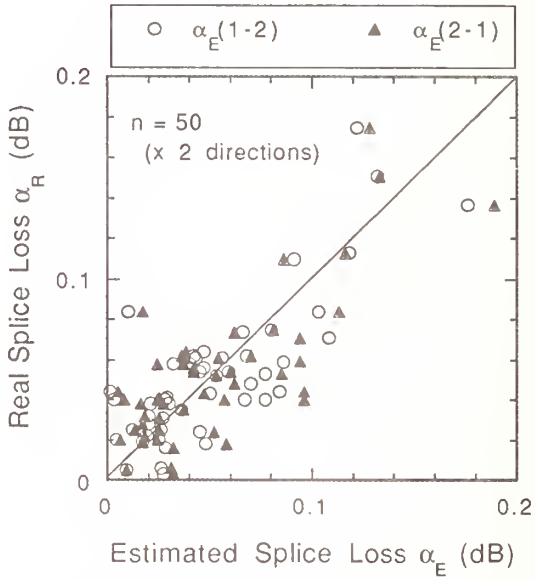

(b) Correlation Between Estimated Splice Loss and Real Loss

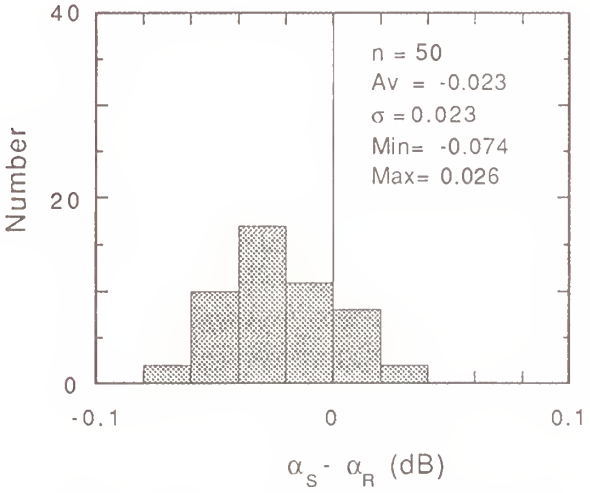

(c) Deviation of Splicer Indicated Loss from Real Loss (in Fig.4 (a))

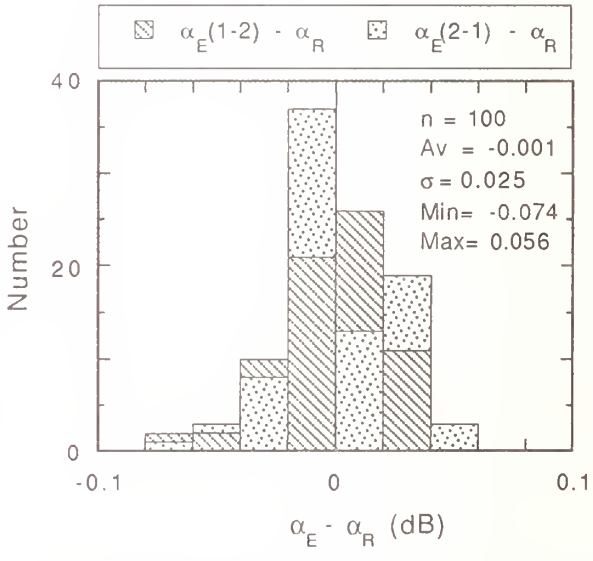

(d) Deviation of Estimated Splice Loss from Real Loss (in Fig.4 (b))

Fig.4 Comparison of Splice Losses by Splicer Indication and Estimation with Real Loss

OTDR Trace Analysis for Fibre Characteristics Evaluation: a "bi-directional" Approach

M.Artiglia (*),A.Chiantore (^),G.Ferri (^),A.Rossaro (*)

(^) FOS - Fibre Ottiche Sud, Battipaglia (SA), Italy
(*) CSELT - Torino, Italy

1.0 Introduction

Optical fibres for telecommunications are nowadays produced in longer and longer lengths: this results into a better handleability of fibre reels from cable manufacturers and a reduction in the total number of measurements which can lead to a lack of characterization of the product. In order to avoid or reduce this drawback, a suitable method is required allowing to check the homogeneity of the fibre characteristics. In this paper, the approach adopted in Europe, according to the indications of the European Telecommunication Standards Insitute (ETSI) and of the Cenelec Electronic Components Committee (CECC), is described: this allows for the measurement of attenuation (longitudinal) uniformity; moreover, a possible definition of an additional parameter, namely the "backscattering uniformity", is discussed. Experimental results are presented, relating the two parameters with the actual characteristics of the fibre (e.g. attenuation and mode field diameter).

2.0 General

The backscattering trace is known to be related to some of the most important fibre characteristics: in the hypothesys of gaussian distribution of the field into the fibre, also an analytical relationship is known [1]. However, taking into account the backscattered power collected from just one end of the fibre introduces some uncertainties and errors in the determination of those parameters, and it has been eventually recognized that the traces from both ends of the fibre ("bi-directional" measurement) need to be considered; in particular it was proposed [2] to calculate the point by point sum (S) and difference (D) of the traces, thus obtaining, on a logarithmic scale [3]:

$$S(z)=K_1+5\log(F(z)) \qquad (2.1)$$

$$D(z)=K_2-\alpha z \qquad (2.2)$$

where

$$F(z)=\left(\frac{\lambda}{2\pi n(z)\omega(z)}\right)^2\cdot\alpha_r(z) \qquad (2.3)$$

and

λ	wavelength	[μm]
n	refractive index	
ω	mode field diameter	[μm]
α_r	Rayleigh coefficient	[μm^{-1}]
α	attenuation coefficient	[dB/km]
K_1,K_2	constants	[dB]

Equations (2.1) and (2.2) show that it is possible to separate the contributions to the backscattered power coming from geometrical parameters (i.e. refractive index and mode field diameter) variations (eq. 2.1) and attenuation variations (eq. 2.2).

3. Attenuation Uniformity

The curve D(z), as defined in (2.2), can be approximated by a best fit straight line, the slope of which is the attenuation coefficient of the fibre.

In order to check the attenuation variations along the fibre, the α value can be compared with a "local" attenuation coefficient, named α_w, obtained considering just the backscattered power from a piece of fibre (window). Allowing this window to slide along the fibre with a given step (e.g. the OTDR distance point), a new function $\alpha_w(z)$ is obtained giving an indication of the local attenuation of the fibre.

The attenuation uniformity parameter X_a can be defined as the maximum (positive) difference between $\alpha_w(z)$ and α. In formulae:

$$X_a = \max(\alpha_w(z)-\alpha) \qquad (3.1)$$

X_a allows to evaluate the longitudinal uniformity of the attenuation coefficient of a fibre; moreover it gives the "worst case" attenuation for any piece of fibre as long as the "window".

An important feature of this method is the possibility to localize and (if necessary) remove any attenuation coefficient discontinuity [4,5].

4. Backscattering uniformity

Starting from the curve S(z), a backscattering uniformity parameter X_b, expressed in dB, can be defined as the maximum vertical distance between two points of the curve S(z).

Assuming that the refractive index variations along the fibres are negligible then the only term depending on z in F(z) is the MFD (ω):

$$S(z)=K_3-10\log(\omega(z)) \qquad (4.1)$$

where K_1 is constant with z.

In order to expand this equation, we assume realistically that the MFD variations are small with respect to its minimum value ω_m:

$$\omega(z)=\omega_m(1+\Delta\omega(z)/\omega_m) \qquad (4.2)$$

$$\Delta\omega(z)/\omega_m<<1 \qquad (4.3)$$

$$S(z)=K_4-4.3\cdot\Delta\omega(z)/\omega_m \qquad (4.4)$$

which in turn, assuming e.g. ω_m=10 μm, results into the following relation beetwen MFD variations and the backscattering uniformity parameter:

$$0.43*\Delta\omega_{max}=X_b \qquad (4.5)$$

This approximation was tested analysing about 100 single mode step index OVD fibres (as per ITU-T Rec. G.652) of different lengths at both 1310 nm and 1550 nm. Figure 1 shows the experimental points as well as the straight line resulting from eq. (4.5) (theoretical line). X_b clearly overestimates the MFD variation, but, however, the fitting error is quite low. The shift between the theoretical and the best fit line is probably due to the noise: a comparison between the MFD variation at 1310 nm and the X_b at 1550 nm, where the SNR is greater, confirms a much lower shift beetwen the two lines (Fig. 2).

In order to better understand the power of X_b in detecting fluctuation of functional fibre parameters, let us consider the Marcuse relation and the well-known cut-off wavelength expression for the step index fibres [6]:

$$\omega = d \left\{ 0.65 + 0.434 \left(\frac{\lambda}{\lambda_c} \right)^{1.5} + 0.0149 \left(\frac{\lambda}{\lambda_c} \right)^{6} \right\} \qquad (4.6)$$

with:

$$\lambda_c = \frac{\pi * d}{2.4} * NA \qquad (4.7)$$

where d is the fibre diameter, NA the numerical aperture and λ_c the cut-off wavelength. Assuming d=8.4 μm and NA=0.12 (typical values) and differentiating:

$$\Delta\omega = 2.3 * \Delta\lambda_c \qquad (4.8)$$

hence:

$$\Delta\lambda_{c,max} \sim X_b \qquad (4.9)$$

where $\Delta\lambda_c$ is in μm: a considerable consequence of this relation is that the X_b parameter could be adopted to verify if the propagation is really single-mode also in long fibres where the cut-off wavelength is only known (measured) at the extremities, i.e. at a distance of 25÷50 km.

In Fig. 3 some data points are compared with eq.(4.9) (theoretical line). The same difference beetwen the two lines and the same behaviour with respect to the SNR is observed as with the MFD variations (Fig. 4).

5.0 Conclusions

The information available from the light backscattered from a fibre has been discussed in the hypothesis of gaussian distribution of the field: this approximation is very accurate for step index single mode (ITU-T Rec.G.652) fibres. Starting from a "bi-directional" trace, two parameters, X_a and X_b, have been introduced; their correlation with structural and trasmissive parameters (MFD, refractive index, cut-off wavelength, attenuation steps) has been proved from both theoretical and experimental point of view, thus suggesting their possible use for quality control purposes on long lengths of fibres.

Further study is necessary to verify if the model is applicable on fibres with non gaussian field distribution, like SM-DS (ITU-T Rec.G.653) fibres.

Finally, it is worthwile to point out that possible limitations in dynamic range and linearity of OTDRs can give rise to incorrect interpretation as fibre defects of noise and/or equipment characteristics.

5.0 References

[1] M.Nakasawa,"Rayleigh backscattering theory for single-mode optical fibers", J.Opt.Soc.Am., Vol.73, No.9, September 1983.

[2] P.Di Vita, U.Rossi, "The backscattering technique: its field of applicability in fibre diagnostics and attenuation measurements", Optical and Quantum El. 11, 17, 1980.

[3] CSELT Techn. Staff, "Fibre Optic Communications Handbook", II ed., T.P.R., 1990.

[4] A.Chiantore et al., "Comparison of algorithms for evaluating fibre attenuation longitudinal uniformity", submitted to Symposium on Optical Fiber Measurements, Boulder (CO), sep.1994.

[5] D.Cuomo, G.Ferri, "Evaluation of fibrel longitudinal uniformity: methods and algorithms", Proc. EFOC&N, Heidelberg, June 1994.

[6] D.Marcuse, "Loss Analysis of Single Mode Fiber Splices", B.S.T.J., May-June (1977).

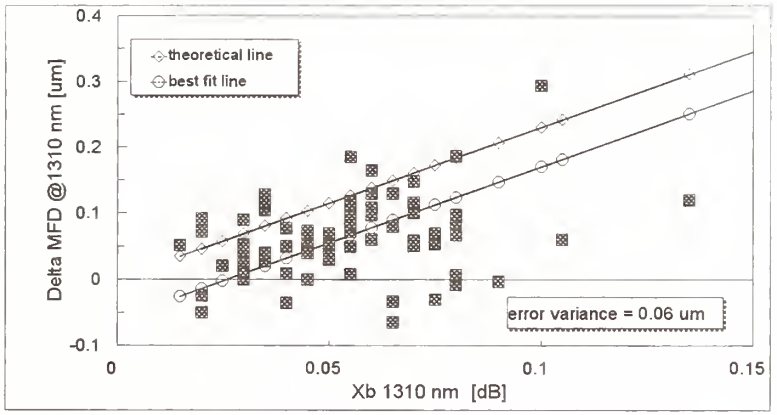

Fig. 1 - MFD variation at 1310 nm versus Xb at 1310 nm. The data points are compared with the theoretical line (---◇---) and the best fit line (---⊖---). The error variance with respect to the best fit line is also given.

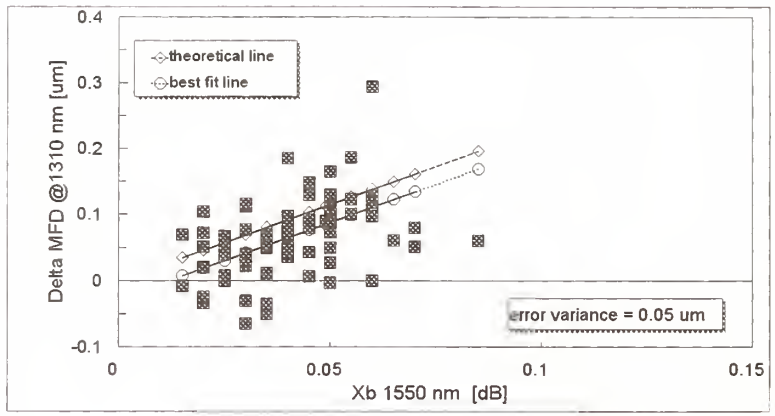

Fig. 2 - MFD variation at 1310 nm versus Xb at 1550 nm. The data points are compared with the theoretical line (---◇---) and the best fit line (---⊖---). The error variance with respect to the best fit line is also given.

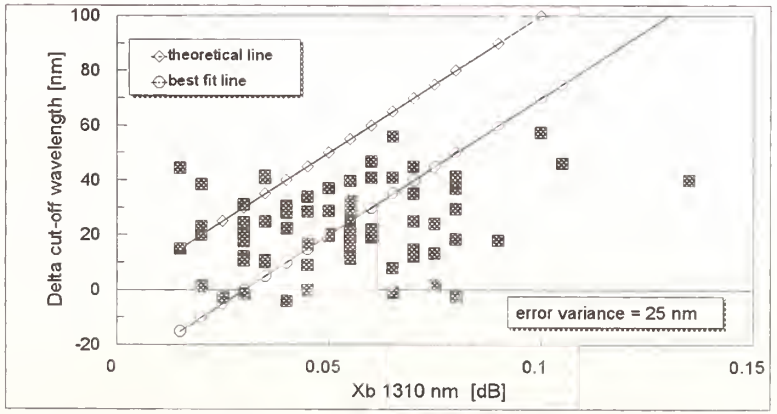

Fig. 3 - Cut-off wavelength variation versus Xb at 1310 nm. The data points are compared with the theoretical line (---◇---) and the best fit line (---⊖---). The error variance with respect to the best fit line is also given.

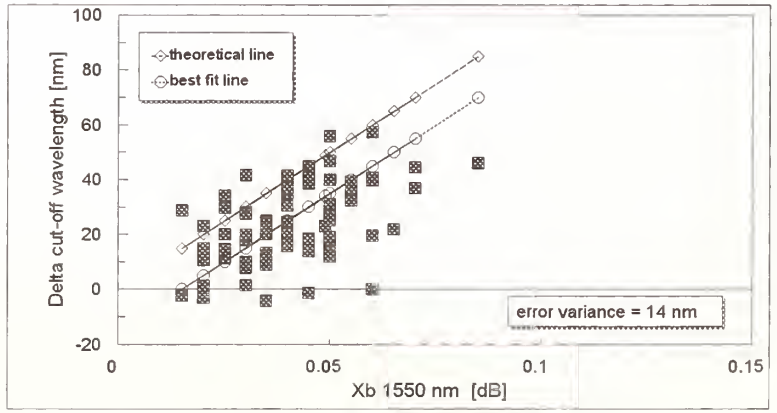

Fig. 4 - Cut-off wavelength variation versus Xb at 1550 nm. The data points are compared with the theoretical line (---◇---) and the best fit line (---⊖---). The error variance with respect to the best fit line is also given.

DETERMINATION OF THE INHOMOGENEITY OF A SINGLE-MODE FIBER ALONG ITS LENGTH BY BIDIRECTIONAL OTDR MEASUREMENTS AT TWO WAVELENGTHS

Clemens Unger , Waldemar Stöcklein
SIEMENS AG, ÖN NK E K 5, Austr. 101, D-96465 Neustadt, Germany

ABSTRACT

The inhomogeneity of the most important fiber parameters along the fiber length, e.g., mode-field diameter (MFD), cut-off wavelength (λ_c), MAC-value (= MFD / λ_c) and zero dispersion wavelength (λ_0) was investigated by means of bidirectional OTDR measurements at two wavelengths. This technique also yields spatially resolved information on both the micro- as well as macrobending sensitivity of fibers.

INTRODUCTION

The development of new optical systems for telecommunication applications or data transmission lead to higher requirements on the optical performance of the fiber. For instance tolerances of the material and waveguide dispersion and the resulting zero dispersion wavelength along the length of the fiber are important in high-capacity, long-distance soliton transmission [1]. Unfortunately the dispersion can be measured only either as an integral value over the whole length of the fiber or on short (2 m) samples taken from the fiber ends.

Furthermore the optical attenuation is a substantial parameter. Current standard single-mode fibers, designed for operation around 1300 nm and 1550 nm, exhibit differing bending losses along the fiber length due to slight variations, e.g. of the core diameter [2]. The newly introduced MAC-value, which is the quotient of the mode-field diameter and the cut-off wavelength, is a suitable measure for the characterization of the bending sensitivity of single-mode fibers [2]. However up to now the MFD and λ_c were always determined by well-known standard techniques (Variable Aperture Method, Transmitted Power Method) on short fiber pieces (typically 2m) from the ends of the fiber. Thus no information on the longitudinal homogeneity is deducible.

Hence the nondestructive measurement of the distribution of the zero dispersion wavelength and the MAC-value along a fiber is of special interest. It has been shown that the signatures of optical time domain reflectometry can be used to determine the Gaussian mode-field diameter [3] and the theoretical cut-off wavelength [4] along the length of the fiber.

In this paper we present the experimental determination of the more customary Petermann II-MFD and the effective λ_c^{exp} by use of the bidirectional OTDR measurement at two wavelengths. In combination with a recently proposed technique these results can be applied to get the longitudinal distribution of the chromatic dispersion and thus of λ_0.

THEORETICAL

It is well known that the backscatter signal $P_{bs}(z)$ from OTDR measurements of a fiber is proportional to the OTDR signature S(z) [3]:

$$P_{bs}(z) = S(z)\cdot\alpha_s(z)\cdot\Delta z\cdot P_0\cdot T_S\cdot 10^{-\frac{2\cdot\alpha\cdot z}{10}} \quad (1), \qquad S(z) = \frac{3}{8\cdot\pi}\cdot\frac{\lambda^2}{n_1(z)^2\cdot MFD(z)^2} \quad (2).$$

It has been shown that the influence of the power decay $10^{-(2\cdot\alpha\cdot z/10)}$ and waveguide inhomogeneity $S(z)\cdot\alpha_S(z)$ may be separated by a bidirectional OTDR measurement. The Gaussian mode-field diameter $MFD^{OTDR}(z)$ [3] and furthermore the theoretical cut-off wavelength $\lambda_c^{theo}(z)$ [4] could be determined along the length z of the fiber by the following relations:

$$\frac{MFD^{theo}\left(a,\lambda_1,\lambda_c{}^{theo}\right)}{MFD^{theo}\left(a,\lambda_2,\lambda_c{}^{theo}\right)} = f\left(\lambda_c{}^{theo},\lambda_1,\lambda_2\right) \overset{!}{=} \frac{MFD^{OTDR}\left(z,\lambda_1\right)}{MFD^{OTDR}\left(z,\lambda_2\right)} \quad \begin{matrix}\lambda_1\ fixed\\ ======>\\ \lambda_2\ fixed\end{matrix} \quad \lambda_c{}^{theo}(z) \quad (3)$$

where the assumption of an almost constant Rayleigh scattering $\alpha_s(z)$ and a modified relation for the MFD (according to the Petermann II MFD, which will be discussed later) was used: (4)

$$MFD^{theo} = 2\cdot a\cdot\left(0.634+1.619\cdot\left(\frac{\lambda}{\lambda_c\cdot V_c}\right)^{1.5}+2.879\cdot\left(\frac{\lambda}{\lambda_c\cdot V_c}\right)^{6}-1.561\cdot\left(\frac{\lambda}{\lambda_c\cdot V_c}\right)^{7}\right)+0.45\,\mu m$$

We recently presented new theoretical and experimental investigations [2], which are in contradiction to former publications, where an increasing macro- and microbending loss with increasing MFD was noticed. The results can be correctly interpreted only by the use of both the effective cut-off wavelength λ_c^{exp} and the Petermann II mode field diameter, that means the MAC-value (= MFD / λ_c^{exp}).

By adding 0.2 µm to the measured Petermann II MFD the Gaussian MFD can be approximated. The experimental cut-off wavelength λ_c^{exp} of a matched-cladding fiber with varying refractive index difference Δ and core radius a within typical manufacturing tolerances may be theoretically calculated [2] from the theoretical cut-off wavelength λ_c^{theo} with an uncertainty of 5 nm (Fig. 1).

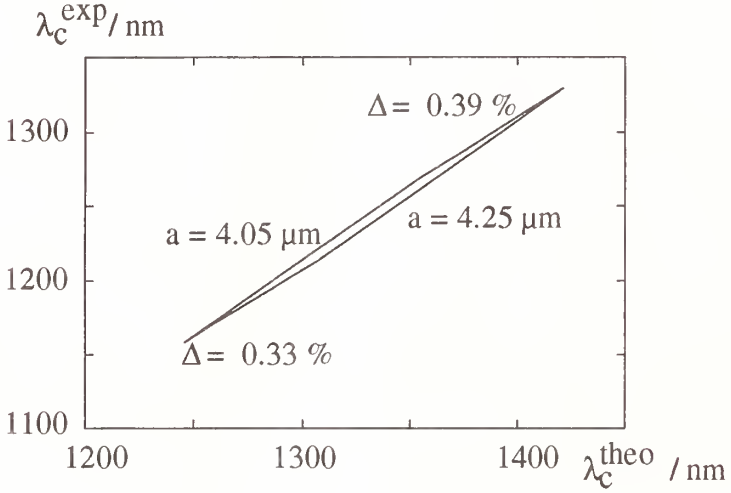

Fig. 1: Experimental cut-off wavelength as a function of the theoretical cut-off wavelength of a matched-cladding fiber (a= 4.05 µm...4.25 µm, Δ = 0.33 %...0.39 %)

The computation of the theoretical cut-off wavelength can be made by use of eq. (4) where the result of the common formula was systematically shifted by 0.45 µm. With this offset we get the best coincidence of the experimental and calculated MFD, where the core radius and the relative index difference were measured by the Refracted Near-Field Technique. This systematic shift is necessary due to a deviation of standard single-mode fibers form an ideal step-index profile, e.g. the central dip.

The determination of the $\lambda_c^{exp}(z)$ by the method mentioned above requires the measurement of 4 OTDR traces (every direction, λ = 1300 nm and 1550 nm) and of 2 MFDs (λ =1300 nm and 1550 nm). Therefore every uncertainty of these values and of the relation between λ_c^{theo} and λ_c^{exp} influence the estimated experimental cut-off wavelength. Hence due to the above mentioned uncertainties this technique is mainly applicable to determine the longitudinal inhomogeneity of λ_c^{exp} (uncertainty ± 10 nm) and not its absolute value. Additionally the effect of the variation of the Rayleigh scattering $\alpha_s(z)$ has to be regarded.

A relatively new aspect of the bidirectional dual wavelength OTDR measurement is the determination of the waveguide dispersion from the wavelength dependence of the MFD [6]:

$$D_{WDis}(\lambda) = \frac{\lambda}{4\pi^2 c \cdot n_K} \cdot \frac{d}{d\lambda}\left(\frac{8\lambda}{MFD(\lambda)^2}\right) \quad . \quad (5)$$

Therefore it should be possible to calculate the chromatic dispersion (the sum of material and waveguide dispersion) and so the zero dispersion wavelength (λ_0) with the knowledge of the longitudinal MFD distribution along the fiber and of the slope of the dispersion at λ_0:

$$\lambda_0(\lambda, z) = \sqrt[4]{\lambda^4 - \frac{4\cdot\left(D_{MDis}(\lambda,z) + D_{WDis}(\lambda,z)\right)}{S_0}\cdot\lambda^3} \qquad \lambda \text{ fixed} \Longrightarrow \lambda_0(z) \quad (6)$$

It is also thinkable to predict the zero dispersion wavelength λ_0 (z) as a funtion of λ_c^{exp} (z), which may be determined from an OTDR measurement. λ_0 of an ideal step-index fiber can be calculated as a function of λ_c^{exp} with a data scatter of ± 1 nm [6] (Fig. 2).

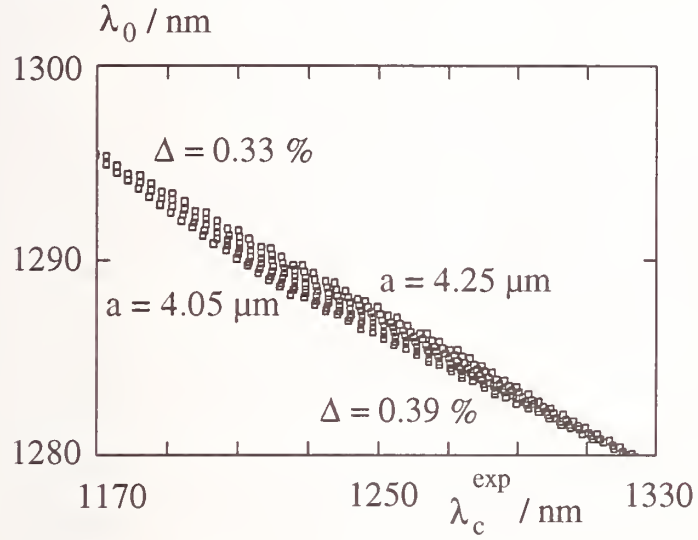

Fig. 2:
Zero dispersion wavelength as a function of the experimental cut-off wavelength of a matched-cladding fiber (theoretical)
(a= 4.05 µm...4.25 µm, Δ = 0.33 %...0.39 %)

EXPERIMENTAL

Measurements on 33 short fiber pieces (2 m) with a Mach-Zehnder-Interferometer (MZI) (Fig. 3) confirm the theoretical dependence of the zero dispersion wavelength and the cut-off wavelength (Fig. 2). The systematic offset of the theoretical data to measured λ_0-values of nearly 23 nm can be explained again by deviations from an ideal step-index profile of the fiber.

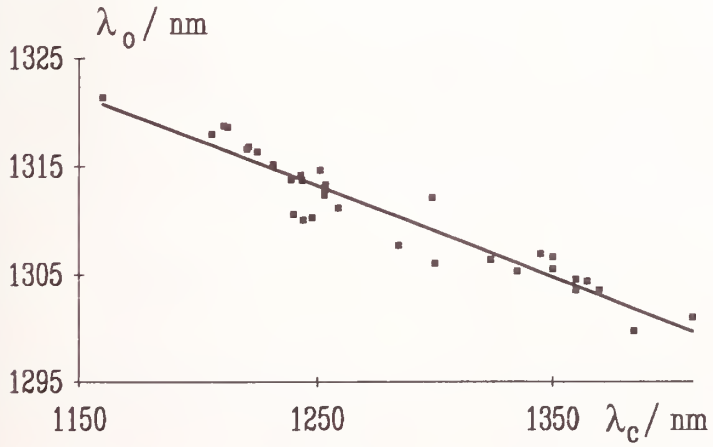

Fig. 3:
Zero dispersion wavelength as a function of the experimental cut-off wavelength of a matched-cladding fiber (experimental)

$$\lambda_0 = -0.0844 \cdot \lambda_c + 1418.6 \text{ nm} \quad (7)$$

Furthermore we selected matched-cladding fibers with a directional dependence of the attenuation value, derived from OTDR-backscatter traces, when measured from both fiber

ends. This typically can be related to a MFD variation along the fiber length. A different variation of the MFD at λ = 1300 nm and 1550 nm is an indicator of a longitudinal change of the cut-off wavelength and accordingly to Fig. 2 and 3 of the zero dispersion wavelength along the fiber.

The chromatic dispersion and consequently the average λ_0 of the whole (2 km long) fiber were determined by a Phase-Shift-Measurement (PSM, horizontal solid line in Fig. 4).

The fiber was cut into short pieces and the MFD-, λ_c-, MAC- and λ_0-values were measured. Additionally the zero dispersion wavelength λ_0 (z) was calculated from the bidirectional dual wavelength OTDR-traces

1) according to Eq. (5) and (6) from the estimated mode-field diameter MFD(z) and
2) according to Eq. (3) and (7) from the estimated cut-off wavelength λ_c (z).

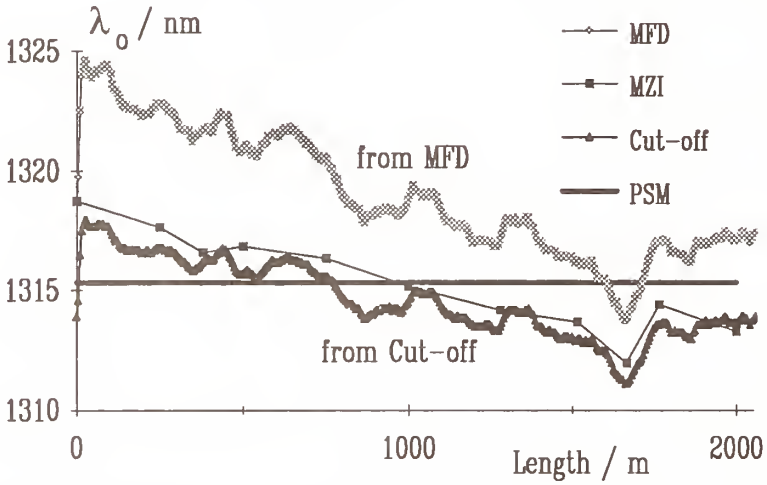

Fig. 4: Experimental λ_0 -distribution of an inhomogeneous matched-cladding fiber calculated from estimated MFD and from estimated λ_c^{exp}; local measurements with a Mach-Zehnder-Interferometer (MZI) and integral value of a Phase-Shift-Measurement (PSM)

The correspondence of the results of the local measurement (MZI) and the calculations verify the reliability of this method. The systematic shift of λ_0 determined by the estimated MFD can be explained by the uncertainty of Eq. (4), where a wavelength dependent term (instead of 0.45 µm) has to be used.

In addition the MAC-value (= MFD(z) / λ_c (z)) can be predicted along the length of the fiber, which characterizes the longitudinal bending sensitivity of the fiber [2]. Therefore it is possible to distinguish between the local attenuation increase in a fiber optic cable due to either a higher bending susceptibility of the fiber or larger encumbrances of the cable.

REFERENCES

[1] V.A. Bogatyrev, et. al.: "A single-mode fiber with chromatic dispersion varying along the length", J. of Lightwave Tech., LT-9, No. 5 (1991) pp. 561-566

[2] C. Unger. W. Stöcklein: "Characterisation of the bending sensitivity of fibers by the MAC-value", Opt. Comm., 107 (1994) pp. 361-364

[3] M.S. O´Sullivan, R.S. Love: "Interpretation of SM fiber OTDR signatures" SPIE Vol. 661, Optical Testing and Metrology (1986) pp. 171-176

[4] K.W. Kowaliuik, J. Ferner: "A technique to estimate the cutoff wavelength profile in single-mode fibers using a switchable dual wavelength OTDR", Tech. Digest Symp. on Optical Fiber Measurements, Boulder (1988) pp. 123-126

[5] M. Ohashi, M. Tateda: "Novel technique for measuring longitudinal chromatic dispersion distribution in single-mode fibers", Electron. Lett. Vol. 29, No. 5 (1993) pp. 426-428

[6] C.D. Hussey: "Characterization and design of single-mode optical fibres", Opt. and Quant. Electron., 14 (1982) pp. 347-358

COMPARISON OF ALGORITHMS FOR EVALUATING FIBRE ATTENUATION LONGITUDINAL UNIFORMITY

A. Chiantore, G. Ferri
FOS - Fibre Ottiche Sud, Battipaglia , SA (Italy)
M. Artiglia, P. Di Vita
CSELT - Centro Studi E Laboratori Telecomunicazioni, Torino (Italy)

Abstract

The proposed algorithms to evaluate the longitudinal uniformity of attenuation in single mode fibres have been compared by means of numerical simulations and elaboration of experimental results taken over a sample of more than 600 fibres. Reliability, effectiveness, area of application and robustness to noise of the algorithms have been investigated in several situations of practical relevance, in view of their possible introduction in international standards.

1. Introduction

Attenuation is a characteristic of optical fibre which is of paramount practical relevance. At present only the global attenuation of a given fibre length is considered in existing standards. Recently, since production lengths have increased and lengths of installed fibre are decreasing as fibre proceeds towards the user, the need emerged for a better understanding and control of the longitudinal variation of fibre attenuation, in order to avoid that pieces cut from a given fibre have attenuation much higher than average attenuation of the whole fibre. Optical Time Domain Reflectometry (OTDR) equipment [1] seems to be a very promising tool to this purpose, since the OTDR backscatter trace is strongly related to the attenuation along the fibre. Moreover, the backscattering instruments are widely diffused since OTDR provides a powerful, versatile and practical tool for testing optical fibre attenuation, loss of fibre joints and for locating fibre defects or faults in an installed fibre line.

There are a number of approaches to characterise the attenuation variation along the fibre, all based on the analysis of OTDR traces taken from both ends of the fibre [2]. These are based on the observation, made some years ago [3], that when two such traces, one taken from each end of the fibre, are averaged, the resulting trace is a straight line the slope of which is the attenuation coefficient of the fibre. In view of a possible introduction of a fibre longitudinal uniformity parameter in international standards, there is an urgent need to assess reliability, effectiveness and robustness to noise of the proposed algorithms. The aim of this paper is to compare two common approaches in terms of the aforesaid requirements. The first approach, known as 'sliding window' method (SW), is the one accepted as a test method for attenuation uniformity in the European Telecommunication Standard Institute (ETSI) and in the Cenelec Electronic Components Commitee (CECC). The second is the approach developed as a national standard in the Electronic Industries Association (EIA), known as 'generalised sliding window' method (GSW) [4]. Results of a comparison of the two methods performed on special cases of practical relevance, such as fibres with splices or attenuation discontinuities, and on the data measured on 600 standard fibres without such non-uniformities, are presented and discussed in order to identify areas of applicability, advantages and drawbacks of the two techniques.

2. Definitions of Longitudinal Uniformity of Attenuation

The basic principles of the two studied approaches are now briefly discussed.

The SW approach is aimed at the evaluation of the optical uniformity of the fibre by separating its two basic components: effects due to variation of MFD and refractive index and effects due to attenuation variation. The former are described by means of the parameter X_b, called backscattering uniformity, which is outside the scope of this paper; the latter are described by the parameter X_a, called attenuation uniformity. This parameter is obtained (together with X_b) from the analysis of the OTDR traces taken from the two

ends of the fibre under test, and is defined as the maximum over the whole fibre length of the function:

$$UA(x_i) = [\alpha_1(x_i)+\alpha_2(x_i)]/2 \quad (1)$$

where x_i is the position along the fibre axis of the i-th sample of the OTDR trace, and $\alpha_1(x_i)$ and $\alpha_2(x_i)$ are the attenuations of a fibre segment of length L_a centred on x_i as seen from the two ends of the fibre under test. $UA(x)$ is a measure of the averaged local attenuation at x and L_a is the length of the sliding window over which local attenuation is evaluated. The parameter X_a is therefore the maximum attenuation coefficient obtainable when cutting a piece of fibre of length L_a. The sliding step and L_a and are chosen according to the most suitable requirements.

On the other hand, the GSW approach is aimed at evaluating only attenuation uniformity of the fibre by means of a parameter called maximum excess loss (MEL) and is able to predict the maximum attenuation that may occur when a piece of fibre is cut from the fibre length under test. In this approach the maximum attenuation coefficient of any fibre segment of length L is defined as:

$$\alpha_{max}(L) \leq \alpha_{ref} + \varepsilon_{ref}/L \quad (2)$$

wherein α_{ref} is the attenuation coefficient of the whole fibre length without non-uniformities and ε_{ref} is the MEL. These parameters, computed by means of a suitable binary search algorithm from measured OTDR traces, shall be given by the manufacturer for each fibre length [4].

3. Results and Discussion

The effectiveness of SW and GSW methods has been investigated both by means of numerical simulations and experimentally. In the tests which will be discussed, the local attenuation coefficients of Eq. (1) were calculated either by best fit procedures, or by difference between the two ends of the sliding window (two-points method). For the seek of brevity, only the results obtained with the two points method will be given in the following. The sliding window width assumed throughout is $L_a = 1$ km.

The first type of test which has been considered is the evaluation of attenuation in a fibre length with an attenuation discontinuity (i.e. a splice). In this test particular emphasis has been given to the dependence of the various attenuation uniformity parameters on the background noise. Typical results of numerical simulations on a 7 km fibre piece with an attenuation jump of 0.025 dB and attenuation coefficient of 0.34 dB/km, are given in Figs.1 and 2. Gaussian noise with zero mean and variable standard deviation was added to the calculated data in order to simulate measurement noise. Figure 1 shows the behaviour of the estimated attenuation versus length as given by the two methods assuming a SNR of 11.8 dB, compared with the actual attenuation of the fibre. Dependence of MEL and X_a on noise power is shown in Fig. 2. It appears clearly that both parameters give a quite good estimate of the attenuation discontinuity even if MEL increases faster with noise power than X_a does. These features have been experimentally confirmed by processing the OTDR traces measured on a very uniform fibre spliced again after being cut. Both methods tend to overestimate the attenuation value with lower signal to noise ratios.

In a second type of test multiple attenuation discontinuities were considered to investigate the variation of the attenuation uniformity parameters with the relative distance of the discontinuities. Numerical and experimental tests on a fibre with two attenuation discontinuities (0.05 and 0.1 dB respectively) have been performed: i) by varying their distance and keeping fixed the optimisation interval of GSW, ii) by varying the optimisation interval and keeping fixed the distance between the defects. It has been observed that the MEL behaves differently for varying distances between the defects. When the distance is lower than the harmonic mean of the optimisation interval (in this case fibre lengths from 1 to 3.5 km were considered, leading to an harmonic mean of 2 km), the MEL gives an estimate of the sum of the discontinuities; when distance is

longer, the MEL gives an estimate of the largest discontinuity, as X_a does (provided L_a is is shorter than the distance between defects).

Finally, in order to test the performance of the methods in practical conditions, the SW and GSW algorithms have been compared using OTDR traces taken at 1310 nm and 1550 nm on a sample of 600 fibres, which comply to factory quality assessment criteria. The results are summarised in Figs. 3 to 6. Figure 3 and 4 show the correlation plots of the obtained values of MEL and X_a on the whole fibre sample at 1310 nm and 1550 nm respectively. Figures 5 and 6 show the correlation plots of the obtained values of maximum attenuation of a 1 km fibre piece predicted for each fibre of the sample by SW method and GSW method at 1310 nm and 1550 nm respectively. It is apparent that the two methods are mutually consistent.

It should be noted that the SW method (contrary to GSW) enables to localise the defects of the fibre, and therefore could be particularly useful for quality control in the fibre factory as well as for cable manufacturers and installers.

4. Conclusions

An extensive comparison between the algorithms for evaluating the fibre attenuation uniformity considered in EIA (GSW) and ETSI (SW) has been carried out on the basis of numerical simulations and elaboration of experimental data obtained on a sample of more than 600 optical fibres. The tests that have been carried out show that the GSW method and the SW method give on average the same results for fibres without attenuation discontinuities. When attenuation discontinuities, such as fibre joints, are present, the SW uniformity parameter X_a gives a good estimation of the maximum attenuation jump and is able to localise the defects. On the other hand, the GSW method yields a robust evaluation of the worst case attenuation for every fibre sub-length, providing to the system designer a good estimate of the maximum attenuation that can be expected when cutting from a bobbin a piece of given length. If more than one discontinuity is present in the fibre the GSW uniformity parameter, the MEL, behaves differently depending on the distance between the discontinuities; in addition, GSW method is unable to localise possible defects into the fibre, which turns to be drawback from the point of view of installers and manufactures of cables and fibres. On the other hand the SW method is unable to provide maximum values for attenuation when defects are present in the fibre.

References

[1] CCITT (now ITU-T) Recommendation G. 650

[2] R.G. Gravely III, S.R. Stokes, E.L. Buckland: *"Fiber optic measurement techniques for improved product and system quality control"*, Proc. of IWCS '93, p. 833

[3] P. Di Vita, U. Rossi: *"The backscattering Technique: its field of applicability in fibre diagnostics and attenuation measurements"*, Optical and Quantum El., vol. 11, p. 17- 22 (1980)

[4] T.A. Hanson: *"Attenuation Uniformity Characterisation"*, proceedings of OFMC'93, Torino (Italy), Sept. 21-22, pp. 41-44

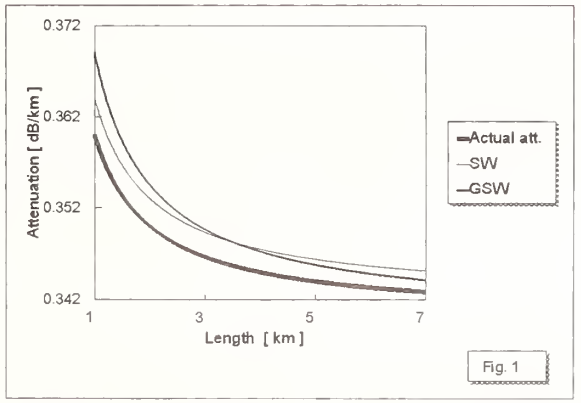

Fig.1 - Estimated attenuation v.s. length as given by SW and GSW (SNR=11.8 dB) compared with the actual attenuation.

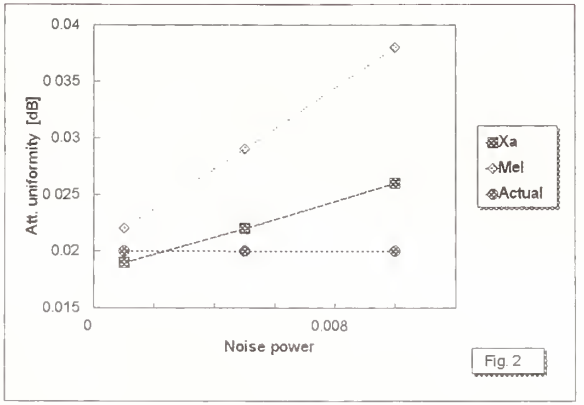

Fig.2 - Mel and Xa vs. noise power.

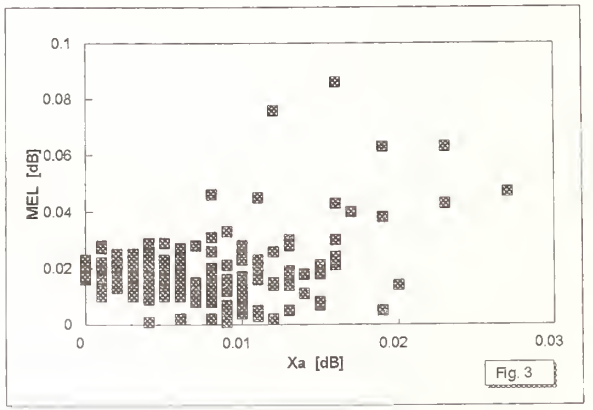

Fig.3 - MEL vs. Xa @ 1310 nm (600 fibres).

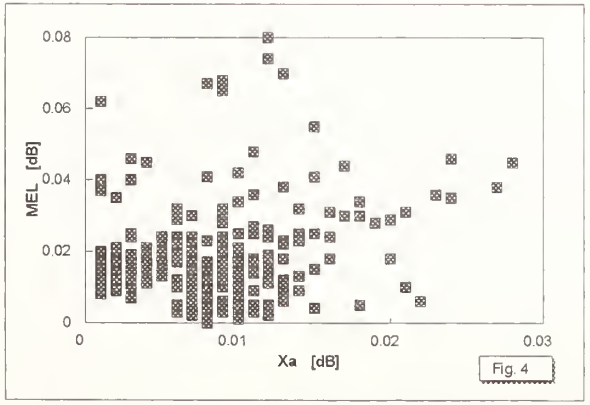

Fig.4 - MEL vs. Xa @ 1550 nm (600 Fibres)

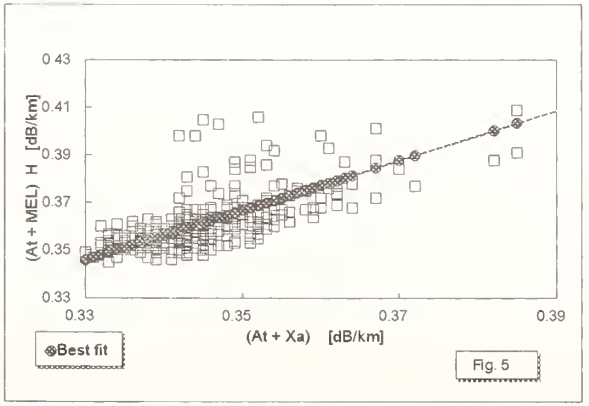

Fig.5 - Maximum predicted attenuation of 1 km segments for each fibre sample: SW vs. GSW @1310 nm (600 Fibres)

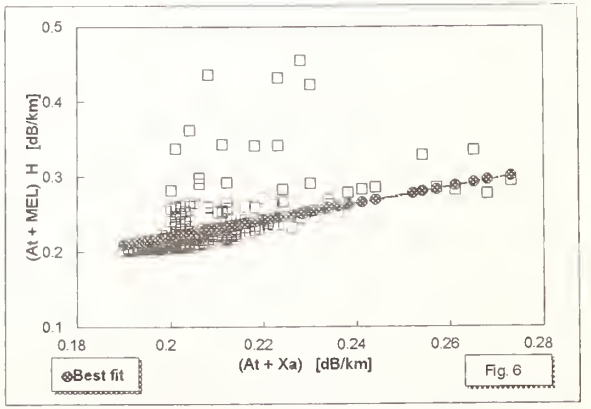

Fig.6 - Maximum predicted attenuation of 1 km segments for each fibre sample: SW vs. GSW @1550 nm (600 Fibres).

1 m spatial resolution measurement of distributed Brillouin frequency shift in single-mode fibers

T. Horiguchi, T. Kurashima, and Y. Koyamada

NTT Telecommunication Field Systems R&D Center
Tokai-mura, Naka-gun, Ibaraki-ken, 319-11 Japan

Abstract

The Brillouin frequency shift can be applied to measure distributed strain and temperature. We describe high spatial resolution measurements of the Brillouin frequency shift in single-mode fibers. We have achieved 1 m spatial resolution by using an 11 km fiber.

1. Introduction

Changes in the frequency of stimulated Brillouin scattering can be used to measure changes in strain and temperature in an optical fiber. Brillouin optical fiber time domain analysis (BOTDA) can be used to measure local changes in strain and temperature along a single-mode fiber [1]. In BOTDA, a pump pulsed light and a counterpropagating continuous-wave (cw) light are launched into a single-mode fiber so that they interact through stimulated Brillouin scattering, and the increase in the cw light intensity due to the Brillouin gain is measured as a function of time with OTDR. The first measurements of distributed strain and temperature using BOTDA were demonstrated with a spatial resolution of 100 m [1]. Since these demonstrations, many efforts have been made to improve on this value. Recently, a spatial resolution of 5 m has been achieved [2] by using 50 ns pulsed light which is obtained by modulating the output of a 1.32 μm wavelength cw diode-pumped Nd:YAG ring laser with an acousto-optical modulator (AOM). The pulsed light width of 50 ns is around the acoustic phonon lifetime in silica optical fibers. If we use a pulsed light whose width is around or shorter than the acoustic phonon lifetime, the measured Brillouin gain bandwidth increases from its intrinsic value. This means that a higher signal-to-noise ratio is required in order to measure accurately the center frequency of the Brillouin gain band, i.e. the Brillouin frequency shift [1]. If, in addition, we take the interaction length of the pulsed and cw lights into account, the increase in the Brillouin amplified cw light power, i.e. the BOTDA signal power, decreases when the width of the pulsed light decreases. These facts make it difficult to achieve a spatial resolution of better than 5 m. In this paper we show that 1 m spatial resolution is possible by using 10 ns pulsed light which is amplified by Er-doped fiber amplifiers (EDFAs).

2. Experimental setup

The configuration of the BOTDA system used in our experiments is shown in Fig. 1. The system is composed of a pump-pulsed light source, a probe cw light source and a 100 MHz bandwidth detector followed by a digital processor that performs signal averaging and analysis. The pump-pulsed light source is a combination of a 1.55 μm DFB-laser diode (LD) and an electro-optical modulator (EOM) with two erbium-doped fiber amplifiers (EDFAs). An optical bandpass filter (BPF) and an acousto-optical modulator (AOM) reduce amplified spontaneous emission noise from the EDFAs in the frequency and the time domain, respectively. The AOM also improves the extinction ratio of the EOM. The pump-pulsed light has a pulse width ranging from 10 ns to 1 μs and a peak power of about 20 dBm in the test fiber which induces Brillouin gain. The dependence of the Brillouin gain on the polarization was decreased by rotating the polarization of the pulsed light with a Faraday cell (FC). We measured the temporal increase in the probe cw light power by integrating 2^8 signals for one frequency difference between the pulsed and cw lights. This measurement was repeated by changing the frequency difference with an interval of 10 MHz around the Brillouin frequency shift of about 11 GHz at a wavelength of 1.55 μm. We determined the Brillouin frequency shift as the center frequency of the Brillouin gain band. Then, we obtained a map of the Brillouin frequency shift along the fiber length. Measurements with the BOTDA system were carried out on an 11 km single-mode fiber composed of two kinds of fibers, type A and type B, as shown in Fig. 2. 10 m, 5 m, 2 m and 1 m fiber spools were formed from the A type fiber, while the rest was the B type fiber. The difference between the Brillouin frequency shifts of the two types of fiber is 50 ± 1 MHz.

3. Results and discussion

The distributions of the Brillouin frequency shift along the 11 km fiber were measured by using 60 ns and 10 ns pump-pulsed light. The results are shown in Fig. 3(a) and (b), respectively. A local change occurred in the Brillouin frequency shift in the 10 m fiber spool as expected and can be clearly seen in Fig. 3(a). The measured Brillouin frequency shift agrees with that of the long A type fiber and the measurement error is better than ±5 MHz. As the strain and temperature coefficients of the Brillouin frequency shift are 5.0 MHz/10^{-4}-strain and 1.0 MHz/K at 1.55 μm, this frequency error corresponds to a strain and temperature measurement error of ±10^{-4} and ±5 K, respectively. Figure 3(a) also shows that a change in the Brillouin frequency shift can be detected even in 5 m, 2 m and 1 m spools, although it is smaller and the spatial resolution is 6 m. The measured change in the Brillouin frequency shift of 1 m fiber spool is 0.1-times the real value. This is because the Brillouin gain spectrum of the 1 m fiber spool which is measured by using 60

ns pulsed light is a superimposition of the spectra corresponding to the 1 m A type fiber and the 5 m B type fiber [3,4]. If we resolve the two spectra, the real Brillouin frequency shift of the 1 m fiber spool can be obtained, although we have not tried it.

Figure 3(b) shows the results of a measurement using 10 ns pulsed light. In contrast to the result for 60 ns pulsed light, the Brillouin frequency shift in the 1 m spool can be clearly seen and as expected is in good agreement with that of the long A type fiber. The measurement error is better than ±10 MHz, which corresponds to a strain and temperature measurement error of ±2 x 10^{-4} and ±10 K, respectively. This measurement error can be decreased by integrating more signals, although the measurement time increases.

Figure 4 shows the Brillouin gain bandwidth dependence on the pulsed light width. It is seen from Fig. 4 that the measured bandwidth for a pulsed light width of 10 ns is two times that for 1 μs. This is because the spectral width of the 10 ns pulsed light exceeds the intrinsic Brillouin gain bandwidth of silica optical fibers. This increase in the Brillouin gain bandwidth reduces the measurement accuracy because the variation of the measured Brillouin frequency shift is proportional to the Brillouin gain bandwidth [1]. In addition, the BOTDA signal power decreases as the pulsed light width decreases. On the basis of the measured results shown in Fig. 3(b) we believe that in spite of these difficulties 1 m spatial resolution is possible.

4. Conclusion

A high spatial resolution BOTDA system has been constructed which uses a combination of an EOM and an AOM to produce 10 ns pulsed light with a wavelength of 1.55 μm and EDFAs to boost it. Experiments confirmed that 1 m spatial resolution is possible with a measurement accuracy of better than ±10 MHz over an 11 km single-mode fiber.

References

[1] T. Horiguchi, T. Kurashima and Y. Koyamada, "Measurement of temperature and strain distribution by Brillouin frequency shift in silica optical fibers," in *Proc. Distributed and Multiplexed Fiber Optic Sensors II*, SPIE vol.1797, pp.2-13, 1992.

[2] X. Bao, D. J. Webb and D. A. Jackson, "32km Brillouin loss based distributed temperature sensor," in *Proc. 9th Optical Fiber Sensor Conference*, 1993, PD-3.

[3] T. Horiguchi, T. Kurashima, M. Tateda, K. Ishihara and Y. Wakui, "Brillouin characterization of fiber strain in bent slot-type optical-fiber cables," *J. Lightwave Technol.*, vol.10, no.9, pp.1196-1201, 1992.

[4] X. Bao, D. J. Webb and D. A. Jackson, "Temperature non-uniformity in distributed temperature sensors," *Electron. Lett.*, vol.29, no.11, pp.976-978, 1993.

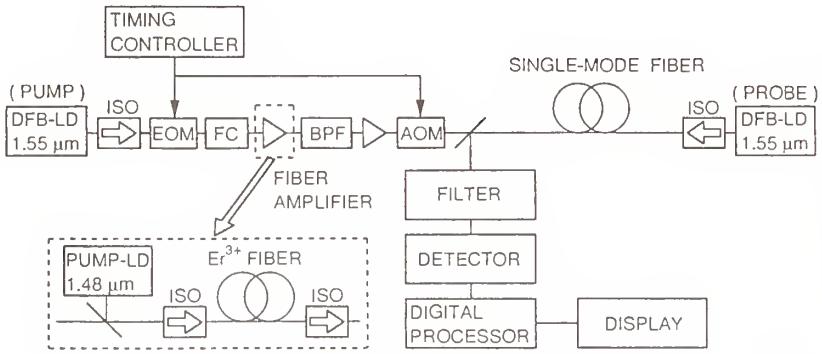

Fig. 1 Configuration of BOTDA system.

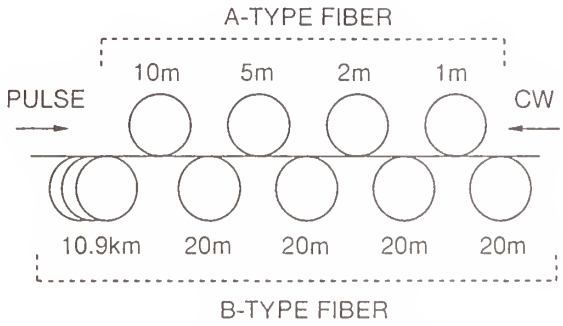

Fig. 2 Measured single-mode fiber

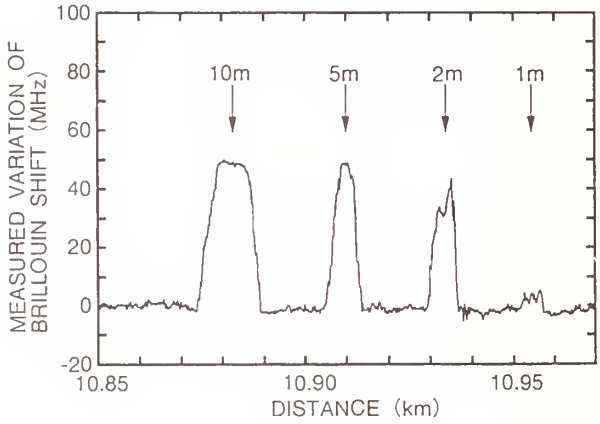

(a)

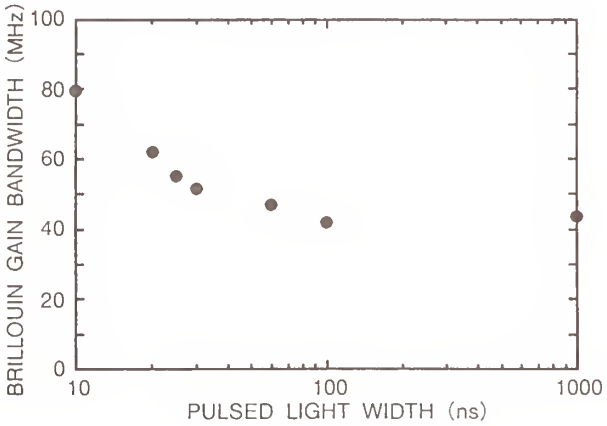

Fig. 4 Relationship of pulsed light width and Brillouin gain bandwidth (FWHM)

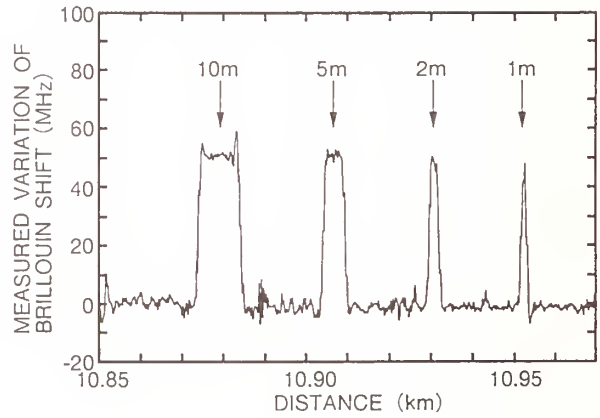

(b)

Fig. 3 Measurement of distributed Brillouin frequency shift by using (a) 60 ns pulsed light and (b) 10 ns pulsed light

THE DEVELOPMENT OF AN OPTICAL FIBRE ATTENUATION STANDARD

N R Haigh[1] and T C E Jones[2]

[1] Communications Cables Division, Helsby Technology Centre, BICC Cables Ltd, Helsby, Warrington, Cheshire WA6 0DJ, UK
[2] Division of Quantum Metrology, National Physical Laboratory, Queens Road, Teddington, Middlesex TW11 0LW, UK

1. Introduction

Measurement of the spectral attenuation of single mode optical fibre is crucial to fibre manufacturing, fibre cabling and fibre installation processes. It is the principal mechanism through which product quality is determined and is used to identify degradation of performance in installed all-optical telecommunication links. Two measurement techniques are used widely to determine the attenuation of single mode fibre. These are the cut-back and the OTDR (optical time domain reflectometry) techniques. The equivalence of the two techniques has been demonstrated [1], but the artefact or method for calibrating an OTDR is still under consideration.

Fibre manufacturers seek traceability for fibre attenuation measurements in order to demonstrate the validity of performance specifications attached to their products. Indeed, many national network providers require demonstration of traceability before fibre can be used in their networks. Traceability is obtained through National Reference Facilities for cut-back measurement, which are maintained by National Standard Laboratories or other organisations with responsibility for maintaining and disseminating attenuation measurements for their country.

International standardisation bodies have placed considerable emphasis on normalising the methods used to determine fibre attenuation [2,3,4]. A number of National Standards Laboratories have set up facilities in accordance with these test methods to provide traceable measurements. However, similar effort has not been applied to the development of transfer standards in order to transfer the accuracy obtainable in National Standards Laboratories to the industrial user. In general, measurements are performed on fibres supplied on standard shipping reels. The measured attenuation of fibre under these circumstances can be highly sensitive to extrinsic factors such as temperature cycling and vibration. Such sensitivity can be increased in a fibre which is not well selected or that is badly wound on the shipping reel, as depicted in figure 1.

NPL in conjunction with BICC Cables Ltd have undertaken a programme of work to develop a 'golden fibre' attenuation transfer standard that can be readily packaged and transported world wide and reliably used for the calibration of spectral attenuation benches and optical time domain reflectometers.

2. Detail

A specification for the fibre transfer standard was formulated along with a design approval test programme that fully qualifies its performance. This testing programme included a rigorous set of environmental tests comprising of the following: Dry heat, 21 days at 70 °C; Damp heat 21 days at 40 °C/93% Relative humidity; Temperature cycling, 10 cycles of - 10/70 °C, Cold storage, 10 days at -40 °C; vibration testing.

The fibre was packaged so that the fibre is protected from the rigours associated with transit, and to avoid any losses due to macrobending. In addition, the transfer standard was designed to facilitate ready access to both ends of the fibre in order to accommodate the destructive 2 metre fibre cut-back to be performed during the spectral attenuation measurement procedure.

Details of the design of the fibre attenuation standard will be presented at the conference. The most significant factor in the design of the fibre standard is related to fibre handling, where it is essential that the fibre is free from stress along its entire length. This is considered to be vital in ensuring that environmentally induced changes in attenuation cannot arise from effects such as tight fibre winding or fibre cross-overs. It also results in the fibre exhibiting a very low level of polarisation mode dispersion.

3. Results

The spectral attenuation of a 6 km standard measured by the two laboratories (NPL and BICC) is shown in Figure 2. The rapid increase in attenuation above 1550 nm which is characteristic of bend loss, and commonly observed for fibres wound on shipping reels (see figure 1) is not observed for the transfer standards. Figure 3 shows the difference in the spectral attenuation values as measured by the two laboratories. In the second and third transmission windows, the difference between the two laboratories is less than ± 0.003 dB/km. However, it should be noted that a relatively large error, of the order of 0.05 dB/km occurs in the 1380 nm hydroxyl ion absorption feature of the attenuation spectrum, where the spectral attenuation of the fibre varies strongly with wavelength. Such an error is not unexpected and is probably indicative of a slight offset in the wavelength calibration of the two spectral attenuation benches. Measurements of fibre attenuation were made during the above environmental test programme. Stability of the fibre attenuation was measured to be better than ± 0.03 dB. To date, the fibre attenuation has been measured to be stable to less than ± 0.03 dB/km during the above environmental test programme. At the end of each environmental test, the fibre spectral attenuation was observed to return, within the measurement error, to its initial value.

4. Conclusions

A 'golden fibre' attenuation standard has been developed with an uncertainty in the total loss of better than ± 0.06 dB (2σ). The short term stability of the attenuation of the standard has been demonstrated to be better than ± 0.03 dB.

Acknowledgement

The assistance of P J Whitesmith, M Harrop, T Holland and M R Shaw of BICC Cables Ltd, in the design and construction of the fibre attenuation standard is gratefully acknowledged.

References

1. A L Vandervort, J L Swecker "OTDR attenuation measurement and effect of wind tension", Proceedings OFME93, Turin
2. International Standard IEC 793/1, " Optical fibres – Part 1: Generic specifications"
3. CCITT Recommendation G.650, "Definition and test methods for the relevant parameters of single mode fibres"
4. FOTP – 78, "Spectral attenuation cutback measurement for single mode optical fibres"

Figure 1 : Variation of the spectral attenuation of a 12 km SMF wound on a shipping spool due to bending losses

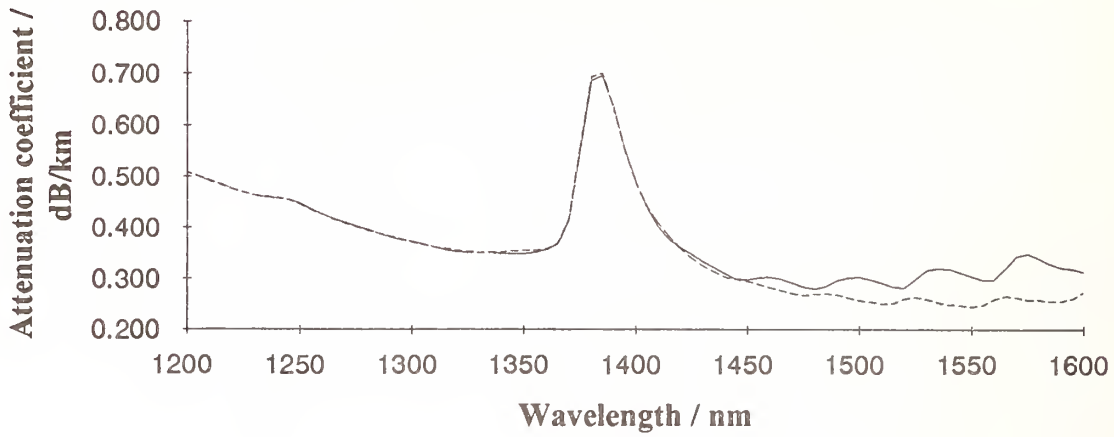

Figure 2 : Spectral attenuation of 'golden fibre' standard as measured by NPL and BICC

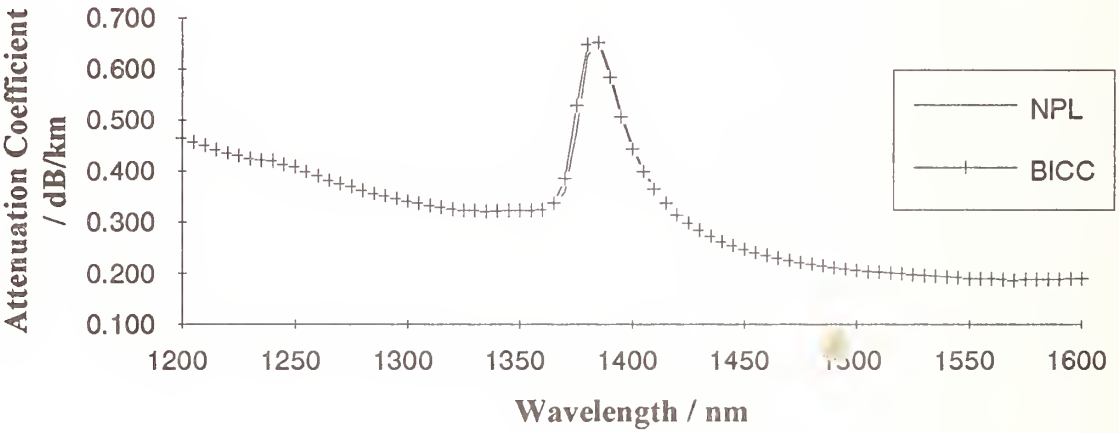

Figure 3 : Difference between NPL and BICC measured attenuation values for golden fibre standard

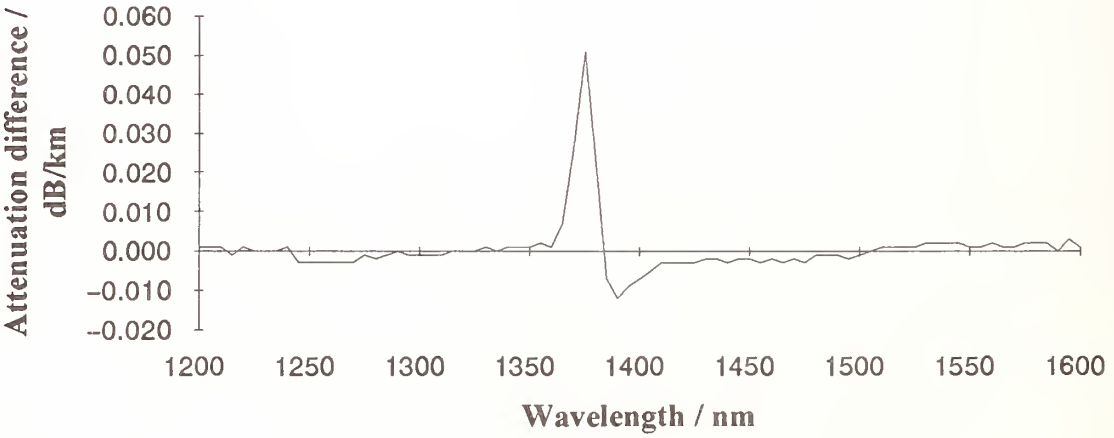

Microwave based Measurements of Optical Fibers

Robert M. Atkins
AT&T Bell Laboratories
Murray Hill, NJ 07974
USA

Microwaves have been utilized to measure the characteristics of a carbon coating used in the production of hermetically coated fiber, and also to measure the cross sectional area of non-circular fibers, such as highly elliptical fibers drawn for use in cladding pumped lasers.

In the first application, absorption of microwave power by the conductive carbon coating applied to a hermetically coated fiber is used to determine the characteristics of that coating[1]. The hermetically coated fiber is passed though a section of WR90 (X band) waveguide as shown in Figure 1. Slots (ca 3mm x 25mm) are cut into opposing broad faces of the waveguide to permit the fiber to pass through. One end of the waveguide is connected to a low power X band microwave source (in one case a Gunn oscillator operating near 10.5 GHz with an output power of 10mW) and the other end of the waveguide is connected to a diode detector. Matching screws were located at each end of the waveguide section and adjusted to obtain the desired impedance match. The output from the detector was fed to a circuit which produced a voltage output in proportion to the change in received power in the presence of an hermetically coated fiber. Using coated fibers whose coating conductance was independently measured off-line, a calibration plot was obtained as shown in figure 2. As can be seen, there is a good linear relationship between fiber conductance and the output from the microwave sensor. Conductance was also found to be directly related to coating thickness, through off line electron microscopy measurements. Results of an on-line test, where hermetically coated fiber was passed through the microwave cavity while being drawn, are shown in figure 3. Deliberate changes made in the hermetic coating process (marked "*"), reflected in later off-line measurements of fiber resistance, are clearly shown in the output from the microwave sensor.

In the second application, the cross sectional area of a fiber was measured via the influence of the fiber on the resonant frequency of a microwave cavity. Figure 4 shows a simple implementation of this technique in which a resonant cavity is formed by two iris plates in a section of WR90 (X band) waveguide. The resonant frequency of the cavity is determined by its physical length (1/2 wavelength at resonance) and by the dielectric constant of its contents. The fiber passes through the center of the cavity via 2 small holes (ca 3mm diameter) in the broad faces of the waveguide. The presence of a silica fiber in the cavity raises the local dielectric constant significantly and results in a drop in the cavity's resonant frequency. The resonant frequency of the cavity may easily be determined through the use of a network analyzer. Using both single optical fibers of known cross sectional areas (determined by microscopy) and multiple fibers whose total cross sectional area was simply the sum of the areas of the individual fibers, a calibration plot of frequency shift vs. cross sectional area was obtained as shown in figure 5. As can be seen, there is an excellent correlation between the two plotted parameters. In contrast to optical fiber diameter sensors, whose output when measuring

elliptical fibers is strongly influenced by rotation of the fibers major/minor axes, the output from the microwave sensor is insensitive to the fiber orientation.

Though these two techniques are superficially similar they are based on different principles. The former technique, for measurement of hermetic coating thickness, depends on the attenuation of microwave power via dissipation due to dielectric heating and is, to first order, insensitive to the microwave frequency. In the absence of a conductive hermetic coat, the bare fiber has little or no effect on the transmission of microwave power through the waveguide. In contrast, the latter technique, for cross sectional area measurement, depends on the changes in resonant frequency of the cavity due to the volume of silica dielectric (bare fiber) in the cavity and is insensitive to changes in microwave power.

Reference

[1] US patent 5013130

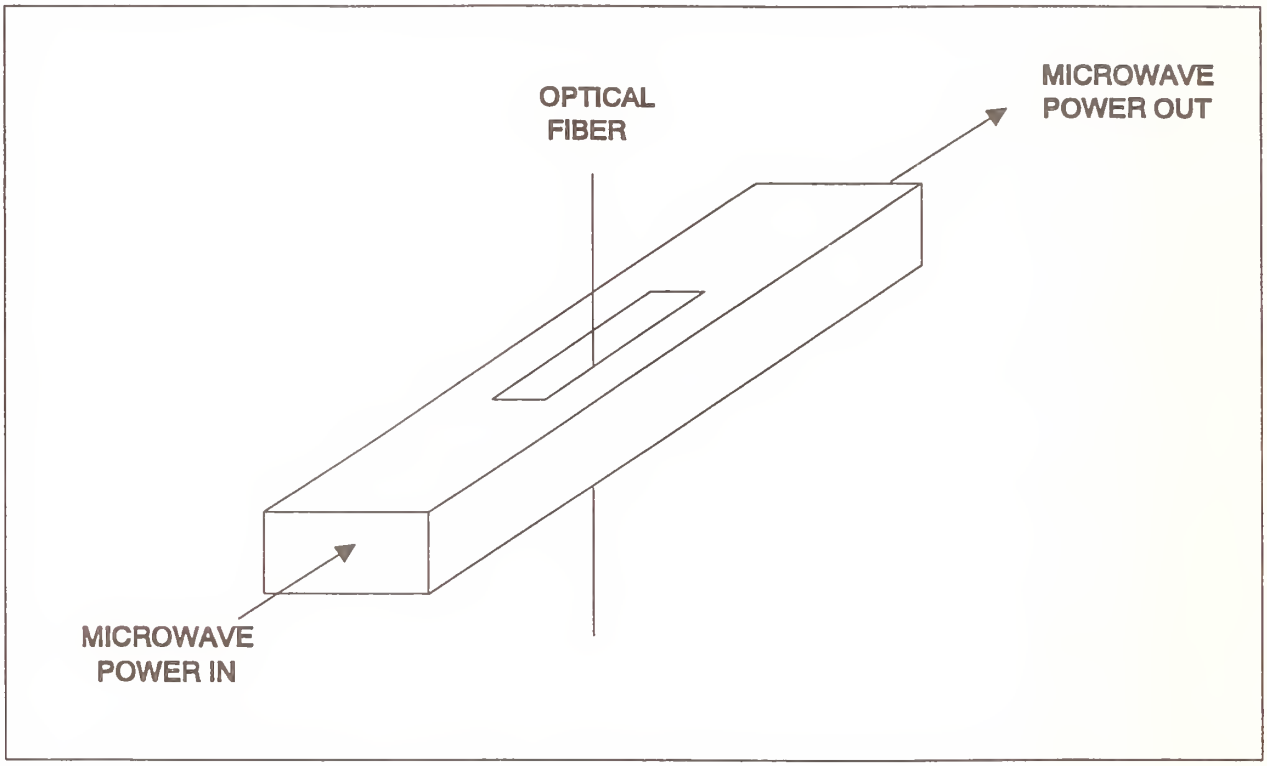

Figure 1 - Schematic of waveguide sensor for hermetic coating conductivity measurement

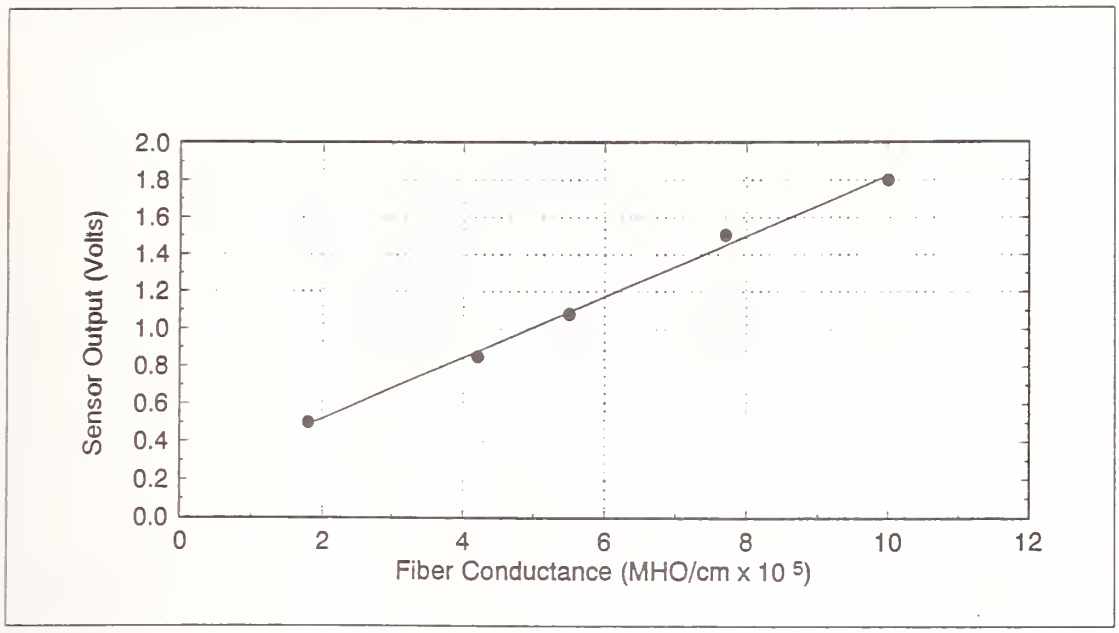

Figure 2 - Calibration of hermetic coating conductivity sensor

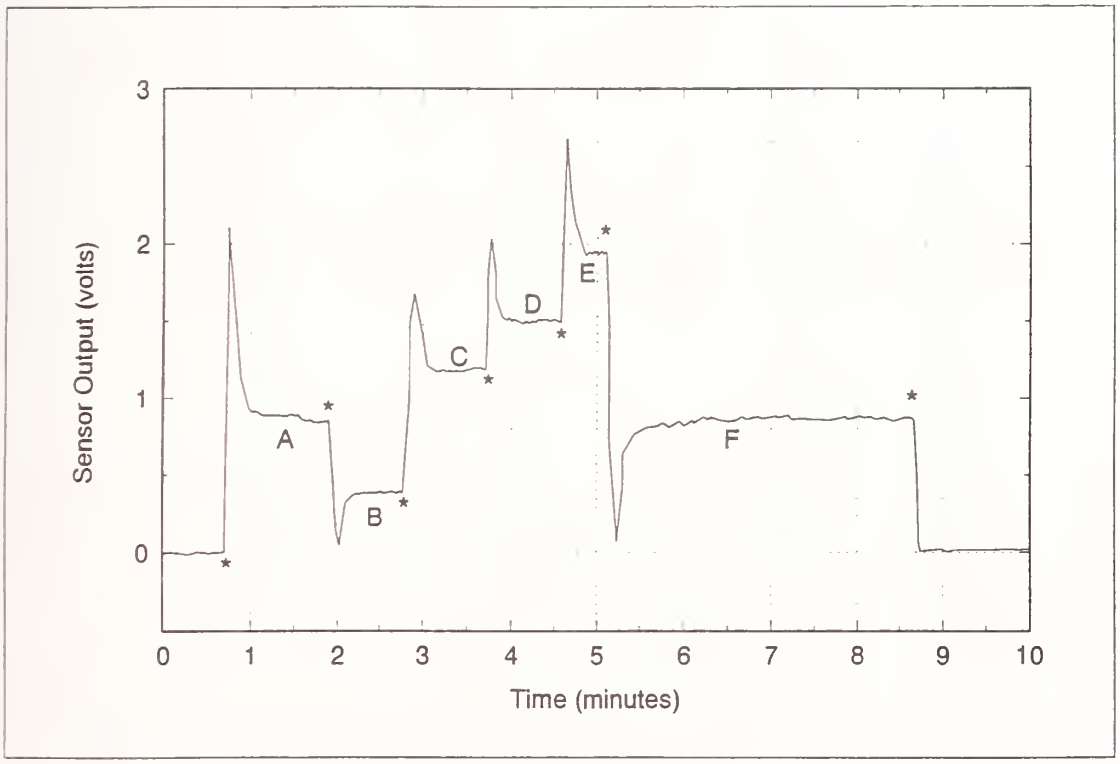

Figure 3 - On-line test of hermetic coating conductivity sensor. "*" marks the change of coating conditions. Coating resitances (measured off-line) were as follows: A - 25 kΩ/cm, B- 54kΩ/cm, C - 18 kΩ/cm, D - 13kΩ/cm, E - 10kΩ/cm and F - 24kΩ/cm

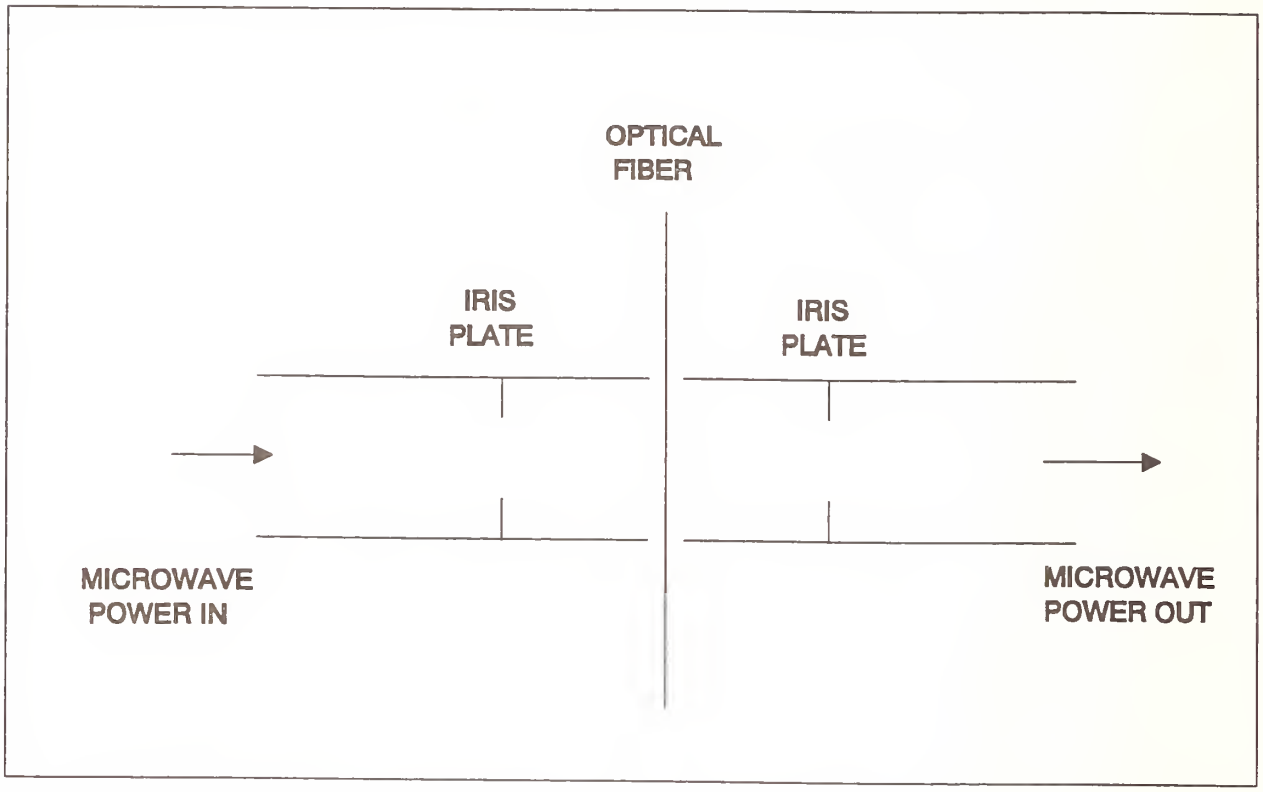

Figure 4 - Schematic of waveguide cavity sensor for fiber cross sectional area

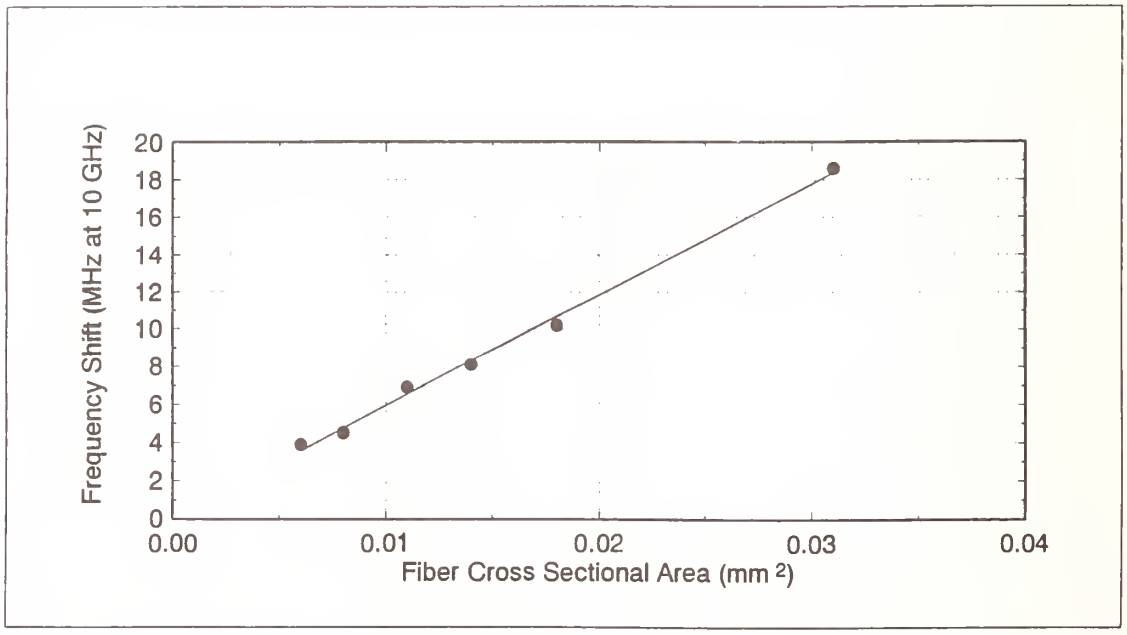

Figure 5 - Calibration of fiber cross sectional area sensor

Characterization of In-fiber Bragg Gratings

K. O. Hill, F. Bilodeau, B. Malo,
S. Thériault, D. C. Johnson, J. Albert,
and T. Kitagawa*

Communications Research Centre
3701 Carling
P. O. Box 11490, Station "H"
Ottawa, Ontario, Canada
K2H 8S2

SUMMARY

Irradiation of the core of an optical fiber with ultraviolet light photoinduces a permanent change in the core refractive index. This photorefractive effect[1] called *"photosensitivity"*, has great practical significance: it makes possible a new family of passive fiber devices that have potential application in optical communications and optical sensors[2]. Photosensitivity technology is reviewed in this invited paper with emphasis on the measurement techniques used in the characterization of in-fiber Bragg gratings. The use of photoinduced in-fiber Bragg gratings and long-pitch mode convertor gratings is proposed as the basis for measurement techniques useful for determining some of the important characteristic parameters of optical fiber.

Characterization of Fiber Bragg Gratings

A Bragg grating photoimprinted in the core of a monomode optical fiber acts as a narrow bandwidth reflector. The key parameters describing in-fiber Bragg reflectors are the resonant wavelength, λ_{Bragg}, the grating length L, and the reflectivity as a function of wavelength. From these quantities the photoinduced refractive index change δn, and the grating coupling constant κ are derived. The grating length is normally not measured but is determined in the fabrication process by a mask that limits the length of the fiber that is exposed to ultraviolet radiation. Thus the principal measurement problem is a determination of the reflectivity of the Bragg reflector as a function of wavelength.

---

* On leave from NTT Opto-Electronics Laboratories, Japan

The reflectivity of a Bragg grating is measured using standard spectroscopic techniques. Light from a broadband light source (superradiant fiber, white light source, or light emitting diode) is coupled into the fiber, passed through the grating and its spectral content measured by means of an optical spectrum analyzer. The experiment gives a signal proportional to the Bragg grating transmission as a function of wavelength of the incident light. To obtain the grating reflection response, the experimental data is processed (normalized) to eliminate the fiber input and output coupling losses. Because the grating spectral responses are narrowband, the signal level in the wings of the Bragg resonant wavelength can be used as the baseline in the normalization process. The equipment used in carrying out the measurements should have a large dynamic range, (~ 60 dB is achievable in practice determined by the intrinsic dynamic range of the instrumentation and the experimental setup), in order to measure a wide range of reflectivities. The measurement of high reflectivities (transmissions less than -60 dB) or very low reflectivities (< 4%) present special measurement problems.

Another approach for measuring the Bragg grating reflection response is to use a single frequency tunable laser diode. The transmission of the Bragg grating is monitored as the diode is tuned through the Bragg resonant wavelength. Alternatively, the diode frequency can be held fixed and the Bragg resonant frequency tuned by stretching (stress tuning) through the single wavelength of the laser. The resonant frequency of a Bragg reflector can be shifted by ~ 12 nm through strain (1%) tuning. This method is useful for measuring Bragg reflectors having very narrow linewidths; linewidths less than 200 MHz have been measured using this approach[1].

Measurement of Photoinduced Refractive Index

The photoinduced refractive index has been measured directly by irradiating one arm of an unbalanced Mach-Zehnder fiber interferometer with UV light, thereby changing its optical path length [3]. From the results, the dispersion in the photoinduced index can be determined.

Characterization of Chirped Bragg Fiber Gratings

Photosensitivity has been used to fabricate chirped (aperiodic) Bragg gratings[4] that have application in dispersion compensation[5]. The gratings are chirped in the sense that the optical pitch (i.e. effective refractive index n_{eff} times the grating pitch Λ varies linearly along the length of the structure. The additional key parameters describing chirped gatings are the percentage chirp and the dispersion-delay characteristics of the Bragg reflector. The Bragg gratings are normally fabricated to have a specified percentage chirp. However, it is useful to relate the chirp to other characteristics of the Bragg reflector. For "weak" bandstop reflectivity (R less than 50%) the full-width-at-quarter-maximum of the spectral response curve of a linearly chirped Bragg grating is given by the percent chirp multiplied by the

center Bragg resonant wavelength of the device, λ_0. Alternately, an approximate theoretical expression for the percent chirp is: $\frac{50\,\lambda_0 |\kappa|^2 L}{n_{eff}\ln[(1-R)^{-1}]}$.

When used as a dispersion compensator, the chirped grating is operated in the reflection mode. Light having a wavelength that is resonant for Bragg reflection near the rear of chirped grating is delayed with respect to light having a wavelength that is resonant for Bragg reflection at the front of the grating. The delay dispersion characteristic of the Bragg grating gives the relative delay for light as a function of its frequency offset from the center Bragg resonant frequency of the chirped grating. The dispersion delay characteristic is measured using apparatus described by K. Takiquchi et al[6].

Measurement of Effective Refractive Index of an Optical Fiber Using Photoimprinted Bragg Gratings

Accurate values of the effective group refractive index of monomode fibers are important for the calibration of the scale in optical time domain reflectometers (OTDRs).

The standard approach for measuring the effective group index of an optical fiber is the pulse time-of-flight technique. The transit time for a short optical pulse to propagate over a precisely measured length of optical fiber is measured[7]. The technique measures the effective group index to $\pm$ 0.0001.

In this paper we propose to measure the effective refractive index of a monomode fiber by photoimprinting a grating in the core of the fiber using the phase mask techniquePf. The effective index is determined by the Bragg resonant wavelength λ_{Bragg} and the phase mask grating period Λ which are related as follows for second order reflections: $n_{eff} = \frac{\lambda_{Bragg}}{\Lambda}$ Since both λ_{Bragg} and Λ can be determined with a high degree of precision, the technique can yields accurate values for n_{eff}. However, for the measured n_{eff} to correspond to the effective index of the test optical fiber it is necessary that the photoinduced refractive index be less than 10^{-4}. From a series of such measurements of effective index at various wavelengths, the dispersion in effective group index can be determined.

Measurement of Optical Fiber Mode Differences Using Mode Converter Gratings

The function of a mode converter is to convert light propagating in one mode of a waveguide to another mode of the waveguide. Mode converters are fabricated by inducing a periodic refractive index perturbation along the fiber length with a pitch that bridges the momentum mismatch (propagation constant difference) between the modes and thus allows phase-matched coupling between the selected fiber modes. Photosensitivity has been used to write spatial[8] and polarization mode converter gratings[9] in optical fibers. Mode converter

gratings provide a means for measuring the difference in propagation constants between two modes in optical fiber.

To fabricate an efficient mode converter using the point-by-point writing technique [8], it is necessary to reproduce by exposure from the side the same holographic pattern that the two modes would trace in the waveguide core at the resonant wavelength for energy exchange between the modes.

In the case of $LP_{01} \leftrightarrow LP_{11}$ fiber mode converters the interference pattern between the modes is highly blazed (because the LP_{11} mode is not circularly symmetric) at an angle of a few degrees with respect to the fiber core. In contrast, for $LP_{01} \leftrightarrow LP_{02}$ mode converters the required blaze is zero because the interfering modes are both circularly symmetric[10].

A feature of the $LP_{01} \leftrightarrow LP_{02}$ mode converter is that it has a single resonance because of the circular symmetry of the modes and of the mode converter. In contrast the $LP_{01} \leftrightarrow LP_{11}$ mode converter has four resonances due to the 4-fold degeneracy of the LP_{11} mode.

The fraction of the launch power in Mode 1 coupled by a uniform mode converter to co-propagating Mode 2 is given by

$$\frac{|\kappa|^2}{|\kappa|^2 + (\frac{\Delta\beta}{2})^2} \sin^2 \left\{ [\, |\kappa|^2 + (\frac{\Delta\beta}{2})^2 \,]^{\frac{1}{2}} z \right\}$$

where κ is the coupling coefficient of the mode converter grating, z is the position coordinate measured along the length of the grating and $\Delta\beta = [\beta_{LP_{Mode\ 1}} - \beta_{LP_{Mode\ 2}} - (\frac{2\pi m}{\Lambda})]$ with m an integer, β is the mode propagation constant and Λ is the periodicity of the grating. LP designates a linearly polarized mode of the waveguide. When phase matching occurs ($\Delta\beta = 0$), the total power transfer is modulated by the $\sin^2$ function and can reach 100 %.

Thus for a mode converter grating operating in first order, the resonant wavelength for efficient coupling between two modes corresponds to the wavelength for which the difference in propagation constant between the two modes is simply $2\pi/\Lambda$.

REFERENCES

1. K. O. Hill, Y. Fujii, D. C. Johnson and B. S. Kawasaki, "Photosensitivity in optical fiber waveguides: Application to reflection filter fabrication", Applied Physics Letters, Vol. 32, No. 10, pp. 647-649, May 15, 1978.

2. K. O. Hill, B. Malo, F. Bilodeau, and D. C. Johnson, "Photosensitivity in optical fibers", Annual Review of Material Science, Vol. 23, pp. 125-157, 1993.

3. B. Malo, K. A. Vineberg, F. Bilodeau, J. Albert, D. C. Johnson, and K. O. Hill, "Ultraviolet Light Photosensitivity in Ge-Doped Silica Fibers: Wavelength Dependence of the Light-Induced Index Change", Optics Letters, Vol. 15, No. 17, pp. 953-955, September 1, 1990.

4. K. O. Hill, F. Bilodeau, B. Malo, T. Kitagawa, S. Thériault, D. C. Johnson, J. Albert and K. Takiguchi, "Aperiodic in-fiber Bragg gratings for optical fiber dispersion compensation", Optical Fiber Communication Conference, OFC'94, San Jose, California, February 20-25, 1994, Technical Digest, Postdeadline Papers, PD17, pp. 17-20, February 24, 1994.

5. K. O. Hill, "Aperiodic Distributed-Parameter Waveguides for Integrated Optics", Applied Optics, Vol. 13, pp. 1853-1856, August 1974.

6. K. Takiguchi, K. Okamoto, S. Suzuki, and Y. Ohmori, "Planar lightwave circuit optical dispersion equalizer", 19th European Conference on Optical Communication, ECOC'93, Montreux, Switzerland, September 12-16, 1993, Proceedings, Vol. 3, Post deadline papers, ThC12.9, pp. 33-36.

7. J. J. Carr, S. L. Saikkonen, and D. H. Williams, "Refractive index measurements on single-mode fiber as functions of product parameters, tensile stress, and temperature", Fiber and Intergrated Optics, Vol. 9, pp. 393-396, 1991.

7. K. O. Hill, B. Malo, F. Bilodeau, D. C. Johnson, and J. Albert, "Bragg gratings fabricated in monomode photosensitive optical fiber by UV exposure through a phase mask", Applied Physics Letters, Vol. 116: 62, No. 10, pp. 1035-1037, March 8, 1993

8. K. O. Hill, B. Malo, K. A. Vineberg, F. Bilodeau, D. C. Johnson, and I. Skinner, "Efficient Mode Conversion in Telecommunication Fibre Using Externally Written Gratings", Electronics Letters, Vol. 26, No. 16, pp. 1270-1272, August 2, 1990.

9. K. O. Hill, F. Bilodeau, B. Malo and D. C. Johnson, "Birefringent Photosensitivity in Monomode Optical Fibre: Application to the External Writing of Rocking Filters", Electronic Letters, Vol. 27, No. 17, pp.1548-1550, August 15, 1991.

10. F. Bilodeau, K. O. Hill, B. Malo, D. C. Johnson, and I. M. Skinner, "Efficient, narrowband $LP_{01} \leftrightarrow LP_{02}$ mode convertors fabricated in photosensitive fibre: Spectral response", Electronics Letters, Vol. 27, No. 8, pp. 682-684, April 11, 1991.

Characterization of Optical Components using High Resolution Optical Reflectometry Techniques

W. V. Sorin, D. M. Baney and S. A. Newton
Hewlett-Packard Laboratories

Introduction: Optical time domain reflectometry (OTDR) has proven to be a very important diagnostic tool for characterizing and trouble-shooting long haul fiber-optic communication links. Characteristics such as the location of a fiber break, attenuation coefficient, splice loss and link degradation can easily be measured with access to only one end of an installed fiber. Naturally, there is a desire to extend this type of measurement capability to address the area of optical component analysis where resolution on the order of 100 μm or less is required. Extrapolation of the techniques used in pulsed OTDR can become very difficult as pulse resolution gets below about 10 mm. One problem is that the reflection sensitivity becomes severely limited by additional noise due to the increased receiver bandwidth. A more fundamental problem exists due to the effects of dispersion, since the short optical pulses will need to propagate through fiber pigtails that are attached to the components being measured.

Frequency Domain Techniques: Due to the difficulties associated with pulsed approaches, many other techniques have been investigated to realize high resolution optical reflectometry measurements. Using the relationship between an impulse response and its Fourier transform, high resolution reflectometry can be performed by using frequency domain techniques. Frequency-stepped sinusoidal modulation of the optical intensity of a probe signal has been used to achieve two-point spatial resolution on the order of a few millimeters.[1] This approach is limited in its reflection sensitivity and dynamic range due to its use of direct detection. A similar but more promising approach is to frequency step or sweep the optical carrier and use coherent detection at the receiver.[2,3]

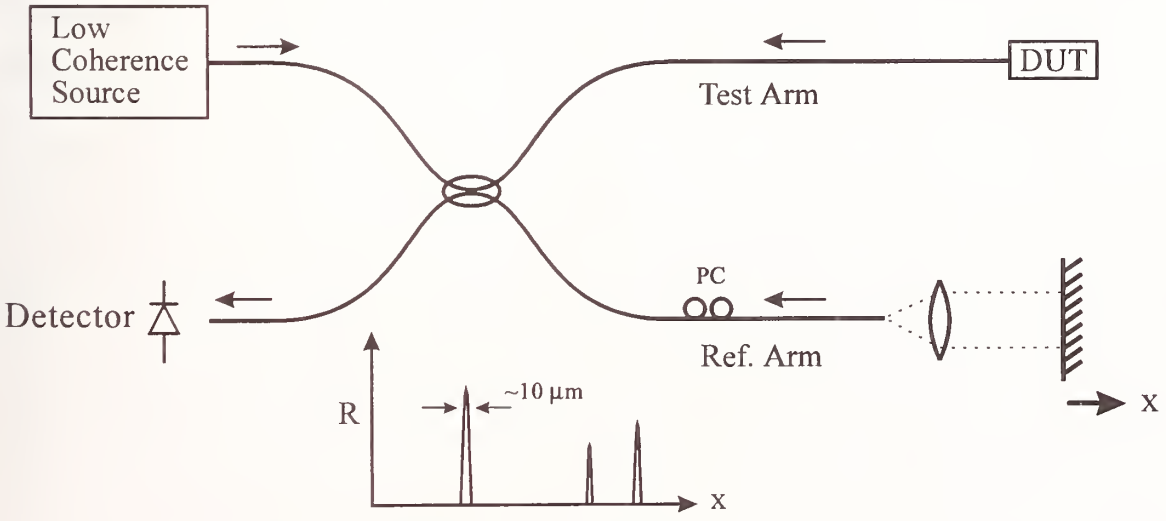

Figure 1. Basic configuration used for optical low-coherence reflectometry.

This technique, known as coherent optical frequency domain reflectometry, can have excellent sensitivity, dynamic range and spatial resolution. Two-point spatial resolution on the order of tens of microns has been demonstrated.[3] Presently, this technique is limited by the availability of practical, narrow line-width, widely tunable optical sources.

Optical Low-Coherence Reflectometry: A more practical approach that does not require the development of any new technology is the use of optical low-coherence reflectometry (OLCR).[4,5] A simplified version of an OLCR is shown in Figure 1. A continuous wave (cw) short coherence length source, such as an edge-emitting LED, is coupled into a fiber-based Michelson interferometer. A movable reference mirror in one arm is translated to provide a variable optical time delay. Any optical reflection from the device under test (DUT), whose time delay matches that from the moving reference mirror will coherently interfere to produce an interference wave packet whose spatial extent is equal to the coherence length of the source. One inherent advantage of this technique is that dispersion broadening due to the component pigtail and fiber interferometer can be completely eliminated by ensuring that an equivalent dispersion is seen by the reference signal. In practice this is easily done by using the same type of fiber in both arms of the interferometer. Other advantages are that the source does not require any complex modulation and only a simple low frequency detector is required. This technique has been demonstrated to achieve spatial resolution below 2 μm[6] and reflection sensitivity greater than -160 dB.[7] Due to its practicality and increasingly wide use, this paper will focus primarily on applications that have been demonstrated using OLCR.

Accurate Time Delay Measurement: One of the strengths of OLCR is its ability to measure optical time delays very accurately. Although the measured impulse response from a reflective surface can have a width on the order of ten microns, it is possible to determine its central position with an accuracy of better than 0.02 μm[8] (this corresponds to an equivalent time delay of 0.07 femtoseconds). Typical applications include trouble-shooting and quality control --- for example, to determine the position of optical components within packaged fiber pigtailed devices such as isolators, laser diodes, and photoreceiver packages. Other applications include accurate characterization of time delays in interferometric optical circuits such as Fabry-Perot cavities, etalons, and Michelson and Mach-Zehnder interferometers.[9] OLCR has also been used to accurately measure silicon wafer thickness.[10]

The time delay measured using OLCR (as in any reflectometer) is the time it takes for an optical pulse to propagate through the test medium. This delay is equal to the product of physical length and group index and should not be confused with the optical path difference which is the product of physical length and refractive index. In many situations, the parameter of interest is either physical length or group index. Being able to independently measure one of these parameters allows for the solving of the other, but in cases where an independent measurement is difficult it may be possible to solve for both parameters simultaneously using only OLCR measurements.[11] Besides measuring isotropic material which are characterized with a single time delay, differential time delays associated with transmission through birefringent material can also be measured. This allows the difference in group velocities to be measured in materials such as polarization maintaining fiber,[12] rutile crystals, and $LiNbO_3$

waveguides.[9] Using a modified OLCR, it is also possible to measure polarization mode dispersion in long optical fiber links.[13]

Backscatter Measurement: In addition to precise time delay measurements, OLCR also provides reflectivity information. Due to its coherent detection scheme, reflection sensitivities as low as -161 dB have been demonstrated.[7] With such high sensitivities, the -120 dB Rayleigh backscatter reflectivity from a 10 μm section of standard single-mode fiber can be measured easily.[7,14] Using a high sensitivity OLCR, backscatter and waveguide imperfections have been measured in glass waveguides, $LiNbO_3$ waveguides, GaAs waveguides, erbium fiber, fused directional couplers and tight fiber bends.[9,15] It should be pointed out that the Rayleigh backscatter signal obtained using OLCR has much more amplitude uncertainty than that obtained using conventional pulsed OTDR methods.[16] This amplitude uncertainty, sometimes referred to as coherence fading, occurs when the spatial resolution is comparable to the source coherence length. In conventional pulsed OTDR measurements, the source coherence length is usually much smaller than the pulse length so coherence fading is not a problem. Besides measuring backscatter from optical waveguides, OLCR applications also include analytical and biomedical applications to determine scattering and attenuation coefficients in liquid suspensions and biological tissue.[17,18]

Return Loss Measurement: When making return loss measurements on optical components, OLCR has several advantages over the conventional technique of using a cw source and measuring the total back-reflected power with a standard power meter.[19] The most obvious advantage is that individual reflections can be spatially resolved. This can be very useful when minimizing the return loss from components that contain many internal reflective interfaces. Another advantage is the ability to measure reflectivities below -70 dB. This becomes very difficult using the cw power meter approach since the background reflected signal due to Rayleigh backscatter in a standard single-mode fiber is about -70 dB per meter. Sensitivities below this value are needed to characterize components such as angle polished connectors and high return loss isolators.

Gratings, Optical Sources and Dispersion: High resolution reflectometry has also been used to characterize photoinduced reflection gratings within single-mode fibers.[20] Information such as the spatial dependence of the reflection coefficient and the grating length can be independently measured.[20,21] OLCR can also be used to probe active devices such as EELEDs, laser diodes and DFB lasers.[9,22,23] Typically the semiconductor device has to be pumped to improve its transparency. In these cases, the amplitude of the reflected signal also depends on the optical gain it experiences through the device. Chromatic dispersion can also be measured using OLCR. This can be accomplished using the phase information within the received interference wavepacket. Due to the wide optical bandwidth of the probe signal, accurate dispersion measurements can be made using relatively short optical delays. This technique has been used to measure how the dispersion through an erbium doped fiber amplifier changes as a function of optical pump power.[24]

Increasing Distance Range: One drawback of OLCR is that long scan ranges are difficult to achieve. This occurs since a reference mirror must be physically translated to provide the required optical delay. In practice, this makes scan ranges larger than about 0.5 meters difficult to achieve. Recently, a new technique has been demonstrated that can increase the scan range by over 2 orders of magnitude.[25] This is achieved by adding a recirculating optical delay into one arm of the OLCR. By extending the measurement range, new applications for OLCR will become practical.

Summary: Characterizing and trouble-shooting fiber-pigtailed components is often a very difficult task. Due to packaging constraints, visual inspection is not usually practical. Transmission characteristics, when obtainable, often give valuable information but in many cases do not provide enough information to characterize an optical device. High resolution optical reflectometry, namely OLCR, has become a very important diagnostic tool in many of these cases.

References

1. D. W. Dolfi, M. Nazarathy and S. A. Newton, "5 mm resolution optical frequency domain reflectometry using a coded phase reversal modulator," Opt. Lett., vol. 13, p. 678, (1988).
2. W. V. Sorin, D. K. Donald, S. A. Newton and M. Nazarathy, "Coherent FMCW reflectometry using a temperature tuned Nd:YAG ring laser," Photonics Tech. Lett., vol. 2, p. 902 (1990).
3. U. Glombitza and E. Brinkmeyer, "Coherent frequency-domain reflectometry for characterization of single-mode integrated-optical waveguides," J. Lightwave Technol., vol. 11, p. 1377 (1993).
4. R. C. Youngquist, S. Carr and D. E. N. Davies, "Optical coherence-domain reflectometry: A new optical evaluation technique," Opt. Lett., vol. 12, p. 158 (1987).
5. B. L. Danielson and C. D. Whittenberg, "Guided-wave reflectometry with micrometer resolution," Appl. Opt., vol. 26, p. 2836 (1987).
6. X. Clivaz, F. Marquis-Weible and R. P. Salathe, "Optical low-coherence reflectometry with 1.9 μm spatial resolution," Electron. Lett., vol. 28, p. 1553 (1992).
7. K. Takada, T. Kitagawa, M. Shimizu and M. Horiguchi, "High-sensitivity low coherence reflectometer using erbium-doped superfluorescent fibre source and erbium-doped power amplifier," Electron. Lett., vol. 29, p. 365 (1993).
8. B. L. Danielson and C. Y. Boisrobert, "Absolute optical ranging using low coherence interferometry," Appl. Opt., vol. 30, p. 2975, (1991).
9. Unpublished measurements performed by authors at Hewlett-Packard Laboratories.
10. C. W. Lawson and R. R. Michael, "Fiber optic low-coherence interferometry for non-invasive silicon wafer characterization," Journal of Crystal Growth, vol. 137, p.37, (1994).
11. W. V. Sorin and D. F. Gray, "Simultaneous thickness and group index measurement using optical low-coherence reflectometry," Photonics Tech. Lett., vol. 4, p. 374, (1992).

12. M. Tsubokawa, T. Higashi and Y. Sasaki, "Measurement of mode couplings and extinction ratios in polarization-maintaining fibers," J. Lightwave Technol., vol. 7, p. 45 (1989).
13. N. Gisin, J-P. Von der Weid and J-P. Pellaux, "Polarization mode dispersion of short and long single-mode fibers," J. Lightwave Technol., vol. 9, p. 821 (1991).
14. W. V. Sorin and D. M. Baney, "Measurement of Rayleigh backscattering at 1.55 μm with a 32 μm spatial resolution," Photonics Tech. Lett., vol. 4, p. 374, (1992).
15. K. Takada, "Low coherence reflectometry for the characterization of fiber and planar lightwave circuits," Symposium on Optical Fiber Measurements, Boulder, Colorado, NIST publication 839, p. 159, (1992).
16. K. Takada, A. Himeno and K. Yukimatsu, "Jagged appearance of Rayleigh-backscatter signal in ultrahigh-resolution optical time-domain reflectometry based on low-coherence interference," Opt. Lett., vol. 16, p. 1433 (1991).
17. J. M. Schmitt, A. Knuttel and R. F. Bonner, "Measurement of optical properties of biological tissues by low-coherence reflectometry," Applied Optics, vol. 32, p. 6032 (1993).
18. D. Huang, E. A. Swanson, C. P. Lin, J. S. Schuman, W. G. Stinson, W. Chang, M. R. Hee, T. Flotte, K. Gregory, C. A. Puliafito, J. G. Fujimoto, "Optical Coherence Tomography," Science, vol. 254, p. 1178 (1991).
19. F. P. Kapron, B. P. Adams, E. A. Thomas and J. W. Peters, "Fiber-optic reflection measurements using OCWR and OTDR techniques," J. Lightwave Technol., vol. 7, p. 1234, (1989).
20. P. Lambelet, P. Y. Fonjallaz, H. G. Limberger, R. P. Salathe, Ch. Zimmer and H. H. Gilgen, "Bragg grating characterization by optical low-coherence reflectometry," Photon. Tech. Lett., vol. 5, p. 565, (1993).
21. P. Lambelet, R. P. Salathe, M. H. Garrett and D. Rytz, "Characterization of a photorefractive phase conjugator by optical low-coherence reflectometry," Appl. Phys. Lett., vol. 64, p. 1079, (1994).
22. E. Brinkmeyer and U. Glombitza, "Complex coherence-domain reflectometry in active laser diodes," Opt. Lett., vol. 17, p. 1441, (1992).
23. J. F. Lucas, L. F. DeChiaro, C. Salla and C. Y. Boisrobert, "Low coherence reflectometry and spectral analysis for detection of gain anomalies in semiconductor lasers," Electron. Lett., vol. 28, p. 2085, (1992).
24. R. K. Hickernell, K. Takada, M. Yamada, M. Shimizu and M. Horiguchi, "Chromatic dispersion of erbium-doped fiber amplifier measured by Fourier transform spectroscopy," Symposium on Optical Fiber Measurements, Boulder, Colorado, NIST publication 839, p. 201, (1992).
25. D. M. Baney and W. V. Sorin, "Extended-range optical low-coherence reflectometry using a recirculating delay technique," Photon. Tech. Lett., vol. 5, p. 1109, (1993).

POLARIZATION-MAINTAINING FIBER ALIGNMENT USING TUNABLE POLARIZATION-MAINTAINING FIBER FABRY-PEROT INTERFEROMETERS

Yufei Bao, Kevin Hsu, and Calvin M. Miller
Micron Optics, Inc., 2801 Buford Hwy, Suite 140, Atlanta, GA 30329, USA

Abstract

A unique and sensitive technique for aligning and characterizing polarization-maintaining fiber joints utilizing a high-finesse polarization-maintaining fiber Fabry-Perot interferometer (PM-FFPI) and polarization resonance splitting effect is reported. The alignment criterion, derived from the phase sensitivity of polarization extinction ratio for elliptical inputs, is also applicable to general PM fiber splicing. PM fiber splices with high polarization extinction ratio (> 38 dB) were fabricated using this method.

I. Introduction

Polarization-maintaining (PM) fibers have been used for various device applications in fiber optic communication systems [1-4], polarmetric fiber sensors [5,6] and laser systems [7], as well as input/output pigtails in laser and integrated optical devices. In a PM system, birefringent axis alignment between PM fibers is important since it directly affects the system performance. In this paper, we demonstrate a unique and sensitive technique which utilizes the polarization resonance splitting effect inside a tunable PM fiber Febry-Perot interferometer (PM-FFPI) to align and characterize PM fiber joints with linear or elliptical inputs.

A PM-FFPI consists of a PM fiber cavity enclosed by two highly reflective plane mirrors. Due to different mode indices associated with the two orthogonal polarization states inside a PM-FFPI, there are generally two distinct sets of resonances produced when cavity length is scanned, as shown on the oscilloscope of the alignment system in Figure 1. Cavity length tuning is achieved by stacked piezoelectric actuators. One set of resonance can be obtained only when a linear input polarization is aligned with one of the birefringent axes of the cavity. Output polarization extinction ratio (PER) can be calculated from the peak intensity ratio of the two polarization resonances. Therefore, a PM-FFPI can function as a polarization analyzer, and be used for aligning and characterizing PM fiber joints.

II. PM fiber joint alignment

Figure 1 illustrates an example in which a PM-FFPI is used to align PM fibers or two PM devices. Two alignment steps are involved here: (1) alignment between the birefringent axes of a PM fiber (PMF-1) and the PM-FFPI at joint-2 as shown in Figure 1(a), and (2) alignment between the birefringent axes of PMF-1 and the second PM fiber (PMF-2) at joint-3 as shown in Figure 1(b). Alignment procedures for both steps are essentially the same. Alignment criterion is derived from the output PER and its maximum variation range. PER is defined as:

$$PER = 10 \cdot \log_{10}\left(\frac{E_{oy}E_{oy}^{*}}{E_{ox}E_{ox}^{*}}\right), \qquad (1)$$

where E_{ox}, E_{oy} are the electric fields of the two polarizations after joint-2. For the first alignment step, E_{ox}, and E_{oy} can be calculated by the following Jones matrix equation:

$$\begin{bmatrix} E_{ox} \\ E_{oy} \end{bmatrix} = A \begin{bmatrix} \cos\theta_2 & \sin\theta_2 \\ -\sin\theta_2 & \cos\theta_2 \end{bmatrix} \begin{bmatrix} e^{i\phi_1/2} & 0 \\ 0 & e^{-i\phi_1/2} \end{bmatrix} \begin{bmatrix} \cos\theta_1 & \sin\theta_1 \\ -\sin\theta_1 & \cos\theta_1 \end{bmatrix} \begin{bmatrix} e^{i\phi_0/2}\cos\theta_0 \\ e^{-i\phi_0/2}\sin\theta_0 \end{bmatrix}, \quad (2)$$

where θ_0 and ϕ_0 are input ellipticity and initial polarization phase difference of a polarized source, θ_1 is the misalignment angle between input polarization and PMF-1 at joint-1, θ_2 is the misalignment angle between PMF-1 and the PM-FFPI at joint-2, ϕ_1 is the polarization phase difference in PMF-1, and A is a complex constant. PER can be a negative number if the ratio of $E_{oy}E^*_{oy}/E_{ox}E^*_{ox}$ is less than 1. It is easy to see that PER is a function of ϕ_1 if $\theta_2 \neq 0$. For example, for an input with $\theta_0 = 0.5°$ and $\phi_0 = 10°$, Figure 2 plots the output PER versus ϕ_1 for different misalignment angle θ_2. Calculation results show that PER is constant or independent of ϕ_1 only when $\theta_2 = 0$, and that the sign of θ_2 causes a 180 degree phase shift in PER. This constant PER (CPER) is determined by θ_0, ϕ_0, and θ_1. There are two positions of θ_2, symmetric to $\theta_2 = 0$, where the phase sensitivity to ϕ_1 is infinite. These two special positions of θ_2 are important in aligning PM fibers, and can be determined by the level of the CPER from the following equation:

$$\theta_{2A} = -\theta_{2B} = \tan^{-1}(10^{CPER/20}). \quad (3)$$

As shown in Figure 2, the CPER of -41 dB results in $\theta_{2A} = 0.51°$. When $|\theta_2| < \theta_{2A}$, θ_2 can be calculated from the maximum variation of PER induced by ϕ_1, and the value of CPER. Figure 3 shows the maximum variation in PER as a function of misalignment angles θ_2 for different CPER levels. When $|\theta_2| < \theta_{2A}$, a higher CPER level results in a higher PER phase sensitivity which enables a better alignment. For instance, a maximum variation of 4 dB in PER indicates $|\theta_2| \sim 0.12°$ if CPER = 40 dB , but represents $|\theta_2| \sim 0.39°$ if CPER = 30 dB. For a fixed elliptical input, i.e. θ_0 and ϕ_0 are fixed, the value of CPER is determined by misalignment angle θ_1. Figure 4 plots the value of CPER as a function of θ_1 for a 1° input ellipticity and different ϕ_0. Calculations show that the higher the input linearity (linear case: $\phi_0 = n\pi$, n = 0, 1, 2, ...), the higher the CPER that can be achieved by adjusting θ_1. CPER is independent of ϕ_0 only when joint-1 is aligned, i.e. $\theta_1 = 0$.

For a fixed elliptical input, theoretical calculations have shown the necessary condition for a proper alignment of joint-2, which is that the PM-FFPI has a constant output PER while ϕ_1 in PMF-1 is changed. The polarization phase difference in a PM fiber can be changed by either wavelength scanning or thermal disturbance. Based on above calculation results, the procedure of aligning θ_2 is designed as follows: (1) iteratively adjust θ_1 and θ_2 to obtain a maximum output PER, (2) with θ_1 fixed, adjust θ_2 while thermally disturbing PMF-1, to locate the two maximum phase sensitive positions θ_{2A} and θ_{2B}, (3) rotate θ_2 to the center of θ_{2A} and θ_{2B}, (4) with θ_2 fixed, adjust θ_1 to obtain the highest PER, (5) heat or cool PMF-1 and monitor the maximum variation range of PER, (6) calculate θ_2 from PER_{min} and PER_{max}, (7) rotate θ_2 in one direction by the calculated value and test the phase sensitivity, (8) if PER becomes a constant with respect to ϕ_1 then the alignment is accomplished. However, if PER results in a higher phase sensitivity, then rotate θ_2 to the other direction by twice the calculated value. Theoretically, a very accurate alignment can be achieved by repeating (6)-(8). One important issue should be addressed here is that the PM fiber must be free of external stress in order to achieve accurate alignment. We have noticed that both PANDA and elliptical-core fibers are extremely sensitive to random stress caused by epoxy used to bond PM fibers inside glass ferrules [8], and that the external stress can completely degrade the alignment. Once θ_2 is aligned, the alignment of joint-3 follows the same process, except that now the polarization phase difference in PMF-2 (instead of PMF-1) should be changed to examine the variation range of output PER.

II. PM fiber joint characterization

A PM-FFPI can also be used to characterize a previously spliced PM fiber joints. The characterization procedure follows the alignment principles discussed previously. First, PMF-1 and the PM-FFPI at joint-2 are aligned by monitoring ϕ_1 in PMF-1. Second, the angular alignment accuracy at joint-3 is calculated using Eqs. (1) and (2) or estimated using Fig. 3 from the measured PER_{min} and PER_{max} while ϕ_2 is changed.

The technique described above has been used to align and characterize several PM fiber joints. Table 1 lists the observed PER_{min} and PER_{max}, calculated CPER, calculated alignment accuracy $\Delta\theta$, and the calculated output PER for a linearly polarized input (PER_L). It shows that all the PM-fiber joints aligned with a PM-FFPI have high polarization extinction ratio for linear input (PER_L> 34 dB). In order to achieve an accurate alignment or characterization, a detector with a wide dynamic range and a scope with high resolution are required.

Table 1

No.	PER_{min} (dB)	PER_{max} (dB)	CPER (dB)	$\Delta\theta$ (deg.)	PER_L (dB)
1	28	35	30.7	0.65	39
2	29	> 50	35.2	1.12	34
3	28.7	33.8	30.9	0.45	42
4	26.4	27.2	26.7	0.12	53
5	29.7	32.6	30.9	0.30	46
6	25.5	30.9	27.7	0.70	38

IV. Summary

The alignment technique using a PM-FFPI is suitable for a PM fiber system which requires a PM-FFPI as a wavelength or a noise filter. The birefringent axis alignment of the system can be easily accomplished in one step by scanning the PM-FFPI. This approach requires no lens and analyzer, thus results in a simple and convenient alignment process. PM-FFPIs can also be used in the following applications: aligning PM fiber pigtails to polarization sensitive integrated optical circuits, and splicing additional PM fiber sections onto an existing PM fiber system.

In conclusion, we have developed a simple and unique technique to align and characterize PM fiber joints using tunable PM-FFPIs. In addition to applications in wavelength and polarization scanning and filtering, tunable PM-FFPIs are also sensitive instruments for aligning and characterizing PM fiber joints.

References:

[1] M. Asobe, H. Itoh, and K. Kubodera, *Opt. Commun.*, vol. 88, no. 4-6, pp.446-50, 1992

[2] T. Morioka and M. Saruwatari, *IEEE J. on Select. Areas in Commun.*, vol. 6, pp. 1186-98, 1988

[3] M. Kobayashi, K. takada, and J. Noda, *J. Lightw. Technol.*, nol. 8, no. 11, pp. 1697-702,1990

[4] B.G. Clay, R. G. Podgornik, J. A. Priest, and C. L. Balestra, *Conf. Digest. LEOS Summer Topical on Optical Multiple Access Networks*, p. 30-1, 1990

[5] S.-M. Tseng and C.-L. Chen, *IEEE J. Lightw. Technol.*, vol. 7, no. 12, 1989

[6] Feng Zhang and John W. Y. Lit, *Appl. Opt.* vol. 32, no. 13, pp. 2213-7, 1993.
[7] I. N. Duling III and R. D. Esman, *Electron. Letters*, vol. 28, no. 12, pp. 1126-7, 1992
[8] Y. Bao, K. Hsu, and C. M. Miller, *Technic. Digest OFC 94*, pp. 96-8, 1994

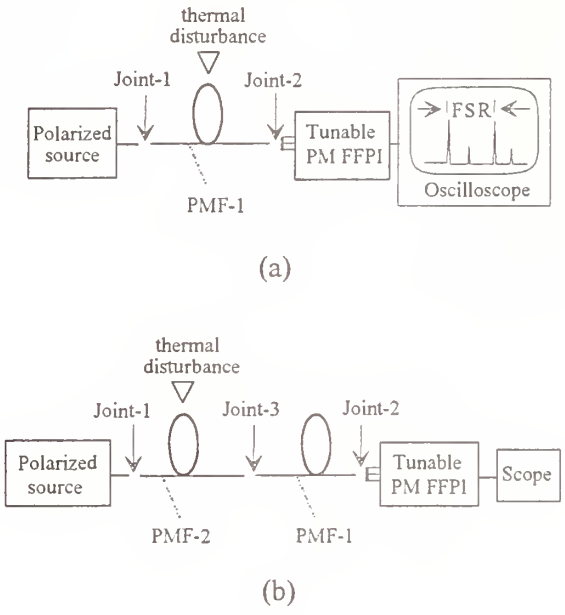

Figure 1. PM fiber alignment illustration. (a) alignment of PMF-1 and PM-FFPI at joint-2, and (b) alignment of PMF-1 and PMF-2 at joint-3.

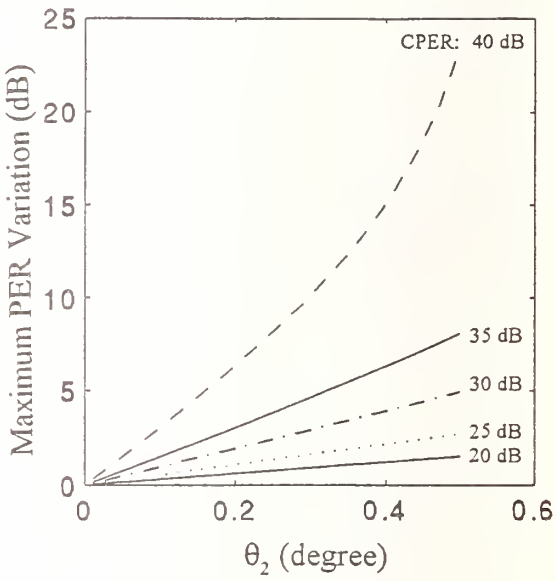

Figure 2 PER versus phase retardation ϕ_1 for an input with 1° ellipticity and 10° initial polarization phase difference when $\theta_1 = 0.5°$.

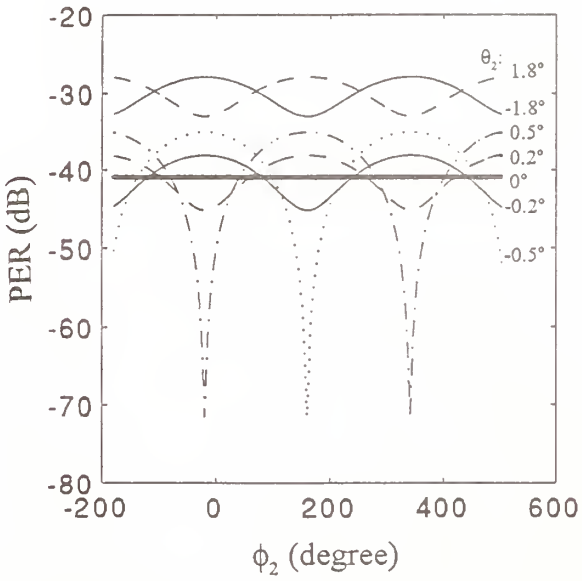

Figure 3. Maximum variation in PER as a function of misalignment angle θ_2 for different output constant PERs (CPER).

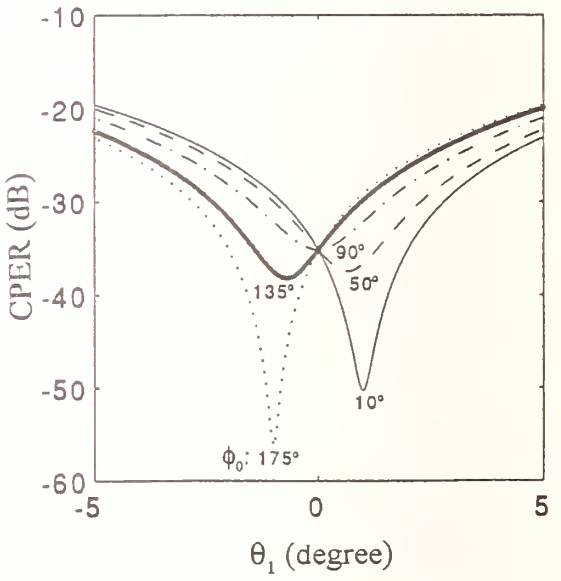

Figure 4. For an input with 1° ellipticity and different initial polarization phase retardations, the constant PER (CPER) is determined by θ_1 at joint-1.

Tapered fiber diameter measurements

Patrick Nebout, Nicolas Godbout, Suzanne Lacroix,
Xavier Daxhelet, and Jacques Bures
Département de génie physique, École Polytechnique de Montréal
P.O. Box 6079, Station "Centre-ville", Montréal (Québec), H3C 3A7, Canada

1 Introduction

It is possible to locally reduce the diameter of a fiber by stretching it while heating it with a small flame. The resulting biconical structure, usually made from a single-mode fiber, is referred to a tapered fiber or, in short, a "taper" [1]. Fabrication parameters are important for they determine the longitudinal profile of the structure which in turn determines the taper response, i.e., its behavior as a function of external parameters such as wavelength, external index or incident power. Relatively large diameters, i.e., larger than $10\,\mu$m, can be evaluated under microscope but the measurement precision is degraded as the diameter decreases. For diameters smaller than $10\,\mu$m which are required for some applications, we developed a non-destructive in-line measurement based on diffraction.

Fiber tapers are made using the fusion tapering technique. A microtorch heats the fiber locally while the fiber is pulled. The fabrication parameters like the pulling rate and the torch position must be controlled in real time. For nonadiabatic tapers, i.e., abrupt tapers such as that of Fig. 1, the radius of the section being pulled can be deduced from the oscillatory transmission of the taper with respect to elongation. However, in adiabatic tapers, the transmission remains by definition constant. Other methods are available but they are unpractical because they must be adapted to each particular taper. Since adiabatic tapers are required for certain applications, we need an alternate method that can ideally be used during fabrication. Because of the small dimensions involved, a method taking advantage of the diffraction is appealing. It can also provide the complete taper profile.

Section 2 is devoted to the theoretical analysis while Section 3 describes the experimental set-up and gives the preliminary results. The last section dicusses prospects and draws the conclusions.

2 Theory

The problem of the transmission of a transparent fiber of radius a is a standard scattering problem by a two-dimensional body. The basis for the theory is well known, and can be found in many textbooks (see, for example, Ref. [3]). For the sake of simplicity, the fiber core effect is neglected and the observation is made at an infinite distance.

Let the incident monochromatic plane wave having a wavevector $\vec{k}_0$ perpendicular to the fiber axis described in a polar coordinates system by

$$E^i(r,\theta) = \exp(k_0 r\cos\theta) \tag{1}$$

For an incident electric field parallel to the fiber axis, the scattered field is shown to be

$$E^s(r,\theta) = \sqrt{\frac{2}{\pi k_0 r}}\exp(ik_0 r)\exp(-i\pi/4)\left(b_0^s + 2\sum_{p=1}^{\infty} b_p^s\cos(p\theta)\right) \tag{2}$$

The series coefficients b_p^s are given by

$$b_p^s = \frac{k_1 J_p'(k_1 a)J_p(k_0 a) - k_0 J_p(k_1 a)J_p'(k_0 a)}{k_0 J_p(k_1 a)H_p^{(1)\prime}(k_0 a) - k_1 H_p^{(1)}(k_0 a)J_p'(k_1 a)} \tag{3}$$

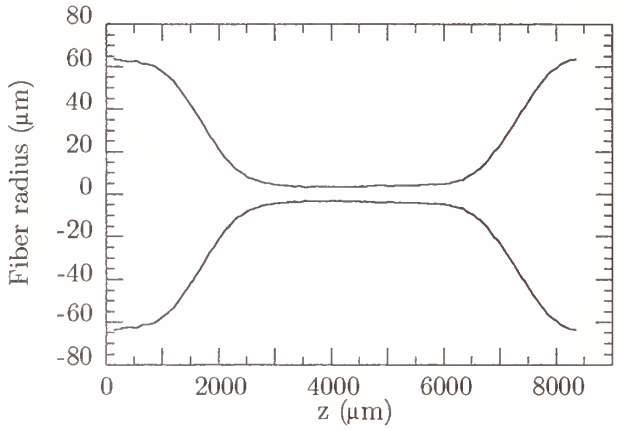

Figure 1: Profile of an abruptly tapered fiber. The untapered fiber parameters are: cladding diameter $\phi_{cl} = 127$ μm and core diameter $\phi_{co} = 4.5$ μm; second mode cutoff wavelength $\lambda_c = 578$ nm.

where k_1 is the wavenumber in the fiber; J_p and $H_p^{(1)}$ are the usual Bessel function and Hankel function of the first kind of order p, J_p' and $H_p^{(1)\prime}$ their derivatives.

The Fourier series of Eq. 2 was computed by adding the terms until their amplitude got smaller than a convergence threshold ϵ, typically $\epsilon = 10^{-8}$. The computation of the series was done in double precision to avoid cancellation errors since a large number of terms is needed. To satisfy the convergence criterion, the calculation for a 10 μm-diameter fiber requires 70 terms and a 125 μm-diameter fiber, 750 terms. The corresponding scattered field intensity profile is then deduced and compared to the experimental one.

3 Experimental results

The Fraunhoffer diffraction pattern is observed with the experimental setup schematized in Fig. 2. To test the method, we made a measurement on a cylindrical fiber with a nominal diameter of 125 μm. The experimental recording using a He-Ne laser is shown in Fig. 3a. It is to be compared with the theoretical prediction in Fig. 3b where the diameter had to be adjusted to 127 μm to obtain a fit in the position and relative amplitude of the peaks. Preliminary measurements have also been made on tapered fibers. As an example, we show the results for a tapered fiber with a quasi-cylindrical central region. We made a nonadiabatic taper and used its oscillatory transmission to measure its diameter: 13.9 μm. The experimental and theoretical diffraction patterns are shown in Fig. 4. The position and relative amplitude of the first maxima and minima is very sensitive to the diameter of the fiber which had to be adjusted to 13.74 μm to obtain the agreement with a measurement precision of the order of 0.1%.

Apart from the diffraction spreading perpendicular to the fiber, an interesting effect has been observed when the beam is pointed on the slopes of the taper. Two systems of interference fringes are then seen: the usual diffraction pattern and another parallel one caused by the prism effect of the conical section of the fiber. Although we did not interpret completely these observations, it appears that the deflection of the secondary fringe pattern is related to the taper slope. The measurement of the corresponding angle will then provide additional information on the local diameter variation.

The results presented here are preliminary and a lot of experimental work remains to be done. The method still has to be tested for very small diameters (under 10 μm), for which it is most needed. For these diameters, we lack an independent measurement to validate the method and thus additional information must be drawn from other diffracted pattern measurements. Since the relation between the diffracted pattern and the fiber dimension is not as simple as it would be for a slit, complementary calculations are also needed.

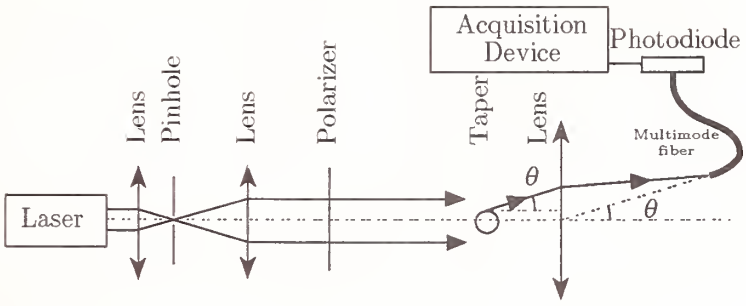

Figure 2: Setup used for the measurement. The parallel polarized laser beam is diffracted by the tapered fiber in the figure plane. A slit perperdicular to the fiber isolates a region of constant diameter. The Fraunhoffer diffraction pattern is observed in the focal plane of a convergent lens. The light is collected by a photodiode through a multimode fiber which explores the diffraction pattern.

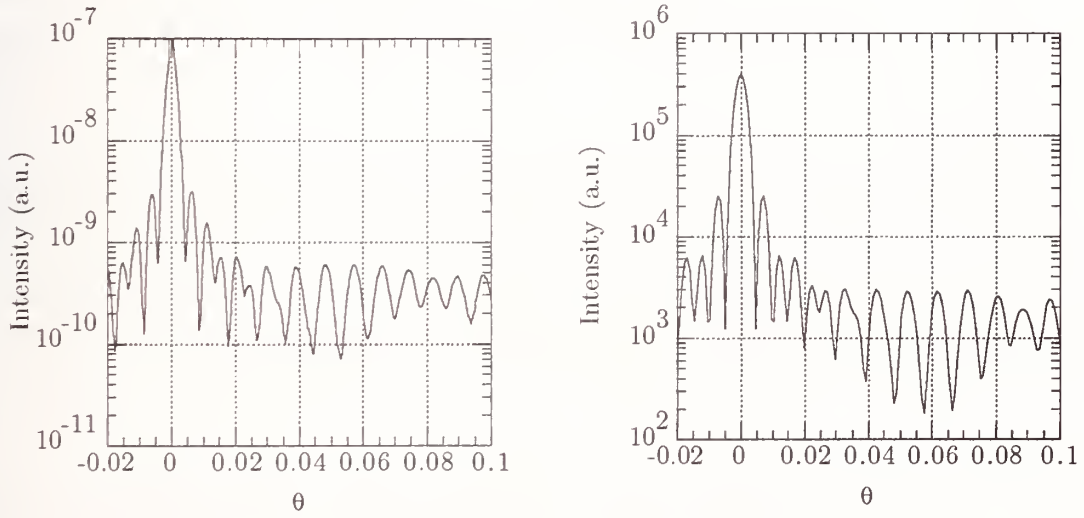

Figure 3: (a) Experimental recording of the diffraction pattern by a fiber with a nominal diameter of 125 μm. The wavelength was here 633 nm. (b) Calculated intensity pattern for a diameter of 127 μm.

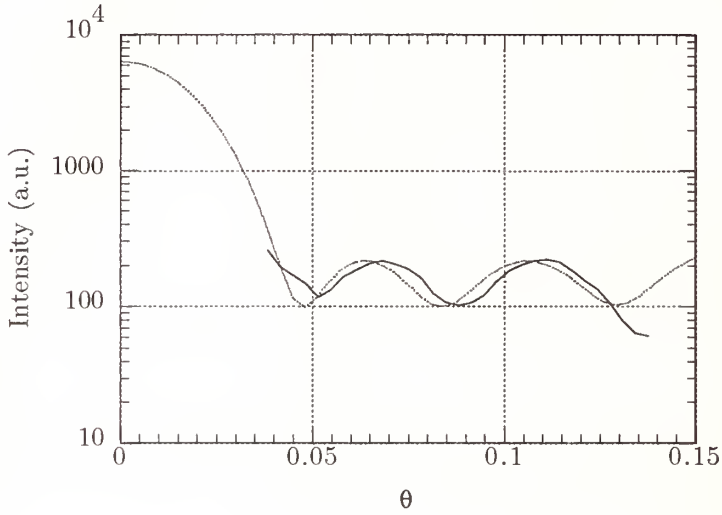

Figure 4: Experimental recording of the diffraction pattern by the central region of a tapered fiber having a diameter of 13.9 μm (solid line). The dashed line shows the calculated intensity pattern for a diameter adjusted to 13.74 μm to obtain the best fit over the limited displacement of the detection fiber.

Different wavelengths might be used as well as different polarizations, the theory remaining to be extended to the perpendicular case. The prism effect mentioned above must also be interpreted and exploited.

4 Conclusion

To measure the geometrical profile of tapered fibers, we developed a method based on the Fraunhoffer diffraction pattern measurement. Despite the apparent complexity of the diffraction patterns, this method is promising because it is a nondestructive method, not depending of the taper adiabaticity and applicable for any diameter of interest ranging from 1 μm to 125 μm. It still has to be refined by complementary theoretical as well as experimental work. In particular, the precision of the method must be explored systematically for different fiber diameters. In the longer term, it is expected to be reliable enough to be implemented in the tapering setup for characterization of the longitudinal profile during taper fabrication.

References

[1] S. Lacroix, "Fused bitapered fiber devices for telecommunication and sensing systems," in SPIE 1994 *International Symposium on Optics, Imaging, and Instrumentation*, San Diego, CA, 1994.

[2] J. D. Love, W. J. Stewart, W. M. Henry, R. J. Black, S. Lacroix, and F. Gonthier, "Tapered single-mode fibres and devices: Part 1. Adiabaticity criteria," *IEE Proc. Pt.J: Optoelectronics*, vol. 138 (5), pp. 343-354, 1991.

[3] H. C. van de Hulst, *Light scattering by small particles*, New York: Wiley, 1957.

Characterization of Silicon Optical Bench Waveguides

C. H. Henry and H. H. Yaffe[1]
AT&T Bell Laboratories, Murray Hill, N.J. 07974

Silicon optical bench (SiOB) waveguides are formed from doped silica films deposited on silicon substrates primarily by low pressure chemical vapor deposition. A typical waveguide has a core 5x5 microns in cross section that is surrounded by 15 micron thick base and cladding layers. The core-cladding refractive index difference is about 0.65 %. These waveguides are well matched to standard optical fibers and have low loss per unit length.

Optical integrated circuits (OICs) differ from fused fiber components in that complex OIC waveguide paths can be precisely patterned by photo-lithography and etching with excellent control over the phase differences between different paths of propagation. Because of the large bend radii that are required for low loss, integrated optical circuits tend to be quite long. Consequently, the large area substrates available in silicon technology are advantageous. We use 5 inch diameter wafers at present. SiOB components include couplers, taps, splitters, star couplers, broad and narrow band multiplexers and low speed switches.

Waveguide insertion loss is a measure of the added loss of placing a waveguide between a pair of optical fibers. This loss is mainly due to fiber-waveguide mode mismatch at the two interfaces. The fibers are aligned to the waveguide with 3 axis piezoelectric positioners. Matching oil is used to remove reflection loss and the effects of saw damage at the facets. Adar and Serbin [1] have measured insertion losses at 1.55 microns of 0.5 dB for standard AT&T fiber and 0.1-0.25 dB using optimally matched fibers.

The loss per unit length is difficult to evaluate by direct measurements because the attenuation length is much greater than the length of a straight optical path. We have overcome this by deducing losses from the finness of a ring resonator coupled to a

---

1. Present address: AT&T Bell Laboratories, Norcross GA 30071

straight waveguide. The recent measurements of Adar et. al. [2] used rings up to 6 cm in diameter. This measurement was aided by the use of an optical fiber laser which was narrow in linewidth and could be thermally tuned without mode hopping [3]. Data on the width of the resonance and the depth of the transmission dip at resonance can be used to separately evaluate both the resonator coupling loss and the loss per unit length. Losses of less than one dB per meter were measured at 1.55 microns. The loss drops off slowly with bend radius and the limiting loss mechanism is not known. The loss versus radius is shown in Fig. 1.

An important application of this technology is in making multiplexers for multiwavelength transmission systems with closely spaced channels. Such future transmission systems are likely to have standard channel wavelengths and it will be necessary to make optical components with transmission band centers within about 1 angstrom of these wavelengths. To determine what the wavelength control of our current technology, we fabricated identical Bragg reflectors over a batch of wafers using deep UV photo-lithography. Fig. 2 shows the distribution of measured Bragg wavelengths. The distribution, which includes the data on 6 wafers, is about 3 angstrom wide. While this spread is narrow, it probably can be improved. The wavelength variations are small because silica has a stable refractive index and our waveguide effective refractive index deviates only slightly from that of pure silica. The observed wavelength spread corresponds to a 10 percent variation in core thickness, which is about what is measured.

A growing number optical waveguide components achieve spectral filtering by controlling the relative phase of diverse paths from input to output. Adar et al. [4] studied sets of nominally identical Mach-Zehnder interferometers (MZIs) to learn to what extent we can control the phase in a waveguide path. Wavelength fluctuations of the MZIs, Fig. 3, result primarily from process induced variations in the waveguide, such as the roughness during etching. These induce a random walk in phase during propagation down the waveguide that is characterized by a rms phase deviation is one radian at a distance of 13 meters. While this is a long coherence length, these fluctuations have noticeable effects that limit the performance of low order MZIs. Additional fluctuations were associated with the photo-lithographic masks. In this case, the pattern of fluctuations repeats from wafer to wafer.

Strain plays an important role in determining the polarization dependence of optical waveguides. The doped silica films are flowed during annealing at about 1000 degreeC.

Strain is relieved at this point. Upon cooling to room temperature, strain develops because the silicon substrate contracts more with cooling than the doped silica films. The compressive strain results in small polarization dependent refractive index changes in the various doped silica materials. These changes produce a variety of effects including small TE-TM splittings of narrow band filters. These splittings and the other polarization dependent effects can be overcome by more sophisticated designs and additional processing. Fig. 4 shows a narrow band Mach-Zehnder interferometer in which these splittings are completely compensated for by the addition of a thin silicon nitride film in part of one arm. [5]

Commercial application of OICs require nearly perfect optical waveguides with very low loss, polarization independence, control of the absolute refractive index and control over the optical phase difference between different paths. The SiOB waveguide technology has the potential to meet all of these needs.

REFERENCES

[1] R. Adar, M. R. Serbin, and M. A. Meixler, "Reduced fiber coupling propagation loss with modified phosphorus doped silica on silicon waveguides", Photonics Technology Letters, (1994).

[2] R. Adar, M. R. Serbin and V. Mizrahi, "Less than 1 dB per meter propagation loss of silica waveguides measured using a ring resonator", J. Lightwave Technol. (in press) (1994).

[3] V. Mizrahi, D. J. DiGiovanni, R. M. Atkins, Y-K Park and J-M. O. Delavaoux, "Stable single-mode erbium fiber-grating laser for digital communication", J. Lightwave Technol. vol 11, 2021-2025 (1993).

[4] R. Adar, C. H. Henry, M. A. Milbrodt and R. C. Kistler, "Phase coherence of optical waveguides", J. Lightwave Technol., vol. 11, 212-219,(1993).

[5] H. H. Yaffe, C. H. Henry, R. F. Kazarinov and M. A. Milbrodt, "Polarization-independent silica-on-silica Mach-Zehnder interferometers", J. Lightwave Technol. vol. 12, 64-67, (1994).

Radius	Finesse	T_{min}	Resonance Width (MHz)	Ring Loss (dB/M)
30mm	132	0.21	8.3	0.85
20mm	108	0.045	15.2	1.22
10mm	68.3	0.077	48.2	4.72
5mm	4.7	0.75	1.46	173

Fig. 1 Bend loss versus ring radius, after Adar et al., [1].

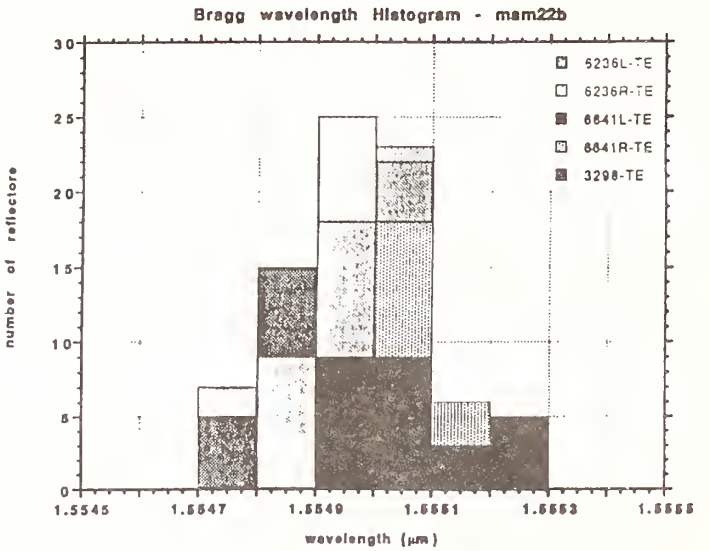

Fig. 2 Distribution of Bragg wavelengths across 6 wafers.

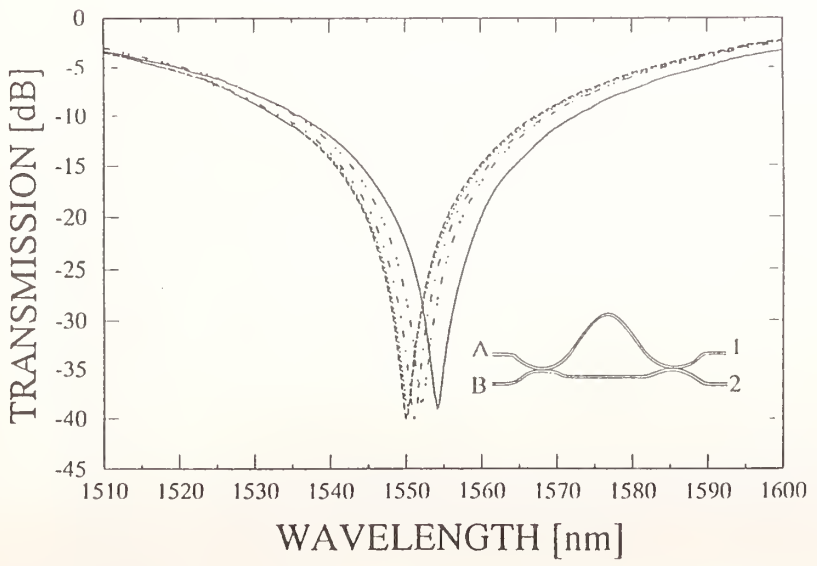

Fig. 3 Fluctuations in transmission of nominally identical Mach Zehnder interferometer of order 9.5, after Adar et. al. [4].

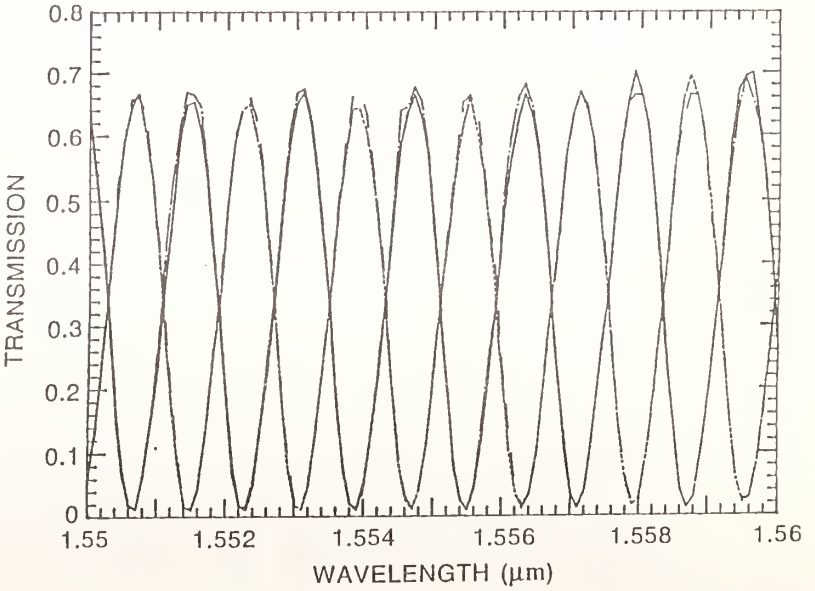

Fig. 4 TE and TM transmission of the both the cross and bar states of a Mach-Zehnder interferometer of order ≈ 1000, after [5].

Diagnosis of Silica-Based Waveguides by Using a Jaggedness-Free OLCR

Kazumasa Takada, Hiroaki Yamada and Masaharu Horiguchi
NTT Opto-electronics Laboratories
Nippon Telegraph and Telephone Corporation
Tokai, Ibaraki-ken, 319-11, Japan

1.Introduction

The optical low coherence reflectometer (OLCR) is sufficiently sensitive to detect Rayleigh backscattering with a dynamic range of more than 20 dB [1-3]. Because of its high dynamic range and the high spatial resolution, the OLCR has great potential for use in measuring the loss distribution in planar waveguides by using Rayleigh backscattering. The measurement principle is the same as that by which OTDRs are used to diagnose optical fiber cables. However, the OLCR has not yet been very successful when used for this measurement [4-6]. This is because the Rayleigh backscatter signal jags randomly along its length due to speckle-like phenomena [7] so that the loss information is concealed by the jaggedness.

This paper describes the loss distribution measurement of silica-based waveguides using a jaggedness-free OLCR. A tunable low-coherence light source is specially designed for the efficient wavelength averaging [8] of the Rayleigh backscatter signal. The OLCR with this averaging scheme, or jaggedness-free OLCR, reduces the jaggedness sufficiently to reveal the mean Rayleigh backscattering profiles of the silica-based waveguides. Their loss distributions can be clearly determined from the profiles.

2.Experimental Setup

2.1. OLCR System: Figure 1 shows the configuration of the OLCR with a [3x3] fiber coupler. The output from the low-coherence light source, which is shown schematically in Fig. 2, is launched into the [3x3] coupler from the source port, and is divided equally into three ports on the output side. Two are used as the probe and local oscillator (LO) ports, while the other is unused. The piezoelectric (PZT) phase modulator incorporated into the probe port is sawtooth ramped through a π radian range in order to produce a serrodyne carrier frequency [9]. The polarization controller (PC) is used to excite one principal mode of the waveguide under test (WUT). The light from the LO port is emitted into the air and reenters the port after being reflected twice at the movable retroreflector and once at the mirror. The LO light and the light returned from the WUT are combined by the coupler. The combined light is detected by a pair of photodiodes after propagating through the two balanced-detection ports on the input side of the coupler.

2.2. Low-Coherence Light Source: The previously-reported tunable low-coherence light source [8] has the following disadvantages. The output is limited to a few milliwatts. The source can be considered to be a Fabry-Perot resonator, in which a fiber amplifier is sandwiched between a mirror and an optical isolator. Since the return loss of the isolator is no more than 60 dB, the round-trip gain in the cavity at higher pump powers exceeds the round-trip loss of about 60 dB. Even when the laser oscillation is suppressed, the gain near the loss produces undesired satellites in the Fresnel response function of the OLCR, widening the hidden space near the facets and an intense WUT reflection.

A tunable high-power low-coherence light source was constructed as shown in Fig. 2. This source uses two optical amplifiers AMP1 and AMP2, which are optically interconnected in such a manner that the laser oscillation is suppressed by optical isolators ISO1 and ISO2. Each amplifier was composed of an erbium-doped fiber, a WDM coupler, an optical isolator and a 1.48-μm pump LD. The optical bandpass filter module FIL1 was used for filtering the broadband superfluorescent light from AMP1. The narrow-band light from the filter, which is amplified by AMP2, is passed through the second bandpass

filter module FIL2 in order to remove the wideband spontaneous emission generated by AMP2. These bandpass filters are automatically tuned by a wavelength controller so that the center wavelengths of the passbands coincide.

One end of the erbium-doped fiber of AMP1 is polished at an angle of 8°, thereby giving a return loss of 60 dB. The total return loss of ISO1 and FIL1 is 60 dB. The light suffers a total loss of approximately 120 dB during a round trip in the Fabry-Perot resonator which is set up between ISO1 and the angled-endface of the erbium-doped fiber. Since the loss greatly exceeds the gain of AMP1, the optical feedback effect can be greatly reduced. Since the second amplifier AMP2 is sandwiched between ISO1 and ISO2 whose return losses are 60 dB, respectively, the effect of the feedback can be reduced as in AMP1.

The center wavelength of the source output was tuned from 1560 nm to 1530 nm in approximately 1 nm steps. Figure 3 shows the optical spectra of the output on a logarithmic scale. The pump power launched into the optical amplifiers was 60 mW. The rotation angle in the figure is that of the bulk-optic filter incorporated into the second bandpass filter FIL2. The output power from the source changed from 10 dBm at 1560 nm to 6 dBm at 1530 nm. Although the power from the source was very high, each output was narrow-band, low-coherence light whose bandwidth was less than 1 nm and whose spectrum had sidelobes that were -40 dB lower than the central peak. We launched each of these low-coherence lights into the OLCR system and found that a deviation of 2.5 mm from a silica-based waveguide endreflector resulted in a signal that was 60 dB lower than that detected at the reflector. Thus the hidden space defined by the full width at -60 dB maximum of the Fresnel response is 2.5 mm x 2= 5 mm.

2.3. Wavelength Averaging: The retroreflector of the OLCR was scanned at 250 μm intervals, and reflection from silica-based waveguides was detected at each position of the retroreflector. The mean value of the Rayleigh backscatter signal detected by the OLCR is proportional to $P^2/\delta\upsilon$, where P is the source output, and $\delta\upsilon$ is its effective bandwidth [10]. The wavelength averaging at each position was carried out by calculating $\sum_{k=1}^{N} I_k (P_s/P_k)^2 (\delta\upsilon_k/\delta\upsilon_s)/N$ after sweeping the entire wavelength range once from λ_1 =1560 nm to λ_N =1530 nm (N = 30) in approximately 1 nm steps. Here the monitored source output P_k and the detected signal I_k were stored in a computer for each wavelength λ_k. $\delta\upsilon_k$ is the effective bandwidth at λ_k. P_s and $\delta\upsilon_s$ are the power and the effective bandwidth of the output at a standard wavelength of λ_s = 1555 nm.

3. Results and Discussion

First, a high loss silica-based waveguide fabricated on a silicon substrate was tested. The waveguide was connected via index matching oil to single mode fibers, one of which was the fiber probe of the OLCR. The TE mode of the waveguide was excited at the input end. Figure 4 shows the mean reflection profile obtained after performing wavelength averaging. The profile is composed of a "Rayleigh backscattering" floor that is revealed by averaging the Rayleigh backscatter signal and from which the loss distribution is obtained, isolated (or point-like) reflections distributed randomly along the waveguide, and an endreflection at its input end (at zero distance). The fluctuations in the floor of the probe fiber (distance < 0) were reduced to within ± 1 dB by using the wavelength averaging method. The index matching oil reduced the endreflection to only -40 dB, whereas the revealed floor level was less than -95 dB.

In spite of such a large endreflection, it was observed that the floor (measured in dB) of the waveguide attenuated linearly with distance by 17 dB in 40 cm, and the attenuation was not affected by the location and reflection of isolated scattering centers. The waveguide receives a constant loss over the waveguide at a rate of (17 dB)/(40 cm)/2 = 0.2 dB/cm, which agrees well with the directly measured value. The behavior of the floor suggests that the origin of the waveguide loss is not these isolated scattering centers, but results from fluctuations such as core-cladding irregularities or inhomogeneity in the core and cladding.

Next, we tested silica-based waveguides fabricated on a different substrate. Nineteen waveguides were fabricated in parallel on the substrate in a "serpentine" configuration and were numbered from 1 to 19 in sequence. With the conventional method for estimating total loss, two waveguides (Nos. 1 and 18) were proved to have extra losses of 4 dB and 8 dB, respectively, as compared with the other waveguides. Figure 5 shows the mean reflection profile of one normal waveguide (No. 7). Although this waveguide had large point-like reflections, the Rayleigh floor attenuated linearly with distance by 4 dB in 40 cm. The waveguide receives a constant loss of (4 dB/40 cm)/2 = 0.05 dB/cm along its length.

The mean reflection profiles of five silica-based waveguides (Nos. 1, 2, 3, 7, and 18) are shown in Fig. 6. The Rayleigh floors of the two normal waveguides (Nos. 2 and 3) exhibited approximately the same attenuation behavior as that of waveguide No. 7. The floor of the waveguide No. 1 decreased in steps of 2 dB and 5 dB at distances of 18 cm and 36 cm, respectively. Waveguide No. 18 decreased by 14 dB at a distance of 26 cm. These reductions mean that extra losses of 2 dB/2 + 5 dB/2 ≈ 4 dB, and 14 dB/2 = 7 dB are added for waveguides Nos. 1 and 18, respectively, whose values agree well with the extra directly measured losses. The loss coefficients at portions other than these points are approximately the same as those of the normal waveguides. These results indicate that the measured extra losses are produced by point defects. One possible origin of the defects is the unexpected adhesion of small particles of dust on the waveguides.

4. Conclusion

We have described the loss distribution measurement of silica-based waveguides by using a jaggedness-free OLCR. A tunable low-coherence light source using two optical fiber amplifiers was specially designed for the diagnosis. The source automatically tuned the central wavelength of the low-coherence light with a spectral width of less than 1 nm over 30 nm. Unavoidable jagged fluctuations observed when using conventional OLCRs were reduced to within ± 1 dB by averaging the wavelength-dependent Rayleigh backscatter signals. The source reduced the optical feedback effect sufficiently to limit the hidden space defined by the full width at -60 dB maximum of the Fresnel response to 5 mm. This OLCR with the wavelength averaging scheme, or jaggedness-free OLCR, revealed the Rayleigh backscattering floors of the waveguides in spite of large endreflections at their input ends. Constant loss distributions such as 0.05 dB/cm and stepwise loss increases of, for example, 1 dB, were clearly observed in the waveguides from the changes in the floors.

5. Acknowledgments

The authors would like to thank Dr. Masao Kawachi for his continuous encouragement. They also thank Dr. Yoshinori Hibino for supplying us with the waveguide samples used in the experiment.

References

1. K. Takada, M. Shimizu, M. Yamada, M. Horiguchi, A. Himeno, and K. Yukimatsu, Electron. Lett. vol. 28, pp. 29-30 (1992).
2. W. V. Sorin and D. M. Baney, IEEE Photon. Technol. Lett. vol. 4, pp. 374-376 (1992).
3. K. Takada, T. Kitagawa, M. Shimizu, and M. Horiguchi, Electron. Lett. vol. 29, pp. 365-367 (1993).
4. K. Takada, N. Takato, and J. Noda, Opt. Lett. vol. 14, pp. 706-708 (1989).
5. M. Kobayashi, H. Hanafusa, K. Takada, and J. Noda, IEEE J. Lightwave Technol. vol. 9, pp. 623-628 (1991).
6. H. H. Gilgen, G. Bodmer, and Ch. Zimmer, in proceedings of 2nd Optical Fiber Measurement Conference, Torino, Italy, pp. 143-146 (1993).
7. K. Takada, A. Himeno, and K. Yukimatsu, Opt. Lett. vol. 16, pp. 1433-1435 (1991).
8. K. Takada and M. Horiguchi, Electron. Lett. vol. 29, pp. 1273-1274 (1993).
9. R. P. Novak, H. H. Gilgen, P. Beaud, and W. Hodel, in Proceedings of Symposium on Optical Fiber Measurement, Boulder, Colorado, pp. 35-38 (1990).
10. P. R. Morkel, R. I. Laming, and D. N. Payne, Electron. Lett. vol. 26, pp. 96-98 (1990).

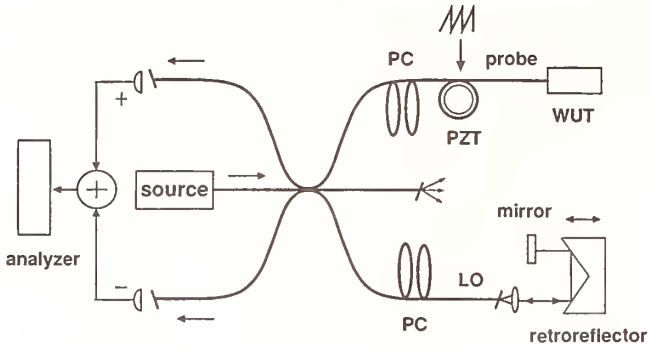

Fig. 1. Experimental setup of OLCR
PC: polarization controller, LO: local oscillator, WUT: waveguide under test

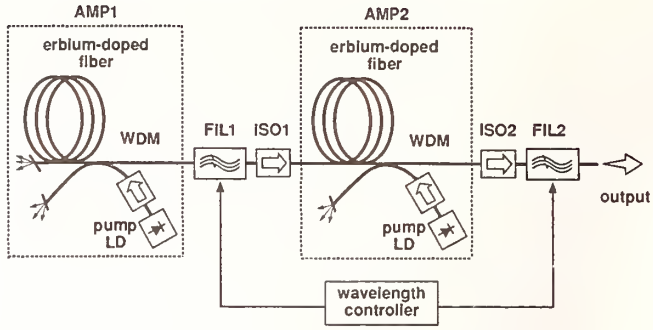

Fig. 2. Experimental setup of tunable low-coherence light source
FIL: optical bandpass filter, ISO: optical isolator, AMP: optical amplifier

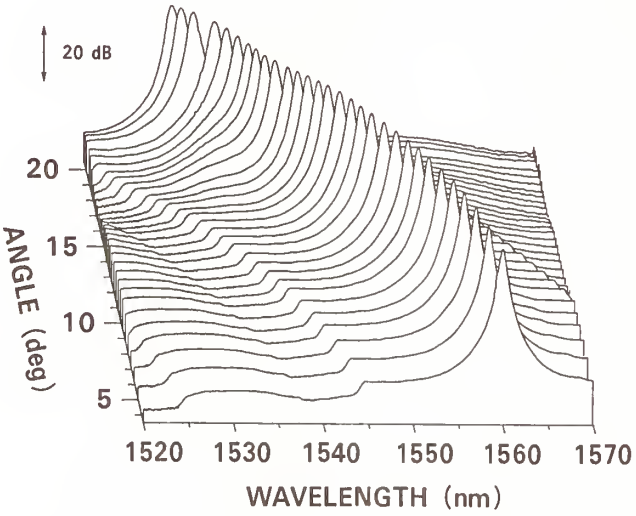

Fig. 3. Change in output spectrum from the low-coherence light source

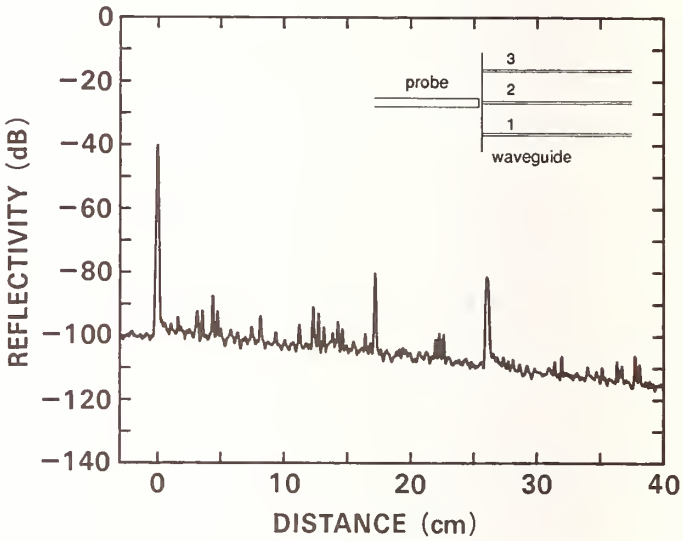

Fig. 4. Mean reflection profile of a silica-based waveguide with high loss

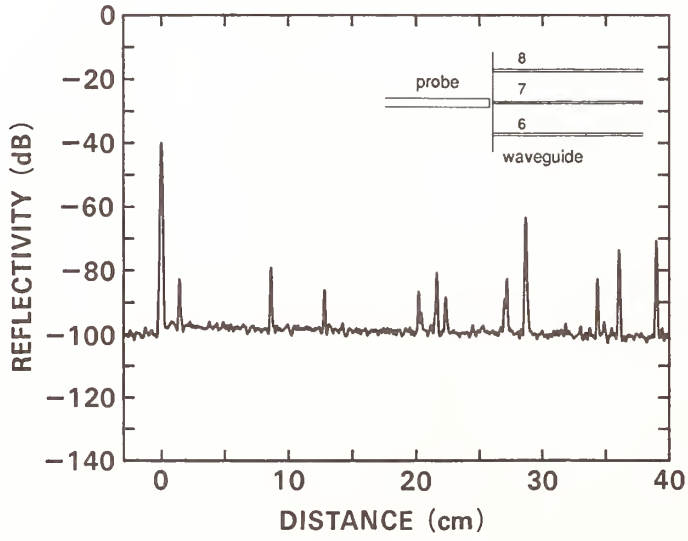

Fig. 5. Mean reflection profile of a silica-based waveguide

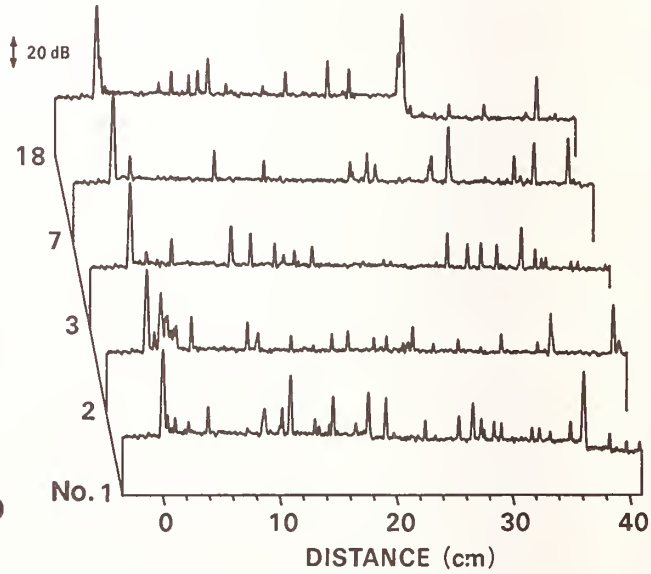

Fig. 6. Mean reflection profiles of silica-based waveguides fabricated on one wafer

MEASUREMENTS OF LOSS AND MIRROR REFLECTIVITY IN SEMICONDUCTOR OPTICAL WAVEGUIDES: A EUROPEAN INTERLABORATORY COMPARISON EXPERIMENT

E. Gini - Institute of Quantum Electronics, ETHZ, Zurich, Switzerland
L.H. Spiekman - Dept. of Electrical Engineering, TU Delft, Delft, The Netherlands
H. van Brug - Dept. of Applied Physics, TU Delft, Delft, The Netherlands
J.-F. Vinchant - Alcatel Alsthom Recherche, Marcoussis, France
S. Morasca, F. Pozzi, C. De Bernardi - CSELT S.p.A. , Torino, Italy
R. Zengerle, W. Weiershausen, W. Noeïl - DBP Telekom, Research Center Darmstadt, Germany
L. Thévenaz, A. Küng - EPFL, Metrology Laboratory, Lausanne, Switzerland
A. Enard, N. Vodjdani - Thomson CSF Laboratoire Central de Recherche, Orsay, France

ABSTRACT

The results of round-robin measurements of waveguide loss and integrated mirror reflectivity in several European laboratories in the frame of the COST 240 project are presented. The Fabry-Perot cavity contrast method was used on semiconductor optical waveguides. The measured losses show a satisfactory agreement (within ±0.5 dB) between all the laboratories, but also point out some aspects which must be taken into account to get meaningful data.

1. - Introduction

Several aspects of the measurement procedure for integrated optical waveguides and components are at a far less evolved stage than for the optical fiber counterparts. The repeatability and reproducibility of measurements, the homogeneity and comparability of results from equivalent or similar methods or set-ups, even for basic parameters like waveguide loss, are just a few of these aspects. To address this problem, within the European Project COST 240 "Techniques for Modelling and Measuring Advanced Photonic Telecommunication Components" it was decided to organize the circulation of waveguide samples in a number of participating laboratories, to perform measurements and compare the results.

As a first test, it was agreed to measure the loss of waveguides fabricated on InGaAsP/InP chips, using the well-known method of Fabry-Perot resonances contrast in the cavity formed by the partially reflecting terminal facets [1]. The choice of this technique was prompted by its sensitivity, non destructiveness and availability (in a few modifications of the basic configuration) at several participating laboratories.

2. - Principle of the technique and experimental set-ups

In a Fabry-Perot resonator operating in a single transverse mode regime, the ratio K between its maximum and minimum transmittance when changing the resonance conditions appears in the following relationship [1]:

$$L\alpha = \ln R + \ln\left(\frac{\sqrt{K}+1}{\sqrt{K}-1}\right) \qquad (1)$$

where L is the geometrical length of the cavity (i.e. the waveguide in the present case), α the cavity attenuation and R the mirror (facet) reflectivity, assumed equal for both ends.

The basic experimental set-up to use this technique for waveguide measurements is shown in Fig. 1; the actual implementations differ in several details, the most significant one being the way

of changing the resonance conditions to scan several periods of the transmission characteristics, and hence to determine K. Two techniques are currently in use: a) a slow heating or cooling of the sample, by which the length of the optical cavity is changed by the combined action of thermal expansion and thermooptic effect, while the wavelength of the narrow-linewidth source is kept fixed; b) small changes of wavelength of the source, while keeping constant the sample temperature and its optical length. AAR, DBP Telekom, EPFL and Thomson CSF used method a), while ETHZ, both TU Delft laboratories and CSELT used method b).

Other minor differences pertain to the source (gas or diode laser), the way of coupling light to the waveguide (lens or single-mode fiber) and the type of control of the input or output polarization state. All the implementations in the participating laboratories use either HeNe lasers operating at 1.532 μm or diode lasers operating in the 1.55 μm range.

3. - Sample structure

Semiconductor chips with stripe waveguides fabricated in the InGaAsP/InP material system were made available for this experiment; the high refractive index of these materials yields natural Fresnel reflectivities for the facets around 0.3, so that good contrast can be achieved without special sample preparation besides cleaving the I/O facets. A first sample with simple straight ridge guides, supplied by CSELT, was used for some initial essays; then a more complex chip, containing both straight guides and different types of integrated mirrors, supplied by ETHZ, was circulated among all the labs and extensively characterized. Its structure is shown in Fig. 2, and all data reported in this paper refer to this sample.

4. - Measurement results and discussion

Measurements of Fabry-Perot contrast were performed on selected waveguides and mirrors on the chip, separately for TE and TM polarizations. From the measured values of K, the total cavity loss was calculated, and the corresponding values are shown in Fig. 3 for the TE polarization. The data show a general agreement between the results of all laboratories, with some occasional discrepancies and more scattered data for particular guides; in two cases (Thomson-CSF and ETHZ data) the measurements were made after a new cleavage of one end (sample length reduced from 9 to 5.6 mm), so that the facets are not the same as for the other laboratories, and their quality may be different. Other differences can arise from cleaning of the sample in different solvents, which was performed in some laboratories to remove the mounting wax used to fix the chip on the holder after the measurements: residual contamination can alter both R (if the facet is affected) and α (if the guide surface is contaminated); a possible example of this effect is the sequence of results from AAR, CSELT and DBP for guides on one side of the chip. Some guides 6 μm wide exhibited multimode behavior, and in this case the contrast values K depended more or less sensitively on the input coupling conditions, thus increasing the uncertainty.

To get the corresponding values of attenuation α (expressed in dB/cm) for the waveguides, in addition to the measured length L, calculated values of modal reflectivity were used for R; these were computed by a Fourier analysis and Fresnel reflection method [2] applied to the actual waveguide structure, and range between 0.315 and 0.319 (TE) or 0.247 and 0.250 (TM) according to the guide width; no experimental value for R was available.

The attenuation values of course exhibit the same trend as the total cavity loss, and the average level is 1.1 ± 0.3 dB/cm for TE polarization; as a comparison, it should be noticed that for this chip length an uncertainty of ±0.1 in the corresponding contrast (K=2.8) amounts to ±0.16 dB/cm, and increases to ±0.5 dB/cm when K=1.75. An uncertainty of ±0.01 in the adopted value of R leads to a corresponding systematic error of ±0.16 dB/cm in the attenuation.

The results for TM polarization are similar, except for a larger spread, due to lower reflectivity, smaller K values and higher loss ($\alpha = 2.4 \pm 0.6$ dB/cm).

The reflectivity of integrated mirrors was obtained by subtracting the average guide loss of the corresponding straight guides; mirror losses of 0.8 ± 0.2 dB and 1.0 ± 0.3 dB were obtained for TE and TM polarization respectively.

5. - Conclusions

An extensive series of optical loss measurements has been performed by several laboratories on semiconductor waveguides by similar set-ups based on the Fabry-Perot fringe contrast method. Agreement within about ±0.5 dB/cm has been found in the vast majority of cases for guide attenuation, and within ±0.2 dB for integrated corner mirros. It has been shown, on the other hand, that maintaining very carefully facet quality and cleanliness is extremely important, and that definitely single mode propagation is essential to achieve meaningful and reproducible results.

References

[1] R.G. Walker, "Simple and accurate loss measurement technique for semiconductor optical waveguides", Electron. Lett., vol. 21, pp. 581-583, 1985.

[2] P.A. Besse, J.S. Gu, H. Melchior, "Reflectivity minimization of semiconductor laser amplifiers with coated and angled facets considering two-dimensional beam profiles", IEEE J.Quantum Electron., vol. QE-27, pp. 1830-1836, 1991.

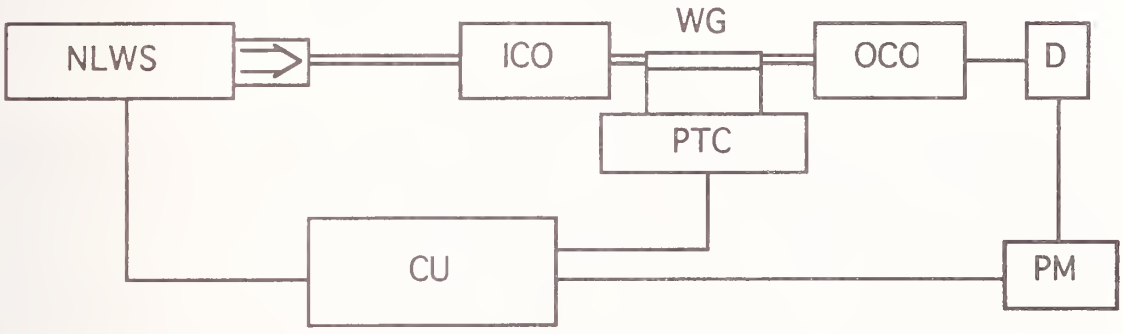

Fig. 1 - Schematic of a basic set-up for measurements of Fabry-Perot fringe contrast in optical waveguides. NLWS: narrow linewidth laser source with optical isolator; ICO: input coupling optics; WG: waveguide under test; PTC: sample position and temperature control; OCO: output coupling optics; D: detector; PM: power meter; CU: control and acquisition unit. Polarization control is present at least in one coupling optics unit.

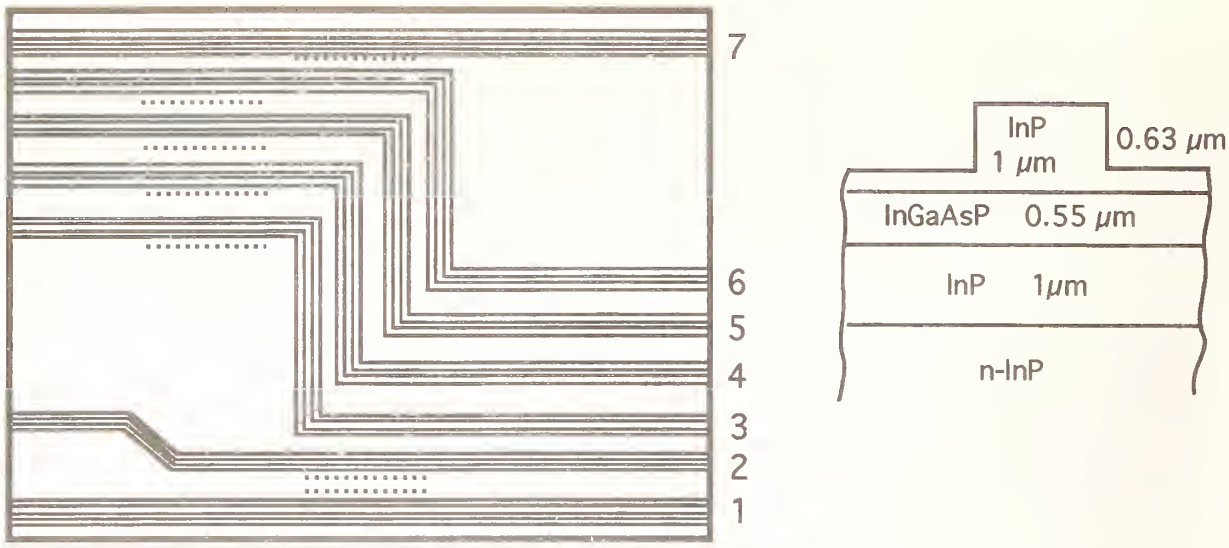

Fig. 2 - Schematic structure of the layout and waveguide cross-section of the ETHZ-supplied chip. Groups 1 and 7 contain sets of straight waveguides 3, 4, 5 and 6 μm wide; group 2 contains pairs of 45° deviating mirrors; groups 3 to 6 contain pairs of 90° deviating mirrors; mirror waveguides have the same widths as straight guides; total chip length 9 mm. The facets have no intentional coating.

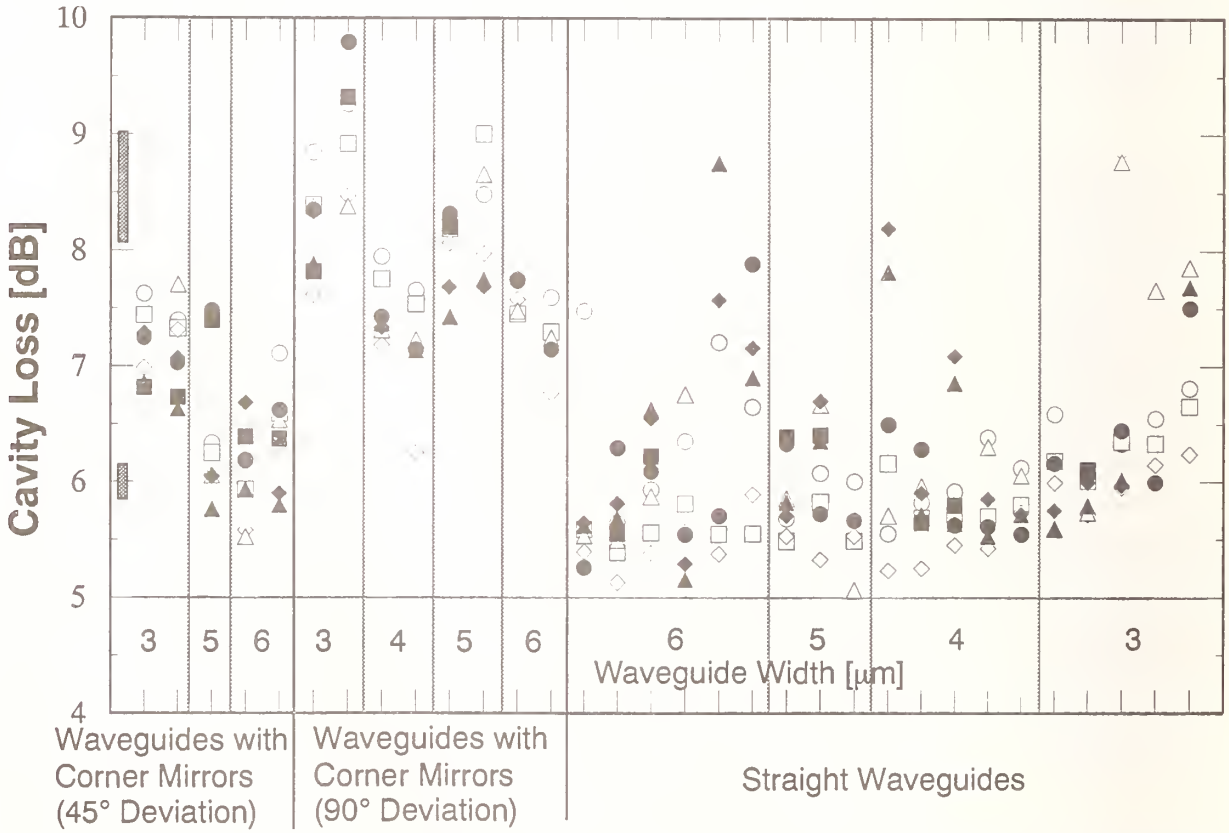

Fig. 3 - Distribution of the measured total cavity loss (propagation plus reflection loss at the facets) for TE polarization. ○ : TUD-EE; □ : TUD-AP; ◇ : AAR; Δ : CSELT; ● : DBP Telekom; ■ : EPFL; ◆ : Thomson-CSF; ▲ : ETHZ (in order of measurement). The line at the 5.0 dB level corresponds to the calculated end facet reflection loss; average attenuation for waveguides is 1.1 ±0.3 dB/cm (see text). The bars at left show the uncertainty coming from a $\Delta K = \pm 0.1$ at different total loss levels.

White-Light Spectral Analysis of Lithium Niobate Waveguides

C. F. McConaghy, K. F. Hugenberg, D. Sweider, and M. Lowry
Lawrence Livermore National Laboratory

R. A. Becker
Integrated Optical Circuit Consultants

1. INTRODUCTION

Optical channel waveguides in lithium niobate are a very useful technique for building a variety of integrated optical components such as modulators, splitters, and frequency doublers. In many of these applications, single mode performance is essential in order to achieve the desired device performance. Determination of single-mode operation can be complicated by the fact that a multi-mode guide can support lower order modes and can appear single mode if the launch conditions for the light into the guide do not excite any of the higher order modes. Typical measurements often made to assure single-mode operation include optical mode spot imaging, and the "blink test". While these measurements are useful, they are strictly qualitative in nature, and thus do not provide the fine detail often desired in practice. In developing waveguide fabrication processes, it is more helpful to know how various process steps affect the wavelength at which the waveguide is single-mode, multi-mode and cut-off. In this paper, we show the usefulness of exciting waveguides with a broadband white-light source and observing the output of the guides over much of the visible and near IR spectrum with a spectrometer. Although this technique is not new, its usefulness in process development and control has not been emphasized[1].

2. EXPERIMENTAL SETUP

Figure 1 shows a block diagram of the white light spectrometer system. A tungsten-halogen lamp is coupled into and out of the waveguide under test by microscope objectives. The lenses which have a numerical aperture of 0.2 are achromatic and fairly well corrected in the visible and IR portions of the spectrum. In addition, a calibration trace is done to calibrate out variations of the lamp and optical system with wavelength. It should be noted that an ideal Gaussian spot when focused will only excite the lowest order mode. However, there is some coupling to the next highest order mode since the actual system is not a perfect Gaussian. The output light is then analyzed with a monochromator and a PIN diode detector. An ideal white light trace is shown in Figure 2. Assuming that the wavelength spans over the range of the lowest order mode and the next higher order mode, the ideal trace can be broken into four regions[2]. In Region 1 both modes are far from cutoff and the ratio of light intensity at the output of the guide $I(\lambda,z_o)$ to the total available input light intensity $Is(\lambda)$ can be described as:

$$I(\lambda,z_o)/I_S(\lambda) = K_{00}(\lambda) + K_{01}(\lambda) \qquad (1)$$

where λ is the wavelength, z_o is the length of the guide, and K_{00} and K_{01} are the input coupling coefficients for the lowest and next higher order modes, respectively. Region 2 describes the λ regime where the I_{01} cutoff is approached. In this case the ratio of output to input intensities is given by:

$$I(\lambda,z_o)/I_S(\lambda) = K_{00}(\lambda) + K_{01}(\lambda)\exp(-a_{01}(\lambda)z_o) \qquad (2)$$

where a_{00} and a_{01} are the modal attenuation coefficients for the lowest order and next higher order modes, respectively. As the wavelength becomes longer the cutoff of the I_{01} mode is passed and region 3 covers the wavelength range where the I_{00} mode is still far from cutoff. This intensity ratio in this region is given as:

$$I(\lambda,z_o)/I_S(\lambda) \approx K_{00}(\lambda) \quad (3)$$

Finally as the I_{00} mode cutoff is approached in region 4, the intensity ratio is :

$$I(\lambda,z_o)/I_S(\lambda) \approx K_{00}(\lambda)\exp(-a_{00}(\lambda)z_o) \quad (4)$$

3. EXPERIMENTAL DATA

For this experiment a mask with straight guide dimensions of 2,3,4, and 5 um was used to pattern channels in oxide on three-inch diameter x-cut lithium niobate wafers. These wafers were then proton exchanged in benzoic acid at 200°C and annealed at 350°C. Figure 3 shows a series of experimental traces corresponding to five different wafers processed at different times over a 12 month time period. These particular guides had a mask width of 3 um and were exchanged for 10 minutes and annealed for 2 hours. The target wavelength for single mode operation of devices made with these guides was 830 nm. It is evident from Figures 2 and 3 that 830 nm is at the beginning of Region 3, just beyond the Region 2 edge for all five wafers. This wavelength corresponds to the tightest confinement of the lowest order mode and occurs just prior to the multimode region. The white light data provides a good measurement of the waveguide process control. For example, the slight variation in wavelength of the regions for the various wafers can be attributed to the degree of control in maintaining the mask linewidth in the masking oxide used on the wafer. Also shown in Figure 3 is a simulated trace assuming the following parameters:

$$a_0(\lambda) = 5.2 \times 10^{-10} \times (\lambda\text{-}1200) \text{ Nepers/nm} \; ; \; K_0(\lambda) = -.0202 + 2.0 \times 10^{-5} \times \lambda$$
$$a_1(\lambda) = 2.1 \times 10^{-10} \times (\lambda\text{-}775) \text{ Nepers/nm} \; ; \; K_1(\lambda) = 0.0128 - 8.0 \times 10^{-6} \times \lambda$$

where as previously mentioned, a simple linear dependence with wavelength is assumed.

Another interesting way to present the white light data is shown in Figure 4. Here, the wavelengths for absolute single mode cut-off, well confined single mode operation, absolute second mode cutoff and well confined double mode are plotted vs. mask width dimension. By looking at the well confined single mode region , it is possible to select the proper mask width to use for a given wavelength of operation. It is apparent from this figure that the well confined single mode regime covers a broad spectrum (350 nm for the 3 um guide). Experiments have also been conducted with devices under bias to observe the lowest $V\pi$ wavelength on a Mach Zehnder and the change in cut-off wavelength under bias on a phase modulator.

4. SUMMARY

We have shown the usefulness of exciting waveguides with a broad spectrum from a white-light source and measuring the guide response vs. wavelength. By proper interpretation of the various steps in these responses, it is possible to quantitatively determine cutoff, single mode operation, and multi-mode regimes and to monitor process variability over time. In conclusion, the white light excitation and spectral analysis technique is an important diagnostic for waveguide and device development in lithium niobate and any other optical waveguide material system.

1. J.E. Baran, Y. Silberberg, P. Perlmutter, "White-light characterization of integrated-optic waveguides and devices," OFC/IOOC, TUO2, 1987.
2. K.A.H. van Leeuwen and H.T. Nijnuis, "Measurement of higher-order mode attenuation in single-mode fibers: effective cutoff wavelength," Opt. Letters, 9, 252 (1984).

Work performed under the auspices of the U.S. Department of Energy by Lawrence Livermore National Laboratory under Contract No. W-7405-Eng-48.

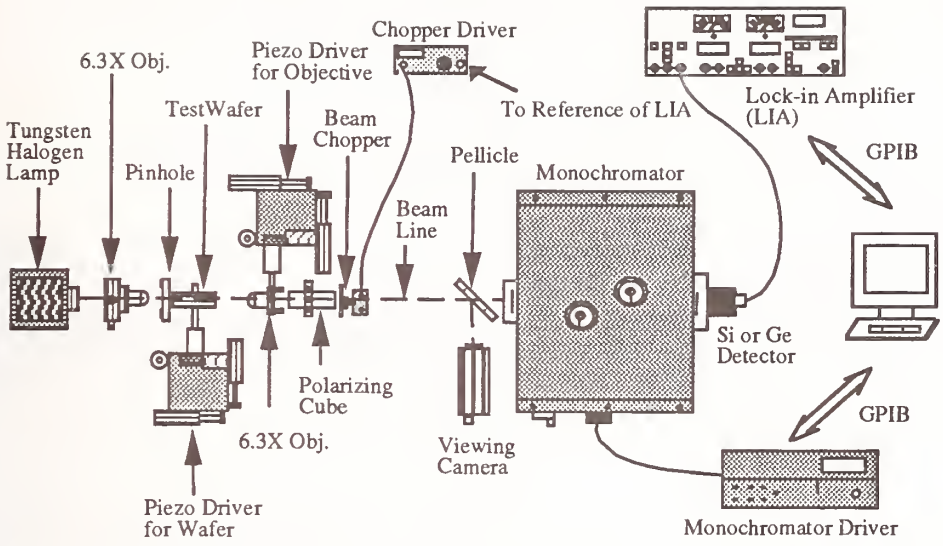

Fig. 1 Experimental setup for exciting waveguides with white light: includes a tungsten-halogen lamp, microscope objectives, apertures, monochromator, and PIN diodes.

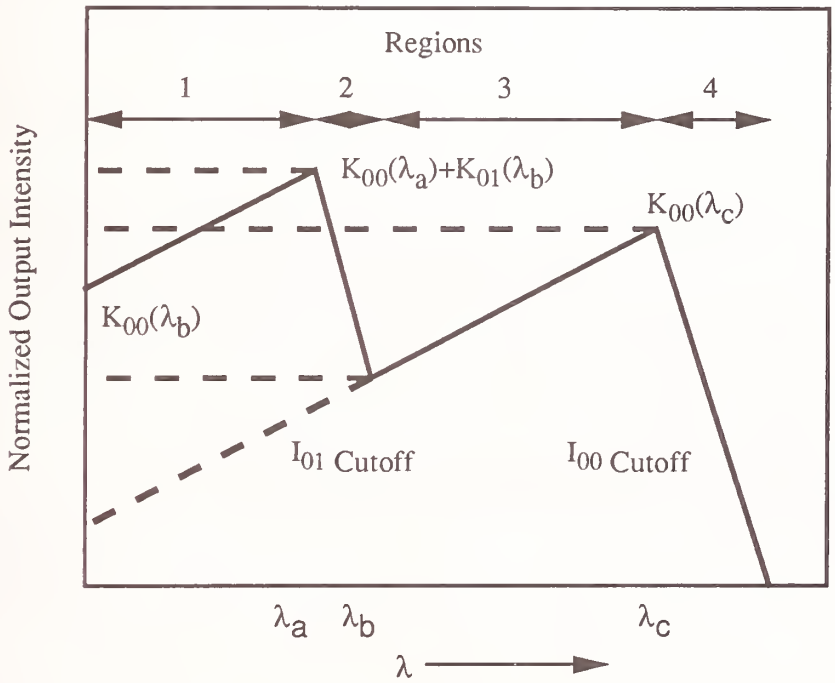

Fig. 2 a) Typical data for a lithium niobate waveguide scanned from 600 to 1700 nm
b) Ideal data showing four regions:
(1) I_{00} and I_{01} modes ; (2) I_{01} cutoff ; (3) I_{00} mode ; (4) I_{00} cutoff

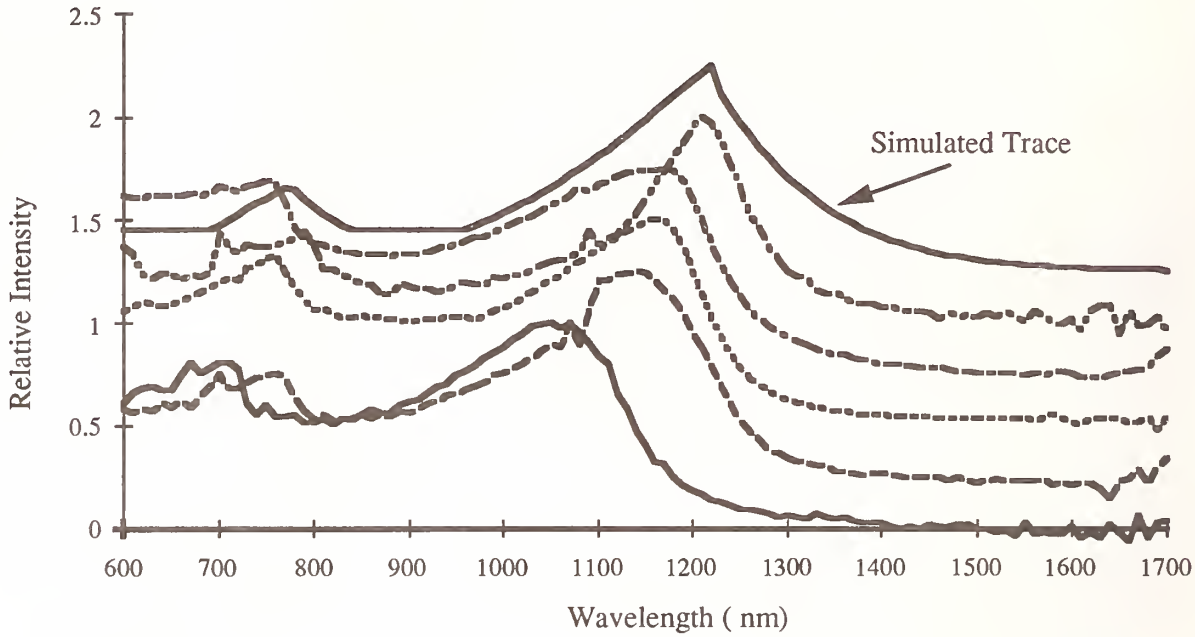

Fig. 3 White-light spectrum for five non-simultaneously processed wafers with a target single-mode wavelength of 800 nm. Also shown is a simulated trace.

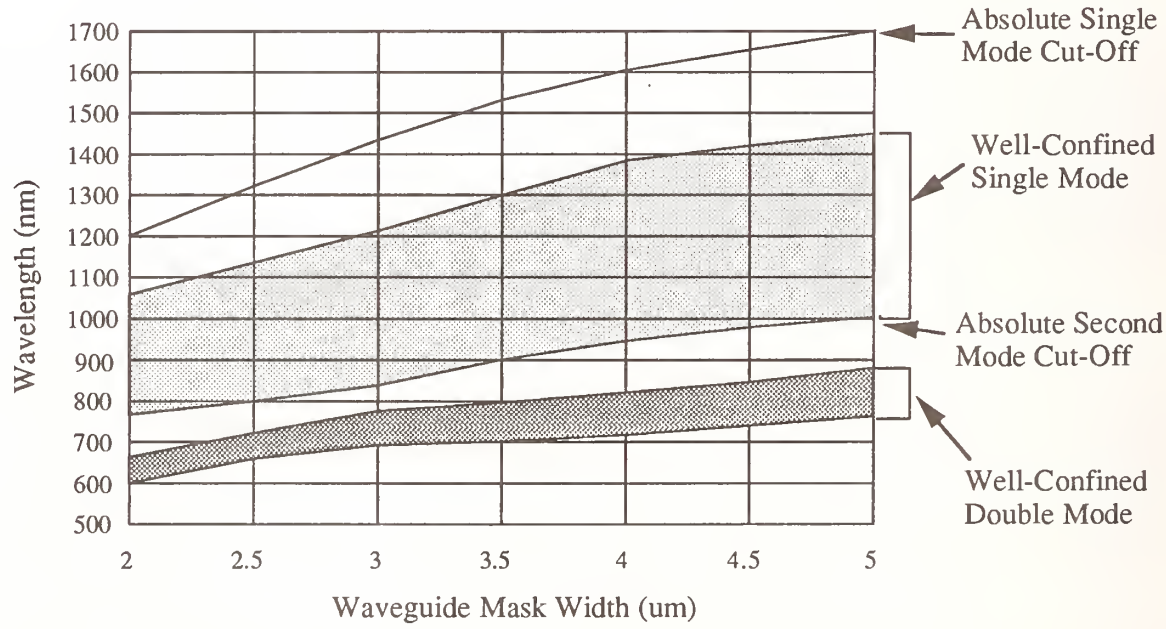

Fig. 4 Wavelengths of operation for single mode,multi-mode, and cutoff vs. mask dimensions for lithium niobate proton exchange guides fabricated with a 10 minute 200°C exchange and 2 hour 350°C anneal.

Frequency response measurements of integrated-optic electrodes

K. F. Hugenberg, P. D. Sargis, C. F. McConaghy
Lawrence Livermore National Laboratory

ABSTRACT

The frequency response of electro-optic waveguides can be determined using a variety of testing methods. In this paper, we compare and contrast three measurement techniques used to test our $LiNbO_3$ devices for improving packages and electrode designs. Each method is described and accompanied by typical results and the experimental setup. Finally, we summarize the advantages and disadvantages of each method.

1. INTRODUCTION

For the purpose of this paper, we use a Mach-Zehnder (MZ) device to demonstrate our measurement techniques for characterizing electro-optic devices. The operation of a Mach-Zehnder device is worthy of review.[1] The phase difference between the two waveguides can be electro-optically induced to form the familiar interference modulation curve. The lowest order mode is excited when the two arms are in phase at their recombination point, and this produces a maximum in intensity out of the device. The minimum of the curve arises when the two arms are 180 degrees out of phase. The recombination in this case excites the first antisymmetric mode or second-order mode which is cutoff. Consequently, the light radiates into the substrate and the transmitted light out of the device is a minimum. The output intensity of the MZ is expressed by:

$$I(t) = I_0 \cos^2\left(\frac{\pi V(t)}{2 V_\pi} m(f) + \frac{\phi}{2}\right) \qquad (1)$$

The function, m(f), represents the frequency dependence of the modulator. It includes the effects of mismatch between the optical and electrical velocities (i.e., walkoff)[1], the electrode's conductance, and other factors related to packaging.[2] V_π represents the half-wave voltage, and Ø/2 is the static phase imbalance in the arms of the interferometer.

2. FREQUENCY RESPONSE MEASUREMENTS

We use a traveling-wave[3,4] titanium-indiffused, lithium niobate Mach-Zehnder to demonstrate our measurement techniques. The electrodes consist of a 28-Ω coplanar strip transmission line having a strip width of 15 μm, a length of 3 mm, a gap width of 10 μm, and a gold-plating thickness of 4 μm. They are fabricated on a 0.2-μm oxide buffer layer to reduce metal loading losses. The rf input of the MZ device is interfaced to a 50-Ω Wiltron K connector using a 4-mm long coplanar taper transition. A 28-Ω termination resistor is included in the package design for impedance matching. The extinction ratio exceeds 20 dB, and the half-wave voltage (V_π) is 27 volts. The 1300 nm single-mode optical waveguides are fabricated on x-cut, y-propagating $LiNbO_3$ substrates.

It is well understood that the frequency response of a traveling-wave electrode design is limited by the optical and electrical velocity mismatch (or "walkoff"), and the frequency-dependent rf propagation loss.[5] We have found that knowledge of the frequency response, m(f) (see eqn. 1), provides very useful information for improving our packaging and electrode designs. We describe three techniques for measuring this parameter.

2.1. Swept-frequency method

In Fig. 1, a swept-frequency synthesizer is amplitude-modulated by a constant low-frequency sine wave. The magnitude of the envelope from the amplitude modulation is then detected using a slow-response detector and a lock-in amplifier. The analysis shows that if the optical bias and the driving source voltage are kept constant, then the rf frequency dependence of the low-frequency signal amplitude directly corresponds to the modulator response.[6]

The optical bias was set at the peak intensity point on the electro-optic transfer function throughout the measurement. The swept-frequency synthesizer was used to drive the rf input from 0.01 to 20 GHz. The rf power input to the modulator was 0 dBm and the repetition rate of the modulating sine wave signal was 5 kHz. The amplitude was kept much less than V_π to satisfy the small signal requirements. (Results are in Fig. 6 (a).) When the driving voltage amplitude is kept small, then the following applies to the optical intensity (I_d) on the detector[7]:

$$I_d \propto [m(f)]^2 \quad ; \text{m(f) refers to eqn. (1)} \qquad (2)$$

2.2. Network analyzer method

The second measurement technique uses a network analyzer. Its function is to compare the transmitted and received rf power as a function of frequency relative to a test or reference path, and it results in a direct measurement of the small-signal frequency response.[8]

The experimental setup is shown in Fig. 2. The optical bias was set in the linear region of the transfer function curve throughout the measurement. A 20 GHz InGaAs photodiode was used to convert the optical modulator output back to an electrical signal. The network analyzer was calibrated to measure the forward transmission coefficient (s_{21}) through the device over a frequency range of 0.045-20 GHz. The rf power at the input of the modulator was approximately –5 dBm. The effects of cables and connectors were eliminated in the calibration process by employing standard techniques for measurements with a network analyzer.

The network analyzer measures frequency response by generating a swept cw signal, and comparing the transmitted and received rf power at each frequency. It results in a transfer function plot with an accuracy of $\pm$ 0.1 dB. The photodiode frequency response was provided by the manufacturer and was subtracted from the result.

In addition to transmission magnitude (Fig. 6 (b)), the network analyzer also measures phase response. The linear component of the phase due to device transit time is removed from the measurement by entering a compensating electrical delay into the network analyzer. As plotted in Figure 3, the phase response slowly degrades as the frequency increases, but no sharp deviations are observed. Therefore, phase-related dispersion is minimal. If the phase response were poor, one could safely conclude that the device has a poor rise time.

2.3. FFT of the impulse response

The third measurement is performed in the time domain using a 15-ps step pulse.[5] An illustration of the experimental setup is shown in Fig. 4. The impulse response of the device is measured by driving the rf electrode with a fast electrical step pulse whose amplitude is much less than V_π (typically 25%). This amplitude is chosen to keep the optical output of the device in its linear region. We biased the device to about 75% of maximum on the transfer curve, and applied a negative-going step pulse having a fall-time of 15 ps and an amplitude of 5 volts (Fig. 5). The resulting optical step was converted using a 20-GHz InGaAs photodiode, and captured on a 50-

GHz sampling scope. The derivative of the input step was then deconvolved from the derivative of the measured output step to provide the true linear impulse response of the MZ. We obtained the result in Fig. 6 (c) by transforming the impulse response to the frequency domain, and subtracting off the photodiode frequency response.

3. SUMMARY

The swept-frequency system has two real advantages: 1) the measurement is insensitive to noise or stray rf signals because it uses a lock-in amplifier, and 2) the measurement is independent of the photodiode bandwidth because signal detection occurs at the 5-kHz modulating frequency. Due to the nature of this measurement, however, the phase response cannot be obtained. The network analyzer technique is the only one that yields usable phase information and a direct measurement of frequency response, rather than a calculated one. However, a disadvantage of this method is that its results cannot be properly transformed to the time domain, due to the finite-width frequency window used. The "FFT" method yields the actual time-domain impulse response of the device. Thus, the response of the device to arbitrary inputs in the linear region of its operating curve can be predicted. Due to the finite time window used to capture the impulse response, however, the FFT may introduce some low frequency errors. Furthermore, differentiation of the input and output waveforms contributes noise to the deconvolution process.

A summary of the advantages and disadvantages of each method is given in Table 1. All three techniques produce similiar results (Fig. 6) and can be used to improve packaging or electrode designs. For example, Fig. 7 shows how LLNL used such data to produce our current 1300 nm devices with much smoother and well behaved frequency responses while decreasing $V\pi$ to 10 volts.

4. REFERENCES

[1] R. C. Alferness, "Waveguide electrooptic modulators," IEEE Trans. Microwave Theory Tech., vol. MTT-30, No. 8, pp. 1121-1137, Aug. 1982.

[2] R. A. Becker, "Traveling-wave electro-optic modulator with maximum bandwidth-length product", App. Phys. Lett. 45, No. 11, pp. 1168-1170, Dec. 1984.

[3] M. Izutsu, Y. Yamame, and T. Sueta, "Broad-band traveling-wave modulator using a $LiNbO_3$ optical waveguide," IEEE J. Quantum Electron., Vol. QE-13, pp. 287-290, Apr. 1977.

[4] M. Izutsu, T. Itoh, and T. Sueta, "10 GHz bandwidth traveling wave $LiNbO_3$ optical waveguide modulator, " IEEE J. Quantum Electron., vol. QE-14, pp. 394-395, June 1978.

[5] S. K. Korotky and R. C. Alferness, "Time- and Frequency-domain response of directional-coupler traveling-wave optical modulators", J. Lightwave Tech., Vol. LT-1, No. 1, 244, pp. 244-251, Mar. 1983.

[6] S. Uehara, "Calibration of Optical Modulator Frequency Response with Application to Signal Level Control", Appl. Opt. 17, No. 1, pp. 68-71, Jan. 1978.

[7] K. Kubota, J. Noda, and O. Mikami, "Traveling wave optical modulator using a directional coupler $LiNbO_3$ waveguide", IEEE J. Quantum Electron., Vol. QE-16, No. 7, pp. 754-760, July 1980.

[8] S. K. Korotky, G. Eisentein, R. S. Tucker, J. J. Veselka, and G. Raybon, "Optical intensity modulation to 40 GHz using a waveguide electro-optic switch", App. Phys. Lett. 50, No. 23, pp. 1631-1633, June 1987.

Work performed under the auspices of the U.S. Department of Energy by Lawrence Livermore National Laboratory under Contract No. W-7405-Eng-48.

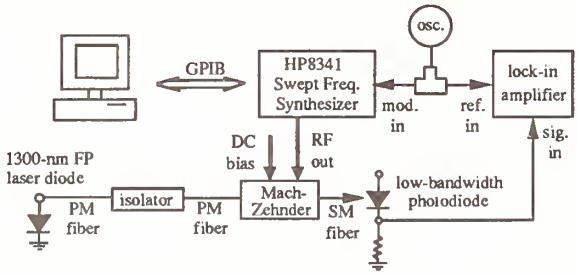

Fig. 1 Experimental setup for swept-frequency measurements.

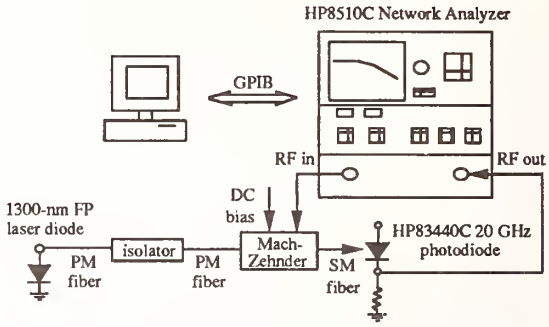

Fig. 2 Experimental setup for network analyzer measurements.

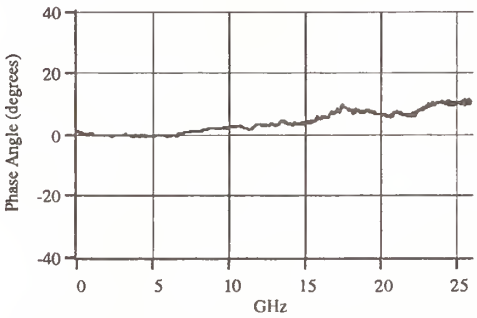

Fig. 3 Phase measurement of a device using the network analyzer.

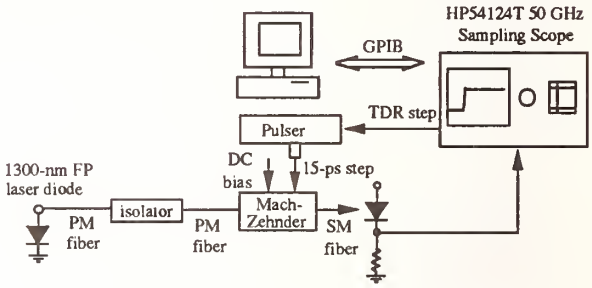

Fig. 4 Experimental setup for impulse response measurements.

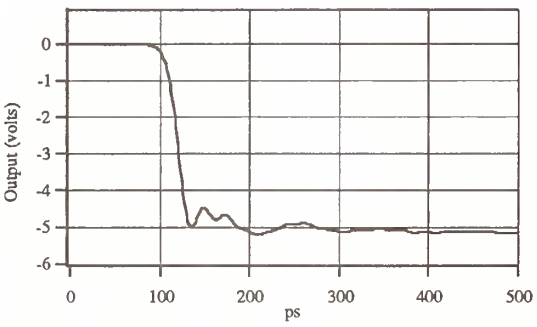

Fig. 5 Step pulse with 15-ps fall time.

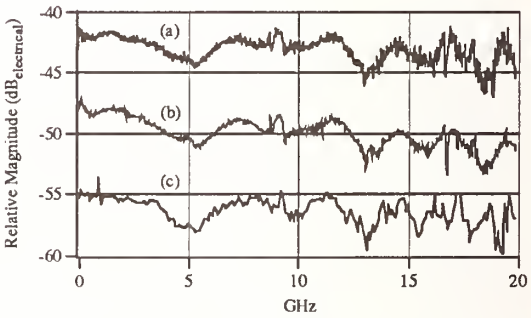

Fig. 6 Frequency response comparison using 3 different methods:
(a) Swept frequency
(b) Network analyzer
(c) FFT of impulse response

Table 1.
Summary of Methods

Method	Advantages	Disadvantages
Swept Frequency	Independent of PD Bandwidth	No Phase Info. No Deconvolution
Network Analyzer	Measures Magnitude & Phase	No Deconvolution
15-ps Step	Actual Impulse Response	Noisy FFT

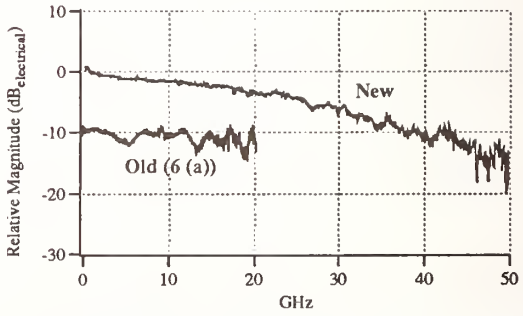

Fig. 7 Swept frequency response of a recent LLNL device with an improved electrode design.

FIBER DIAMETER FROM THE BACKSCATTERED LIGHT PATTERN

John Baines[1], Catherine Frehill[2], Ken Raine[1]

1 - National Physical Laboratory
Queens Road
Teddington
Middlesex TW11 0LW
UK

2 - School of Physical Sciences
Dublin City University
Glasnevin
Dublin 9
Ireland

ABSTRACT

We have used the method proposed by van der Mark & Bosselaar [1] to determine the diameter of single mode fibers from the backscattered light pattern. Measurements of the mean diameter of three fibers using this method agreed to 0.02μm with measurements using a scanning confocal microscope with interferometrically measured stage movement. A fourth fibre with large noncircularity demonstrates the limitation of the method.

BACKGROUND

Marcuse & Presby [2] investigated light scattered by optical fibers with arbitrary refractive index distributions. They found good agreement between measured light distributions and those predicted by scattering theory. They noted, however, that the observed backscattered pattern was extremely sensitive to changes in diameter and refractive index. The so-called inverse scattering problem, that of determining the properties of the scatterer from the observed scattering pattern, is complex. In the present case the backscattered pattern has periodic solutions which depend on both the diameter and the refractive index of the fiber. van der Mark & Bosselaar proposed observing the backscattered pattern at two wavelengths to remove the ambiguity due to uncertainty in the refractive index.

METHOD

All of the fibers measured here were single mode; van der Mark and Bosselaar have shown that the effect of single mode cores on the backscatter pattern is insignificant. The values for the fitted refractive index confirm earlier results [3] that the cladding index is raised during the fiber drawing process by about 0.000 4. For the dispersion from 543nm to 633nm we have used the known value for bulk silica. To remove the ambiguity caused by multiple solutions the approach we have used therefore is to assume the refractive index of the sample is known to within about 0.000 02 and the diameter is known to about 0.2μm.

Light from the laser was expanded then collimated and passed through a wedged beam splitter with low and high reflectance coatings on the front and rear surfaces respectively. The laser sources were plane polarized and in the experiment the plane of polarization was rotated using a half-wave plate. The fiber was perpendicular to the beam and backscattered light was reflected by the rear surface of the beam splitter onto a linear CCD array with 2048 pixels. The intensity profile across the backscatter pattern between about -5° and +15° was then digitized and stored on the computer. We measured backscatter patterns from four telecommunications

fibers with nominal diameters of 125μm at a wavelength of 633nm and two of these fibres at were also measured at 543nm.

We have calculated backscatter patterns using Bohren and Huffman's program [4] (modified by van der Mark) for fibers in the diameter and refractive index ranges shown in the table below and then searched by eye for the best fit between the observed and calculated patterns. The patterns were calculated for light with the plane of polarization parallel (p) and perpendicular (s) to the plane of incidence.

Laser wavelength	Diameter range (μm)	Refractive index range
633nm	124.0 - 126.0	1.457 2 - 1.457 6
543nm	124.0 - 126.0	1.460 0 - 1.460 5
Increment	0.01 μm	0.000 1

We found that it is essential to pay particular attention to minimizing stray reflections from the optical components and fittings. The wedged beam splitter, its coatings and the beam dump are also important to make sure the recorded backscatter pattern was not distorted.

RESULTS

We have compared the results from the backscatter method with measurements made at NPL using a scanning confocal microscope (SCM) [5] and also, for three of the fibers, at NIST using a contact micrometer [6]. The results at 633nm are shown in the table below together with the estimated uncertainty in the result. Note that fiber 4 was not measured by NIST.

Fiber #	Diameter (μm)	Refractive index	NIST Micrometer value (μm)	NPL SCM value (μm)
1	125.03	1.457 3	125.02	125.00
2	125.56	1.457 4	125.55	125.55
3	125.11	1.457 4	124.91	124.86
4	125.25	1.457 3	-----	125.25
Estimated Uncertainty (95%)	0.03μm	0.000 1	0.03μm	0.05μm

Fibers 1 and 2 were also measured at 543nm and the results are also shown in the table below.

Fiber #	Diameter (μm)	Refractive index
1	125.03	1.460 5
2	125.54	1.460 5

The values for the measured diameter are the means of the results obtained for the two polarization states. Since the fibers are elliptical rather than circular the results given are the means of measurements with the fiber at two orientations 90° apart.

DISCUSSION

The tables show that, except for fiber 3, the three methods show excellent agreement (less than 0.02μm). Fibers 1, 2 and 4 have low noncircularty (less than 0.3%) but that of fiber 3 is significant (about 0.8%). The SCM and micrometer results for this fiber differ by 0.05μm but the backscatter method measures about 0.2μm too high. For a constant refractive index the backscatter pattern almost repeats every 0.18μm at a wavelength of 633nm. Since the differences in the pattern between one solution and the next are subtle they can be masked by instrumental effects. It is therefore possible that the periodicity of the solutions can account for this result.

No fiber is exactly circular in cross section but deviations from circularity are nearly always elliptical. For all cases we have observed, as the fiber is rotated perpendicular to the collimated beam the backscatter pattern changes but is always symmetric about 0°. Note that the program assumes circular symmetry. However, the pattern at a given orientation seems to be the same as would be seen from a fiber with the same diameter as the projected diameter and so measurements on elliptical fibers can be made. The search procedure is simplified considerably if the diameter of the fiber is known within about 0.2μm. If a fibre has a noncircularity greater than one period in diameter space then an ambiguity may arise.

Because the fitting procedure by eye can be tedious and the goodness of fit is difficult to quantify one of us (Frehill [7]) has investigated using various techniques to automate the process and quantify the fitness of the solution. Genetic algorithms have proved suitable for efficiently solving complex optimization problems. They are highly parallel search procedures which follow simple rules to mimic the processes of evolution by natural selection to converge to an optimum solution. Preliminary results using noiseless test data show that, with a proper choice of fitting parameters, genetic algorithms can successfully search refractive index and diameter space to find the best fit to the backscatter pattern. Whether or not the method is practicable with real data remains to be seen.

CONCLUSIONS

We have implemented the proposal by van der Mark and Bosselaar to use the measured backscatter pattern to infer the diameter of optical fibers. With careful experimental design the

results obtained agree with other reference methods to less than 0.02μm for fibers with low noncircularity. The approach we have used requires that approximate values for the refractive index and diameter are known but these values are easily obtainable. The method is perhaps most suitable as an independent check of other methods used for calibration. The method has the advantage of needing no calibration other than the wavelength of the laser provided the refractive index is known. The four fibres we measured had an index within 0.000 05 of 1.457 35. Measurements at a second wavelength can be used to verify the diameter.

REFERENCES

[1] van der Mark, M. B., Bosselaar, L., "Fibre diameter calibration with 10nm accuracy potential", Conference Digest, OFMeC / COST 217 Conference on Optical Fibre Measurements held at York, England, September 1991, pp 147 - 150.

[2] Marcuse, D., Presby, H. M., "Light scattering from optical fibers with arbitrary refractive index distributions", J. Opt. Soc. Am., vol 65, no 4, pp 367 - 375, 1975.

[3] Raine, K. W., Baines, J. G. N., King, R. J., "Comparison of refractive index measurements of optical fibres by three methods", IEE Proc, vol 135, part J, no 3, pp 190 - 195, 1988.

[4] Bohren, C. K., Huffman, D. R., "Absorption and scattering of light by small particles", Wiley Interscience, New York, Appendix C, 1983.

[5] Collyer, A., Raine, K. W., Baines, J. G. N., "Investigation into the use of a scanning confocal microscope as a primary method for determining optical fibre diameter", Conference Digest, OFMeC / COST 217 Conference on Optical Fibre Measurements held at York, England, September 1991, pp 143 - 147.

[6] Young, M., Hale, P. D., Mechels, S. E., "Optical Fiber Geometry: Accurate Measurement of Cladding Diameter", J. Res. Nat. Inst. Stds. Tech., vol 98, no 2, pp 203 - 216, 1993.

[7] Freehil, C., "Backscatter Analysis using Genetic Algorithms", Final Year Report, Dublin City University, Ireland, 1994.

ACKNOWLEDGEMENTS

The authors would like to thank Martin van der Mark of Philips Research, Eindhoven for suggesting this work and providing the software to calculate the backscatter patterns. We would also like to thank Matt Young of NIST for permission to use the micrometer data.

FIBER GEOMETRY: RESULTS OF AN INTERNATIONAL INTERLABORATORY MEASUREMENT COMPARISON

Timothy J. Drapela, Douglas L. Franzen, and Matt Young

United States Department of Commerce
National Institute of Standards and Technology
Mail Stop 814.02, 325 Broadway, Boulder, CO 80303-3328

Improvements in technology have led to a tightening of tolerances for optical fiber geometrical parameters. This, in turn, has led to the need for improved measurement accuracy. Of the geometrical parameters, cladding diameter accuracy has been technically the most difficult to improve. Accuracy on the order of ±0.1 μm is needed for the industry to comfortably meet specified tolerances of ±1.0 μm.

In order to compare results with previous interlaboratory comparisons, we report average measurement spread per fiber, for each measured parameter. We obtain this number, for a given parameter, by first calculating the sample standard deviation for each fiber. We then calculate the arithmetic average of these standard deviations. Although this is not a statistically valid overall measurement spread, it does give an indication of the relative agreement among participants.

In 1989, the Consultative Committee on International Telegraph and Telephony (CCITT, now the International Telecommunication Union - ITU) completed and reported on an international interlaboratory comparison of fiber geometry measurements.[1] The average measurement spread per fiber for mean cladding diameter was 0.38 μm and deemed to be unacceptably high. Each participant received a separate set of fiber specimens, so measurements were not made on the same fiber ends. Longitudinal nonuniformity could have therefore influenced the results. The high measurement spread pointed to the need for all measurements to be made on the *same* cleaved fiber ends and also to the desirability of some type of calibration artifact.[2]

In North America, a second interlaboratory comparison was coordinated by the National Institute of Standards and Technology (NIST) for the Telecommunications Industry Association (TIA) and reported on in 1992.[3] Participants serially measured the same cleaved fiber ends, which could be retracted into an aluminum housing for protection between measurements and during shipping. These housings use a brass barrel that is moved to extend or retract the fiber and is marked to identify the angular orientation of the fiber. The housed fiber specimens became the basis for the NIST calibration artifact or Standard Reference Material (SRM), which became available to the industry in late 1992.[4]

The average measurement spread per fiber for mean cladding diameter measurements in the 1992 comparison improved to 0.15 μm. There were also reductions in the measurement spreads of the other measured parameters: cladding noncircularity and core/cladding concentricity error. Participants' cladding diameter measurements were also compared to measurements made by the NIST contact micrometer, which is the measurement method for characterization and certification of the SRMs. The contact micrometer is accurate within ±0.045 μm (3 standard deviations) for mean cladding diameter measurements on the housed specimens.[5] The cladding diameter measurement spread observed in the 1992 study was largely due to systematic differences between participants, and further improvement in this spread was anticipated with the use of calibration artifacts such as the NIST SRMs.

The present ITU international comparison was administered by NIST, with help from regional coordinators in Europe and Japan. Housed fiber specimens were again used. Because the housed fibers could become damaged with repeated shipping, and in order to complete this comparison in a reasonable time, three sets of specimens were prepared for three different regions: North America (A), Europe (E), and Pacific (P). Each set contained seven housed fiber specimens, including both very nearly circular and noncircular (up to 1.5 %) fibers. All fibers were measured by the NIST contact micrometer, to allow for inter-regional comparison. As of this writing, twenty-two participants have reported results; the number

should approach thirty by completion of the comparison. Of the current twenty-two, twenty used the gray scale measurement method,[6] and two used image shearing.[7] Of the gray scale participants, three used home-made test sets, while the others used commercial test sets from three different commercial vendors.

Table 1 shows the average measurement spreads per fiber, for each of the three measured parameters, for the present as well as the previous comparisons. It also breaks down the present results into the three regions. With the use of the housed fiber specimens, the spreads for cladding noncircularity and for core/cladding concentricity error have improved significantly for all three regions since the 1989 comparison. In North America, where the NIST SRMs are in widespread use for calibration, the average spread per fiber for mean cladding diameter measurements has again improved, to 0.08 μm. The European and Pacific spreads remain higher, both at ≥0.30 μm, although both deserve qualification. In Europe, many of the participants are now calibrated to the National Physical Laboratory (NPL) in the United Kingdom, through a program similar to the NIST SRMs,[8] involving either fiber or chrome-on-glass artifacts. If we include data from only those participants, the European spread improves to 0.07 μm. In the Pacific, only two Japanese participants are calibrated to a national standards laboratory, by use of fibers certified by the Japanese Quality Assurance Organization (JQA). Furthermore, a couple of Pacific participants (including one of the above-mentioned calibrated Japanese participants) reported compatibility problems between the fiber housings and their test sets, so they could not easily and confidently measure the housed fiber specimens. In a separate comparison, on three different non-housed fiber specimens measured by the NIST contact micrometer and the Pacific participants, a corresponding spread of roughly 0.11 μm was obtained. Also, while virtually all data from North American participants have been received, there are several European and Pacific participants, from whom we anticipate data, who have not yet received or measured the comparison fibers.

Figure 1 shows the cladding diameter results for the present comparison, as a plot of offsets from NIST contact micrometer values versus participant. Up to seven points are plotted per participant, representing the seven fibers in each set of measurement specimens. The participants are grouped by region. Filled-in circles show gray scale participants who are calibrated by means of a NIST SRM. Filled-in squares show gray scale participants who are calibrated to NPL. Filled-in diamonds show gray scale participants who are calibrated to JQA. Open stars show gray scale participants who reported compatibility problems between their test sets and the fiber housings. Other gray scale data are denoted by open squares. Open triangles denote the two participants who used the image-shearing method. This graph clearly shows that those participants who are calibrated to one of the national standards laboratories are usually in better agreement than those who are not; in some cases, the improvement is nearly an order of magnitude. Agreement generally appears to be just as good for noncircular fibers as for circular ones. One unexplained observation, presently under study, is that most of the participants calibrated to one of the national standards laboratories have positive offsets from the NIST contact micrometer. In other words, they systematically measure slightly higher than the contact micrometer.

Two other meaningful quantities can be calculated from the statistics of these measurement offsets. For each participant, an average offset (average of the seven plotted offset values) can be calculated, as can the standard deviation of the seven offset values about that average. The average offset indicates systematic offset from the NIST contact micrometer, and when compared to the same quantity for other participants, it indicates the extent of systematic disagreement between them. The magnitude of this quantity can be minimized by calibration. The second quantity, the participant offset standard deviation or offset spread, is a reflection of, among other things, the participant's random uncertainty; this value would not be expected to improve with calibration. For most of the participants who are not calibrated to one of the national standards laboratories, the absolute values of their average offsets, what we call their offset magnitudes, are greater than their offset spreads. Such participants could be anticipated to benefit significantly from calibration. All participants who are calibrated to one of the national standards laboratories have offset magnitudes of ≤0.16 μm, and all but three have <0.1 μm.

Table 2 shows the average participant offset magnitude and average participant offset spread from the present comparison: overall, broken down into the three regions, and for only those participants who are calibrated to one of the national standards laboratories. The same numbers from the 1992 TIA North American comparison are also shown. In North America the average offset magnitude has reduced from 0.114 μm in 1992, when there were no SRM calibrations, to 0.073 μm in the present comparison in which nearly all of the North American participants are calibrated by means of SRMs. The European average offset magnitude is somewhat higher, apparently due to the few European participants who are not calibrated to NPL. If we include only those who are calibrated to NPL, the number reduces to 0.071 μm. The average offset magnitude is also higher in the Pacific, where only a couple of participants so far are calibrated to any national standards laboratory. Again, the higher average offset spread in the Pacific is likely due to those test sets that had difficulty measuring the housed fiber specimens.

In conclusion, this comparison shows better agreement among participants, for all three fiber geometry parameters, than did the 1989 comparison. Where there are substantial disagreements, they seem to be systematic; this was not always the case in the 1989 comparison, where there was more random spread in the data. Those participants whose test sets are calibrated to one of the national standards laboratories, through calibration artifacts, generally show significantly better agreement.

ACKNOWLEDGMENTS

Thanks to: all participating laboratories in the United States, Canada, United Kingdom, France, Italy, Finland, Netherlands, Sweden, Japan, and Australia; to John Baines of NPL for coordinating and overseeing the European measurements and to Masaharu Ohashi of NTT for coordinating and overseeing the Japanese measurements; to Bill Kane and Tom Hanson at Corning, Inc. for keeping us aware of ITU goals and deadlines and for reporting the results; to Casey Shaar of Photon Kinetics for providing the prototype design of the fiber specimen housings; to Steve Mechels of NIST for his expert end-preparation on the measurement specimens.

REFERENCES

1. CCITT Study Group XV, "Results of a Round-Robin Study into Measurement of the Geometrical Properties of Single-Mode Fibres," September, 1989.

2. John G. N. Baines, Andrew G. Hallam, Ken W. Raine, and Nick P. Turner, "Fiber Diameter Measurements and Their Calibration," *J. Lightwave Technol.*, vol. 8, no. 9, pp. 1259-1267, September, 1990.

3. Timothy J. Drapela, Douglas L. Franzen, and Matt Young, "Single-Mode Fiber Geometry and Chromatic Dispersion: Results of Interlaboratory Comparisons," *Technical Digest: Symposium on Optical Fiber Measurements, 1992*, Nat. Inst. Stand. Technol. Spec. Publ. 839, ed. by G. W. Day and D. L. Franzen, pp. 187-190, September, 1992.

4. National Institute of Standards and Technology, Standard Reference Material Program, Bldg. 2, Rm. 204, Gaithersburg, MD 20899; (301) 975-6776. Refer to SRM 2520, Optical Fiber Diameter Standard.

5. Matt Young, Paul D. Hale, and Steven E. Mechels, "Optical Fiber Geometry: Accurate Measurement of Cladding Diameter," *J. Res. Nat. Inst. Stand. Technol.*, vol. 98, no. 2, pp. 203-216, March-April, 1993.

6. Fiberoptics Test Procedure FOTP-176, "Method for Measuring Optical Fiber Cross-Sectional Geometry by Automated Grey-Scale Analysis," Telecommunications Industry Association - Electronic Industries Association, 2001 Pennsylvania Avenue, NW, Washington, DC 20006.

7. M. J. Downs and N. P. Turner, "Application of Microscopy to Dimensional Measurement in Microelectronics," *Proc. Soc. Photo-Opt. Instrum. Engrs.*, vol. 368, Microscopy-Techniques and Capabilities, pp. 82-87, 1982.

8. J. Baines and K. Raine, "Review of Recent Developments in Fibre Geometry Measurements," *Technical Digest: Symposium on Optical Fiber Measurements, 1992*, Nat. Inst. Stand. Technol. Spec. Publ. 839, ed. by G. W. Day and D. L. Franzen, pp. 45-50, September, 1992.

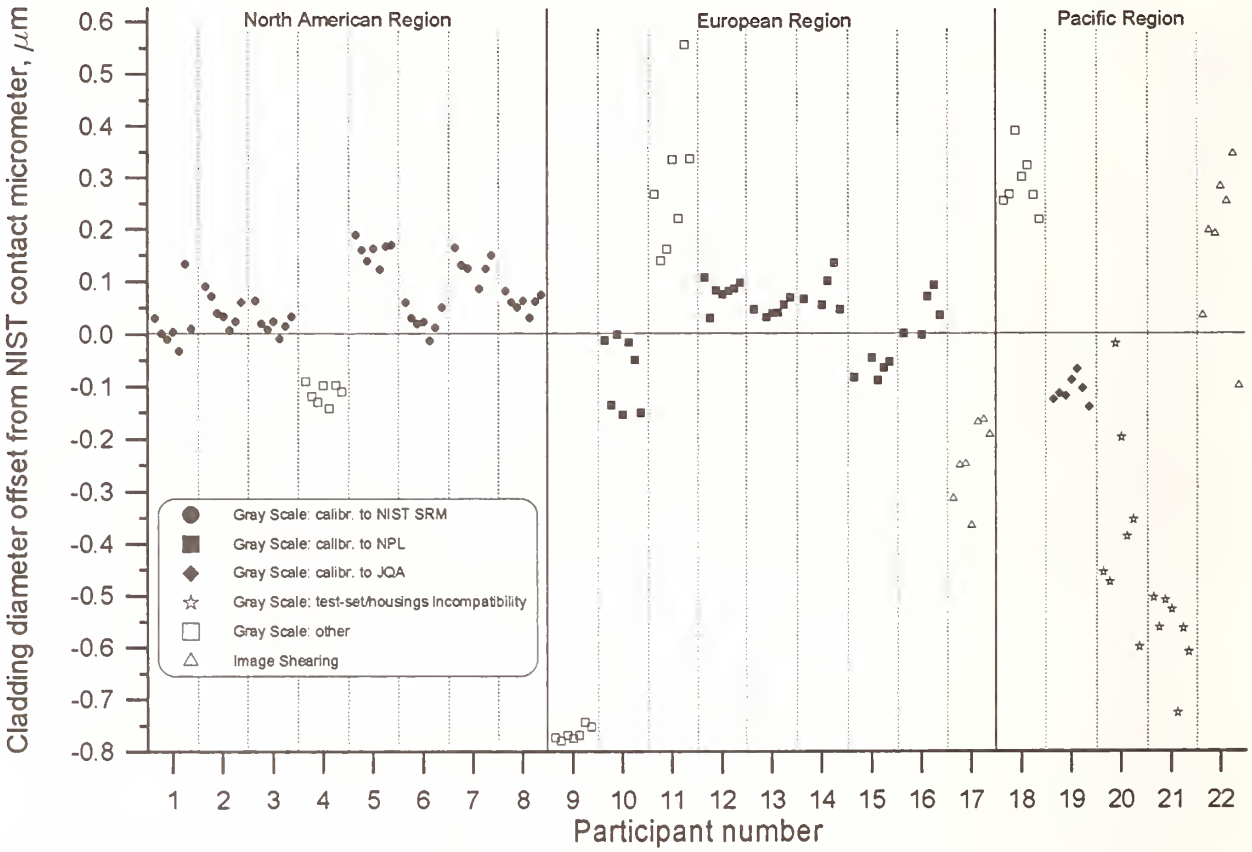

Figure 1 Offsets of participants' mean cladding diameter measurements from NIST contact micrometer. Up to seven points plotted, for each participant, represent the seven fibers in the measurement samples.

Average Measurement Spreads per Fiber			
	Cladding Diameter, μm	Noncircularity, %	Concentricity Error, μm
'89 CCITT Comparison	0.38	0.27	0.17
'92 TIA (North American) Comparison	0.15	0.05	0.04
Present Comparison	0.24	0.09	0.08
"A"	0.08	0.05	0.06
"E"	0.30	0.11	0.12
"P"	0.33	0.12	0.07

Table 1 Average measurement spreads per fiber (arithmetic average of standard deviations for each of the fibers), for all three measured parameters, for the current comparison, as well as past comparisons. Current results are also broken down by region: North America (A), Europe (E), and the Pacific (P).

Average Statistics for Participants' Cladding Diameter Offsets from NIST Contact Micrometer		
	Average Offset Magnitude, μm	Average Offset Spread, μm
'92 TIA (North American) Comparison	0.114	0.032
Present Comparison	0.171	0.052
"A"	0.073	0.027
"E"	0.188	0.048
"P"	0.299	0.101
those calibrated to nat. standards labs (all regions)	0.069	0.030

Table 2 Average cladding diameter offset statistics per participant for current comparison (overall, regional, and only those calibrated to national standards laboratories) and '92 North American comparison. Average offset magnitude is the average of the absolute values of participants' average offsets from NIST contact micrometer. Average offset spread is the average of the Participants' standard deviations about their average offsets.

Contact and non-contact interferometry for optical fiber diameter measurement and calibration

Claude Brehm, Olivier Mercereau, Geneviève Lipinski *, George Pierre Vailleau *.

Alcatel Alsthom Recherche UFP, route de Nozay 91460 Marcoussis, France
* LNE Laboratoire National d'Essais, 1 rue Gaston Boissier 75015 Paris France

Introduction

• Fiber outside diameter measurements must be made on-line during fiber drawing in order to be as close as possible from the nominal value of 125 µm on the whole fiber length.
On-line measurement techniques which are typically used in fiber manufacturing units are laser scanning fiber shadow equipments. These are very reliable and quite convenient for a close-loop control on capstan speed during fiber drawing. However they show two main drawbacks :
- 1) they are quite slow and cannot detect localized fiber diameter variations at high drawing speed.
- 2) calibration is made with metallic wires which are known with a limited accuracy (125 ± 0.2 µm) and give a systematic discrepancy with fiber end cut measurement.
Therefore a dynamic-interferometry device for high speed measurement of fiber diameter fluctuation has been promoted and a new non-contact interferometry static measurement device has been build and tested [1].
This second equipment can be used to characterise standards for the calibration of dynamic interferometer and other diameter measurement devices.
The purpose of this presentation is to describe more extensive tests which have been made both in Alcatel Alsthom Recherche and in Laboratoire National d'Essais (LNE) where a comparison with contact interferometry measurements has also been made .
Contact interferometry for fiber diameter measurements has already been described and compared by various laboratories such as NIST [2], NPL [3], and Corning [4].

Contact interferometry for measurement of outside diameter of optical fiber

• Principle of measurement
Our investigations concerning the choice of a principle of measurement for the determination of outside diameter of optical silica fiber lead us to select a measuring method allowing a direct traceability to the definition of the meter.
The method is based on an interferometric technique using the fringe fraction measurement. A Michelson interferometer lighted by two stabilised He-Ne laser sources : a green one (λ= 543 nm) and a red one (λ= 633 nm), which was used for the calibration of gauge blocks, has been modified to measure the diameter of small cylinder. The fiber is inserted between two gauge blocks of 10 mm of nominal length. The lower gauge is wrung on one of the metallic optical flat mirror of the Michelson interferometer. The upper gauge block is supported by a small sphere and by the fiber (along a generating line). The parallelism of the upper gauge with the optical mirror is ensured by vertical motion of the supporting sphere induced by piezo actuators.
The interferential image is composed by two fringe patterns, one is produced by the reflection on the surface of the upper gauge and the second is produced by the reflection on the mirror. A CCD camera digitalize this image and an image processor gives the fringe fraction. The length of the two gauges has been measured previously with the same method. The assembly composed by the gauges and the fiber is then measured [$h = (h_1 + h_2) / 2$] and the fiber diameter is deduced (figure 1 side and top views).

• First results and estimation of measuring uncertainty.
This method allows to measure a mean outside diameter on a fiber length of 9 mm.
It is also possible to repeat measurement, after rotation of the fiber around its axis, in order to estimate fiber non-circularity. This contact method is independent of optical parameters of the fiber.
The measuring uncertainty has been estimated by using the method described in the guide to the expression of uncertainty in measurement, recently published by ISO
The different sources of uncertainty have been considered as independent, so that the combined uncertainty is : u_c =47 nm (see table 1) and the expanded uncertainty, with a covering factor of k = 2 is : U = ± 94 nm.
The analysis of different sources of uncertainty shows that the main component is repeatability. It is estimated by the standard deviation of a set of successive measurements after rotation of the fiber on its axis. It is mainly limited by two factors : the repeatability of the measuring process itself and the geometrical defects like fiber non-circularity. Presently the main limiting factor for the uncertainty is the geometrical quality of the fiber which is now being improved.

Non-contact interferometry : scattering pattern from a side-illuminated optical fiber.
• As shown in figure 2, two rays are involved, R_e reflected at the fiber surface and T refracted into the fiber. These two rays do not have the same incident angle i, therefore interference appears. If D is the fiber diameter, θ the scattering angle and n the refractive index of the fiber, the optical path difference, ∂, is :
$\partial = D. (\sin \theta/2 + (n^2+1-2n \cos \theta/2)^{1/2})$.
Between two scattering angles the number of interference fringes is only dependent on the fiber refractive index and on the fiber diameter. This gives a direct measurement of the fiber diameter if the fiber index is known.
For single-mode fibers the core diameter is less than one tenth of the fiber outside diameter and therefore the core-cladding index difference has no effect in the scattering angle range used for measurement, i.e. θ between 10 and 80° .
• A schematic layout of the measuring equipment is shown in figure 3. The beam of polarised He-Ne laser is focused on the fiber which is placed at the center of a goniometer. Polarisation and fiber axis have the same direction. The scattering pattern is focused on the photo detector which is set on a motor-driven rotation stage. A crossed polarizor is placed in front of the photo detector to avoid saturation in the direction of incident ray. Measurement is made on a fiber height of 100 µm. Power data is collected every 0.01° for the determination of fringe pattern limits and every 0.03° for fringe counting. Averaging is done on 2000 sample points at 20 kHz. Measurement accuracy then is better than 0.1 µm.

Comparative measurements
• Measurements have been made on a typical single-mode fiber, repeatability is less than 10 nm (1standard deviation). Five successive sets of 100 measurements on a 10 mm fiber's height have been made, each one after a rotation of 72° of the fiber on its axis (mean value : 125.13 µm). The data, minimum and maximum values for each angle, is gathered on figure 4; it shows a fiber non-circularity close to 0.2 µm. These data are consistent with diameter measurements made by fiber end cut with a York S 20 grayscale optical microscope system (mean value : 125.14 µm). They are also very consistent with measurements made at the French National Standard Laboratory (L.N.E.) with a two wavelength Michelson interferometer (mean value : 125.14 µm). Here also, measurement repeatability is low, due to the fiber non-circularity
• A fiber with a lower non-circularity has been taken for a second set of comparative measurements Data are shown on figure 5. Fiber non-circularity has been check with the two interferometric methods by rotating the fiber on its axis in 5 different directions, it is then close to 0.05 µm. Mean values are 124.90 µm with contact interferometry (LNE) and 124.81 µm with non-contact interferometry.

Conclusion

• Data about outside diameter, obtained out of pieces of the same fiber close from one to another, are very similar and in the range of uncertainty. Slight geometrical imperfection mainly non-circularity, remaining in the fiber tested, is still limiting measurement uncertainty. Better quality fiber could be useful for an even more accurate comparison of these two measuring techniques.

• For measurement of outside diameter of optical fiber, interferometry with two mechanical contacts is the only method to reach a high accuracy without any need of data about the effective refractive index of the fiber under test. Presently the main limiting factor for the uncertainty is the geometrical quality of the fiber, such as surface defects and non-circularity. Length of the mechanical contact which is presently of 9 mm could also be reduced to improve the measurement accuracy.

• The non-contact static interferometry equipment has the ability to become, in each fiber producing unit, a secondary standard maker for a more accurate calibration of various fiber diameter measurement devices. Silica fiber of appropriate dimension can be used for the calibration of various laser scanning shadow measuring heads instead of metallic calibration wires.

Acknowledgements.

The authors would like to thank H. Gagnaire (Universite de St Etienne), G. Orcel, P. Darbon, P. Dupont (Alcatel Fibres Optiques), B. Minvielle (Alcatel Alsthom Recherche).

References

[1] C. Brehm, P. Darbon, B.Minvielle, H. Gagnaire "New technique for optical fiber outside diameter measurement and calibration" IWCS 1993 pp 817-821

[2] M. Young, P. Hale, S.Mechels "Accurate measurements of fiber cladding diameter" Symposium on optical fiber measurements 1992 pp 55-58.

[3] J. Baines, K. Raine " Review of recent developments in fiber geometry measurements" Symposium on optical fiber measurements 1992 pp 45-50.

[4] K.A. Emig "A comparison of interferometric techniques for fiber cladding diameter measurements" Fiber and integrated optics 1990 vol.9 pp 375- 379.

Sources of uncertainty	Value of stondord uncertointy u(xi)
A 1 : Repetobilty	45 nm
B 1 : Air wavelength	2 nm
B 2 : Wringing effect	1.7 nm
B 3 : Fringe fractian	1.7 nm
B 4 : Phase carrectian	3,3 nm
B 5 : Optical defect of the interferometer	3.3 nm
B 6 : Carrectian of the exponsion	4.6 nm
B 7 : Expansion caetficient	2.7 nm
B 8 : Fiber compression	1.4 nm
B9 : Length of the upper gouge	6 nm
B10 : Length af the lower gauge	6 nm
B 11 : Lacal flatness of gauge blacks	8 nm

Table 1

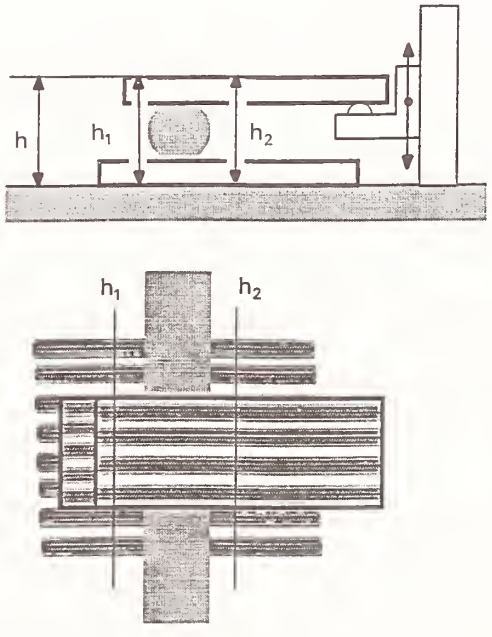

Figure 1 : Fiber O.D. contact interferometric technique used at LNE.

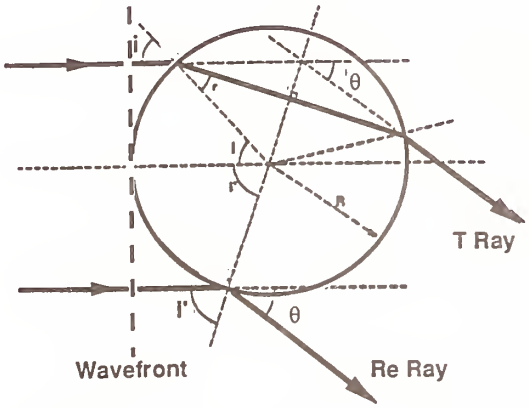

Figure 2 :
Fiber cross-section : optical path difference between two rays Re and T scattered in the same direction

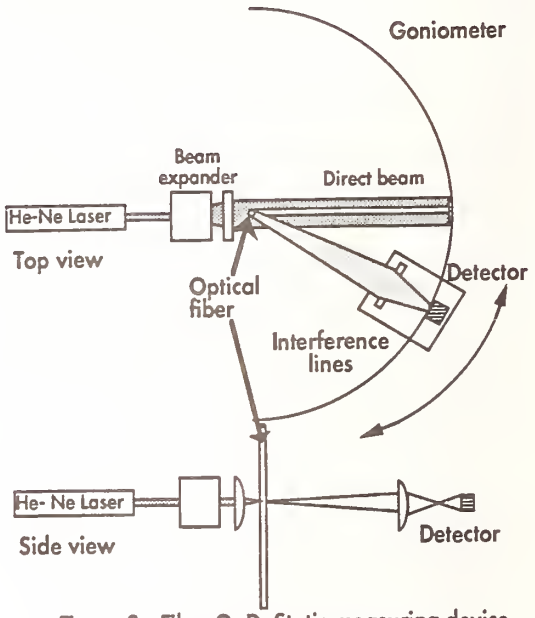

Figure 3 : Fiber O. D. Static measuring device based interference analysis

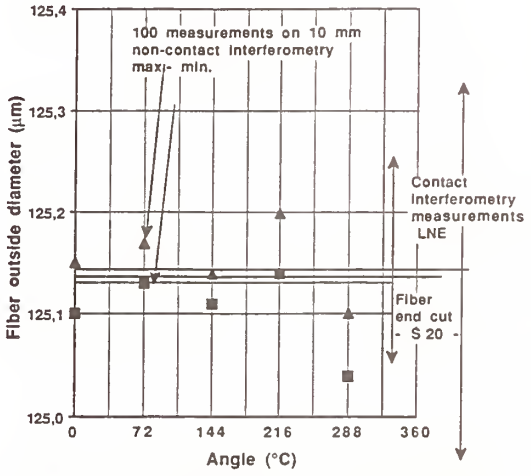

Figure 4 : O.D. meosurements on the some fiber
- by end cut (York 520)
- by contoct interferometry (LNE)
- by non contoct interferometry with 5 rototion ongles of the fiber on its oxis

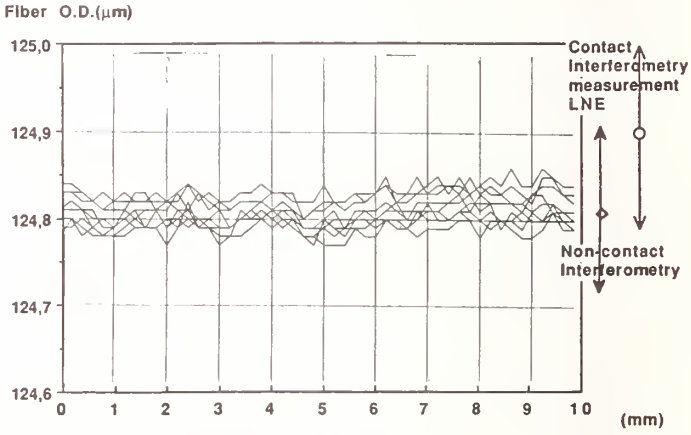

Figure 5 : O.D. measurements on the same fiber
- by non contoct interferometry
  (each 0.2 mm on o 10 mm fiber length, i. e. 50 points
  ond with 9 rototion ongles of the fiber on its oxis, i. e. o totol of 450 points)
  meon volue : 124.81 µm - minimum : 124.77 µm - moximum 124.86 µm
- by contoct interferometry (LNE) on o 9 mm fiber length
  meon volue : 124.90 µm - non-circulority ~ 0.05 µm

Light Scattering Fiber/Coating Eccentricity Measurements for Thin Coatings

D. H. Smithgall

AT&T Engineering Research Center
Box 900
Princeton, New Jersey 08542-0900

I. Introduction

The concentricity of 125 μm fiber in a typical 250 μm polymer coating is determined by measuring the symmetry of a forward scattered light pattern, which appears as a well-defined bright bar, about an illuminating laser beam [1]. The distinct edge to this bright pattern results from the concentration of light near the fiber/coating interface. As the ratio of coating diameter to fiber clad diameter decreases, the pattern width increases and the contrast decreases until for coating diameters below 185 μm the bright bar pattern is no longer distinguishable.

The lack of concentrated light energy in the scattering patterns produced by thin coatings results in the emergence of an interference pattern produced by light refracted through the coated glass and light reflected from the surface of the coating. This pattern corresponds to that used to measure clad fiber diameter [2]. Since all of the refracted light passes through the fiber, the interference pattern will be influenced by fiber eccentricity, as well as refractive index and coating diameter. Thus, a measure of fiber eccentricity is available by comparing the fringe patterns on either side of the optical axis.

II. Ray Trace Model

Referring to Figure 1, a fiber which is eccentric within the polymer coating can be modeled as two concentric circles with the center of the fiber offset from the center of the coating a distance, d, at an angle, ϕ, with respect to the optical axis. The diameter of the fiber is 2a and the diameter of the coating is 2b. Assume that this structure is uniformly illuminated by a collimated coherent laser beam. The intensity of the forward scattered light pattern at any given angle, θ, results from the interference of light refracted through the structure and light reflected from the surface of the coating. When the outer layer of this structure is much larger than the center circle, some light passes only through this outer layer, and the diameter of this outer layer can be determined by a simple expression [3]. In addition, the eccentricity of the fiber can be determined from light which passes through both the fiber and coating, projecting a bright bar into the forward scattered pattern [1]. When the coating is thin, eg. $a/b > 1/n$, all light passes through the fiber, and only the forward scattered interference pattern exists.

Referring to Figure 1, the eccentricity of the fiber within the coating can be described in terms of an offset amplitude, d, and orientation with respect to the optical axis, ϕ. The path of a light ray refracted through this structure is determined from the equations:

$$x = \sin(\alpha_0) = n \sin(\alpha_1) \qquad 0 < x < 1 \tag{1}$$

$$\gamma_1 = \sin(\alpha_2) = (b \sin(\alpha_1) - d \sin(\alpha_0 - \alpha_1 + \phi)) / a \tag{2}$$

$$\gamma_2 = n\,\gamma_1 / n_g \tag{3}$$

$$\sin(\alpha_5) = n\,\sin(\alpha_4) = (\,a\,\sin(\alpha_2) + d\,\sin(\alpha_0 - \alpha_1 + 2\,(\,\alpha_2 - \alpha_3\,) + \phi\,))\,/\,b \tag{4}$$

When the fiber is slightly eccentric, eg. when d/b << 1, γ_1, γ_2, and (4) are all less than 1, and the refracted ray scattering angle is

$$\theta = \alpha_0 - \alpha_1 + \alpha_5 - \alpha_4 + 2\,(\alpha_2 - \alpha_3)\ . \tag{5}$$

The reflected ray which scatters at the same angle, θ, is described by

$$\theta = \pi - 2\,\beta_0 \tag{6}$$

The optical path lengths of the two rays between two planes normal to the entrance and exit paths are determined for the refracted ray by:

$$q_0 = b\cos(\alpha_1) - a\,\cos(\alpha_2) + d\,\cos(\alpha_0 - \alpha_1 + \phi) \tag{7}$$

$$q_2 = b\,\cos(\alpha_4) - a\,\cos(\alpha_2) - d\,\cos(\alpha_0 - \alpha_1 + 2(\alpha_2 - \alpha_3) + \phi) \tag{8}$$

$$p_1 = n\,(q_0 + q_2) + n_g\,2\,a\,\cos(\alpha_3)\,, \tag{9}$$

and for the reflected ray by:

$$p_2 = b\,(\cos(\alpha_0) - \cos(\beta_0)) + b\,(\cos(\alpha_5) - \cos(\beta_0)) \tag{10}$$

If two angles are selected in the forward light scattering region, θ_a and θ_b, then the number of interference fringes, N, between these angles is

$$N = (\Delta_b - \Delta_a)\,/\,\lambda\ , \tag{11}$$

where λ is the wavelength of the incident radiation, and each Δ is the optical path length difference, $p_1 - p_2$, at each angle.

When two identical angle ranges are selected, symmetric about the optical axis of the incident laser beam, the difference in the number of fringes $N^+ - N^-$ depends upon the amplitude and orientation of the fiber/coating offset, since the clad and coating diameters and material refractive indices are identical for both angle ranges.

As an example of the model-predicted results, consider a 125 μm fiber, coated with a 170 μm diameter polymer coating. The refractive indices of the fiber and coating are 1.4571 and 1.54, respectively, at the HeNe laser wavelength of 0.6328 μm. Figure 2 illustrates the fringe pattern differences in the angle range θ_a = 38° to θ_b = 52°.

In order to test this method of measurement, a fiber sample was mounted in a test apparatus, which is described in Section III. Fringe measurements in the range 38° - 52° on either side of the optical axis were made for 9 angular orientations of the fiber. Computing the maximum fringe difference from the data, and comparing to the modeled results in Figure 2 predicted a 5 μm eccentricity. The fiber sample was also measured by immersing the sample in index matching fluid and using a microscope filar eyepiece to measure the maximum side wall

variation. These readings differed 6 and 5 μm from the nominal 22.5 μm concentric wall thickness, which is comparable to the light scattering measurements, within the microscope measurement accuracy.

III. Implementation

Figure 3 illustrates the arrangement of components used to measure the differential fringe patterns. The coated fiber is orthogonally illuminated by a HeNe laser beam, such that scattering patterns of substantially equal intensity are generated on each side of the optical axis. The detectors are arranged symmetrically about the optical axis.

Each detector section comprises a lens which images the scattering pattern onto a line scan array, located in the back focal plane of the lens. When properly aligned, the detected pattern is stationary for axial and lateral movement of the coated fiber. The focal length and f/# of the lens determine the image size, the distance from the fiber to the lens and the window within which the fiber may be located without affecting measurement accuracy.

The output from each diode array is a sample-hold boxcar signal, scanned from the array at a rate of 1000 images per second by the detector electronics circuit. The two fringe patterns are separately processed in circuits which measure the total number of fringes, or equivalently the total phase in the fringe patterns in the fixed angle range defined by the line scan detector [3].

V. Summary

A technique has been developed to measure fiber/coating eccentricity in thin coated fibers using forward light scattering. It has been used for in situ process control, with average eccentricities less than 3.5 μm over multikilometer lengths of fiber.

Acknowledgement

To C. M. Schroeder and D. F. Marcille for their assistance in evaluating this measurement technique.

References

1. D. H. Smithgall, R. E. Frazee, Jr., "Measurement and Control of Fiber Coating Concentricity", BSTJ, Vol. 60, No. 9, November, 1981, pp 2065 - 2080.
2. L. S. Watkins, "Scattering from Side-Illuminated Clad Glass Fibers for Determination of Fiber Parameters", JOSA, Vol. 64, No. 6, June, 1974, pp 767 - 772.
3. D. H. Smithgall, R. E. Frazee, Jr., "Improved Real-time Optical Fiber Diameter Measurement System", Technical Digest of CLEOS '80, February 26, 1980, San Diego, CA, pp. 10-11.

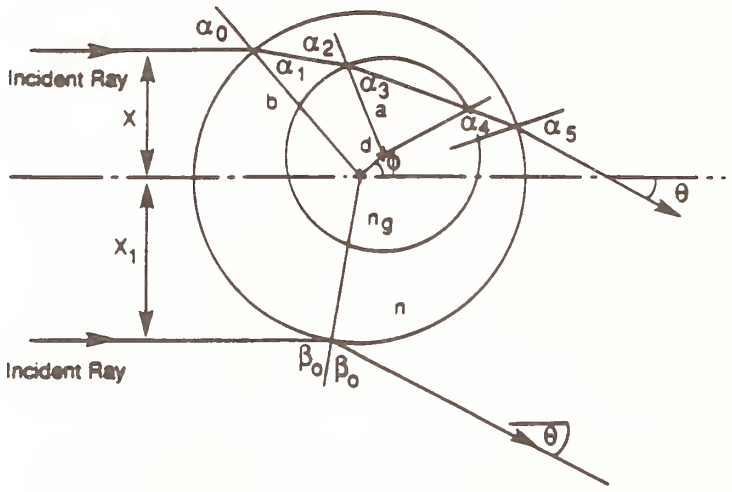

FIGURE 1

RAY TRACE THROUGH ECCENTRIC COATED FIBER CROSS-SECTION

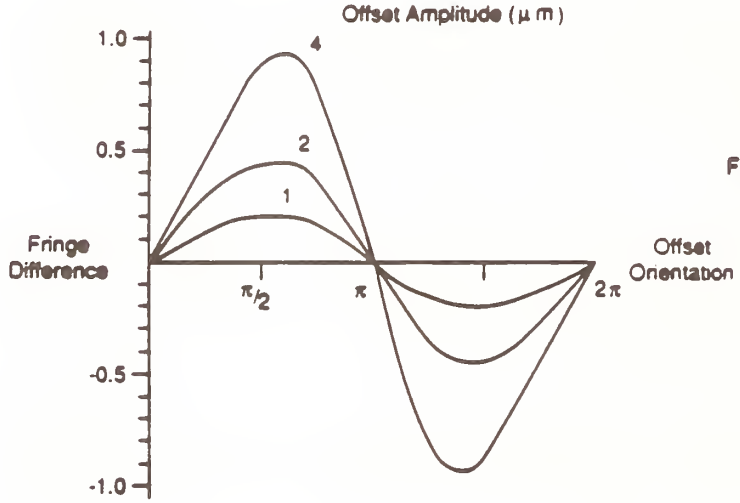

FIGURE 2

FRINGE DIFFERENCE AS FUNCTION OF FIBER OFFSET AMPLITUDE AND ORIENTATION
Coating Index 1.54

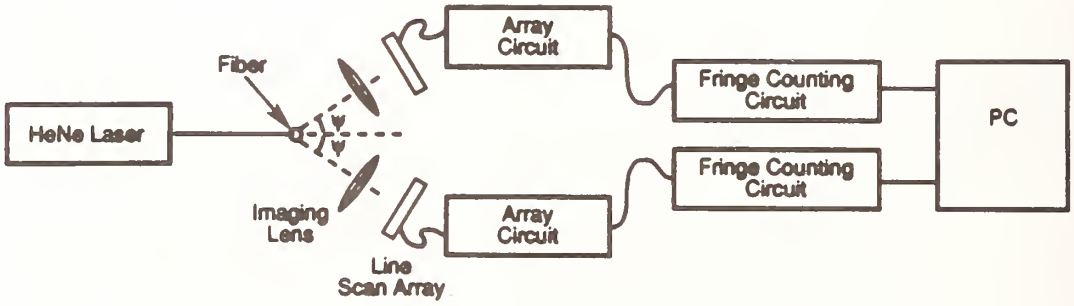

FIGURE 3

MEASUREMENT OF FORWARD LIGHT SCATTERED PATTERNS FROM THIN-COATED FIBER

Transverse Optical Scattering Measurements of the Core Radius of High-Δ Fibers with 1-nm Resolution

Peter N. Saeta
AT&T Bell Laboratories, 600 Mountain Ave., Murray Hill, NJ 07974 and NIST/JILA, Campus Box 440, University of Colorado, Boulder, CO 80309-0440

Benjamin I. Greene, David J. DiGiovanni, and Anne E. Miller
AT&T Bell Laboratories, 600 Mountain Ave., Murray Hill, NJ 07974

Abstract

An optical technique for measuring the core radius of high-Δ optical fibers is proposed in which a laser beam is scattered off the core of a fiber immersed in index-matching fluid. Using a fiber segment that was pulled to form a near-field optical tip, the technique is used to measure variations in the core radius of step-index fibers down to the scale of 1 nm.

Introduction

Standard techniques for measuring the index profile of optical fibers rely on scanning a focused spot of visible light across the cleaved fiber face. Their resolution is therefore limited approximately to the wavelength of visible light, or about 0.5 μm. For step-index fibers with large relative index difference, Δ, and core radii of only a few micrometers, this limited resolution results in a significant distortion of the measured profile. Much greater resolution could theoretically be obtained with scattering or interferometric techniques, ideally to a small fraction of the wavelength. Measurements at the nanometer scale could provide useful information on draw-induced changes in the profile and could conceivably test theories that attribute the abnormally high loss of high-Δ fibers[1,2] to fluctuations in the core radius.[3,4]

This paper describes a high-resolution scattering technique suitable for high-Δ step-index fibers. The method consists of scattering a focused laser beam off the core of the fiber and analyzing the fringes of the scattering pattern away from the forward direction. It is similar to a conventional light scattering technique[5-7] used to provide real-time feedback to control the fiber diameter during the draw, except that the fiber is immersed in index-matching fluid. This effectively removes the cladding, vastly simplifies the scattering pattern, and permits much more direct information about the core to be obtained. Analysis of the resulting scattering pattern permits nanometer-scale fluctuations of the core radius to be observed.

Theory

Light scattering from fibers has been used for many years to monitor the fiber diameter during the draw and provide feedback to minimize diameter fluctations.[6,7] The theory for scattering plane electromagnetic waves off infinite homogeneous dielectric cylinders and cylindrical annuli has been discussed by many authors.[5,8,9] Briefly, we assume the index profile to be a piecewise-constant function of the radius, r, and equal to the cladding index, n_{clad}, for $r > b$. Then the scattered electric field, $E(\phi)$, can be expressed[10] as a cosine series in the azimuthal angle, ϕ, having complex coefficients determined by boundary conditions at the interfaces between successive annuli. To obtain spatial resolution along the fiber axis and to maximize the signal with respect to scatter from the cell and the fluid, a lens is used to focus the laser beam at the fiber core, taking care that the beam waist, w, satisfies $w >> b$. The power detected in an angle $\Delta\phi$ in the far field is then given by

$$\frac{P}{P_{inc}} = \frac{\lambda\Delta\phi}{2\pi^2 w}\left|\sum_{\nu=0}^{\infty} c_\nu \cos\nu\phi\right|^2 , \qquad (1)$$

insofar as the deviations of the incident wave from plane can be ignored.

While the sum in Eq. (1) is infinite in the order parameter ν, the coefficients c_ν fall off rapidly for $\nu > 2\pi n_{clad} b\lambda^{-1} \equiv N$. For the case of scattering from standard fibers in air, $N \approx 620$,

which produces a pattern of very high angular frequency dominated by the air-cladding interface. The portion of this pattern near the backscattered direction has recently been used to measure cladding diameter to ~10 nm.[11] In the present case of a nominally step-index fiber with $b \approx 1.2$ μm, N is approximately 15, so that the fringe spacing is roughly 180°/15 = 12°.

Figure 1 shows the scattered power calculated using Eq. (1) for a step-index fiber using typical experimental conditions. The dashed line shows how the pattern changes for a 1% increase in b. Clearly if stray light can be suppressed and the pattern around $\phi = 90°$ can be measured with even modest sensitivity, resolution better than 12 nm can be achieved in these fibers.

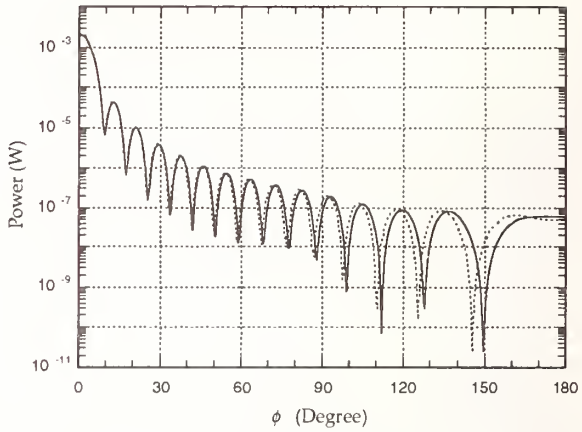

Fig. 1 Calculated scattering pattern for a step-index fiber ($\Delta = 0.023$, $b = 1.2$ μm) using 1 W of 0.5145-μm light focused to $2w = 40$ μm. A slit width of 0.25° is assumed. The dashed line shows the modified pattern for a 1% increase in core radius b.

Experiment

The experiments were performed on optical fibers with their polymer jackets removed. The setup was a slight modification of one previously described in detail.[10,12] The fibers were suspended in a 2.3-cm-diameter silica cell filled with index-matching fluid. Either the 0.488-μm or the 0.5145-μm beam of an argon-ion laser was focused by a 13.5-cm focal-length spherical lens into the center of the scattering cell. The beam was vertically polarized (parallel to the fiber axis); typical beam power was 1 W.

Two detection schemes were employed. In the first, the beam was chopped to permit lock-in detection and the scattered light was detected with an unamplified silicon photodiode mounted on an optical rail atop a computer-controlled rotation stage at a distance of ~20 cm from the fiber. The acceptance angle of the detector was determined by an adjustable-width vertical slit mounted 10 cm from the fiber on the rotating rail; typical acceptance angles were 0.1–0.3°. In the second, a cylindrical lens was placed near the cell and the collected light was imaged on a photodiode array.

Results and Discussion

The fiber used for most experiments (Fiber A) had a silica cladding layer and a germanosilicate core (18% GeO_2), yielding a nominal Δn of 0.030 ($\Delta = 2.1\%$) and core radius of ~1.2 μm. When immersed in index-matching fluid and illuminated with either argon line, the scattering pattern was easily visible by eye through angles exceeding 90° from the forward direction and appeared symmetric about the forward direction. When the index-matching fluid and the cladding had slightly different indices of refraction, the pattern was modulated by shallow high-frequency fringes having a line spacing of a fraction of a degree.

The scattering pattern measured using the single photodiode is shown in Fig. 2

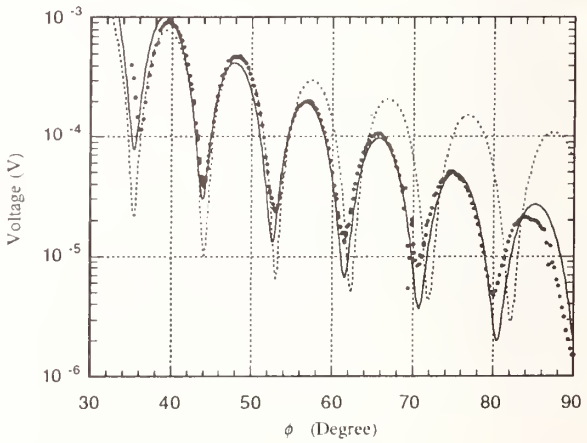

Fig. 2 Observed scattering pattern for Fiber A, a nominally step-index high-Δ fiber. Dashed curve is best fit for step-index profile; solid curve is the best fit, giving a core radius of 1.22 μm.

for the range $35° \leq \phi \leq 90°$. On the vertical scale of diode voltage, the background level detected when the fiber was removed from the cell was between 10^{-7} and 10^{-6} V over this range. The data agree qualitatively with the calculated pattern of Fig. 1, having roughly the same fringe spacing, although the successive maxima fall off more rapidly than in the calculation for the idealized step-index core profile (dashed curve). Qualitatively, the rate of fall-off of the successive maxima is a measure of the broadening of the index step. An attempt was made to fit the data using a core index profile function with a smoothed transition from n_{core} to n_{clad}. Several forms were tried, and the solid curve in Fig. 2 shows the best fit obtained. The fit follows both the spacing of the minima and the decrease in the maxima with ϕ fairly well; the discrepancy at the minima results primarily from the finite slit width.

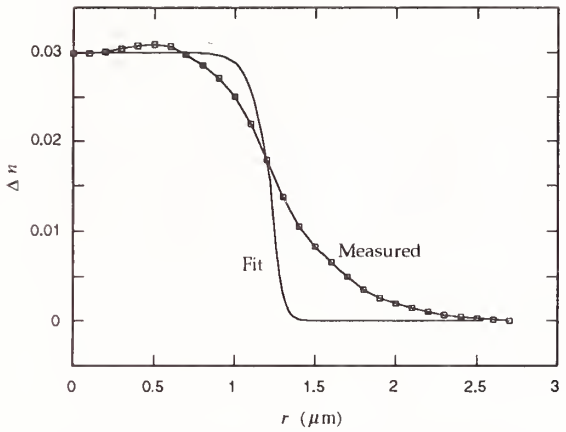

Fig. 3 Index profile as measured using the refracted near-field method with a York model S14 fiber profiler (heavy line) and as obtained from the fit shown in Fig. 3 (thin line).

The index profile corresponding to the fit of Fig. 2 is compared in Fig. 3 to measurements made using the refracted near-field method with a York model S14 fiber profiler. The profile obtained from the fit has an approximate transition width of 0.1 μm, whereas the measured one is roughly eight times broader. The broadening is primarily due to the ~0.5-μm spot size of the laser used to make the measurements, which necessarily smooths abrupt index changes. The scattering pattern calculated from the measured profile shown in Fig. 3 falls off much more rapidly with ϕ than the data and, unlike the data, shows minima of quite variable depth. It is likely, therefore, that the fit gives a much more accurate picture of the transition region from core to cladding.

An array detector was used to investigate the cores of two fibers from the same preform drawn at the same speed but at different tensions and temperatures. A cylindrical lens was used to direct and compress the radially scattered light onto the linear diode array. The data in Fig. 4 were not corrected for the resulting nonlinear relation between pixel and angle. The scattering pattern of the fiber drawn at lower tension (higher temperature) decays more rapidly with angle, indicating that the transition region between core and cladding is broader than in the fiber drawn at higher tension (lower temperature).

Simulations showed that the pattern is much more sensitive to the core radius, b, than to Δ. They also displayed the common feature that for small changes in b, $\delta b/b \propto -\delta\phi_{min}/\phi_{min}$, where ϕ_{min} is the position of a local minimum in the scattering pattern. This suggests that even if a satisfactory fit cannot be made to the data, useful information about changes in the core radius can be obtained by accurately measuring the position of one or more minima in the pattern as a function of distance z along the fiber.

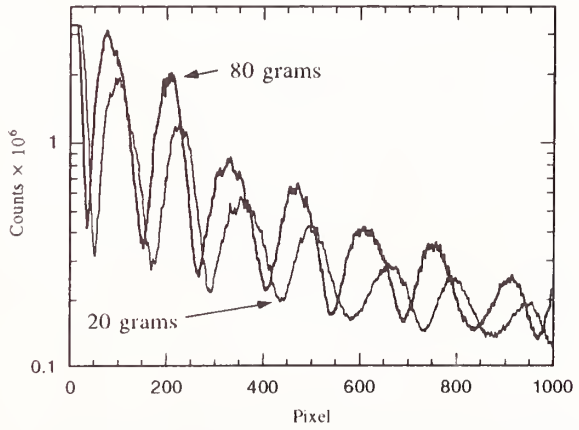

Fig. 4 Scattering patterns from two fibers differing only in draw conditions observed with a photodiode array showing that a higher draw temperature produces a more broadened transition from core to cladding index.

To investigate the sensitivity of this information, a segment of Fiber A was laser-heated under tension, causing it to neck down to a point and break in the heated region. Scattering measurements were then made of this "tip" starting in the region of the fiber that had not been heated. The relative change in radius, $\delta b/b$, was calculated based on the minima near $\phi = 44°$ and 53°, and the results are shown as a function of z in Fig. 5. These are compared to a profile deduced from a micrograph taken of the neck-down region of the fiber, based on the assumption that the relative change of the core is equal to the relative change of the outside fiber diameter. The agreement between the two curves calculated from the shift in minima is excellent—better than a part in 1000 in the unmodified region ($z < 100$ μm), and quite good throughout. Since $b \approx 1.2$ μm, this implies that the technique can resolve fluctuations in core radius smaller than 1 nm.

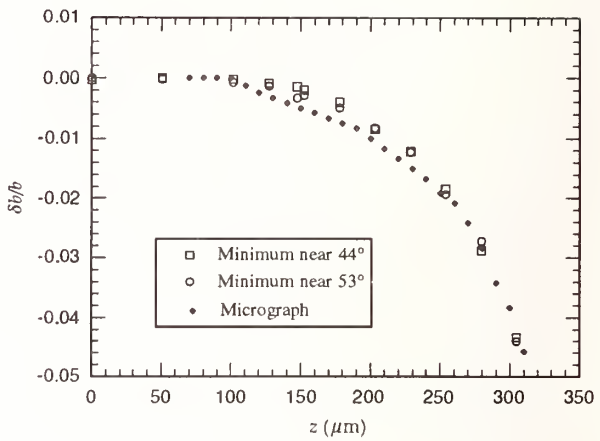

Fig. 5 Plot of the relative change in core radius along the length of the fiber in the neck-down region. The filled diamonds were taken from a digitized micrograph; the open symbols were obtained from the relative shift in the position of minima near 44° and 53°.

It should be noted that the analysis assumes perfect circular geometry. Deviations from roundness certainly exist at some level in fibers, and they will perturb the scattering pattern. Accounting for them is a challenging theoretical problem. Nonetheless, Fig. 5 suggests that this technique provides useful information on the nanometer scale.

Conclusions

The angular scattering pattern produced from a high-Δ, nominally step-index fiber immersed in index-matching fluid has been recorded and shown to provide a sensitive measure of the core radius. While attempts to deduce the exact index profile from the scattering pattern were unsuccessful, small variations in core radius produce proportional shifts in the angular position of sharp minima in the scattering pattern. These shifts were used to profile the neck-down region of a fiber tip with resolution better than 1 nm in the core radius.

Acknowledgments

We gratefully acknowledge R. E. Betzig, L. R. Copeland, D. M. Krol, C. R. Kurkjian, S. L. McCall, and W. A. Reed for help and useful discussions.

References

1 B. J. Ainslie, K. J. Beales, C. R. Day, and J. D. Rush, IEEE J. Quantum Electron. **QE-17**, 854 (1981).
2 S. T. Davey, D. L. Williams, D. M. Spirit, and B. J. Ainslie, SPIE **1171**, 181 (1989).
3 D. Marcuse and R. M. Derosier, Bell Sys. Tech. J. **48**, 3217 (1969).
4 D. Marcuse, Appl. Opt. **23**, 1082 (1984).
5 D. Marcuse and H. M. Presby, J. Opt. Soc. Am. **65**, 367 (1975).
6 H. M. Presby, J. Opt. Soc. Am. **64**, 280 (1974).
7 H. M. Presby and D. Marcuse, Appl. Opt. **13**, 2882 (1974).
8 J. A. Stratton, *Electromagnetic Theory* (McGraw-Hill, New York, 1941).
9 H. C. Van de Hulst, *Light Scattering by Small Particles* (Wiley, New York, 1957).
10 P. N. Saeta, to be published in Appl. Opt. (1994).
11 M. B. van der Mark and L. Bosselaar, J. Lightwave Technol. **12**, 1 (1994).
12 A. E. Neeves and W. A. Reed, Appl. Opt. **31**, 2072 (1992).

Measurement of Fiber Core Position for Fiber Array

K. Ozawa , S. Ogawa , H. Ishida and Y. Hattori

Sumitomo Electric Industries, Ltd.

1, Taya-cho, Sakae-ku, Yokohama, 244, Japan

1. ABSTRACT

A new measuring method of the offset of fiber core position in a fiber array was investigated. In this method, the offset of the fiber core position in the master array is measured in advance, and the sample array is set face to face with the master array, and measured the relative offset of its fiber core position. Using this method, the core position can be measured in a short time and by a simple equipment compared with the conventional way[1]. The repeatability of the measurement is under 0.05μm in the case of single mode fiber, so we can apply this method to the inspection of fiber arrays.

2. INTRODUCTION

The Planar Lightwave Circuits(PLC) are coming into practical use as passive optical parts such as couplers, splitters, filters. Fiber arrays are necessary for the connection between these optical parts and fibers and they will play a more important role in the future.

One of the most important specification of the fiber array is the offset of the fiber core position at its endface. That is because the offset has a direct influence on the coupling loss with another optical devices.

The offset of the fiber core position means the deviation from the proper arrangement of fiber cores in the endface of a fiber array. Fig.1 shows the example of this offset in the case of a 4-core fiber array. G is the barycenter of the centers of the four cores C1,C2,C3, and C4, and l_X is the straight line obtained by the least squares method from these four centers. A new coordinate system is considered, in which G is the origin, l_X is X axis, and l_Y, the perpendicular of l_X passing G, is Y axis. In this coordinates system the proper positions of the core D1,D2,D3, and D4 are arranged on l_X with certain distance a. The offset distance of the fiber core is defined as the distance d between this proper position and the actual center of the core. And the direction of the offset is defined as $\Delta\theta$ in this coordinate system.

There is conventional method to measure the offset of fiber cores for a multi-fiber connector[1]. A CCD camera, precision XYZ stages, and laser interferometers are used in this method. The sample connector is fixed on the XY stages and the CCD camera on the Z stage gets the core image on the endface of the connector by launching white light from the opposite side of the fiber. The core position can be obtained by the image processing of the CCD camera and the laser interferometers. Needless to say, this method can be applied to fiber arrays, and the repeatability of measurement is within 0.04μm.

But the cost of the equipment is high and time for measurement is rather long. So we investigated a simpler measuring method of the fiber core position.

3. PRINCIPLE

In this method, the sample array is set face to face with the master array, the fiber core offset of which have been already measured. The master array and the sample array are set face to face and the clearance between the both endfaces is kept in a certain distance d around 30μm. The master array is

fixed on the high speed actuator which put the master array in circular motion. The axis of this circular motion is parallel to the optical axis of the fiber, the radius is around 0.5μm, that is relatively small compared to the diameter of the fiber core.

As shown in Fig.2, by this circular motion, the center of the fiber core is also circulated about the center O. If the distance between O and the center of the fiber core of the sample array P is not so large as the coupling coefficient approaches zero, the coupling coefficient shows a periodic change, the frequency of which is equal to the frequency of the circular motion. $\Delta\theta$ is the direction of the offset of the fiber core of the sample array from O, and $\Delta\theta$ is related to $\Delta\varphi$ which is the phase difference between the periodic change of the coupling coefficient and the circular motion by the following equation:

$$\Delta\theta = \Delta\varphi \tag{1}$$

Since the radius of circular motion r is relatively small compared to the radius of the mode field of the fiber w, the mean coupling coefficient during the circular motion T_d is almost equal to the coupling coefficient in the case that the lateral misalignment is d which is the distance between O and P. So, T_d is expressed as follows[2]:

$$T_d = T_0 \exp\left[-\frac{T_0}{w^2} d^2\right] \tag{2}$$

$$T_0 = \frac{4}{4 + \frac{\lambda^2 z^2}{\pi^2 w^4}} \tag{3}$$

where λ is wave length, z is fiber separation distance, and w is mode field diameter. The range of the periodic change of the coupling coefficient by the circular motion T_R is given by:

$$\begin{aligned} T_R &= T_{d-r} - T_{d+r} \\ &= T_0 \exp\left[-\frac{T_0}{w^2}(d-r)^2\right] - T_0 \exp\left[-\frac{T_0}{w^2}(d+r)^2\right] \end{aligned} \tag{4}$$

And the ratio of T_R to T_d is related to d as follows:

$$\begin{aligned} \frac{T_R}{T_d} &= 2\exp\left[-\frac{T_0}{w^2} r^2\right] \sinh\left[\frac{T_0}{w^2} 2dr\right] \\ &\cong d \times \left[\frac{4T_0 r}{w^2}\right] \exp\left[-\frac{T_0}{w^2} r^2\right] \end{aligned} \tag{5}$$

It means that d is approximately in proportion to the ratio of T_R to T_d. As it is clear from the above, in regard to the offset of the fiber core, the direction can be obtained by measuring the phase difference $\Delta\varphi$, and the distance can be obtained by measuring the ratio of T_R to T_d.

4. EXPERIMENTAL APPARATUS

Fig.3 shows the system block diagram of measuring the core position. Single mode fiber arrays are used in this experiment. The actuator for the circular motion of the master array is a tube type piezo actuator shown in Fig.4. This actuator is specially made by changing the shape of the electrodes of the piezo actuator that is used for the probe scanning mechanism of STM. By applying sine-wave voltage to four electrodes around the tube and delaying each phase by $\pi/2$, the master array fixed on the tip of the actuator is given circular motion. In this experiment the radius is 0.5μm and the frequency is 1kHz. In

Fig.3, the light from LED, the wavelength of which is 1.31μm, is incident into the master array fibers, transmits to the master array endface, radiates to the sample array. Part of the light is coupled to the sample array fiber and detected by the photo diode. The phase difference between the detected signal and the sine- wave voltage applied on the piezo actuator, and the amplitude of the periodic change of the detected signal power are measured by two-phase lock-in amplifier. The mean power of the signal is measured by the voltmeter through the smoothing circuit. The sample array is fixed on the precision XYZ stages and the displacement of the stages are measured by linear scale, the resolution of which are 0.01μm.

5. EXPERIMENT

For the confirmation of this method, the experiment to obtain the relation between the detected signal at the photo diode and the displacement of the fiber core of the sample array was made. The clearance between the master array and the sample array is adjusted at 30μm. This clearance is filled with matching oil and one of the fiber cores in the master array is aligned to the fiber core in the sample array by the XY stages with accuracy better than 0.05μm. Then monitoring the lock-in amplifier and DC amplifier, the X and Y stages are stepped by 0.1μm. The displacement of the stages are measured by the linear scales.

6. RESULTS

Table.1 shows the relation between the phase difference $\Delta\varphi$ and the direction of the offset of the fiber core at the offset of 1μm. The relative accuracy of the measurement is ±1°. Fig.5 shows the relation between T_R/T_d and the distance. As equation (5) indicates, T_R/T_d is in proportion to the distance . These results confirm that by measuring $\Delta\varphi$ and T_R/T_d, the direction and the distance of the offset of the fiber core can be obtained. The repeatability of the measurement of T_R/T_d is under 0.05μm in the case that the distance of the offset is around 1μm.

7. CONCLUSION

In this work, we investigated on the measurement method of the offset of the fiber core position of the fiber array. Now we are developing the practical equipment for measuring the offset of fiber arrays using this method. The cross-check between this method and conventional method is necessary.

8. REFERENCES

[1] M. Shigehara, "Investigation on Fiber Core Position Measurement Method for Multi-Fiber Connectors", OFMC Proceedings, 1993, pp. 57 - 60.

[2] D. Marcuse, "Loss analysis of single-mode fiber splices", BellSyst. Tech. J., vol. 56, pp. 703-718,1977

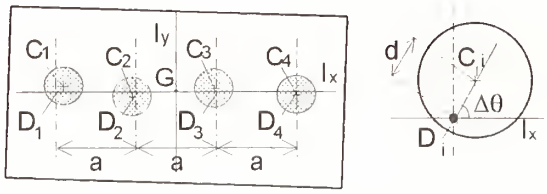

Figure 1. Offset of core position

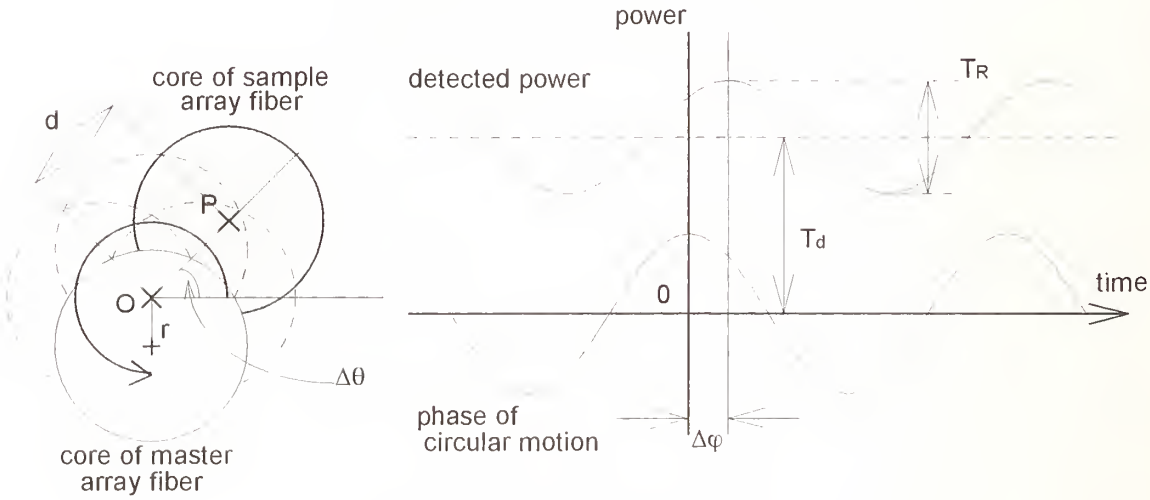

Figure 2. Principle of measurement

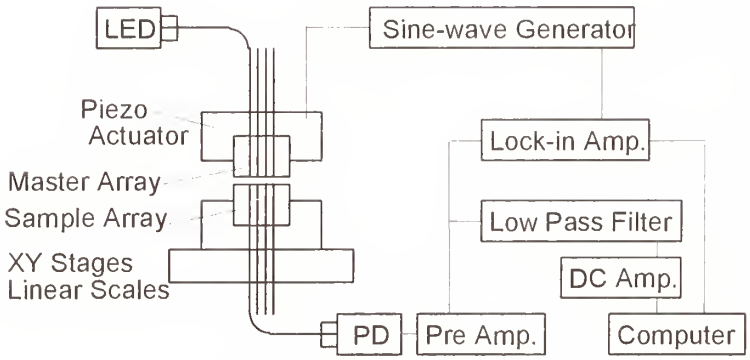

Figure.3. System block diagram

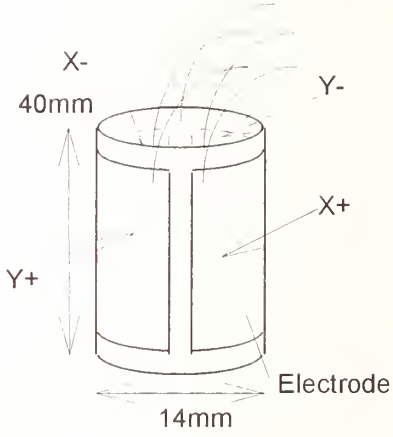

Figure.4. Piezo actuator

Table 1. Measured phase difference

	Phase Dif.	$\sigma_{(n=10)}$
0°(x:+1μm)	[0°]	-
90°(y:+1μm)	90.6°	0.3°
180°(x:-1μm)	179.9°	0.4°
270°(y:-1μm)	269.3°	0.4°

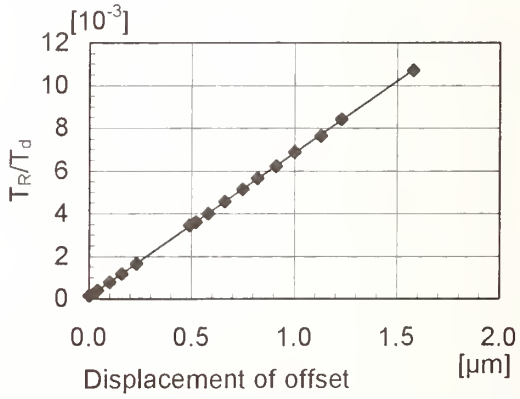

Figure.5. Relation between T_R/T_d and distance of offset

Polarization Mode Dispersion: Definitions, Measurements and Statistics

N. Gisin
Group of Applied Physics
University of Geneva, 1211 Geneva 4, Switzerland

1 Introduction

Polarization Mode Dispersion (PMD) has the same effect on light signals in optical fibers as other kinds of dispersion. In particular it limits the bandwidth and the linearity. It is caused by asymmetries in the geometry and/or the stress distribution in the fiber core. Locally PMD is due to the presence of two group velocities, one for each polarization mode. Globally this effect is combined with random polarization mode coupling. Consequently, PMD is a relatively subtle phenomenon.

In this contribution we like bring together several practical aspects of PMD: its definition, different measurement methods, and the statistical aspect of Polarization Mode (PM) delays. In the next section we summarize three measurements methods. A figure illustrates the setups and corresponding typical results, and a table presents advantages and drawbacks of each method. In section 3 two definitions of PMD are proposed. They are related to each other and to the measurement methods. Some advantages of each definition are discussed. Finally, in section 4 the probability that the instantaneous PM delay is larger than N times the mean PMD is computed and presented in a graph.

2 Measurement methods

The various measurement methods distinguish mainly by the coherence of the light sources.

The polarimetric methods [1, 2, 3, 4] and the wavelength scanning method [5, 6, 7] all use high coherent sources, that is light sources with a coherence time larger than the PM delay of the optical link under test. The reason is that all these methods require the light at the output of the link to be still polarized. The way these methods analyze that outcoming polarization state varies, but they all require that state to be stable during the measurement. Consequently, these quite elegant measurement methods have two main limitations. First, they are limited to relatively low PM delay (lower than the light source coherence time). This difficulty is severe, since all these methods require a wavelength scanning that can only be realized either with relatively expensive tunable lasers or at the cost of the dynamics of the measuring setup. Next, the outcoming polarization state is highly sensitive to environment perturbations (vibrations, stresses, pressure, etc). Even a very local perturbation, on the centimeter scale, can deteriorate the measurement of km long optical links.

The interferometric measurement method [8, 9, 10, 11], on the contrary, uses a low coherent light source, like a LED. The outcoming light is thus depolarized and a local perturbation along the link has only a limited effect on the measurement outcome, as for the measurements of other quantities, like the attenuation for instance. This measurement is closely related to the direct measurement in the time domain: it essentially measures the autocorrelation of the outcoming "light pulse" [12]. The coherence time of the light source playing the role of the pulse width. This coherence time determines thus the smallest measurable PM delay to about 0.15 ps.

The figure 1 and 2 illustrate the basic measurement methods, typical setup and results, and their relative advantages and drawbacks. All other measurement methods can be considered as different technical implementations of these basic methods. In [13] the interferometric method is compared to the polarimetric method, and in [14] it is compared to the fixed analyzer method. In all cases the numerical results agree well then computed according to the same definition of PMD.

3 Definitions

There are essentially two possible definitions of an appropriate mean PMD.

The first definition follows closely the definition of modal dispersion for multimode fibers [15]. This is natural since a "single" mode fiber actually supports several modes: the polarization modes. In the absence of PM coupling, one has only two modes. But, in the more realistic case of random PM coupling, the fiber behaves as a many-mode fiber and the natural definition for PM delay is the mean square deviation of the time of flight of the various PM:

$$PMDelay_1 = \Delta\tau = 2(< t^2 > - < t >^2)^{\frac{1}{2}} = 2\left(\frac{\int I(t)t^2dt}{\int I(t)dt} - (\frac{\int I(t)tdt}{\int I(t)dt})^2\right)^{\frac{1}{2}} \quad (1)$$

where $I(t)$ is the intensity of the light pulse after propagating through the fiber, assuming an initial delta pulse. In the high PM coupling regime, $I(t)$ is a gaussian of width $\Delta\tau = D\sqrt{\ell/h}$ where D is the modal birefringence, h the mean PM coupling length and ℓ the fiber length. The relation to the various measurement methods is illustrated on figure 3.

The second definition follows more closely optical communication applications where the laser source coherence time may be larger than the PM delay. In that case, for fixed PM couplings and a fixed wavelength, each polarization state has a fixed group velocity. The fastest and slowest polarization states are called the principal states [1]. Note that these principal states, and the difference between their group velocities, are very sensitive to the wavelength and to the PM couplings. However, it is natural to call instantaneous PMD the delay between the principal states and to consider their average. This leads us to our second definition:

$$PMDelay_2 = \ll \tau(\omega) \gg_\omega = \frac{\int_{\omega_1}^{\omega_2} \tau(\omega)d\omega}{\omega_2 - \omega_1} \quad (2)$$

We are now confronted to two "natural" definitions for one physical quantity! There is quite some confusion in the literature about these definitions, and most comparative measurements have overlooked the definition problem. However, in the cases of main practical interest (high and low PM coupling) these two definitions are easy to relate:

$$For\ low\ PM\ coupling : PMDelay_2 = PMDelay_1$$
$$For\ high\ PM\ coupling : PMDelay_2 = PMDelay_1/1.085 \quad (3)$$

The "magic number" 1.085 ($\approx \sqrt{3\pi/8}$) comes from the Maxwellian statistics of the delay between the principal states [16, 17, 18] and from the following basic relation between measurement results with high and low coherent sources [19, 13]:

$$\boxed{PMDelay_1 = \Delta\tau = \left(\frac{\int_{\omega_1}^{\omega_2} \tau(\omega)^2 d\omega}{\omega_2 - \omega_1}\right)^{\frac{1}{2}}} \quad (4)$$

This relation is fundamental for the understanding of PMD, since it relates measurement results with high and low coherent sources. Let us emphasize that this fundamental relation 4 is valid for any degree of PM coupling. This is why we believe that the first definition, $PMDelay_1$, is preferable: it is directly accessible by all measurement methods, without any assumption neither about PM coupling nor about statistical distributions.

4 Statistics

In the high PM coupling regime, the statistics of the delay between the principal polarization states follows a Maxwell distribution [16, 17, 18, 13]. This is well established, as well from a theoretical point of view, as from experimental evidence. Whether this regime is realized is a given fiber can be checked with the polarimetric measurement method by directly investigating the statistics of the delay between the principal states. It can also be controlled with the other two methods by comparing the interferogram

(or the fourier transform of the wavelength scanning data) to a gaussian. Indeed, the interferometric method essentially measures the statistics of one component of the principal state vector. The statistics of these components is Gaussian whenever the statistics of the norm of the principal state vector (which represents the delay) is Maxwellian (like the distribution of velocity of particles in a gas is Maxwellian whenever the distribution of the velocity components is Gaussian). Figure 4, for instance, illustrates an interferometric results in a case where the high PM coupling regime is **not** obtained. This figure should be compared with the theory based on the telegraphers equation [9]. It clearly indicates that this fiber is inbetween the low and high PM coupling regime.

The high PM coupling regime is the most relevant one for practical applications, since the other regime appear only in special fibers or in fibers with large geometrical defects. In this case the probability that the instantaneous PMD is larger than N times the mean PMD $\Delta\tau$ (1^{st} definition) is given by:

$$Probability(PMD > N * \Delta\tau) = \int_{N*\Delta\tau}^{\infty} \frac{\tau^2}{\sqrt{\pi/2}\ (\Delta\tau)^3} exp(-\frac{\tau^2}{2(\Delta\tau)^2}) d\tau \qquad (5)$$

and is illustrated in figure 5.

5 Conclusion

Polarization Mode Dispersion is an important parameter for optical communication, as well for CATV (linearity [20]) as for long distances. The actual PMD of installed cables varies greatly, even from one fiber to another in the same cable. Typical values range from lower than $0.1ps/\sqrt{km}$ to $1ps/\sqrt{km}$, with exceptional values as high as $4ps/\sqrt{km}$ [21, 22].

Reliable PMD measurement are nowaday feasible in a routine way. However, attention should be paid to the definition of the mean PMD and to the statistics of the instantaneous value of PMD.

6 Acknowledgments

Financial support from the swiss "Office Fédéral de l'Education et de la Science" within the COST 241 european project is gratefully acknowledged.

7 References

1. C.D. Poole and R.E. Wagner, El. Lett. **22**, 1029 (1986).
2. B.L. Heffner, IEEE Photon. Tech. Lett., **4**, 1066, 1992.
3. D. Andresciani et al, Optics Lett. **12**, 844, 1987.
4. N.S. Bergano, C.D. Poole and R.E. Wagner, J. Lightwave Tech. **5**, 1618, 1987.
5. C.D. Poole, Optics Lett. **14**, 523, 1989.
6. L. Thévenaz and Ph. Robert, ECOC'90, 1990.
7. C.D. Poole and D.L. Favin, "PMD measurements based on transmission spectra through a polarizer", J. Lightwave Tech., in press, 1994.
8. N. Gisin, J.P. Pellaux and J.P. Von Der Weid, Symposium on Optical Fiber Measurements, pp 119-122, 1990.
9. N. Gisin, J.P. Pellaux and J.P. Von Der Weid, J. Lightwave Tech. **9**, 821, 1991.
10. Y. Namihira et al., J. lightwave Tech. **1**, 329, 1989.
11. Y. Namihira et al., J. Optical Communication **12**, 1-8, 1991.
12. Let us emphasize that the spread Δ (ie the standard deviation) of an autocorrelation function is always $\sqrt{2}$ the spread of the initial function f: $\Delta(f * f) = \sqrt{2}\Delta(f)$
13. N.Gisin, R. Passy, JC Bischoff and B. Perny, IEEE Photon. Tech. Lett., **5**, 819, 1993.
14. N.Gisin, R. Passy and J.P. Von der Weid, Photon. Tech. Lett., "Definitions and Measurements of Polarization Mode Dispersion: Interferometric versus fixed analyzer methods", in press, June 1994.
15. CCITT Recommendation G.651 - Characteristics of a 50/126 micron graded index optical fibre cable. COM. XV-R-89 E, May 1992.
16. F. Curti, B. Daino, G. de Marchis and F. Matera, IEEE J. Lightwave Tech. **8**, 1162 (1990).
17. N. Gisin, Opt. Communications, **86**, 371, 1991.
18. G.J. Foschini and C.D. Poole, J. Lightwave Tech. **9**, 1439, 1991.
19. N. Gisin and JP. Pellaux, Optics Commun. **89**, 316, 1992.

20. C.D. Poole and T.E. Darcie, J. Lightwave Tech. 11, 1749, 1993.
21. N. Gisin, B. Perny and R. Passy, Proc. Optical Fiber Measurement Conference, York, 1991.
22. N. Gisin, OFMC'93, Torino, 1993.

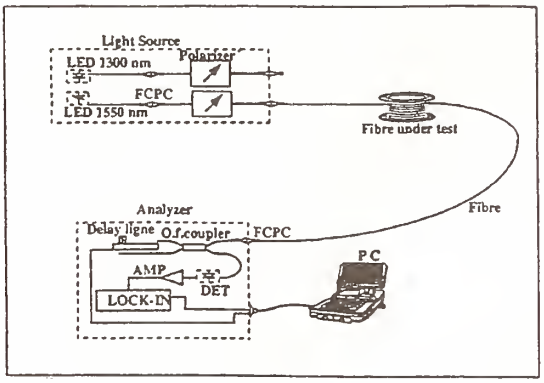

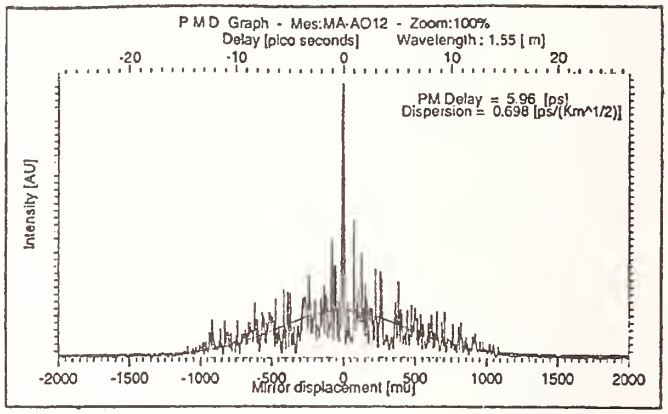

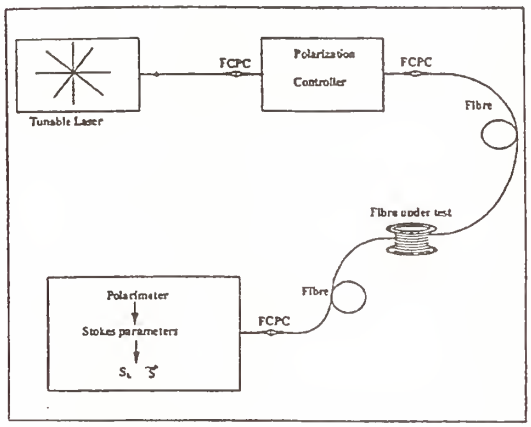

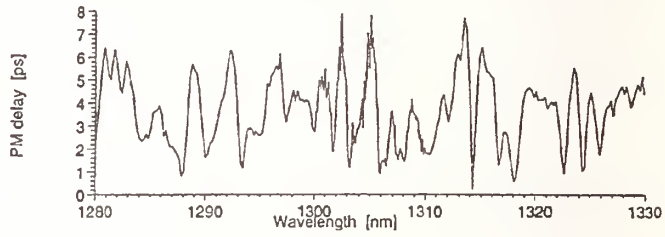

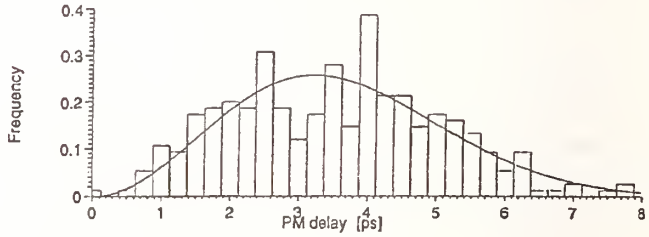

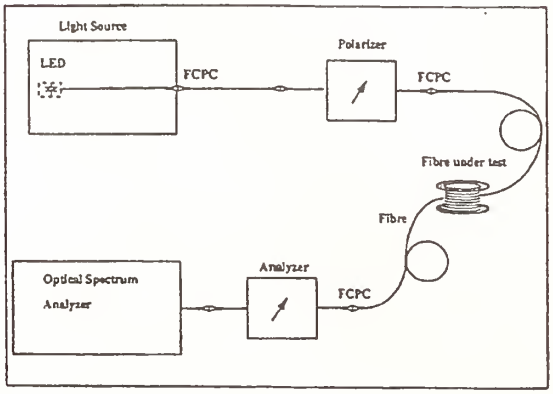

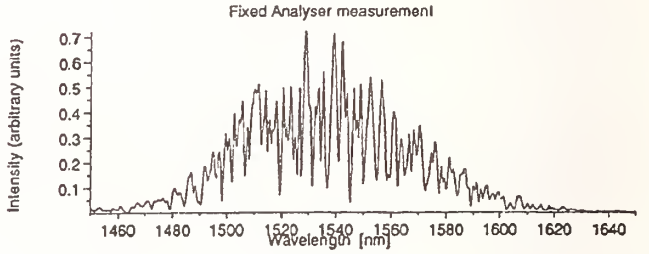

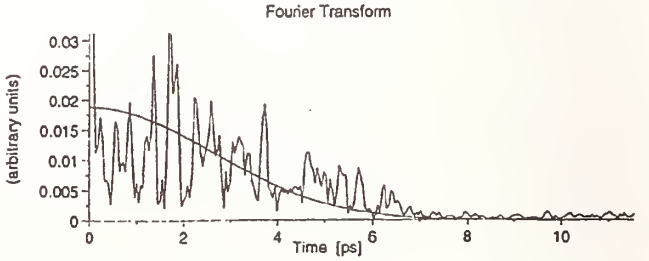

1. Typical measurement setups and results for the three basic measurement methods for PMD. a) interferometric, b) wavelength scanning, c) polarimetric

	Interferometric	Fixed Analyzer	Stokes Analyzer
Advantages:	♥ Most direct for measurement of mean PMD ♥ Fast ♥ Insensitive to vibrations ♥ Range up to 100 ps	♥ Equipment available in most labs ♥ Fast	♥ Most direct for measurement of delay between Principal States ♥ Information about Principal States ♥ Provides the statistics of PMD ♥ Range from 0.03 ps up to tens of ps
Drawbacks:	• Minimum measurable PMD: 0.15 ps •No information about principal states	• Minimum measurable PMD: 0.15 ps • Indirect • Tradeoff between high dynamics (large spectral width) and high range (small spectral range) • No information about principal states • Sensitive to vibrations	• Slow • Sensitive to vibrations
PMD computed from measured data (L=fiber length):	$\sqrt{\frac{\sum_{\lvert t_j\rvert \geq \tau_c} t_j^2 \bullet Intensity(t_j)}{L \bullet \sum_{\lvert t_j\rvert \geq \tau_c} Intensity(t_j)}}$ τ_c=coherence time of broadband source	1. Fourier transform of Intensity 2. Same as for the Interferometric method	$\sqrt{\frac{\sum_{\omega_j=\omega_1}^{\omega_2} \tau_{\omega_j}^2}{L \bullet N}}$ N=number of Data

2. Advantages and Drawbacks of the 3 measurement methods for PMD.

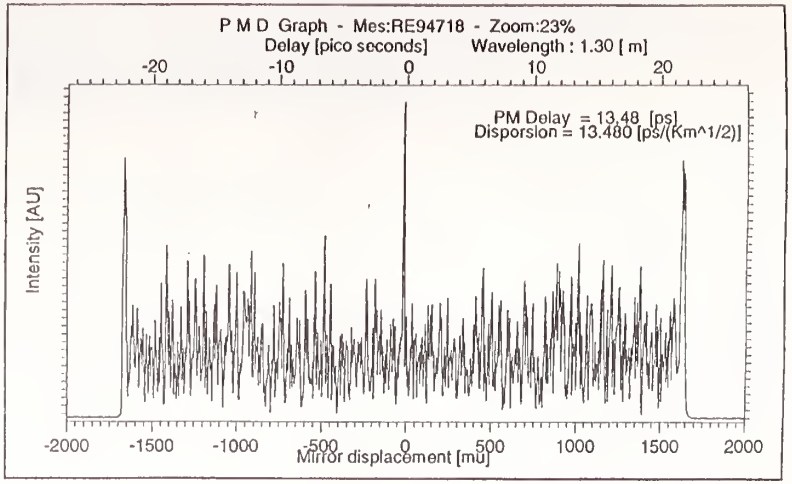

4. Interferometric measurement result for a case of moderate PM coupling.

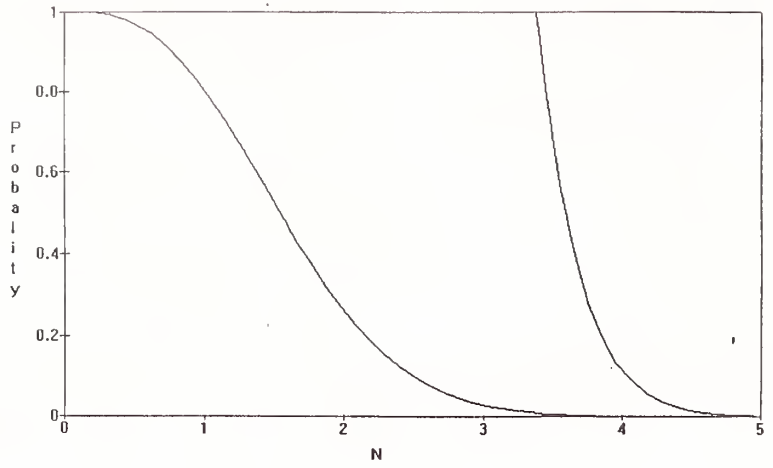

5. Probability that the instantaneous PMD is larger than N times the mean PMD $\Delta\tau$ (1^{st} definition), see eq. (5). The second curve, one the right hand side, represents this same probability, but multiplied by 100.

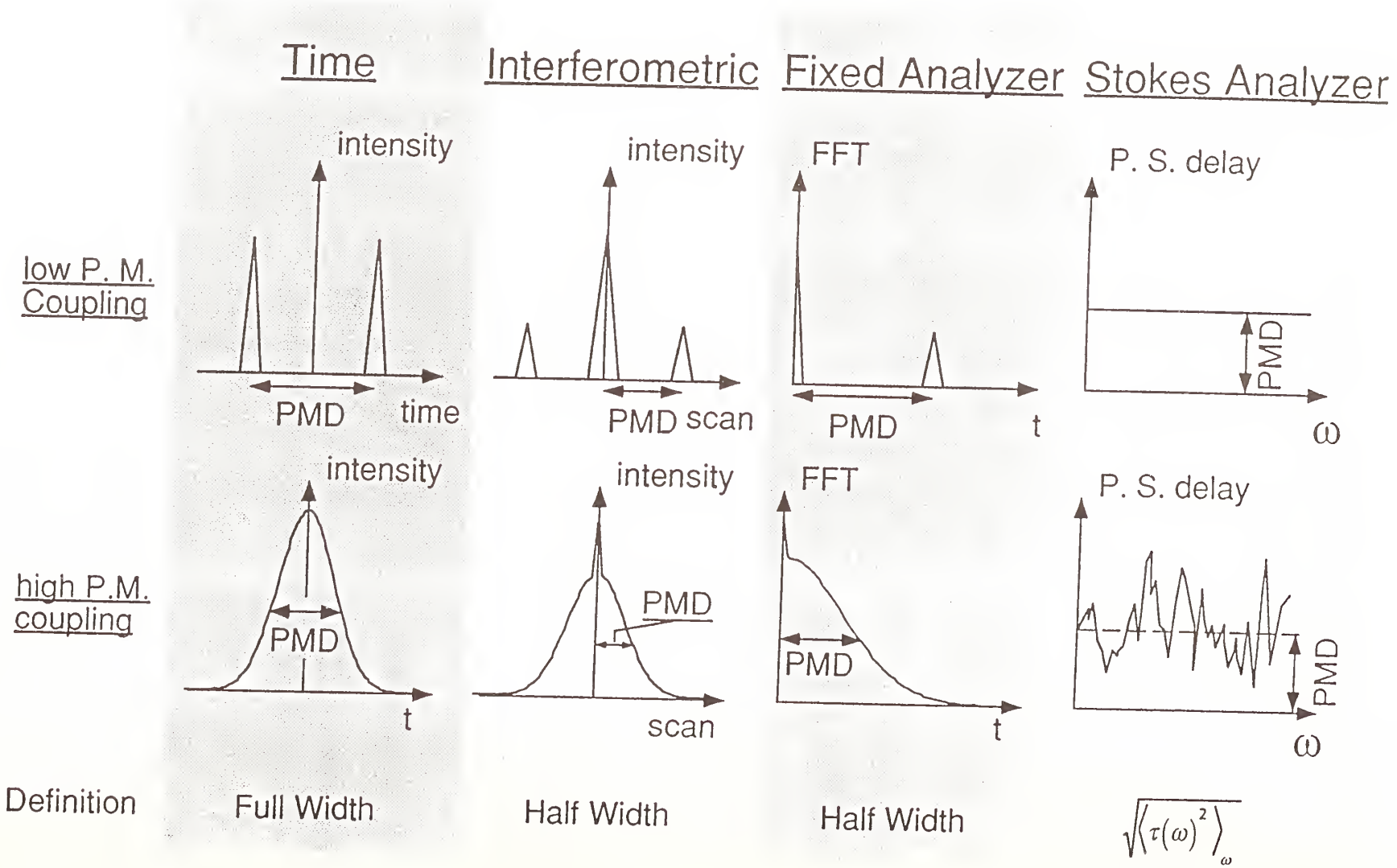

Fig. 3. PMD measurement result and definition versus measurement method.

MODE COUPLING MODEL FOR THE JONES MATRIX EIGENANALYSIS METHOD

D. A. NOLAN AND D. Q. CHOWDHURY

CORNING INC., SULLIVAN PARK, CORNING N.Y. 14831

TEL 607 974 9000, FAX 607 974 3675

Abstract:

A simple model is proposed for estimating an effective fiber birefringence and mode coupling length from the wavelength dependence of a fiber's polarization mode dispersion (PMD). The model is particularly well suited for use with the Jones Matrix Eigenanalysis (JME).

I. Introduction

A number of measurement techniques have been proposed for measuring PMD. The Jones matrix eigenanalysis method is well suited for determining this parameter. With this technique, one can determine the wavelength dependence of PMD as well as a mean PMD value over a range of 100 nms. We present a model whereby one can use this data to determine an effective mode coupling length and also the effective intrinsic fiber birefringence. In Section II, we develop the model, and the parameters of interest are derived. As an example, we then calculate these parameters from the wavelength dependent data of a dispersion shifted fiber with a moderate amount of PMD.

II. Model

Fiber-polarization mode dispersion is modeled using a concatenation of low birefringence polarization maintaining fibers and wavelength independent couplers, Fig. 1. The PM fibers simulate, for example, the effect that core deformation has on polarization dispersion. The fibers are chosen to be of equal length. This simplification is not necessary, but at this point is imposed for the purpose of keeping the model simple. The validity of this assumption can be checked as discussed below. The field amplitudes after propagating through n - 1 couplers can be expressed as

$$\begin{vmatrix} \psi_a \\ \psi_b \end{vmatrix} = \begin{vmatrix} \exp[-j\omega\delta\tau_N] & 0 \\ 0 & 1 \end{vmatrix} \prod_{i=1}^{N-1} \begin{vmatrix} a_i & b_i \\ b_i & a_i \end{vmatrix} \begin{vmatrix} \exp[-j\omega\delta\tau_i] & 0 \\ 0 & 1 \end{vmatrix} \begin{vmatrix} \psi o_a \\ \psi o_b \end{vmatrix} \quad (1)$$

where a_i and b_i are the mode coupling and are estimated as

$$a_i = \sqrt{(1 - \alpha_i)}$$

$$bi = j\sqrt{(\alpha_i)} \quad (2)$$

In eq. (2), the coupling coefficients (α_i) are chosen to be .5 in order to impose a square root length dependence on the link PMD. From the field amplitudes, the time delay differences can be calculated using the Jones matrix technique[1].

$$\Delta\tau = |\mathrm{Arg}(\rho 1/\rho 2)/\Delta\omega| \quad (3)$$

In eq. (3), ρ_1 and ρ_2 are the eigenvalues as determined in Ref. 1, and $\Delta\omega$ is a difference in optical frequency. Using this equation, we have calculated the wavelength dependence of the PMD for a number of different model parameters. The frequency of the oscillations in all cases is directly related to the value of $\delta\tau_i$, as was predicted also in Ref. 2.

Similar to the predictions of our model, Fig. 2 shows the dependence of PMD as measured on 2 kilometers of dispersion shifted fiber. Based on our model, one can determine the $\delta\tau_i$ as measured from the maximum of the Fourier transform or other power spectral density methods.

$$P(\delta\tau_i) = 1./2\pi \int \mathrm{PMD}(\omega)\exp[j\omega\delta\tau_i]d\omega \quad (4)$$

The value of $\delta\tau_i$ can also be estimated by picking wavelength differences at which a phase change of $\pi/4$ occurs and using the expression

$$2\pi c[1./\lambda_1 - 1./\lambda_2]\ \delta\tau_i = \pi/2. \quad (5)$$

For this fiber and using these techniques, we have determined $\delta\tau_i$ to be .02 psecs. The effective mode coupling length, l_i, is now determined by imposing a square root length dependence on the polarization dispersion and using (see Ref. 3, for example)

$$\langle PMD \rangle_L = \delta\tau_i [l_i/L]^{.5} \qquad (6)$$

In eq. (6), <PMD> represents the wavelength average of the link PMD. Using .2 psecs for the link PMD, 2 Kms for the link length, and .02 psecs for $\delta\tau_i$, we determine the l_i to be 40 meters for this particular fiber. The assumption of similar $\delta\tau_i$ s throughout the fiber is valid if the fourier transform of eq. (4) has only one strong maximum. This fiber did show only one strong maximum. In a subsequent publication, we will consider the case of variable $\delta\tau_i$ s.

In summary, a mathematical model used in conjunction with the Jones matrix eigenanalysis technique can be used to interpret fiber mode coupling parameters, i.e. coupling length and effective birefringence, $\delta\tau_i/l_i$.

REFERENCES

1. B. L. Heffner, 'Automated Measurement of Polarization Mode Dispersion using Jones Matrix Eigenanalysis'. PTL 4, 930-932, 1992.

2. N. Grisin and J. P. Pellaux, 'Polarization Mode Dispersion: Time Versus Frequency Domains', Opt. Comm. 89, 316-323, 1992.

3. D. A. Nolan, R. M. Hawk, and D. B. Keck, 'Multimode Concatenation Modal Group Analysis, JLT 5, 1727-1732, 1987.

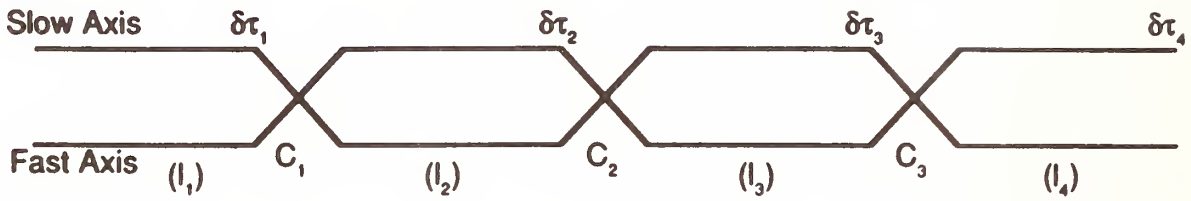

- l_i are lengths that introduce PMD through core ovality
- C_i are couplers simulating mode coupling through bends and twists

Fig. 1: Concatenation of PM Fibers and Discrete Couplers

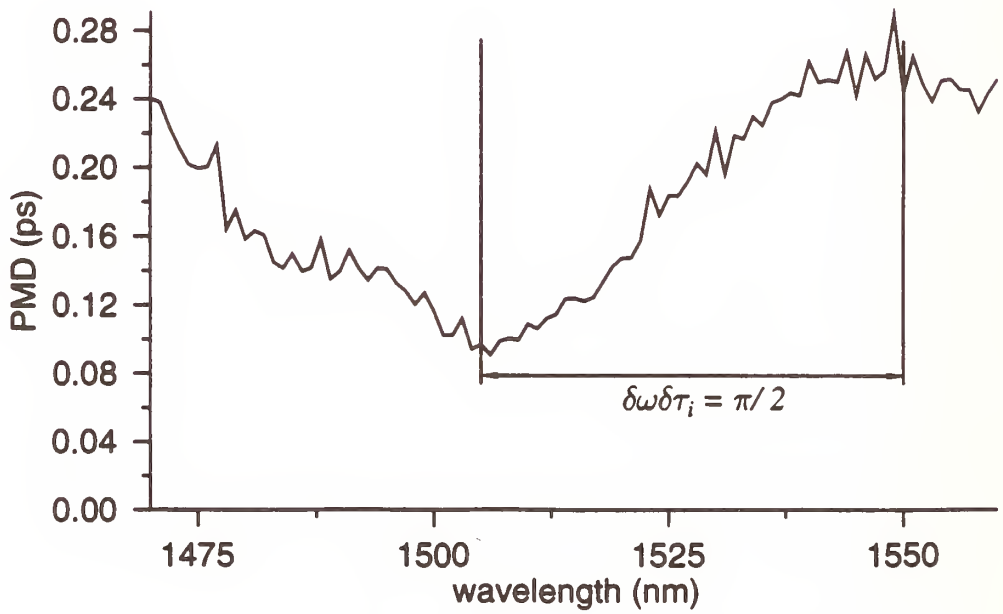

Fig. 2: Wavelength vs. PMD

Study on A Conservation Quantity in PMD Measurements

Osamu Aso, Isamu Ohshima and Haruki Ogoshi
Furukawa Electric Co., Ltd.
6, Yawata Kaigandori, Ichihara, Chiba 290, Japan

1. Introduction

Recent progress of optical amplifier and chromatic dispersion compensation technique makes it possible to realize high-bit rate and long haul repeaterless communication system. When chromatic dispersion is completely negligible, PMD will limit the system performance. Then suitable PMD compensation technique is necessary.
In spite of the above importance of PMD compensation, random mode coupling and its time evolution makes it difficult to estimate PMD of single-mode fibers sufficiently.
In this paper, through the evaluation of the critical wavelength step-size[1][2] using 10 - 90km dispersion shifted single-mode optical fibers (DSF), we will study the accurate measurement technique of the Jones matrix eigenanalysis.
In Sec. 2 for the convenience of the reader, we give a brief summary of the significance of critical wavelength step-size $\Delta\lambda_c$. In Sec. 3 a novel method to determine the $\Delta\lambda_c$ is introduced. In Sec. 4 experimental results are shown. Finally, conclusion and discussion are given in Sec. 5.

2. Critical wavelength step-size $\Delta\lambda_c$

According to Jones matrix eigenanalysis[3], in order to estimate the group delay difference of principal states at a wavelength λ, it is necessary to measure Jones matrix over the wavelength interval $\Delta\lambda$, *i.e.*, at λ and $\lambda + \Delta\lambda$. As shown in ref [1]and [3], optimum wavelength step-size should be narrow enough to satisfy exponential approximation but wide enough to provide the best accuracy (the wider the step-size the better the accuracy). Recently the authors confirmed experimentally[2] , using an about 90km DSF, that the exponential approximation region almost coincides with the Poole's first order approximation region[4]. Thus hereafter we will use the word " first order " approximation to be synonym with " exponential " approximation.
The above discussions indicates the existence of the transition point $\Delta\lambda_c$; the critical value of transition from the first order dominant region to the higher order region. Obviously $\Delta\lambda_c$ depends the type and magnitude of birefringence, thus estimation of this value will give an important information on accurate PMD measurements. In all the following discussion, we will call the above optimum step-size as critical step-size $\Delta\lambda_c$.

3. Experiments

We used Jones matrix eigenanalysis described in Sec. 2 and ref.[3] to measure PMD of DSFs. Light from a λ = 1550nm (zero-dispersion wavelength) and $\lambda + \Delta\lambda$ are passed through the test fibers and measured degree of polarization was greater than $\sim$ 95% after traversing test fibers. All of the DSFs used in our experiments were fragments of a 90km optical fiber. Fibers were wound onto 280mm diameter drum at 20gw tension. In order to evaluate whether a wavelength step-size $\Delta\lambda$ is inside the first order approximation region or not, we consider the global and local measurement (see Fig. 1).
First of all PMD is measured over the wavelength interval (λ, $\lambda + \Delta\lambda$). This measurement is called hereafter

"global " measurement and its result is described as $\Delta\tau$. Then $\Delta\lambda$ is divided into $\Delta\lambda$ / 10 intervals and PMD is measured over these intervals respectively. This is called " local " measurement and each result is $\Delta\tau_i$ (i = 1, 2, ..., 10). When $\Delta\lambda$ is larger than $\Delta\lambda_c$, higher order effect is not negligible and principal states will be violated over the wavelength interval. Thus, in order to evaluate whether the step-size $\Delta\lambda$ allows first order approximation or not, we consider following *ansatz* for the satisfying condition of the first order region.

$$\left| \langle \Delta\tau \rangle - \frac{1}{10} \sum_{i=1}^{10} \Delta\tau_i \right| \leq \sigma \quad , \qquad (1)$$

where, $< \Delta\tau >$ and σ is averaged value and standard deviation of the 10 times global measurements. In Fig. 2, we will show the comparison between global and local measurements in the case of 30km DSF. From this result, critical wavelength step-size is estimated as $\Delta\lambda c = 6.0 \pm 1.0$ nm.

4. Results

Fig. 3 and Fig. 4 show the length dependence of PMD and critical wavelength step-size respectively. Relation between PMD and fiber length L is suitably approximated $\Delta\tau / L^{1/2} = 0.048$ psec. km$^{-1/2}$, and also the relation between critical wavelength and fiber length seems to be obtained $\Delta\lambda_c \ L^{1/2} = 42.8$ nm km$^{1/2}$.

The above discussions are confirmed to by considering the following quantity Λ :

$$\Lambda \equiv \Delta\tau \cdot \Delta\lambda_c \ . \qquad (2)$$

As shown in Fig. 5, Λ is almost independent of fiber length L and its value is estimated as $\Lambda = 2.05$ psec. nm.

5. Conclusion and discussion

Optimum wavelength step-size was discussed experimentally as a critical step-size due to the transition from first order dominant region. A practical method to determine $\Delta\lambda_c$ was obtained and length dependence of $\Delta\lambda_c$ was estimated. In our result, $\Delta\lambda_c$ is proportional to $L^{-1/2}$ and this result implies the existence of a conservation (length independent) quantity. Hence we proposed Λ-term, which is defined as the product of the critical wavelength step-size and PMD value measured by this step-size. As shown in Fig. 5, this quantity is almost independent of fiber length.

Finally, we consider the application of Λ-term. As shown in Fig. 6, we plotted the curve $\Delta\tau \ \Delta\lambda = \Lambda$ in Fig. 2. This curve pass through the transition point and we obtained almost same results from other measurements with various length. Thus Λ-term could hopefully be a tool to confirm PMD measurement accuracy. Of course this is a result of our experiments. Then to confirm reproducibility of this result is necessary.

References

[1] Hewlett Packard Co., " *HP 8509 Lightwave Polarization Analyzer, Technical Data* ", (1993).

[2] O. Aso, I. Oshima and H. Ogoshi, " *A Study on The First Order Effect of The Phenomenological PMD Model in Long DSF.* ", in Press (1994).

[3] B. L. Heffner, " *Automated Measurement of Polarization Mode Dispersion Using Jones Matrix Eigenanalysis.* ", IEEE Photon. Technol., Lett., vol. 4, No. 9 (1992) 1066 - 1069.

[4] C. D. Poole and R. E. Wagner, " *Phenomenological Approach to Polarization Dispersion in Long Single-Mode Fibres* ", Electron. Lett., vol. 22, No. 19 (1986) 1029 - 1030.

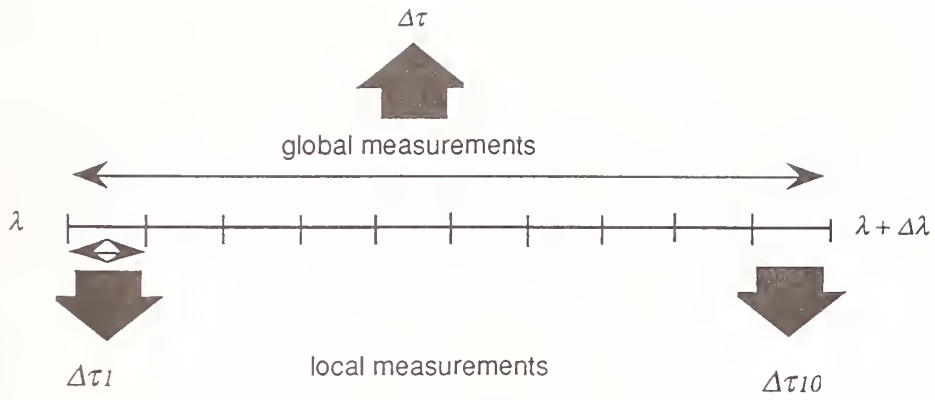

Fig. 1 Schematic diagram of global and local measurements.

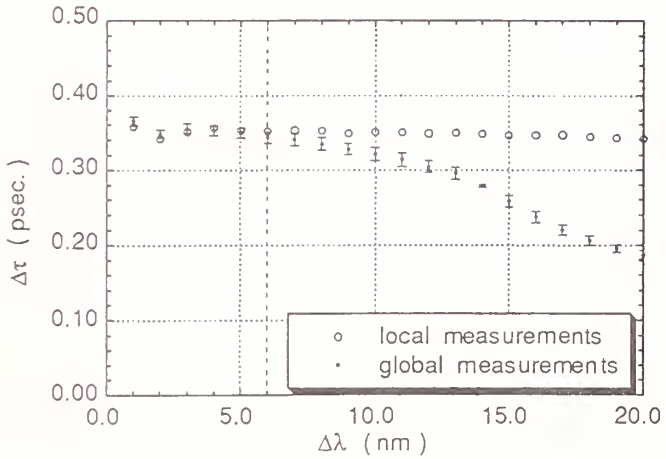

Fig. 2 Comparison of global and local PMD measurements. ● and ○ indicates $<\Delta\tau>$ and averaged value of local measurements respectively. Error bar represents standard deviation.

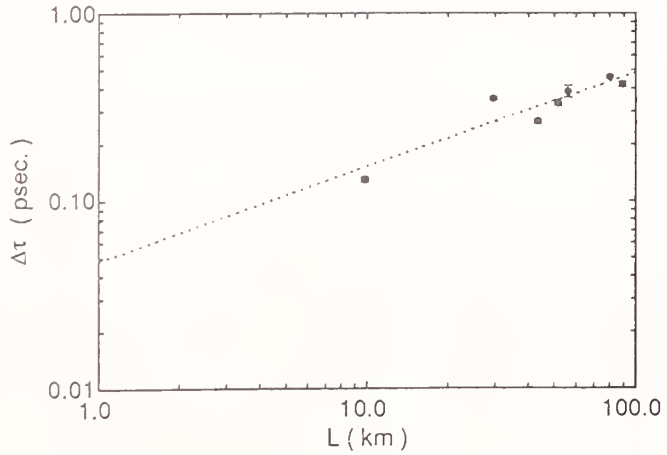

Fig. 3 Plot of PMD value as a function of fiber length. Error bar indicates standard deviation from 10 times measurements. Dashed line represents fitting formula: $\Delta\tau / L^{1/2} = 0.048$ psec./ km$^{1/2}$.

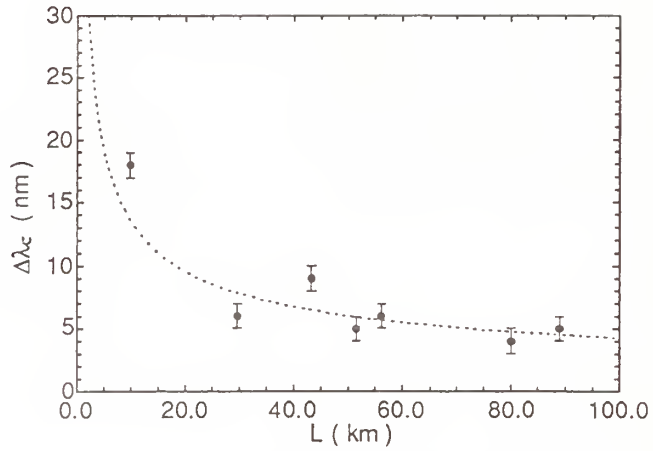

Fig. 4 Plot of critical wavelength step-size as a function of fiber length. Error bar indicates standard deviation from 10 times measurements. Dashed line represents fitting formula: $\Delta\lambda c L^{1/2} = 42.8$ psec. $km^{1/2}$.

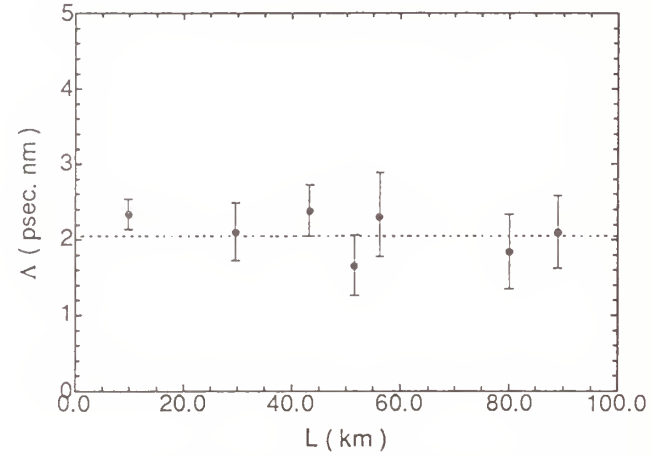

Fig. 5 Plot of Λ term as a function of fiber length. Error bar indicates standard deviation from 10 times measurements. Dashed line represents fitting formula: $\Lambda = 2.05$ psec. $km^{1/2}$.

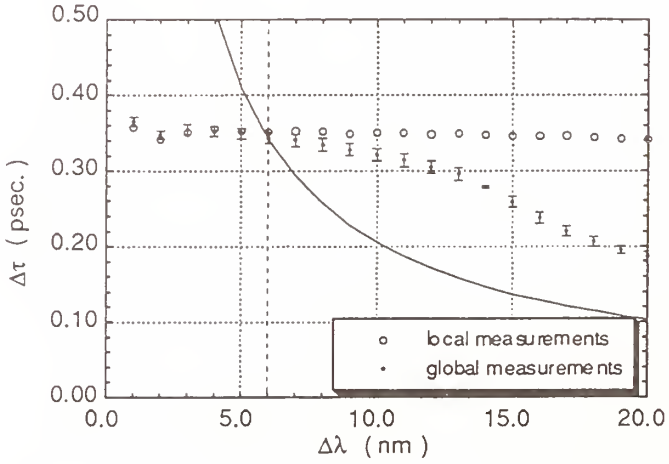

Fig. 6 Same figure with Fig. 2. Solid line represents $\Delta\tau\,\Delta\lambda = \Lambda$.

Quantitative comparison between the Jones matrix eigenanalysis & the wavelength scan method for polarization mode dispersion measurement: a simulation study.

D. Q. Chowdhury and **D. A. Nolan**
Corning Inc., Sullivan Park, Corning, NY 14831
Phone: (607) 974-3593 Fax: (607) 974-3675

Abstract

A model representing a long optical fiber by a random concatenation of small linearly birefringent fibers is used to simulate the measurement of the polarization mode dispersion (PMD) with the use of the Jones matrix eigenanalysis (JME) method and the wavelength scanning (WS) method. Simulations indicate that for the WS method the ensemble average power spectral density (PSD) is a Gaussian and the final ensemble average PMD values agrees well for a large number of random samples. However, PMD values obtained with the use of a single measurement of both methods could differ significantly.

1 Introduction

There exists several methods for measuring PMD of a long optical fiber. All of them can be categorized under three fundamental methods: (1) Jones matrix eigenanalysis; (2) wavelength scanning technique; and (3) interferometric technique. Since there is no industry standard on the PMD measurement technique, it is of interest to compare each of the methods quantitatively. However, the fact that the PMD of a given fiber is a statistical variable has made such comparisons with actual measurement very time consuming and impractical. The statistical variation of PMD depends on both the inherent fiber perturbations built-in during fabrication and the environmental perturbations from the deployment conditions. Consequently, numerical simulation is one of the easier ways to make such a quantitative comparison between different measurement techniques.

In this paper we compare two of the above three techniques on a quantitative basis using computer simulation. First, a brief description of the theory of simulation is presented. Then some quantitative comparison between the JME method and the WS method are presented. Using a Monte-Carlo simulation we show that the ensemble average Fourier transform of the WS method approaches a Gaussian as the number of random samples increases.

2 Model

A model to simulate the PMD measurement with the use of the JME and the WS method is developed based on the derivations in Ref. 1. The concatenation model is slightly altered in

order to model the WS measurement. The PMD at the end of the N^{th} link of a concatenated fiber is given by $|\boldsymbol{m}_{out}^{N}|$ [2] where

$$\boldsymbol{m}_{out}^{N} = \gamma_N \boldsymbol{e}_N + (\boldsymbol{m}_{out}^{N-1} \cdot \boldsymbol{e}_N)\boldsymbol{e}_N + \cos(\gamma_N \omega)[\boldsymbol{m}_{out}^{N-1} - (\boldsymbol{m}_{out}^{N-1} \cdot \boldsymbol{e}_N)\boldsymbol{e}_N] - \sin(\gamma_N \omega)\boldsymbol{e}_N \times \boldsymbol{m}_{out}^{N-1} \quad (1)$$

In the above Eq. $\boldsymbol{m}_{out}^{N}$ is a vector representing the principal states of polarization (PSP) at the output of the N^{th} link on the Poincaré sphere, $\boldsymbol{e}_N$ is the PSP vector for the link N, γ_N is the total mode group delay between the the two PSP's of link N, and ω is the angular frequency of the incident light.

In order to simulate the WS method, we use an x-polarized incident wave propagating through the randomly concatenated fiber links. The output state of polarization (SOP) is given by the recursive relation

$$\boldsymbol{n}_{out}^{N} = (\boldsymbol{n}_{out}^{N-1} \cdot \boldsymbol{e}_N)\boldsymbol{e}_N + \cos(\gamma_N \omega)[\boldsymbol{n}_{out}^{N-1} - (\boldsymbol{n}_{out}^{N-1} \cdot \boldsymbol{e}_N)\boldsymbol{e}_N] - \sin(\gamma_N \omega)\boldsymbol{e}_N \times \boldsymbol{n}_{out}^{N-1}, \quad (2)$$

where $\boldsymbol{n}_{out}^{N}$ is the vector indicating the output SOP at the end of the N^{th} link on the Poincaré sphere. The polarization of the detected light is also assumed to be x-polarized. Since the concatenation is random, the direction of the detected polarization really does not matter. The intensity of the detected polarized light is computed as

$$I_x = |E_x|^2 = 0.5(1 + \boldsymbol{n}_{out}^{N} \cdot \boldsymbol{e}_x), \quad (3)$$

where $\boldsymbol{e}_x$ is the unit vector along the x-direction in the Poincaré representation. Note that $\boldsymbol{m}_{out}^{N}$ is a vector representing the PSP and could be greater/less than unity in magnitude. Whereas, $\boldsymbol{n}_{out}^{N}$ is a vector representing the SOP with a magnitude of unity for a lossless fiber.

3 Processing the WS data

There are two different ways to obtain the PMD value from the WS data. One of them uses the number of peaks in the WS data within a given wavelength interval. The other method fits the power spectral density (PSD) of the wavelength scan with a Gaussian of the form $\exp[-\tau^2/2\sigma^2]$ and the PMD is given by the average deviation $\sigma\sqrt{2/\pi}$. For the WS method we use the latter of the techniques to obtain the PMD value.

In order to obtain a PMD value from the WS measurement we use a fast Fourier transfrom (FFT) algorithm [3] to obtain the PSD which is then fit with a Gaussian function. For the FFT algorithm the polarized intensity vs. frequency data is already normalized in our model since the fiber is assumed lossless. The computed data is multiplied by a Hanning window [3]. Mathematically expressed

$$R(i) = R(i)\,\frac{1}{2}\left[1 - \cos\left(\frac{2\pi i}{J-1}\right)\right], \quad (4)$$

where $R(i)$ is the FFT data set, J is the total number of data points in the FFT. We subtract the average of the wavelength scan over the scanned range from the data to make the average zero and thus remove the zero-frequency contribution.

4 Results and Discussion

In our simulation the number of concatenated links, N, representing a long optical fiber is computed from the fiber length and the average link-length. Since the PMD of a given fiber is statistical in nature, in order to compare PMDs measured with the use of JME and WS methods, a large number of random environment (deployment) samples are required. In our simulation a random number generator is used to vary the individual link lengths about the average along with their PSP orientations. For a quantitative comparison 400 random seeds are used in the simulation to compute the average PMD using both methods. The average and the standard deviation of the PMD for the JME simulation is computed using all the wavelength values for all the random samples.

$<\Delta\tau>_{JME}$	σ_{JME}	$\sigma_{JME}/<\Delta\tau>_{JME}$	$<\Delta\tau>_{WS}$	σ_{WS}	$\sigma_{WS}/<\Delta\tau>_{WS}$
0.0290	0.0123	0.4223	0.0296	0.0123	0.4171
0.0394	0.0166	0.4223	0.0370	0.0170	0.4596
0.2522	0.1090	0.4322	0.2078	0.0744	0.3582
0.3585	0.1592	0.4442	0.2976	0.1196	0.4020
0.5676	0.2474	0.4359	0.4373	0.1546	0.3536
0.7865	0.3407	0.4332	0.6332	0.2519	0.3978

Table 1: Comparison between the JME and the WS method measurement simulations. $<\Delta\tau>$'s are the average PMDs and σ's are the corresponding standard deviations of the average PMDs. 400 random samples are used. The subscripts indicate the method simulated. Fiber length was 1 km composed of 20 links with an average link-length of 50 m. The PMD values in the table are in ps/km.

Table 1 shows that for a low PMD fiber the average PMD and the standard deviation of the average agree well. Also note that in the JME simulation, even for a low PMD, the ratio of the standard deviation to the average is much closer to the same ratio for a Maxwellian distribution (0.422). For larger PMDs both the simulated averages and the standard deviations for the WS method differ from those for the JME method. Also for the WS simulation the ratio between the standard deviation and the average differ from 0.422. This is also true for the WS method for a long fiber with a low per-unit-length PMD.

The typical WS instrument currently has a precision of about 2 nm in wavelength, in other words, $\Delta\lambda$ could be as small as 2 nm. This $\Delta\lambda$ corresponds to a Fourier transformed range of 1.6 ps ($\approx 2\pi c\Delta\lambda/\lambda^2$) within the typical available wavelength range (1150 - 1700 nm). The accuracy of the Gaussian fit should start to deteriorate at PMDs greater than 1.0 ps.

Because of the statistical nature of the PMD, we decided to look at the ensemble average of the FFT taken over a large number (200) of random samples. Figure 1 shows the average FFT of 1, 6, and 200 random samples generated by the computer. Power spectral densities (PSD) computed for a single random sample using the maximum entropy method (MEM) [3] are also shown in the figure.

Figure 1 shows that as the number of random samples in the ensemble average increases, the FFT converges to a Gaussian. Even with as few as 6 random samples the average FFT

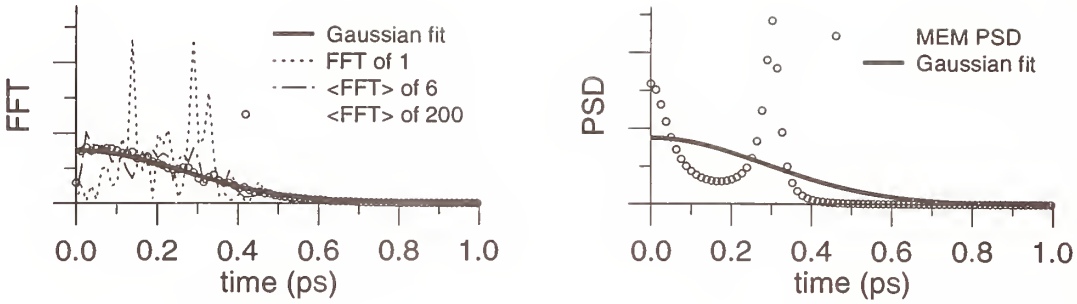

Figure 1: The average FFT for 1, 6, and 200 random samples along with the Gaussian fit for the average FFT of 200 random samples. The power spectral density (PSD) computed with the use of the maximum entropy method (MEM) and the corresponding Gaussian fit is also shown. The PSD is estimated for a single wavelength scan for which the FFT is also shown. Average PMD obtained from the average FFT of 200 samples is 0.28 ps, and the average PMD obtained from the single MEM PSD is 0.23 ps. Average PMD for a single FFT is 0.35 ps.

approaches a Gaussian distribution. Figure 1 also indicates that to estimate the PMD from a Gaussian fit of a single WS data could be erroneous. However, simulations (not shown here) suggests that the MEM could provide a more stable solution to this problem. Unlike FFT, MEM does not assume that the WS data is periodic after the measured wavelength range and, hence, provides a more realistic estimate of the PSD.

5 Conclusions

With the use of computer simulations we have shown that when an ensemble average is considered, the JME and the WS method agree well. However, for a single measurement, the WS measurement could differ significantly from that of the JME measurement. The fact that the ensemble average FFT is Gaussian gives more credibility to the FFT method than the "peak-counting" method, also used to obtain PMD values from WS data. However, PMD value obtained from a Gaussian fit to the FFT of a single WS data could be erroneous. A possible solution could be to use a more realistic PSD estimator, for example, MEM. The largest PMD that can be measured with the use of the WS method and FFT is limited by the resolution of the wavelength increment. This could be a limiting factor if a solid-state monochromator is used to spectrally resolve the wavelength vs. relative amplitude data.

References

[1] N. Grisin and J. P. Pellaux, "Polarization mode dispersion: time versus frequency domains," *Opt. Comm.* **89**, 316–323 (1992).

[2] Equation 3 in Ref. [1].

[3] W. H. Press, B. P. Flannery, S. A. Teukolsky, and W. T. Vetterling, *Numerical Recipes, The Art of Scientific Computing* (Cambridge University Press, Cambridge, 1989).

POLARISATION MODE DISPERSION MEASUREMENT USING FOURIER ANALYSIS: INVESTIGATION OF MODE COUPLING BEHAVIOUR IN FIBERS

A J Barlow, EG&G Fiber Optics, Wokingham, U.K.

Introduction

Several techniques for the measurement of polarisation mode dispersion (PMD) have been proposed, and recently compared [1]. Many of these methods operate in the frequency domain, relying on relatively simple instrumentation and data collection, and Jones or Stokes analysis methods to predict the PMD. Conceptually, however, there are some difficulties [2] in using the matrix techniques to relate to the real picture of pulse broadening in the fiber, which is the root cause of PMD-related bit errors or analog distortions in optical communications systems. Methods which display this data [1], [3] succinctly have great appeal.

Another major factor is that PMD in communications fiber is inherently statistical, and any measurement approach must take this into account. PMD is not a single-valued parameter, and the full distribution of pulse arrival times is required. Measurements are often required in the final operating environment to characterise the actual fiber deployment. The Fourier transform technique used here is inherently statistical in approach and combines the twin advantages of data collection in the frequency domain, and a succinct visual data output of the pulse arrival time distribution. In this paper, this method is applied to several fibers to investigate their mode coupling behaviour.

Background

The well-known cycle counting (spectral scanning) or fixed analyser method is essentially a polarimetric (frequency domain) method, where the light transmission thorough the fiber between randomly oriented polarisers is monitored as a function of wavelength, relative to a scan without the output polariser (analyser) [3]. A typical spectral scanning transmission plot $R(\lambda)$ for a 4.4km standard fiber on a shipment spool is shown in Figure 1. The periodicity of this waveform is determined from the minima and maxima of the waveform over a given wavelength interval, and the PMD found from the number of cycles in the waveform. Moreover, because it uses a very large spectral range, it is possible to obtain a good spectral average or "ensemble" of the fiber mode coupling effects, and thus a reasonable prediction of the total fiber PMD [1], and moreover with relatively simple instrumentation.

Nevertheless, considerable additional information can be obtained from the data in figure 1, by making use of the obvious relationship between the frequency domain where the data is collected and the time domain in which we require our PMD output, namely the Fourier Transform. A Fourier transform on $R(\lambda)$ transforms the optical frequency domain data to the time domain yielding directly the light arrival time distribution $P(\delta\tau)$ and

RMS pulse spreading $\langle\Delta\tau\rangle$ [2]. The Fourier method is applicable to all fibers with weak or strong mode coupling as well a fiber components eg isolators.

To briefly show this relationship, the fiber under test between the polariser and analyser/polarimeter is modelled by a birefringent element placed between crossed polarisers, each at +/- 45° to the fiber birefringence axes. The light transmission ratio R as a function of optical frequency $\nu = c_0/\lambda$ given by:

$$R = \sin^2 (\pi.\{\Delta n.L/c_0\}.\nu) \qquad (1)$$

where

c_0 is the velocity of light in vacuo.

Δn is the linear birefringence of the fiber per unit length,

L is the fiber length

Now, the PMD of the device is defined as:-

$$\delta\tau = \Delta n.L/c_0 \qquad (2)$$

where we have neglected any (usually small) dispersion term in Δn for clarity. Using equations 1 and 2 we obtain a cosine wave of oscillation frequency of $\delta\tau$. The spectral content of R obtained by Fourier transformation would exhibit a single 'spike', at $\delta\tau$, so the PMD is the centroid of this spike.

For the case where the fiber has strong mode coupling, we can see that the individual coupled 'paths' will arrive at specific relative times, giving rise to a corresponding periodicity in $R(\lambda)$ and hence a 'spike' in the Fourier transform distribution, with an amplitude corresponding to the relative power being carried. The actual Fourier Transform obtained is a "folded" symmetrical one, since negative $\delta\tau$ values appear as positive. Random coupling leads to a Gaussian distribution; non-random coupling to an undefined distribution pattern. In either instance, the second moment, σ_R, of the distribution $P(\delta\tau)$, is related to the expected value of PMD $\langle\Delta\tau\rangle$ - the RMS pulse broadening - of the fiber. The Fourier method offers extremely rapid and statistically accurate characterisation of the PMD and the distribution within the broadened output pulse. By chi-squared testing of the distribution $P(\delta\tau)$, we can determine within statistical limits of uncertainty whether the data 'sample' taken during a measurement is Gaussian and therefore indicative of random mode coupling in the fiber [3].

Results

An example of the Fourier transform output obtained in a 25km long fiber on a normal shipment spool is shown in Figure 2. In this case the data is indeed Gaussian (random) as expected for such a long fiber with multiple layered windings. Experience shows that a great many such fibers are mainly Gaussian, provided they are greater than ~10km in length. Spooled fibers shorter than this can sometimes be non-random, and an example is given in Figure 3, which is the FFT plot for the 4.4km fiber data of Figure 1. A prominent lobe in the distribution is clearly visible, and appears to correspond to the bend birefringence at the spool diameter. The bend birefringence appears to provide suffi-

cient deterministic birefringence behaviour to dominate other sources of mode coupling (eg twist) so the fiber starts to behave non-randomly. Here of course, the PMD no longer builds up with a root-length dependence. Only when the fiber length and number of winding layers build up, does sufficient mode coupling apparently occur to randomise the effect of the bend. Further investigation and results will be presented at the Conference in order to confirm this.

Discussion

It is clear from these examples, that the PMD pulse broadening can vary enormously from fiber to fiber, and further study of these effects is warranted. Given that the pulse distribution data can visualised in any fiber by the Fourier method, further study using this method has considerable merit. Because of its statistical nature, PMD data must necessarily be gathered over many fiber samples in order to validate any conclusions of such a study.

As shown above, the Fourier method is able to provide the full pulse broadening distribution data in a matter of minutes in both lab and field conditions. The short measurement time allows routine field and/ or production measurements of PMD to be contemplated, in order to build up sufficient fiber samples for an adequate study. Of significant concern is that fiber deployment conditions, eg measurement drum, shipment spool, cable, installed cable, will significantly affect the PMD that results.

Conclusion

PMD measurements using the Fourier Analysis (Spectral Scanning) technique have been described. The method offers the advantage of relatively low cost simple instrumentation, coupled to direct visual output of the broadened output pulse resulting from PMD and mode coupling.

The method has been applied to investigate the mode coupling conditions prevailing in typical fibers, relating these to the deployment and fiber length.

Finally, by enabling the user to quickly and easily examine the pulse power distribution, the Fourier method offers significant potential for routine production and field PMD measurement, which will also contribute to the understanding of PMD and mode coupling in fibers under a variety of production and deployment conditions. A full understanding of these effects is essential to the reliable control of PMD levels in installed fiber links, based on simple rapid production screening of PMD.

References

1). N. Gisin, "Definition of Polarisation Mode Dispersion", to be published.

2). B Heffner, "Polarisation Mode Dispersion", Tutorial paper ThE, OFC 94.

3). TIA FOTP-113 "Polarisation Mode Dispersion Measurement for Single-mode Fibers by Wavelength Scanning", draft, FO. 6.6.5.

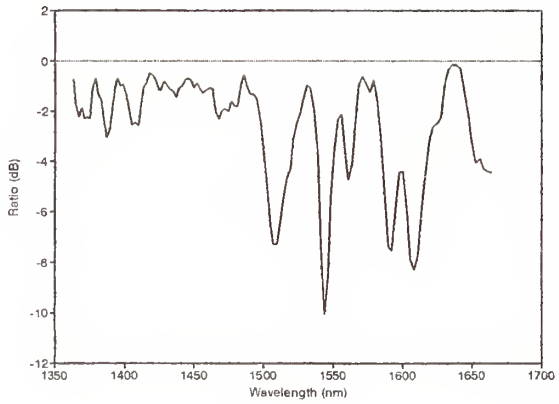

Figure 1: Ratio Plot obtained for 4km fiber on shipment spool.

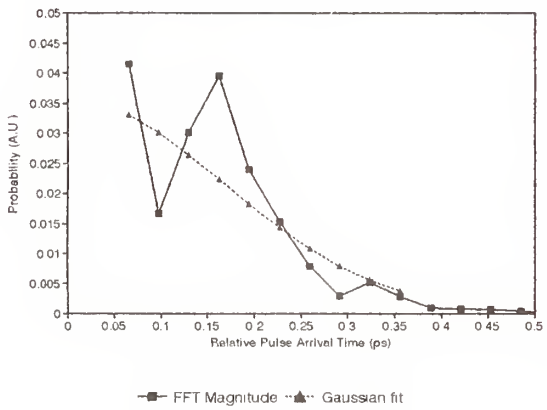

Figure 2: Fourier Transform for 25km fiber on shipment spool.
Data is GAUSSIAN

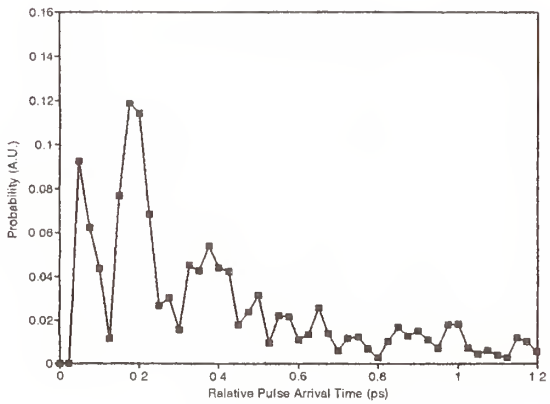

Figure 3: Fourier Transform for 4km fiber on shipment spool, corresponding to the ratio plot In Figure 1.
Data is NON GAUSSIAN

INTER-LABORATORY POLARIZATION

MODE DISPERSION MEASUREMENT STUDY

W. B. Gardner, TIA Ad Hoc Group*
AT&T Bell Laboratories
Norcross, GA 30071

*A. J. Barlow (EG&G Fiber Optics);
K. A. Emig (Corning); Scott Grindstaff (AT&T Fitel);
Paul Hernday (Hewlett-Packard); W. C. Jones (Bellcore);
Tom Olson (Alcatel); D. K. Roland (SpecTran).

1. INTRODUCTION

Polarization Mode Dispersion (PMD) causes optical pulse spreading which could impair the performance of systems. PMD also causes the state of polarization (SOP) to vary with wavelength, and this latter effect provides a convenient means for measuring PMD. One version of this is the wavelength scanning method[1], sometimes referred to as the "fixed analyzer" method[2]. Three ways of implementing wavelength scanning are illustrated in Fig. 1. Each relies on measuring how rapidly the SOP emerging from the test fiber changes as the wavelength is scanned. This paper reports the results of an inter-laboratory comparison of PMD measurements using wavelength scanning, initiated by TIA's FO-6.6.5 Working Group on Single-Mode Fiber.

2. BACKGROUND

Light from a narrow-band source will encounter a differential group delay time $\Delta\tau$ between the two orthogonally polarized principal states[3] of polarization. A long fiber produces sufficient random coupling between polarization modes to cause PMD to be a stochastic variable. PMD is defined as $\langle\Delta\tau\rangle$, where $\langle\ \rangle$ denotes the average. The average can be taken over time, temperature, or wavelength. The wavelength scanning method used in this study averages over wavelength. The differential delay time $\Delta\tau$ causes spreading of digital pulses in the time domain. In the limit of strong mode coupling, $\langle\Delta\tau\rangle$ is directly related to the rms pulse broadening. Fibers in practical systems are nearly always in this regime, and in that case the PMD coefficient is defined as $\langle\Delta\tau\rangle/L^{1/2}$, where L is the fiber length.

3. THE MEASUREMENT METHOD

In versions (a) and (b) of wavelength scanning shown in Fig. 1, the transmitted power $P(\lambda)$ is measured as a function of wavelength. This measurement is repeated with the Analyzer removed from the beam. The resulting power, $P_o(\lambda)$, can be used to eliminate the spectral dependence of the measurement system components and the test fiber loss. Typical plots of the ratio $R(\lambda)$ =

$P(\lambda)/P_o(\lambda)$ are shown in Fig. 2. Version (c) produces three normalized Stokes parameter responses from a single measurement.

If $R(\lambda)$ has N maxima (or minima) within the window $\lambda_1<\lambda<\lambda_2$, then

$$<\Delta\tau>=\frac{kN\lambda_1\lambda_2}{(\lambda_2-\lambda_1)c} \tag{1}$$

where c is the speed of light in vacuo. k is a mode coupling factor which equals 1.0 in the absence of mode coupling, and 0.82 in the limit of strong mode coupling[4]. This factor accounts for the fact that the direction of the polarization dispersion vector on the Poincare sphere varies with frequency in the presence of mode coupling. The PMD in Eq. (1) is interpreted as an average over the wavelength range $\lambda_1<\lambda<\lambda_2$.

Algorithms for identifying peaks in $R(\lambda)$ have been developed. Power spectral density estimation techniques, such as the Fourier Transform, are an alternative to cycle counting. Participants A through G used peak counting, while H used Fourier Analysis[5].

4. RESULTS AND DISCUSSION

Two depressed-cladding MCVD single-mode fibers, each about 5 km in length, were wound under 30 grams tension onto 15 cm dia. spools. PMD values from Eq. (1) were divided by the square root of the fiber length, and are listed in Table 1 in the order in which the measurements were made. Since the purpose of the study was to compare test sets, k in Eq. (1) was taken to be 1.0 for all measurements.

Although the standard deviations (σ) in Table 1 may appear to be large, the biggest contributor to σ is in fact the random fluctuations in $\Delta\tau$. This contribution to σ is given by Eq. (38) in Ref. 4:

$$\sigma^2/<\Delta\tau>^2 \cong 0.21\lambda_1\lambda_2/\left[<\Delta\tau>(\lambda_2-\lambda_1)c\right] \tag{2}$$

This contribution, which appears in the first row of Table 2, is inherent in the nature of PMD, and would be present even with perfect test sets.

5. CONCLUSIONS

Eight participants used the wavelength scanning method to measure the PMD of two 5 km fibers. The statistical uncertainty inherent in PMD (about 20% for the fibers and wavelength ranges used in this study) is the major contributor to the observed inter-laboratory variation.

References

1. C. D. Poole, "Measurement of PMD in Single-Mode Fibers with Random Mode Coupling," Optics Lett. 14, 523 (1989).

2. Y. Namihira and J. Maeda, "Polarization Mode Dispersion Measurements in Optical Fibers," NIST Symp. on Opt. Fib. Measurements, Boulder, September 15-17, 1992, p. 145.

3. C. D. Poole and R. E. Wagner, "Phenomenological Approach to Polarization Dispersion in Long Single-Mode Fibers," Electronics Lett. 22, 1029 (1986).

4. C. D. Poole and D. L. Favin, "PMD Measurements Based on Transmission Spectra Through a Polarizer," J. Lightwave Tech 12, to be published (1994).

5. A. J. Barlow, "PMD Measurement Using Fourier Analysis: Investigation of Mode Coupling Behavior in Fibers," submitted to NIST Symp. on Opt. Fib. Measurements, Boulder, September 13-15, 1994.

TABLE 1. Inter-Laboratory Comparison

Participant	Window (nm)	PMD Coefficient ($ps/km^{1/2}$) Fiber 1	Fiber 2
A	1400-1600	.117	.116
B	1400-1600	.070	.116
C	1470-1570	.072	.150
D	1450-1640	.091	.135
E	1465-1563	.053	.078
F	1200-1550	.041	.084
G	1300-1600	.044	.090
H	1363-1563	.088	.089
	Mean	.072	.107
	σ	.026	.026

TABLE 2. Measurement Uncertainty

	$\sigma/\langle\Delta\tau\rangle$ Fiber 1	Fiber 2
Inherent Statistical Uncertainty (Eq. (2))	0.24	0.19
Inter-Laboratory Measurement Results (Table 1)	0.36	0.24

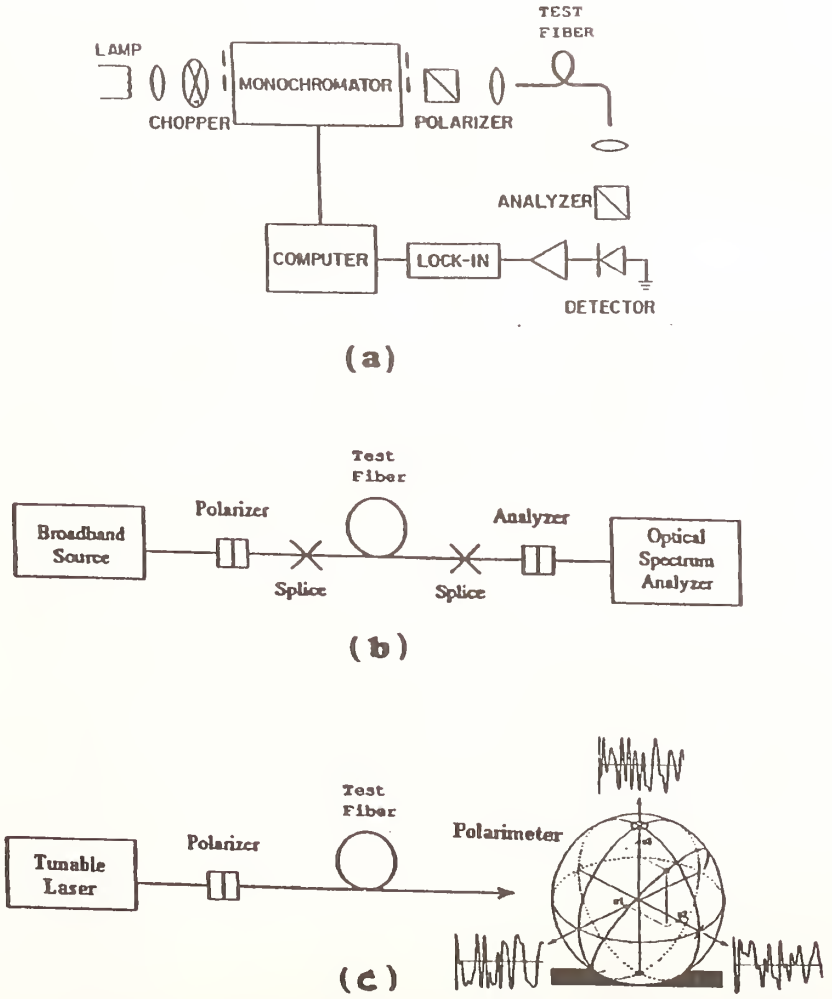

Figure 1. Schematic diagram of equipment (typical).

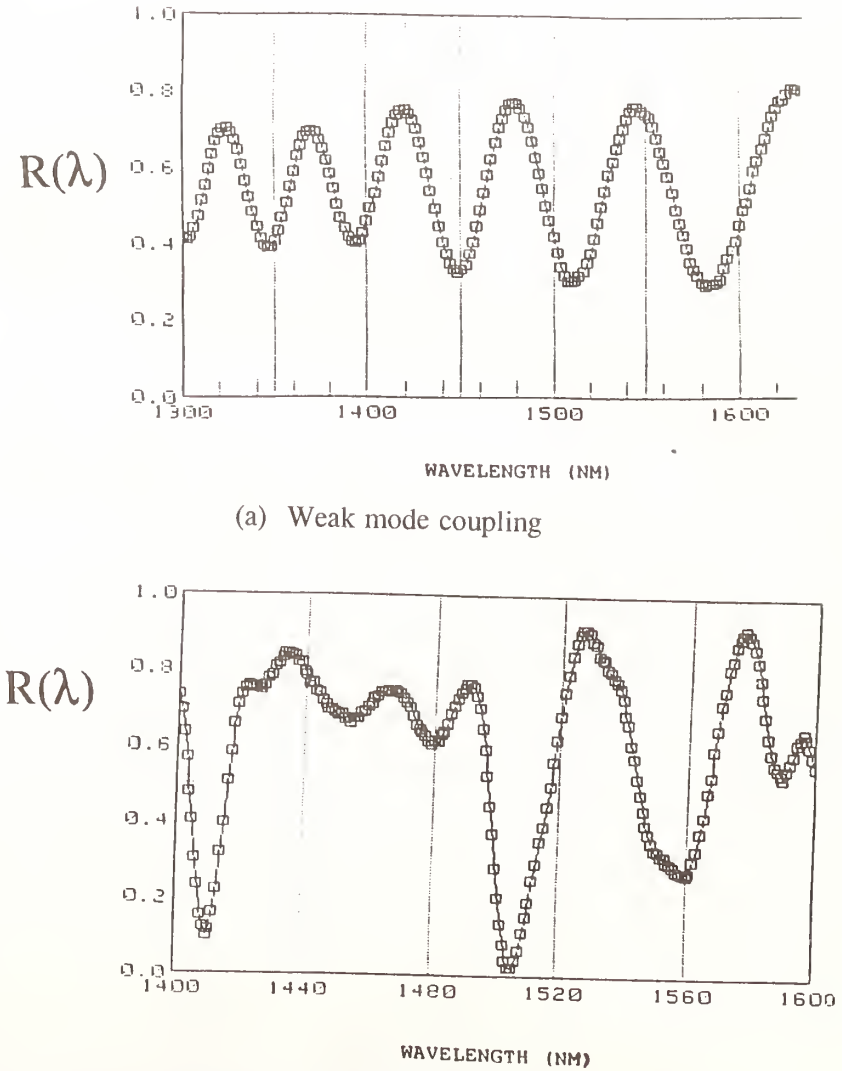

Figure 2. Typical data obtained in measuring PMD.

Characterization of dispersion compensating fibers

Ashish M. Vengsarkar and Anne E. Miller
AT&T Bell Laboratories, 600 Mountain Avenue, Murray Hill, NJ 07974

I. Introduction

Highly efficient erbium doped fiber amplifiers with broadband amplifying capability in the 1.53-1.56 μm range are now commercially available. The absence of comparable amplifiers in the 1.31 μm window has spurred system designers to consider the possibility of upgrading earlier generation 1.31 μm systems for use at 1.55 μm. The replacement of bit-rate-dependent electronic regenerators by all-optical bit-rate-independent amplifiers can lead to i) increased span lengths between amplifiers and/or ii) higher data rates. Optical amplifiers can compensate only for the loss in the system; the issue of dispersion, however, remains unresolved since conventional single-mode fibers embedded in the ground have a zero dispersion wavelength of 1.31 μm and a positive dispersion of ~ 17 ps/nm-km at 1.55 μm. This positive dispersion places a limit on the maximum achievable bit-rate distance products - for example, an externally modulated system with a dispersion penalty of less than 1 dB can be operated at a data rate of 10 Gb/s over spans shorter than 62 km.[1] As a consequence of this limitation, any upgrade of a 1.31 μm system to a high bitrate system operating at 1.55 μm requires dispersion compensating elements.

Bulk-optic devices for dispersion compensation were proposed several years ago;[2-4] more recently, there has been a surge of interest in the development of all-fiber compensators[5-12] that provide large negative dispersions. The principle of operation of all these devices is fairly simple - at periodic distances in the system one introduces a dispersion compensator with a dispersion that is equal in magnitude and opposite in sign to that of the fiber span to be compensated. Practical fiber-based dispersion compensators can be broadly divided into two categories: i) Fundamental mode designs, where an appropriate choice of the refractive index profiles result in the LP_{01} mode being used for dispersion compensation,[8-12] and ü) Higher-order mode designs, where a higher-order spatial mode (typically the LP_{11} mode) operated close to cutoff delivers the high negative dispersion.[5-7]

In this paper, we will describe in detail the measurement issues that are specific to the complete characterization of dispersion compensating fibers (DCFs). At first glance, the characterization of DCFs may be perceived to be very similar to that of conventional communications fibers since it involves the measurement of several standard fiber parameters such as loss, chromatic dispersion, cutoff wavelength, mode-field diameter, polarization mode dispersion and geometry/index profile. While one may expect no surprises in the measurement of these parameters, some of these measurands are more important than others. It is the object of this paper to highlight these differences.

The underlying principle of most DCFs is to enhance the negative waveguide-induced dispersion by using high Δ's (normalized index differences) in the core and/or by adding multiple cladding layers of varying refractive-indices around the core. The presence of high Δ's in the core and a trench (negative Δ) in the immediate cladding layer raises issues of increased losses and sensitivity to bends. Bend losses are particularly important since several kilometers of fiber may be wound on small spools to achieve a compact package. The variation of any of the aforementioned parameters as a function of bend radius thus becomes an important issue. An unusual distribution of modes may be observed if the design is chosen such that higher order modes can copropagate with the fundamental mode. Inadvertent mode mixing should be avoided for error-free operation of the compensated system.

II. Performance Evaluators

Five parameters that need to be measured in the characterization of DCFs are now described. The discussion is most applicable to single-mode DCFs although some of these criteria can also be applied to the higher-order mode technique.

A. Chromatic Dispersion

The first parameter of relevance is the dispersion of the compensating fiber. Since conventional fiber (e.g., AT&T

5D fiber) has a positive dispersion of ~17 ps/nm-km at 1.55 μm, the dispersion compensating fiber should have a negative dispersion at the same wavelength. It is also desirable that the magnitude of the dispersion of the compensating fiber be very large. Large negative dispersions will lead to short lengths of the dispersion compensating fiber and thus reduce space requirements at the regenerating stations. Since dispersion scales linearly with length, the total dispersion in a compensated link is given by

$$D_{TL} = (D_{DCF} \cdot L_{DCF} + D_{5D} \cdot L_{5D}) / L_{TL} , \quad (1)$$

where D is the dispersion, L is the length, and the subscripts TL, DCF and 5D denote total link, dispersion compensating fiber and a conventional 5D (AT&T) fiber, respectively. In calculating the total link dispersion typical values of D_{5D} = 15.6 and 17.3 ps/nm-km at 1530 and 1560 nm, respectively, can be used.

An additional desirable property of the dispersion performance relates to the slope of the dispersion versus wavelength curve. Since the dispersion of a conventional 5D fiber has a positive slope, the DCF dispersion should have a negative slope, thus enabling dispersion compensation over a broad wavelength range, specially over the 1530 - 1560 nm range of the erbium-doped fiber amplifiers. For optimal broadband compensation, the ratio of the slopes of the dispersions (denoted by D′) of the DCF and 5D should approximately equal the ratio of the dispersions of the two fibers, i.e.,

$$\frac{D_{DCF}}{D_{5D}} \approx \frac{D'_{DCF}}{D'_{5D}} . \quad (2)$$

The degree of proximity of the slope equality in the above expression sets the dispersion penalties on individual channels in a wavelength-division-multiplexed (WDM) system.

B. Polarization Mode Dispersion

As in conventional fibers, the effect of PMD can be fairly significant in DCFs specially if long lengths of fibers are to be compensated. An added aspect of the measurement of PMD for DCFs is its dependence on bend radius since the bend-induced birefringence and the winding conditions can affect the PMD. It is therefore recommended that PMD be measured on the final spool size that will be incorporated into the package.

C. Losses

Every DCF segment introduce a loss which is typically compensated by a booster amplifier. This additional amplifier, in turn, adds noise to the system and degrades the optical signal-to-ratio (SNR). This SNR degradation is of concern to system engineers. An efficient DCF should therefore have low losses.

Intrinsic losses in fibers have been shown to depend on the germania content in the core as well as draw-conditions.[13] Communications grade fibers have normalized index differences Δ of approximately 0.2-0.3% and typical losses of ~ 0.20 dB/km. It has been observed that as the core Δ's increase, the losses gradually increase up to Δ ≈ 1.0 % and then rise rapidly for higher Δ's. Since DCFs have high Δ's ranging from 1 - 3 % the losses can be expected to be higher than communications-grade fibers.

A conventional matched-clad fiber design always allows the propagation of the fundamental mode. Multilayer waveguides, on the other hand, can be designed to make the LP_{01} mode leaky beyond a given wavelength. This property of a multiclad fiber to have a nonzero fundamental mode cutoff wavelength (λ_{c01}) is used effectively in some of the designs by operating the DCF close to λ_{c01} in order to achieve large negative dispersion. The presence of multiple layers and the operation close to cutoff raises the issue of bend sensitivity of the fiber. Bend losses in a fiber can be evaluated theoretically for fibers with simple matched-clad refractive-index profiles; for multilayer waveguides, however, theoretical predictions are not accurate. Also, the analysis of bend losses depends on the bend

radius prescribed by the system designers. An empirical method of evaluating the bend performance of the fundamental mode in fibers involves the calculation of a MAC-number,[14] defined by

$$MAC = \frac{MFD}{\lambda_c}, \tag{3}$$

where MFD is the mode-field diameter and λ_c is the cutoff wavelength of the next higher order mode. For matched-clad single-mode fibers it has been shown that a MAC-number < 8.5 ensures a bend-loss < 0.1 dB (@ 1.55 μm) for 50 bends over a mandrel diameter of 60 mm. During the design process, one can simply use the qualitative feature that smaller MAC-numbers imply better bend performance. By experimentally measuring the bend losses in several multiclad fibers, the designer can then determine the upper bound on the MAC-number. When the loss in a DCF is plotted as a function of wavelength, the bend loss component tends to start rising rapidly at a wavelength λ_d which depends on the MAC-number and the bend radius. One would ideally like to design the fiber such that λ_d > 1560 nm so that only the intrinsic loss would affect the figure of merit of the compensator (defined below).

Another loss mechanism introduced in a packaged DCF module is the splice loss that results from mismatched mode field diameters, a property we consider next.

D. Mode Field Diameter

The mode field diameter (MFD) of the DCF is an important measurement parameter for two reasons. First, when the DCF is fusion-spliced to a conventional 5D fiber, the induced splice loss is directly related to the mismatch of the MFDs. One way to solve the splice-loss problem is to use the thermally expanded core (TEC) technique[15] to match the mode-field-radii of the two fibers prior to splicing. The second constraint on the MFD of the DCF is governed by the maximum power that can be launched into the DCF without introducing nonlinearities. The specific nonlinearities of concern are self phase modulation (SPM) and stimulated Brillouin scattering (SBS).[16,17] The maximum amount of power that can be transmitted without inducing SPM or backward SBS is directly related to the cross-sectional area (A_{eff}) of the mode field and hence to the square of the MFD. In order to minimize the deleterious effects of both these nonlinearities, it is desirable to design the DCFs with large MFDs. The MFD also impacts bend losses of the DCF, as seen in the previous subsection.

E. Modal Noise

Multiple layer fiber designs with larger core diameters allow the copropagation of higher order modes (typically, the LP_{11} and/or LP_{02} modes) which can lead to mode-mixing. If the dispersion characteristics of the higher order modes are different from the fundamental mode dispersion values, modal filters may be needed in the DCF module. Alternatively, methods of launching only the fundamental mode should be available at the input end of the DCF. One method that can be used for analysis is viewing the far-field at the output end of the DCF and looking for spatial patterns that indicate the presence of higher order modes.[18] A more accurate measurement technique involves the measurement of the system BER performance as a function of different mode-coupling conditions. This measurement becomes more important for techniques that require intermodal convertors, e.g., the higher-order mode compensation technique.

III. Compensator Comparison

A figure-of-merit (FOM) for DCFs has been defined in the literature [8] as the ratio of the dispersion in the fiber to the loss of the fiber, viz.,

$$FOM_1\ (ps/nm\text{-}dB) = \frac{D_\lambda\ (ps/nm\text{-}km)}{\alpha_\lambda\ (dB/km)}. \tag{4}$$

The FOM_1 can be used for a direct comparison of different types of DCFs as well as in system designs to evaluate

the decrease in optical signal to noise ratio (SNR) due to the addition of the DCF. An alternate definition, coined by Poole,[19] is given by

$$FOM_2\ (dB/km) = \frac{\alpha_\lambda(dB/km)}{\Gamma}\ , \qquad (5)$$

where Γ is the dispersion D_λ (ps/nm-km) divided by 17 ps/nm-km (dispersion of conventional fiber). In Eq. (5), a smaller FOM_2 implies a better DCF.

It must be noted that the FOM should not be the sole criterion on which DCFs are compared; for example, a DCF with D_λ = - 51 ps/nm-km and α = 0.22 dB/km would have an impressive FOM of 232 ps/nm-dB but for compensating the dispersion in a 360 km span, one would need 120 km of the DCF ! Also, the loss of the DCF, α in Eqs. (4) - (5), should include not only the intrinsic losses of the fiber but also length-normalized values of i) the bend loss which depends on the diameter of the spool on which the fiber is wrapped, ii) splice losses resulting from mismatched mode-field radii and iii) other insertion losses introduced by mode-conversion devices (if a higher-order spatial mode propagates in the fiber). Furthermore, Eqs. (4)-(5) do not take into account the nonlinearity-imposed-limitation on the maximum power that can be transmitted through the DCF. A more comprehensive definition for FOMs is clearly needed.

IV. DCF Examples

Examples of multilayered DCFs fabricated at AT&T are now presented,[20] with a partial listing of the properties described in the previous section.

One multilayered waveguide structure is shown in Fig. 1. This design was primarily chosen for the analysis of the bend performance of the fiber. The preform was drawn to three different outer diameters, namely, 108, 116 and 125 μm. The corresponding core diameters were measured to be 3.4, 3.6 and 3.9 μm, respectively. A spectral loss measurement was made with 200 meters of the fiber wound on a drum of 30 cm diameter. The data (Fig. 2) showed a steep rise in the loss at a wavelength (λ_d) dependent on the fiber diameter. An exact fiber profile was used in a theoretical model[21] for the determination of the mode-field diameter (MFD) of the fundamental mode and the cutoff wavelength (λ_c) of the higher-order mode of the fiber. The ratio of the two parameters provided the MAC-number, which was seen to be directly related to the wavelength at which the steep bend loss edge was observed. Table I shows some of the properties of the fibers. In order to maintain $\lambda_d > 1560$, we see that a MAC-number < 6.0 is desirable. Furthermore, if the fiber is to be wrapped on smaller diameter spools, a smaller MAC-number would be required.

Table I. Bend loss performance of multiclad fibers wound on a 280 mm diameter drum.

Diameter (μm)	λ_d (nm)	λ_c (nm)	MFD (μm)	MAC	D_λ (ps/nm-km)
108	1410	1114	17.62	15.82	- 150
116	1540	1131	7.02	6.21	- 70
125	1640	1420	4.96	3.49	- 30

A fiber preform with a refractive index profile shown in Fig. 3 was drawn to a core diameter of 3.5 μm. The MFD of the fibers was calculated to be 5.40 μm, while the cutoff wavelengths was estimated to be in 1.46 to 1.50 μm range, thus resulting in MAC-numbers of ~ 3.70. The dispersion of the fiber was measured to be -93 ps/nm-km (Fig. 4), with a total loss of 0.40 dB/km when the fiber was wound on a drum of 30 cm diameter. A figure of merit of 232 ps/nm-dB was thus obtained. The dependence of the MAC-number on bend radius was studied by wrapping the

fiber on spools of varying diameters. The chromatic dispersion and PMD increase with decreasing bend radius, while the wavelength at which the loss rises rapidly (λ_d) decreases, as summarized in Table II.

Table II. Performance variation as a function of bend radius.

Bend Radius (mm)	λ_d (nm)	PMD (ps/ $\sqrt{km}$)	D_λ (ps/nm-km)
140	1560	0.18	- 93
76	1530	0.19	- 94
44	1485	0.27	- 95

V. Conclusion

Recent advances in preform fabrication techniques and fiber designs have allowed researchers to reach FOMs of 250 -300 ps/nm-dB making the use of DCFs very practical from a system viewpoint.[20,22] The design issues of DCFs have been studied fairly exhaustively and the accent is now on production, packaging and qualification. A key issue of DCFs that intertwines all the above is the measurement of the important parameters. While the measurement techniques are expected to be the same as those for conventional fibers, it is our hope that this brief summary of the critical parameters and the trade-offs involved will help set the guidelines for the measurement community.

VI. References

1. A. F. Elrafaie, R. E. Wagner, D. A. Atlas, and D. G. Daut, *J. Lightwave Technol.* **6**, pp. 704-709 (1988).
2. E. B. Treacy, *IEEE J. Quantum Electron.* **QE-5**, p.454 (1969).
3. O. E. Martinez, *IEEE J. Quantum Electron.* **QE-23**, p.59 (1987).
4. A. Yariv, D. Fekete, and D. M. Pepper, *Opt. Lett.* **4**, pp. 52-54 (1979).
5. C. D. Poole, K. T. Nelson, J. M. Wiesenfield, and A. R. McCormick, *Opt. Lett.* **17**, pp. 985-987 (1992).
6. A. M. Vengsarkar, W. A. Reed, and C. D. Poole, *Opt. Lett.* **17**, pp. 1503-1505 (1992).
7. C. D. Poole, J. M. Wiesenfield, and D. J. DiGiovanni, *IEEE Photon. Technol. Lett.* 5, pp. 134-136 (1993).
8. J. M. Dugan, A. J. Price, M. Ramadan, D. L. Wolf, E. F. Murphy, A. J. Antos, D. K. Smith, and D. W. Hall, *Proc.OFC '92*, Post Deadline Paper, PD-14, pp. 367-368 (1992).
9. H. Izadpanah, C. Lin, J. Gimlett, H. Johnson, W. Way, and P. Kaiser, *Proc. OFC '92*, Post Deadline Paper, PD-15, pp. 371-372 (1992).
10. A. V. Belov, S. I. Miroshnichenko, and V. A. Semenov, *OFC '93*, Paper ThJ2, pp. 203-204 (1993).
11. A. M. Vengsarkar and W. A. Reed, *Opt. Lett.* **18**, pp. 924-926 (1993).
12. A. M. Vengsarkar, A. E. Miller, and W. A. Reed, *Proc.OFC '93*, Post Deadline Paper, PD13, pp. 56-59 (1993).
13. S. T. Davey, D. L. Williams, D. M. Spirit, and B. J. Ainslie, *Proc. SPIE* **1171**, pp. 181-190 (1989).
14. S. -V. Chung, *Proc. Internat. Wire & Cable Symp.* **37**, pp. 704-709 (1988).
15. H. Hanafusa, M. Horiguchi and J. Noda, *Electron. Lett.* 27, pp. 1968-1969 (1991).
16. G. P. Agrawal, *Nonlinear Fiber Optics*, Chapter 4, Academic Press, New York (1989).
17. Y. Aoki, K. Tajima, and I. Mito, *J. Lightwave Technol.* **6**, pp. 710-719 (1988).
18. E. Snitzer and H. Osterberg, *J. Opt. Soc. Amer.* 51, pp.499-505 (1961).
19. C. D. Poole, "Dispersion compensation for lightwave systems", OFC Tutorial ThJ1, *Proc. OFC '94*, San Jose, February 1994.
20. A. M. Vengsarkar, A. E. Miller, W. A. Reed, M. Haner, A. H. Gnauck, and K. L. Walker, Paper ThK2, *Proc. OFC '94*, San Jose, February 1994.
21. T. Lenahan, *Bell Sys. Tech. J.* **62**, pp. 2663-2694 (1983).
22. M. Onishi, H. Ishikawa, M. Shigematsu, H. Kanamori, M. Nishimura, Paper ThK1, *Proc. OFC '94*, San Jose, February 1994.

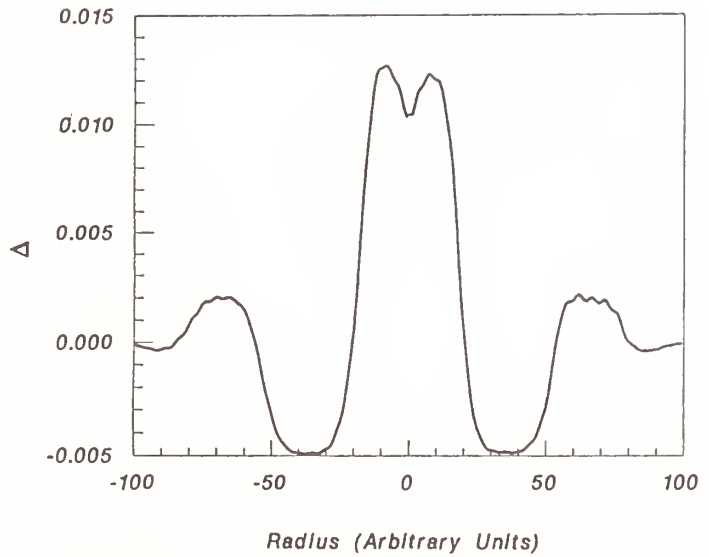

Fig. 1. Refractive index profile of DCF preform used in the analysis of bend performance vs. MAC-number.

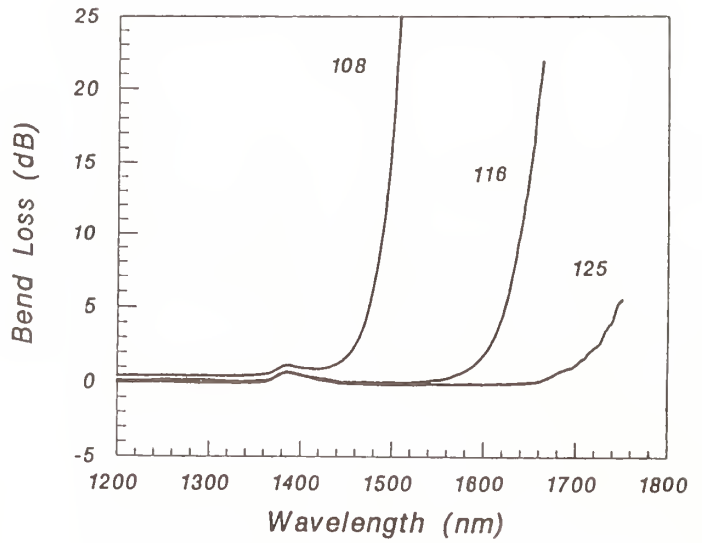

Fig. 2. Bend loss variation for DCFs of Fig. 1 drawn to different diameters (shown in μm). See Table I.

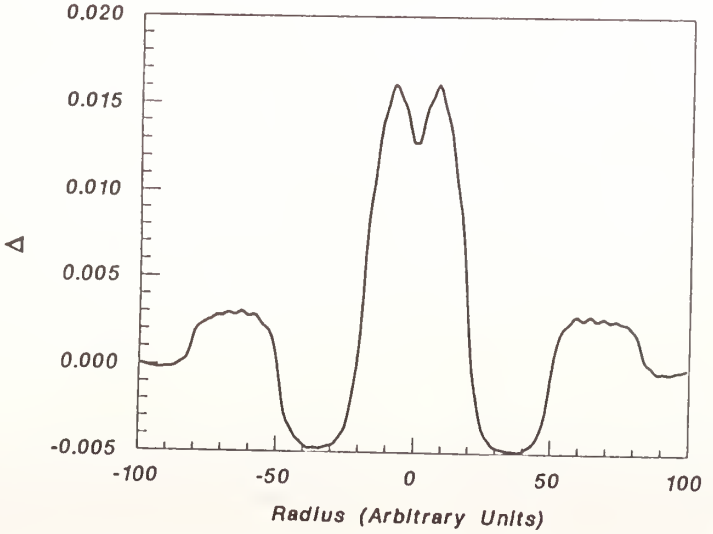

Fig. 3. Refractive index profile of DCF preform used in the analysis of fiber properties vs. bend radius.

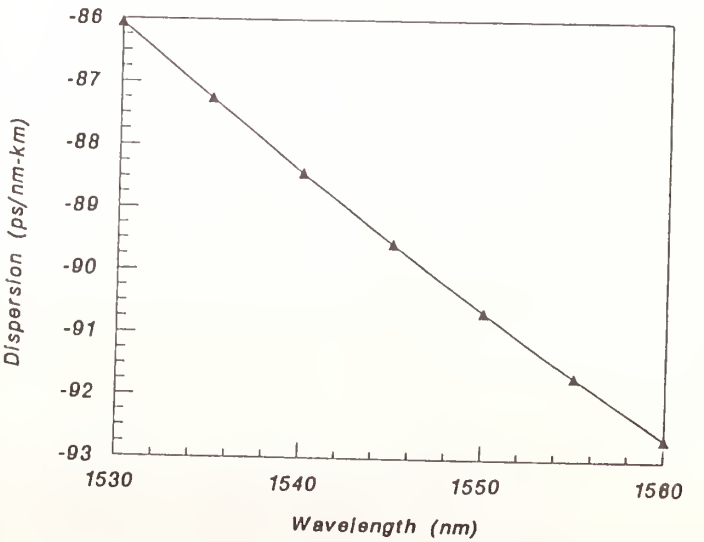

Fig. 4. Measured dispersion of DCF of Fig. 3. Note the negative slope of the dispersion curve. See Table II.

Tailoring of Dispersion Compensation Fibers with High Compensation Ratios up to 30

R. Boneß (TU Dresden), J. Vobian (FTZ Darmstadt), S. Unger, J. Kirchhof (IPHT Jena)

In the last two years, a considerable interest in the development of dispersion compensating fibers (DCF) has been taken. This is due to the possibility of upgrading the installed systems from the 1.3 μm to the 1.55 μm window using equalizing fibers. At the OFC ' 91 and OFC '92 some papers were presented with various compensation fibers with a compensation ratio (CR) up to 30. But this ratio has been achieved with a two-mode fiber which is difficult to handle and expensive. With pure monomode fibers only a CR of about 13 has been achieved [1]. Up to now systematical investigations of such DC fibers have not been carried out.

In this paper we will show methods for tailoring DC fibers with a high CR for monomode fibers with various profiles. We started with an iterative numerical optimization of the refractive - index profile and radius parameters with a prescribed CR up to 30 or even higher. Being interested in the second order dispersion compensation, we have to prescribe the dispersion values in the vicinity of 1.55μm. It is necessary that the dispersion decreases monotonically near λ=1.55μm. We have shown [2] that it is not trivial to fulfill these preconditions. Principally we can investigate any smooth or nonsmooth refractive-index profile, but, first of all, we have restrained our studies on W , TC (triple clad) and QC - fibers.

The optimization programme minimizes the standard deviation of the actual dispersion-, field radius- and cutoff frequency values from the prescribed parameters for some discrete wavelengths with the GAUSS-LEVENBERG-MARQUARDT-algorithm [3]. Although this method is globally convergent, in general, it may happen that no solution exists for the prescribed parameters. Nevertheless the algorithm finds solutions (relative refractive-index steps, radius) in dependence on the initial profile, in most cases. We also control the PETERMANN-I and PETERMANN-II field radii (w_f and w_n). These values strongly depend on the spectral dispersion function and cannot be defined independently of the dispersion behaviour.

Our programme is based on a very stable and accurate method for dispersion calculations without any numerical differentiation [4]. In this way, we obtained a high stability which is absolutely necessary for the unconstrained optimization method due to the operation near the cutoff frequency of the LP_{01}- mode.

In this paper we will present some calculated optimized profiles for the compensation ratios CR=13, 20 , 30, 40, 50 and the corresponding dispersion and field-radii curves in dependence on the wavelength. Furthermore we will discuss the results and show that technological barriers make it difficult to achieve CR greater than 30, as a consequence of the high refractive-index steps ($\geq$ 3%). Moreover, the w_f/w_n-ratio increases monotonically to 3...4 with increasing CR. This ratio is a measure of the sensitivity of the fiber to deformations. The required accuracy cannot be implemented in practice.

As an example, we present some spectral dispersion- and field radius curves of fibers with QC-profiles (Fig. 1).

Figure 1. demonstrates that the chromatic dispersion decreases monotonically with increasing wavelength. With increasing CR the ratios w_f/w_n spread monotonically.

First experiments were undertaken to implement DC fibers. As an example, we present results of a triple clad (TC) fiber fabricated by MCVD. Fig. 2 shows the geometry. The core diameter is 1.68 µm, the cladding diameter 125.2 µm. As the consequence of the very small core diameter, it is not possible to measure a quantitatively correct n(r)-profile using the conventional RNF-measuring technique. The core level $n(r \cong 0)$ cannot be resolved and is, therefore, too low. For the n(r)-measurements shown in Fig. 3 a part of the preform was drawn to a fiber with an outer diameter of 300 µm.
The optical loss at 1.55 µm wavelength was measured to be 5 dB/km. This value can be improved to a certain degree, but a natural limit is given by the high dopant concentration.

In Fig. 4 the measured group delay curve and the calculated (5-term Sellmeier fit) dispersion curve are presented.

The characteristic data are:
D (1300 nm) = -247.2 ps/km·nm
D (1540 nm) = -166.7 ps/km·nm
D (1550 nm) = -157.6 ps/km·nm
λ_0 = 1687.9 nm.

The chromatic dispersion measurements were performed with the aid of a Raman fiber laser with a mode-locked Nd:YLF laser used as pump source. The peak power of the optical pulses is up to 4.5 kW (≤ 17 W cw power), the pulse width is about 35 ps, the output power stability is better than ± 0,8 %. The spectral range extends from 1100 to 1800 nm. A large number of equidistant measuring points (up to 30) can be obtained. By these means a high accuracy, a good reproducibility can be achieved. The standard deviation is comparable with that of interferometric measuring methods. It is important to determine the zero-dispersion wavelength λ_0 of dispersion compensated ultralong hauls for high-bit rate transmission systems, soliton systems, e.g., as exactly as possible.

References:

[1] A.M.Vengsarkar, A.E. Miller, M. Haner, A.H. Gnauck, W.A. Reed, K.L. Walker: Fundamental-mode dispersion-conpensating fibers: disign considerations and experiments Thk2, pp. 225-227, OFC'94, San José

[2] Boneß, R., Vobian, J. , Kirchhof, J. and Unger,S.: Tailoring of Dispersion Compensating Fibers with high Compensation Ratios up to 30. COST- WORKSHOP 94, OPTICAL TELECOMMUNICATIONS pp. 40 -41, Nice

[3] Ortega, J. M. , Rheinboldt, C. : Iterative Solution of nonlinear Equations in several Variables. New York, Academic Press 1970

[4] Boneß, R., Nowak, W. : Lichtwellenleiter mit besonderem Dispersionsverhalten. Nachrichtentechnik/Elektronik Berlin 42 (1992) 5, S.184 - 187

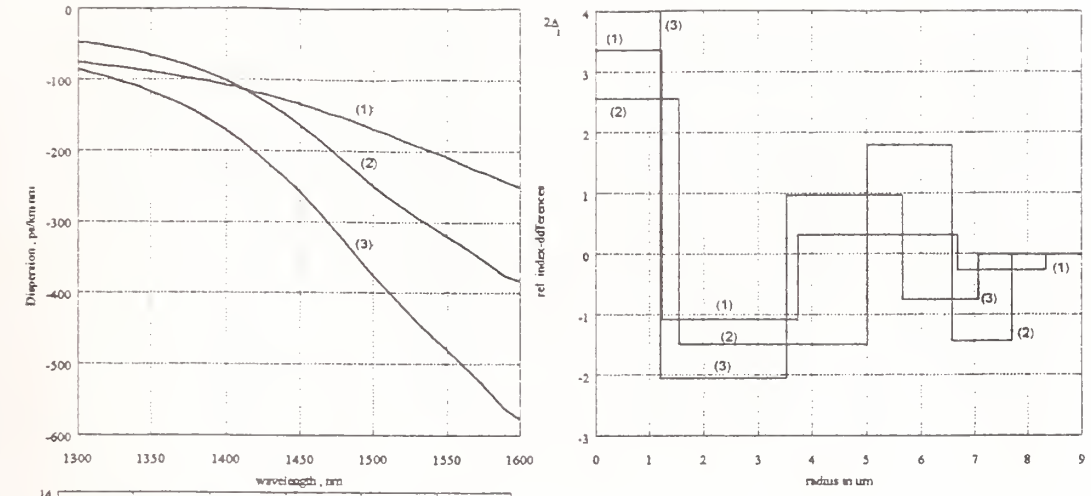

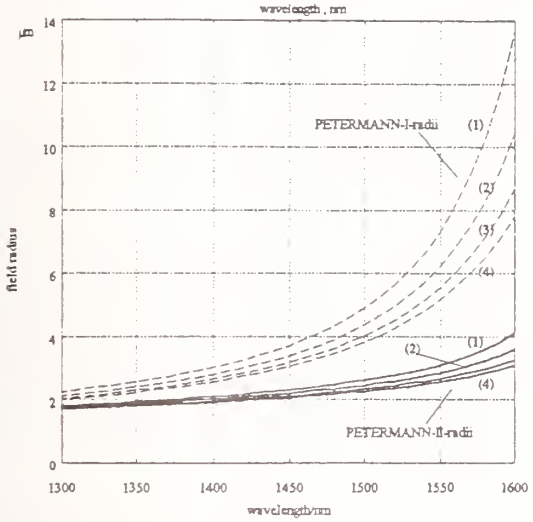

Fig. 1 QC-profiles, chromatic dispersion and field radii. CR=13 (1), CR=20 (2), CR=30 (3)

D(1550nm) = -280, -320, -480 ps/km·nm

Fig. 1 QC-profiles,,chromatic dispersion and field radii. CR=13 (1), CR=20 (2), CR=30 (3) D(1550nm)=-280, -320 and -480ps/km nm

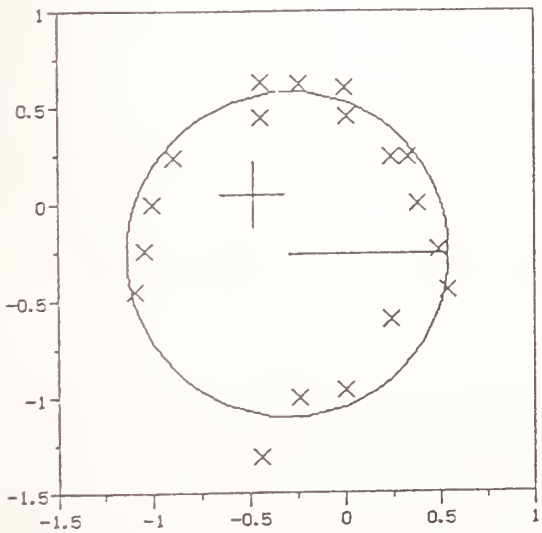

Fig. 2 Core geometry of the triple clad (TC) fiber

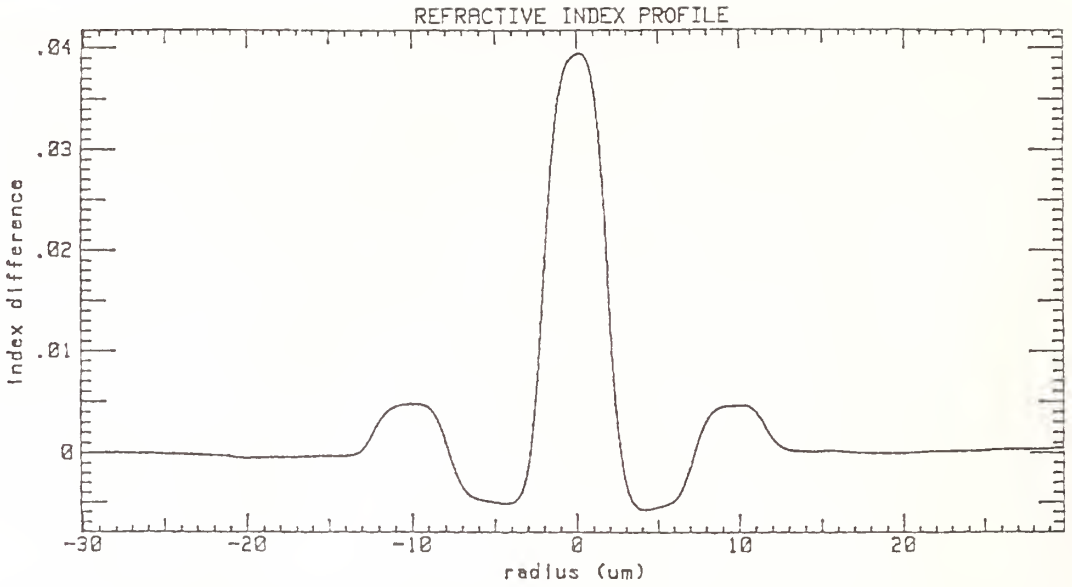

Fig. 3 Refractive index profile of the triple clad fiber

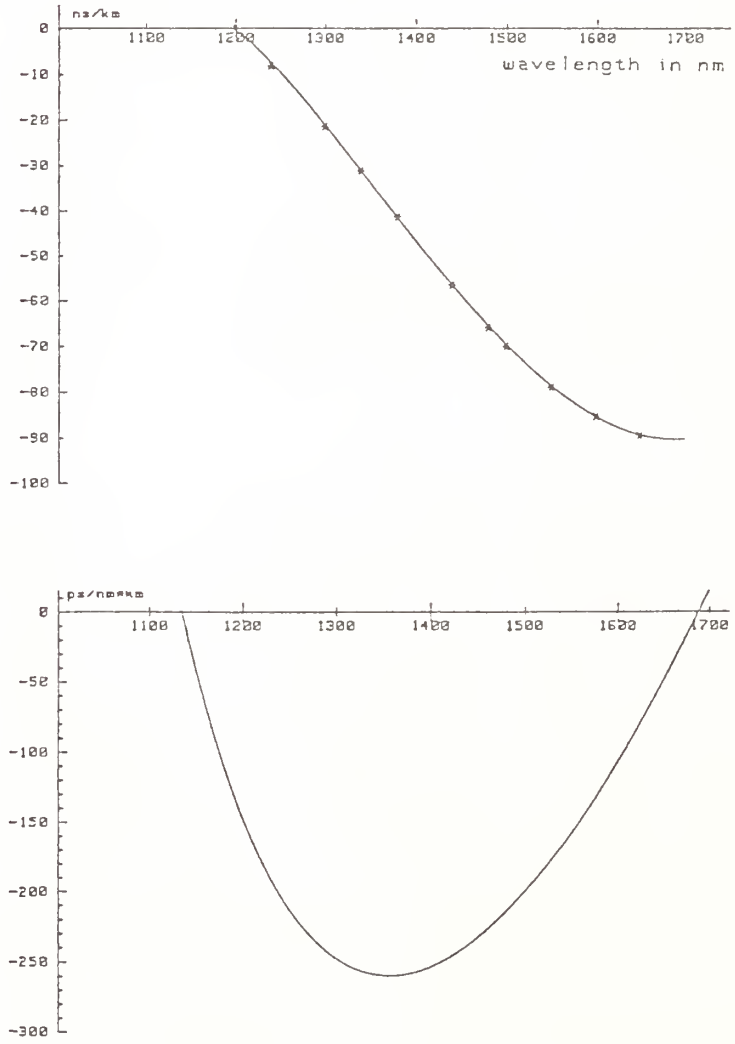

Fig. 4 Group delay and chromatic dispersion of the TC-fiber

Characterization of Single Polarization Fiber

M. J. Messerly, R. E. Budewitz, and B. K. Nelson
3M Fiber Optics Laboratory
MS 260-5B-08
St. Paul, MN 55144-1000
and
R. C. Mikkelson
Department of Physics and Astronomy
Macalester College
1600 Grand Avenue
St. Paul, MN 55105

Introduction

Single polarization (PZ) optical fiber[1,2,3,4], like polarization maintaining (PM) fiber, has a birefringent core that removes the degeneracy between the two polarization states of the fundamental mode. Unlike PM fiber, PZ fiber polarizes light; typically, the extinction is better than 40dB after a few meters. The fiber has recently found favor as a pigtail for electro-optical devices, and as a polarizing element in sensors.

Most of the important characteristics of the PZ fiber are common to telecommunications fiber, and are measured by the same techniques. Some are unique, though, and require new or modified methods. In this paper we describe the measurement of attenuation, cutoff, and width of the operating band. In addition, we compare the traditional technique of measuring extinction to the method devised by Feth and Blake[5].

Fundamental Mode Attenuation

We measure the spectral attenuation of a fiber's two principal polarization states with commercially available equipment (Photon Kinetics FOA2000), modified by placing a Glan-Thompson polarizer between the source and launch objective. The equipment is not intended for polarization measurements, and has (understandably) two shortcomings. First, the monochromator slightly polarizes light from the source (by about 5dB). Second, the objectives are not free of strain and tend to mix the polarization states. We sidestep the first problem by making a cutback measurement for each polarization (rather than rotating the polarizer to compare the two), and accept that the second limits the dynamic range of a polarization measurement to roughly 15dB.

Figure 1 shows the attenuation of the fast and slow polarization states of a 4m sample of fiber, wrapped eight times on a 75mm mandrel. The logarithmic plot shows that the loss increases exponentially with wavelength. The data in the Figure, while repeatable, are atypical in two ways. First, it is linear over 100nm; most curves are only linear over about 70nm. Second, the slope of the two lines is nearly the same; fairly often, the

slope of one polarization is significantly steeper than that of the other. (But after 150 measurements we see no bias -- the fast state cuts off at a steeper rate as often as the slow.) We attribute deviations from linearity to the equipment shortcomings described above. We are not sure if the differences in slope are real or a measurement anomaly.

Early attenuation data suggest that the loss per wrap is a better metric than the loss per unit length. Figure 2 shows the loss of the fast polarization state of a sample wound 4, 8, and 16 times on a 75mm mandrel; the data are normalized by the number of wraps. Since we hold the wrap diameter at 75mm, a plot of the loss per unit length looks the same; to distinguish the two, we also vary the wrap diameter. Figure 3 shows similar plots for the same sample wound 4, 8, and 24 times on 150mm, 75mm, and 25mm mandrels, respectively. Figure 3a is a plot of the loss per unit length; Figure 3b is a plot of the loss per wrap. The latter indicates that the loss per wrap, rather than the loss per length, stays constant.

We thought these results might have been affected by the 10nm FWHM spectral width of the monochromator or the equipment limitations described above. To check, we measured the samples of Figure 3 with laser sources and strain-free optics. Reassuringly, these points fall in line the others; the laser-based measurements are plotted as +'s.

Cutoff and Operating Width

Cutoff. We define cutoff to be the wavelength at which the attenuation of the fast polarization state hits 1dB per wrap. We choose this number because, for a typical number of wraps, it falls within the limits of our equipment. The cutoff of the sample in Figure 1 is 860nm, determined by a least-squares fit.

Operating Width. We define the operating width to be the difference between the 0.01dB per wrap wavelength of the slow polarization and the 1dB per wrap wavelength (cutoff) of the fast, divided by the fast cutoff wavelength. The operating width of the sample fiber of Figure 1 is 10%.

Extinction

We measure extinction by the method devised by Feth and Blake[5]. It requires four power readings, taken with both the polarizer and analyzer parallel or perpendicular to the guiding axis, and with one parallel and the other perpendicular to it (both permutations of the latter). The extinction is the ratio of the power read when the two are parallel to the guiding axis to the power read when they are perpendicular. We find that it is typically 35dB to 40dB for a broad-band source such as an SLD, and often exceeds 70dB (measurement limited by power) for a laser source.

A more common technique involves exciting the two principal polarizations equally, then analyzing the light emitted by the fiber to determine the extinction (the "50/50 launch").

Even the best strain-free objectives limit this method to 40-45dB, as Figure 4 shows. The 50/50 launch saturates at roughly the extinction we measure for the pair of objectives in our setup (43dB), even though the four-point method suggests that some samples produce much higher values.

Summary

Early data suggest that the best metric of fiber loss is the attenuation per wrap, which increases exponentially with wavelength. We define cutoff to be the wavelength at which the fiber's fast polarization state hits 1dB of loss per wrap, and propose a measure of operating width. We also present data from two hundred extinction measurements, which show that even strain-free lenses limit the traditional technique to 40dB. In contrast, the technique devised by Feth and Blake appears capable of reliably measuring much higher values.

References

1. J. R. Simpson *et al.*, "A single-polarization fiber," *J. Lightwave Technol.*, vol. LT-1, pp. 370-373, 1983.

2. K. Tajima *et al.*, "A new single-polarization optical fiber," *J. Lightwave Technol.*, vol. 7, pp. 1499-1503, 1989.

3. M. J. Messerly *et al.*, "A Broad-band single polarization optical fiber," *J. Lightwave Technol.*, vol. 9, pp. 817-820, 1991.

4. Y. Kubo, M. Takagi *et al.*, "Development of an absolute single-polarization optical fiber," *Sumitomo Electric Tech. Rev.*, pp. 60-63, 1991.

5. J. Feth and J. Blake, "Characterization of high birefringence fiber for sensor applications," *Tech. Digest - Symposium on Optical Fiber Meas.*, NIST Special Publication 792, 1990, pp. 109-114, 1990.

Figure 1
Attenuation of a PZ Fiber

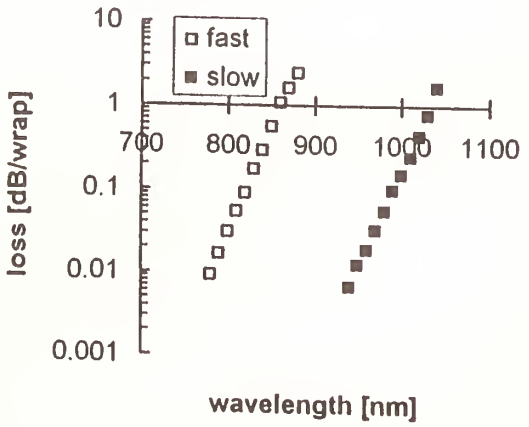

Figure 2
Effect of # of Wraps on Loss

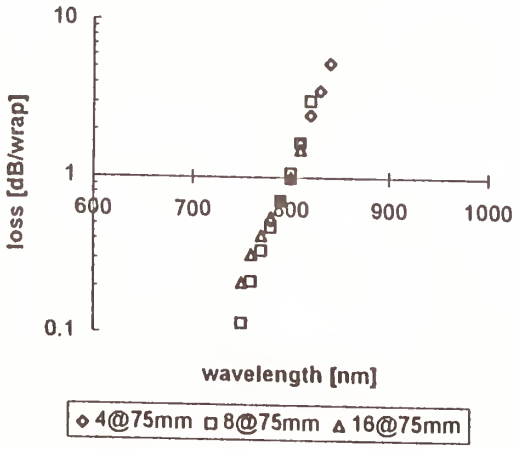

Figure 3a
Effect of Wrap OD on Loss

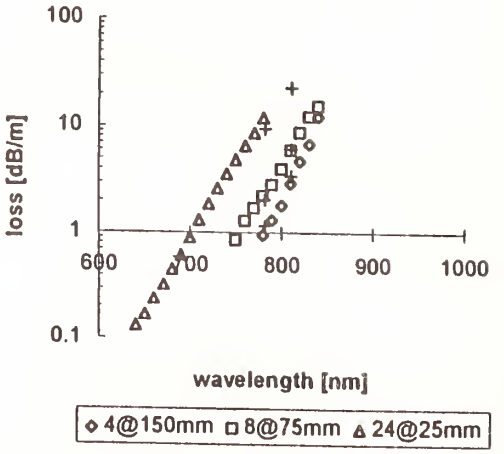

Figure 3b
Effect of Wrap OD on Loss

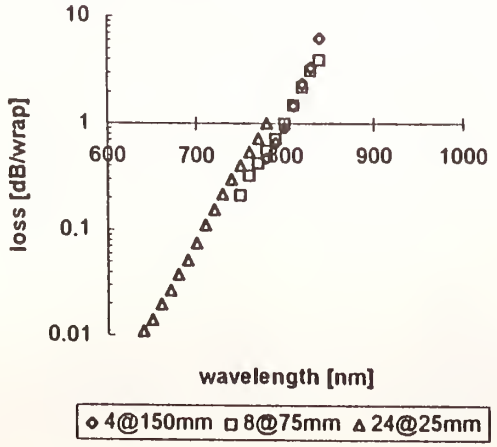

Figure 4
Comparison of Extinction Measurements

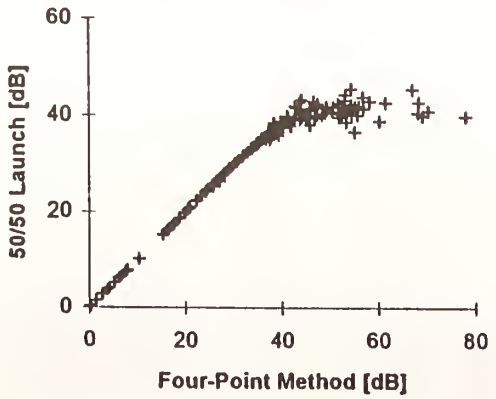

New Direct Measurement Technique of Polarization Dependent Loss with High Resolution and Repeatability

Naoyuki Mekada, Abdallah AL-Hamdan *, Tomohiro Murakami, Masanori Miyoshi

Santec Photonics Labs., Komaki-shi, Aichi-Ken, Japan
*Santec U.S.A Corp. , Holmdel, New Jersey

Abstract

Polarization Dependent Loss (PDL) of optical components is a very important parameter to specify with high resolution and accuracy. In this letter, we describe a new direct measurement technique especially designed for low PDL optical components and provide high resolution (0.001 dB) and high repeatability ($< \pm 0.003$ dB). This technique is not sensitive to the light source intensity fluctuations.

Introduction

Polarization Dependent Loss (PDL) is the maximum insertion loss variation in optical components as the input light's state of polarization is varied over all polarization states. Accumulation of PDL for various optical components in light-wave systems can produce large variations in optical power as the state of polarization changes due to environmental conditions. Therefore, It is very important to quantify PDL with high resolution and accuracy for optical components.

Conventional PDL measurement techniques, such as the power meter technique, are limited by the residual PDL of the measurement equipment with an uncertainty of more than 0.01 dB[1]. A technique, with an uncertainty of $\pm$ 0.001 dB, was proposed utilizing an erbium-doped fiber (EDF) as a depolarizer to reduce the detector PDL [2]. The main disadvantage of pervious techniques is that, they require a highly stable light source. In this letter, the proposed measurement technique is simple direct measurement technique and not sensitive to the light source intensity fluctuations [3].

Measurement Technique

The new technique is based on the fact that the maximum and minimum insertion losses are located at orthogonal polarization states and lie at the same vertical trace on the poincare' sphere. The measurement set up is shown in Fig. 1. The light emitted by the LED light source is filtered out using an interference filter with a 3 dB bandwidth of 1.0 nm, then travels through the polarizer located in the automatic polarization controller to generate a linear polarization.

After the polarizer, the light travels into the half wave plate (HWP) which rotates 90^o with a step of $\Delta\phi^o$ ($\approx 1.8^o$). This will rotate the polarization state around the equator of the poincare' sphere in 0.25 seconds, fig.2 shows the trace generated from rotating the HWP 90^o with a step of $\Delta\phi^o$.

The light continues through the quarter wave plate (QWP) in which the polarization state of the light is transferred into a vertical plan resulting in a vertical trace for a 90^o rotation of the HWP, as shown in fig. 3.

For every full rotation of the HWP, the QWP will rotate with a step of $\Delta\alpha^o$ ($\approx 3.6^o$) covering a total of 90^o and generating N vertical traces to cover all polarization states. Fig. 4 shows the poincare' sphere with N vertical traces.

PDL is measured within 0.25 seconds for each vertical trace resulting in N values for PDL, then the worst case PDL is selected.

$$\mathbf{PDL = Max. \{ PDL_1, PDL_2,.....PDL_N\}}$$

Since the PDL measurement of each trace takes only 0.25 seconds, this technique is not sensitive for the light source power fluctuations. An automatic two dimensional calibration, using a short SM fiber, compensates for the loss variations of the polarization controller. The detector used in this experiment is selected with a very low PDL value of less than 0.002 dB.

Measurement Results

Fig. 5 shows the PDL test results for a 30 cm SM fiber without disturbing the measurement. PDL values ranging from 0.001 dB to 0.003 dB, were measured with a high resolution of 0.001 dB and a repeatability of ± 0.001 dB, measurement was repeated 20 times.
Fig. 6 shows the PDL test results for the same fiber while disturbing the measurement, the repeatability is ± 0.0025 dB, and measurement was repeated 20 times.
Fig. 7 shows the test results for the beveled fiber with 8° angle. The beveled fiber, with 8° angle, has a theoretical PDL value of about 0.017 dB. The measured average PDL value is 0.0153 dB with a repeatability of ± 0.0005 dB, measurement was repeated 100 times. The beveled fiber might be a good candidate standard for PDL measurement.
Fig. 8 shows the PDL test results for an isolator, a PDL value of 0.08 dB was measured. The graph also shows the loss variations versus the rotation angle of the HWP and the QWP.

Conclusions

A simple direct measurement technique with a high resolution of 0.001 dB and repeatability of ± 0.003 dB has been introduced. This technique is not sensitive to the light source intensity fluctuations while covering all polarization states.

References

[1] Bellcore, *TA-NWT-001073*, no. 2.
[2] Bruce Nyman and Gregory Wolter, *IEEE Photonics Technology Letters*, VOL. 5, NO. 7 July 1993
[3] Santec Photonics Labs, *Optical Module Test System for PDL Measurement Technical Notes* , V 2.9.94

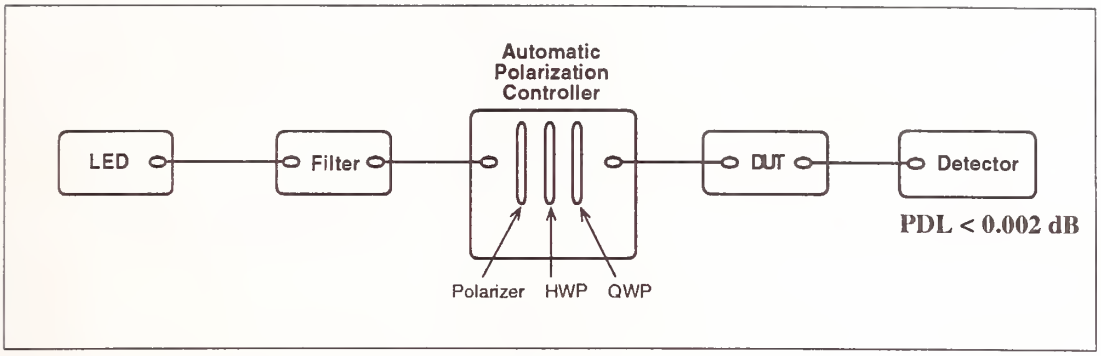

Fig.1
PDL Measurement Experimental Set up

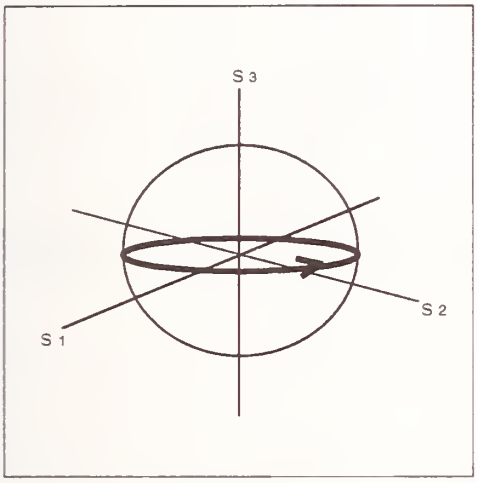

Fig.2
Polarization State Trace after HWP
(90° HWP rotation)

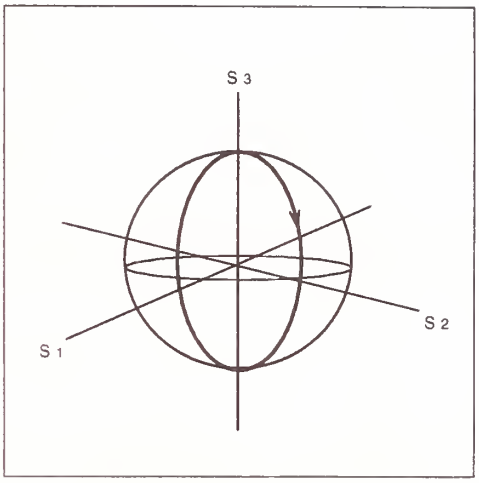

Fig. 3
Polarization State Trace after QWP
(90° HWP rotation)

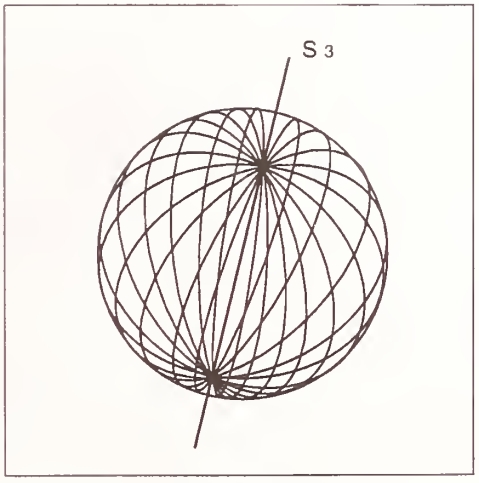

Fig.4
N Plarization state Traces with 90° rotation of QWP
and 90° rotation of HWP

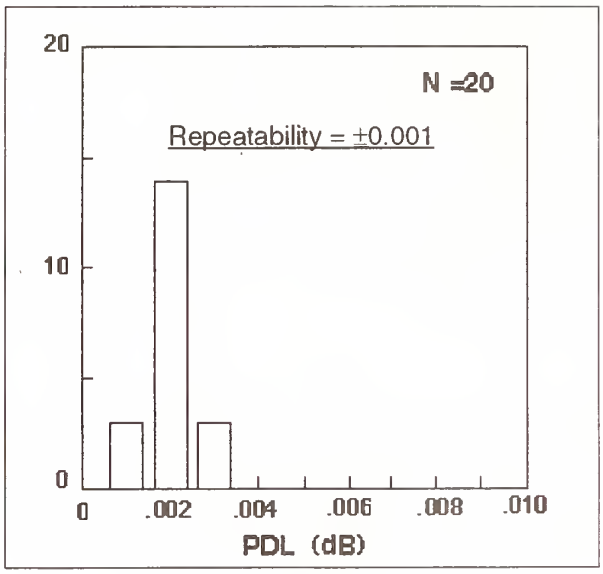

Fig. 5

PDL measurement results for SMF(30cm)

(measurement is repeated 20 times w/o disturbing fiber)

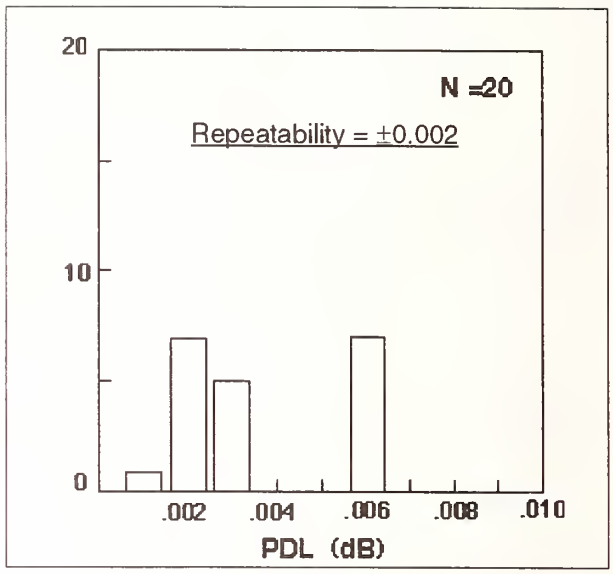

Fig . 6

PDL measurement results for SMF(30cm)

(measurement is repeated 20 times with disturbing fiber)

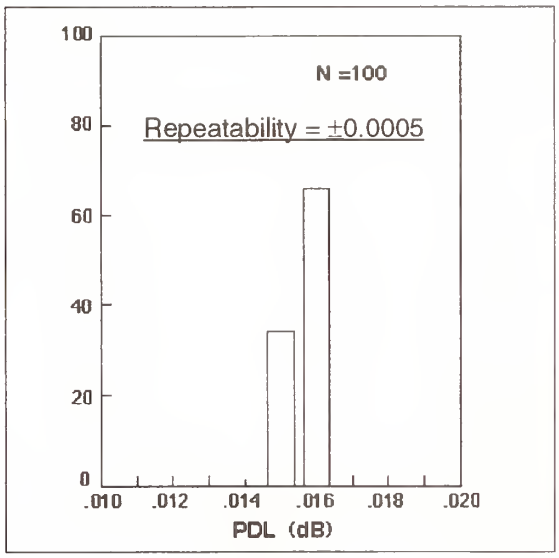

Fig. 7

PDL measurement results for 8° fiber(30cm)

(measurement is repeated 100 times w/o disturbing)

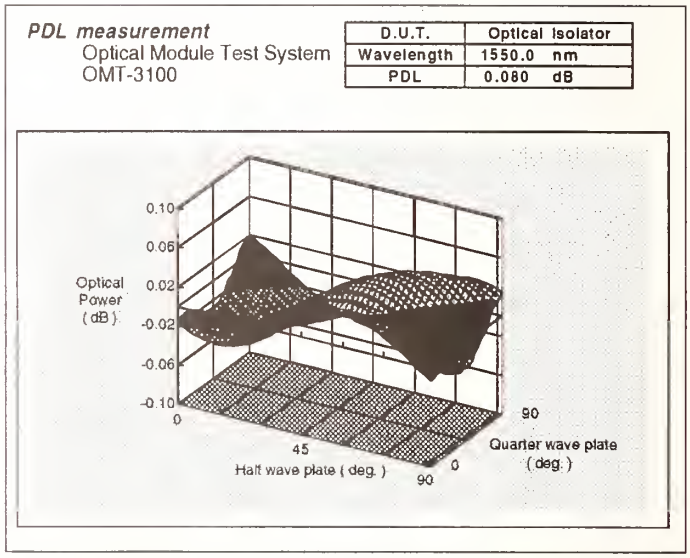

Fig . 8

PDL Measurement results for an Isolator

(Loss variations-vs-HWP and QWP angle)

The Statistics of Polarization Dependent Losses

N. Gisin
Group of Applied Physics
University of Geneva, 1211 Geneva 4, Switzerland

Abstract

The statistics of the attenuation of systems containing several components with polarization dependent losses are described.

1 Introduction and Definitions

In systems containing several elements with Polarization Dependent Losses (PDL) connected by standard optical fibers, the global attenuation and the global PDL may fluctuate. This will affect the systems performance [1, 2, 3]. Note that the global attenuation is generally **not** the sum of the attenuation (in dB) of the elements! Moreover, this is also true for unpolarized light sources. Indeed, the first PDL element will partially polarize the light, hence the attenuation of the second PDL element depends on the relative orientation of the two PDL elements and on the polarization rotation produced by the connecting standard fiber.

The fact that the attenuation of systems with PDL may fluctuate has clearly an impact on the characterization of such systems. Indeed, if the attenuation measurements show some variations, it should not all be attributed to the instrument's limitations, but it should, at least in part, be interpreted as due to the physics of PDL.

For the description of polarization states, we shall use the Poincaré sphere. Remember that the degree of polarization is equal to the length of the vector $\vec{M}$:

$$degree\ of\ polarization = |\vec{M}|,$$

and that the vector $\vec{M}$ relates simply to the Stokes parameters $S_0, \vec{S} = (S_1, S_2, S_3)$:

$$\vec{M} = \frac{\vec{S}}{S_0}$$

The transmission coefficient T through an optics with PDL can be characterized by two numbers between 0 (opaque) and 1 (transparent): the maximum transmission coefficient T_{max} and the minimum transmission coefficient T_{min}. The corresponding polarization states $\vec{M}_{max}$ and $\vec{M}_{min}$ need not be linear, but they their degree of polarization is always maximal: $|\vec{M}_{max}| = |\vec{M}_{min}| = 1$. Furthermore, they are always orthogonal: they are opposite on the Poincaré sphere: $\vec{M}_{max} = -\vec{M}_{min}$. Unpolarized light can be considered as an equal mixture of any pair of orthogonal polarization. In particular unpolarized light can be considered as an equal mixture of the polarization states corresponding to the maximum and minimum transmission coefficients. Hence the corresponding transmission coefficient, T_{depol}, is the average of the maximum and minimum transmission coefficients:

$$T_{depol} = \frac{T_{max} + T_{min}}{2} \tag{1}$$

Note that such a simple relation does not hold if one expresses the transmission coefficients in dB.

For PDL we propose the following notation and definition:

$$PDL = \Gamma = \frac{T_{max} - T_{min}}{T_{max} + T_{min}} \tag{2}$$

Often it will be useful to define a vector $\vec{\Gamma}$ parallel to $\vec{M}_{max}$ and of norm defined as above. The transmission coefficient for an arbitrary incident polarization state $\vec{M}_{in}$ is then given by:

$$T = T_{depol}(1 + \vec{M}_{in}\vec{\Gamma}) \tag{3}$$

Sometimes PDL is defined as the difference between T_{max} and T_{min} expressed in dB [2, 4]:

$$PDL_{dB} = 10Log(\frac{T_{max}}{T_{min}}) = 10Log(\frac{1+\Gamma}{1-\Gamma}), \tag{4}$$

but, as for T_{depol}, we shall see that dB is not a convenient "units" for the present investigation.

2 Combination of several components with PDL

Real optical links in LANs incorporate many PDL elements. Their relative orientations can not be controlled. Moreover they are not fixed, but fluctuate in time due to the effect of the connecting fibers. A statistical analyses of the attenuation is thus necessary. In this section we shall consider the mean attenuation, its standard deviation and the maximum and minimum values, all expressed in transmission coefficient (number between 0 and 1) and in dB.

The attenuation of the connecting fibers will not be considered separately, but is included in the mean attenuation T_{depol} of the PDL elements.

The mean attenuation and its maximum and minimum values are easy to express [5]:

$$M(T_{1..N}) = T_{depol1}T_{depol2}...T_{depolN} \tag{5}$$

$$T_{max1..N} = T_{max1}T_{max2}...T_{maxN} \tag{6}$$

and similarly for $T_{min1..N}$. The global PDL $\vec{\Gamma}_{1..N}$ however is given by a complicated expression [6], leading also to intractable expressions for the standard deviation of the global attenuation $\sigma(T_{1..N})$. Consequently, in the following we shall restrict ourself to the case of small PDL: $\Gamma_j \ll 1$. This is anyway the case of practical interest in realistic optical networks. Under this condition, the global PDL $\vec{\Gamma}_{1..N}$ and the standard deviation of the global attenuation $\sigma(T_{1..N})$ simplify to:

$$\vec{\Gamma}_{1..N} = \Sigma_{j=1..N}\vec{\Gamma}_j + O(\Gamma^2) \tag{7}$$

$$\sigma(T_{1..N}) = M(T_{1..N})\sqrt{\frac{N(N-1)}{6}}\Gamma^2 + O(\Gamma^3) \tag{8}$$

These approximate expressions have been checks by comparing them to "exact" solutions obtained with a Monte-Carlo numerical simulation. The agreement is excellent. Figure 1 illustrates the above relations, the maximum and minimum transmission coefficients are also displayed. The mean losses and PDL of each of the 20 elements have been chosen identical, but the orientations are chosen at random.

Decibels are not appropriate units for fluctuating losses, since the Log of a mean differs from the mean of the Log. However, under the same condition as above of small PDL, $\Gamma_j \ll 1$, the expression for the mean and standard deviation simplify:

$$M(-10Log(T_{1..N})) = -10\Sigma_{j=1..N} Log(T_{depolj}) + O(\Gamma^4) \tag{9}$$

$$\sigma(-10Log(T_{1..N})) = \frac{10}{Ln(10)}\sqrt{\frac{N(N-1)}{6}}\Gamma^2 + O(\Gamma^3) \tag{10}$$

These approximate expressions have also been checks by comparing them to "exact" solutions obtained with a Monte-Carlo numerical simulation. Again the agreement is again excellent, as illustrated on Figure 2.

3 Conclusion

Polarization Dependent Losses influences the system performance and its characterization. The coherence of the light propagating in the network becomes relevant. Moreover, even neglecting this effect, simple concepts like the attenuation become more subtle due to the random orientations of the various components with PDL. As a consequence attenuation is a random number. Expressions for the mean attenuation and its standard deviation have been derived and checked against numerical simulations.

For small PDL, the global attenuation is well approximated by the sum of the attenuation (in dB) of the components. The standard deviation, eq. (10), grows essentially linearly with the number of components with PDL and is proportional to the square of mean PDL of the components.

4 Acknowledgments

Financial support by the Swiss Telecom is gratefully acknowledged.

References

[1] E. Lichtman, OFC'94 Technica Digest, pp 257-258, 1994.

[2] C.D. Poole and T.E. Darcie, J. Lightwave Tech. **11**, 1749, 1993.

[3] Burgmeijer J.W. and al., COST 217 interlaboratory comparison of optical measurement on single-mode fibre couplers, Technical Digest, Symposium on Optical Fiber Measurements, p. 7-10, 1990.

[4] B.L. Heffner, Photon. Tech. Lett. **4**, 45, 1992.

[5] The depolarization of the light due to Polarization Mode Dispersion (PMD) is assumed negligible, that is the coherence of the light source is assumed larger than the delay due to PMD.

[6] N. Gisin, *Statistics of Polarization Dependent Losses*, preprint, University of Geneva, 1994.

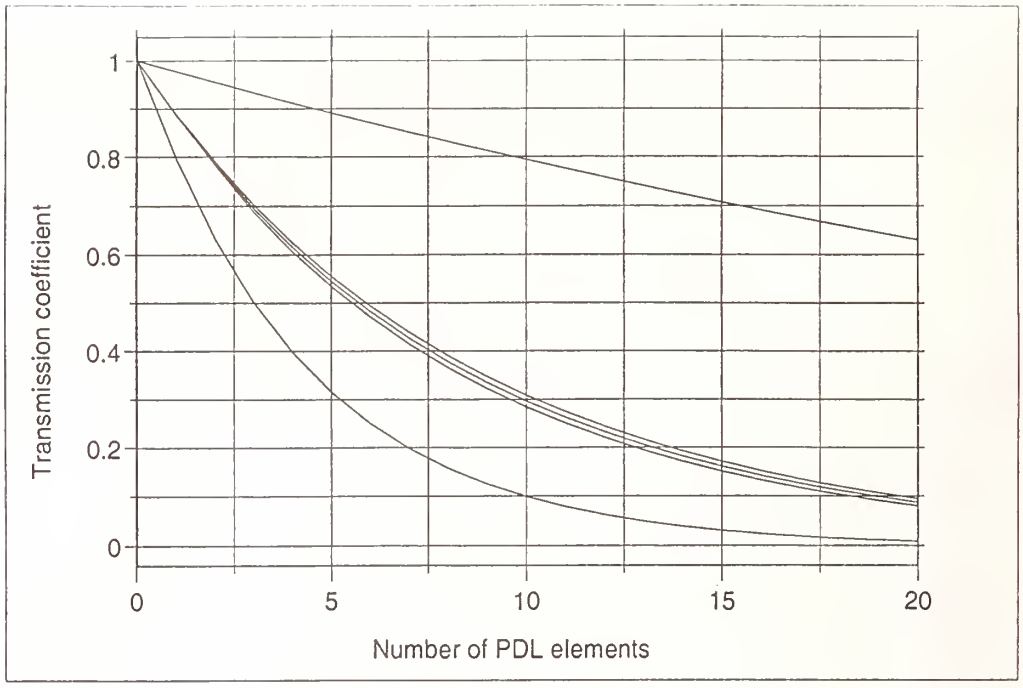

1. Monte-Carlo simulation of the transmission coefficient through 20 components with PDL. The top and lower curves represent the maximum and minimum transmissions. The central curve is the mean over 30.000 realizations, whereas the the last two curves represent the mean plus and minus one standard deviation. The characteristics of the components have been kept fixed: $T_{max} = 0.98 = 0.1dB$, $T_{min} = 0.79 = 1dB, ieT_{depol} = 89 = 0.53dB$, $\Gamma = 0.1 = 0.9dB$, but the relative orientations have been chosen at random with a uniform distribution on the sphere.

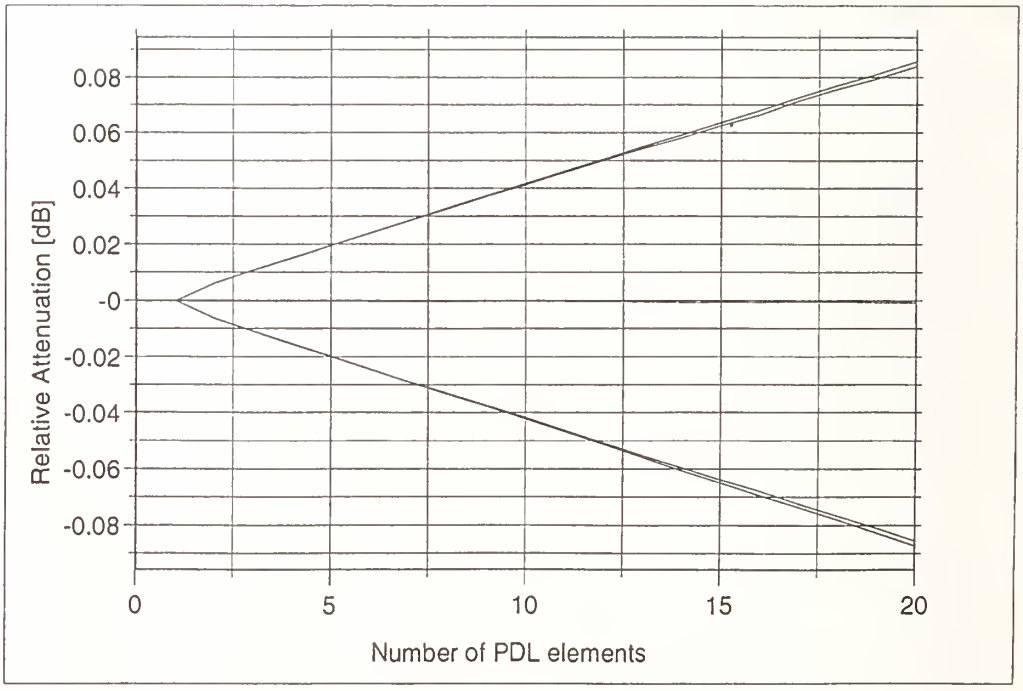

2. Monte-Carlo simulation of the transmission coefficient expressed in dB through 20 components with $PDL = 0.05 = 0.43dB$. In order to simplify the figure, the mean loss has been subtracted. Hence the central curve (mean loss) is displayed close to zero. The two bottom and top curves represent the standard deviation as found with a 30.000 realizations numerical simulation and with the approximate expression (10).

Effects of fiber nonlinearity and polarization mode dispersion on long-distance transmission systems with optical in-line amplifiers

Takamasa Imai, Makoto Murakami, and Tetsuo Takahashi
NTT Transmission Systems Laboratories
1-2356 Take, Yokosuka-shi, Kanagawa, Japan

I. Introduction Recent developments in Er-doped optical amplifiers enable very-long transmission systems to be created without regenerating repeaters[1], [2]. However, in very long fibers, nonlinear effects, especially four-wave mixing(FWM)[3]-[9] and self-phase modulation(SPM)[10]-[13], and polarization mode dispersion(PMD)[14]-[17] become important and must be taken into account. This is because they can seriously degrade the transmission performance.

In this paper, we demonstrate the effects due to nonlinearity and PMD, quantitatively. Countermeasures to these effects and the key points in measuring fiber and system parameters are also discussed.

II. Transmission performance degradation due to fiber nonlinearity and PMD

The transmission performance of the system shown in Fig. 1(a), is determined by the received SNR(signal-to-noise ratio)[18]. It is degraded by intensity noise accumulation and waveform distortion. Fundamentally, the accumulation in intensity noise is caused by the amplified spontaneous emission(ASE) as shown in Fig. 1(b). Furthermore, FWM between the signal and ASE induces excess intensity noise.

SPM causes spectral broadening and results in strong waveform distortion in combination with group-velocity dispersion(GVD) as shown in Fig. 1(c). Polarization mode dispersion also degrades the waveform in a long-distance transmission system.

Quantitative impact of these effects is discussed later.

A. Noise enhancement due to fiber nonlinearity Much effort has been devoted to clarify the noise enhancement effect due to FWM by numerical simulations and analytical methods[3]-[9]. These studies indicate that the effect is significant when the signal wavelength is very near the fiber zero dispersion wavelength or in the anomalous dispersion region.

To design a practical system, it is important to confirm the effect experimentally. Accordingly, we performed a recirculating fiber loop experiment and confirmed the intensity noise enhancement due to fiber nonlinearity as function of the GVD value[19]. As shown in Fig. 2, when an optical attenuator replaced the fiber loop, the intensity noise after direct

detection increased as per the theoretical plot, and well matched the calculated results considering only fundamental beat noise[18]. This result confirms that excess noise is not created by the attenuator. Also, no significant excess noise was observed after replacing the optical attenuator by a fiber with the normal dispersion value of -0.26 ps / nm / km. In contrast to the above results, we clearly observed the emergence of excess intensity noise at distances over 1500 km when using the fiber with the anomalous dispersion value of +0.35 ps / nm / km.

Figure 3 shows the intensity noise dependence on dispersion for distances up to 6000 km. It is clear that the noise increases with dispersion value for all distances in the anomalous dispersion region. On the other hand, no significant excess noise was observed in the normal dispersion region, which agrees with the numerical and analytical results.

Considering enhanced noise suppression, these results confirm that long distance transmission systems should operate in the normal dispersion region.

B. Waveform distortion due to SPM and GVD In long-distance transmission systems, SPM causes spectrum broadening, which enhances the waveform distortion by GVD. This effect was studied by numerical simulation[11]. Also, pulse width broadening due to SPM and GVD was discussed analytically[12]. These calculations indicate that the corresponding demodulated eye opening penalty is approximated by the following equation.

$$P_{eye,SPM}\,(\mathrm{dB}) = \eta\,(|D|\,\lambda^2 / \pi c)\,B^2 L^2 \gamma_{NL}\,Prep,out\,\{1 - \exp(-\alpha\,Lrep)\} / (\alpha\,Lrep) \quad (1)$$

D is the chromatic dispersion parameter, λ the signal wavelength, c the light velocity in vacuum, L the transmission distance, γ_{NL} the nonlinear coefficient, B the bit rate, L_{rep} the repeater spacing, and α the fiber's loss coefficient. Coefficient η, whose value was found to be around 20 from numerical simulations[12], depends on the transmitted signal pulse shape.

We confirmed eqn. (1) by a 10 Gbit / s signal transmission experiment[13]. The experimental results shown in Fig. 4 indicate that waveform distortion is negligible, even after 3000 km transmission, when the signal wavelength equals the zero dispersion wavelength. There is some degradation, however, when the signal wavelength is detuned from the zero dispersion wavelength. Here, we suppressed the noise enhancement due to FWM by carefully ordering fibers according to the GVD values[5]. Quantitatively, as shown in Figs. 5 and 6, the eye opening penalty is proportional to signal wavelength detuning and repeater output power. The results calculated from eqn. (1), shown in Figs. 5 and 6, well match the experimental results.

The above results are plotted in Fig. 7 and indicate the accumulated dispersion needed to suppress the eye opening penalty to under 1 dB. The required GVD value is inversely proportional to the square of the total transmission length.

C. Waveform distortion due to PMD Polarization mode dispersion also induces waveform distortion. The eye opening penalty due to PMD was theoretically and experimentally confirmed[15]-[17] under the first order approximation[20], ignoring spectral characteristics. These studies indicate that the demodulated eye opening penalty due to PMD, is approximated by the following equation.

$$P_{eye,\,PMD}\,(\mathrm{dB}) = C\ (\,1 - \gamma_{\mathrm{PMD}}\,)\gamma_{\mathrm{PMD}}\,(\frac{\Delta\tau}{T})^2 \qquad (2)$$

γ_{PMD} is the relative power launched in the two principal states, $\Delta\tau$ is the differential group delay time between two principal states, and T is the one bit duration. Coefficient C, whose value was found to be around 50, depends on the transmitted signal pulse shape.

Experimentally, PANDA fibers were used to confirm the relation instead of a transmission line[17]. Figure 8 shows the observed waveform degradation due to PMD. Figure 9 shows the corresponding eye opening penalty as a function of PMD. The results calculated from eqn. (2), shown in Fig. 9, well match the experimental results.

Because of random polarization mode coupling in transmission fibers, a statistical analysis of PMD is necessary[21]-[22]. By considering that the probability density of PMD has a Maxwellian distribution[20],[22], the mean PMD of 5 ps is required for a 10 Gbit / s system in order to limit the probability of Q penalty exceeding 0.5 dB to less than 10^{-9}.

III. Countermeasures to noise enhancement and waveform distortion

To suppress both the excess intensity noise due to FWM and waveform distortion due to SPM and GVD, it is useful to arrange the various fiber sections as described below. At the points in the fiber of high signal power, negative dispersion fibers should be used to suppress the excess intensity noise due to FWM. By using positive dispersion fibers only where the signal power is weak, the average dispersion of the transmission line is tuned to be zero; this eliminates the waveform distortion due to SPM and GVD[5].

The measured GVD of the total system must be within the required GVD value shown in Fig. 7. For example, average GVD must be of the order 10^{-3} ps / nm / km for a 10 Gbit / s, 9000 km transmission system. To suppress the excess intensity noise, care is needed because even a single fiber, usually 10 to 50 km in length, can exhibit swings in dispersion value[23],[24]. That is, while the overall dispersion value may be negative, some parts of the fiber may have high, positive dispersion values.

To suppress the waveform degradation due to PMD, the mean PMD of the total system must not exceed the value shown in Section II. To confirm the mean value of the total system, we must measure the statistical ensembles at the signal wavelength. To obtain the average PMD of the fiber, the wavelength ensemble of the PMD is usually measured instead of the statistical ensemble because the average over both ensembles coincide[25] and the wavelength ensemble

can be measured in a short time. However, this method is difficult to apply if the system uses optical-in-line amplifiers because the optical bandwidth of the cascaded EDFAs is relatively narrow, around several nm or less. Thus, the statistical ensembles of the system must be obtained, and much time is needed to obtain the mean value because of the very slow fluctuation of PMD in the installed fiber as shown in Fig. 10[26].

IV. Conclusion In conclusion, the effects of SPM, FWM, and PMD on the performance of a transmission system with optical in-line amplifiers were demonstrated quantitatively. This enables system design to include countermeasures to these effects. Also, the key points in measuring fiber and system parameters were also discussed.

Acknowledgments The authors would like to thank Dr. S. Saito and Mr. A. Naka for their critical discussion on the theoretical analysis. They also thank Dr. H. Ishio, Dr. T. Ito, and Dr. M. Aiki for their encouragement.

References: [1] T. Imai, M. Murakami, Y. Fukada, M. Aiki and T. Ito, Electron. Lett., Vol. 28, pp. 1484 - 1485, 1992.
[2] H. Taga, N. Edagawa, H. Tanaka, M. Suzuki, S. Yamamoto, H. Wakabayashi, OFC'93, Paper PD-1, San Jose, 1993.
[3] J. P. Gordon and L. F. Mollenauer, Opt. Lett., Vol. 15, No. 23, pp. 1351 - 1353, 1990.
[4] M. Murakami and S. Saito, IEEE Photonics Technol. Lett., Vol. 4, No. 11, pp. 1269 - 1272, 1992.
[5] D. Marcuse, IEEE J. Lightwave Technol., Vol. 9, No. 3, pp. 356 - 361, 1991.
[6] D. Marcuse, IEEE J. Lightwave Technol., Vol. 9, No. 10, pp. 1330 -1334, 1991.
[7] K. Kikuchi, IEEE Photonics Technol. Lett, Vol. 5, No. 2, pp. 221 - 223, 1993.
[8] A. Naka, S. Saito, OFC'94, Paper FC1, San Jose, 1994
[9] S. Saito, ECOC'93, Paper MoC-1.1, Montreux, 1993.
[10] O. Audouin, L. Prigent and J-P. Hamaide, ECOC'91, Paper We A6.1, Paris, 1991.
[11] A. Naka and S. Saito, J. Lightwave Technol., Vol. 12, No. 2, pp. 280 - 287, 1994.
[12] D. Marcuse, J. Lightwave Technol., Vol. 10, No. 1, pp. 17 - 21, 1992.
[13] T. Imai, M. Murakami, and A. Naka, Electron. Lett., Vol. 29, No. 16, pp. 1409 - 1410, 1993.
[14] R. E. Wagner, A. F. Elrefaie, OFC'88 Paper TuI6, New Orleans, 1988.
[15] C. D. Poole, R. W. Tkach, A. R. Chraplyvy, and D. A. Fishman, IEEE Photonics Technol. Lett., Vol. 3, No. 1, pp. 68 - 70, 1991.
[16] F. Bruyere and O. Audouin, IEEE Photonics Technol. Lett., Vol. 6, No. 3, pp. 443 - 445, 1994.
[17] T. Takahashi, T. Imai and M. Aiki, Electron. Lett., Vol. 30, No. 4, pp. 348 - 349, 1994.
[18] N. A. Olsson, J. Lightwave Technol., Vol. 7, pp. 1071 - 1082, 1989.
[19] M. Murakami, Y. Fukada, and T. Imai, ECOC'94, to be presented.
[20] G. J. Foshini and C. D. Poole, J. Lightwave Technol., Vol. 9, No. 11, pp. 1439 - 1456.
[21] N. Gisin and J. P. Pellaux, Optics Communications, Vol. 89, pp. 316 - 323, 1992.
[22] N. Gisin, R. Passy, J. C. Bishoff and B. Perny, IEEE Photonics Technol. Lett., Vol. 5, No. 7, pp. 819 - 821, 1993.
[23] K. Inoue, J. Lightwave Technol., Vol. 10, No. 11, pp. 1553 -1561.
[24] M. Ohashi and M. Tateda, Electron. Lett., Vol. 29, No. 5, pp. 426 - 428, 1993.
[25] N. Gisin, Optics Communications, Vol. 86, No. 5, pp. 371 - 373, 1991.
[26] T. Takahashi, T. Imai, and M. Aiki, Electron. Lett., Vol. 29, No. 18, pp. 1605 - 1606.

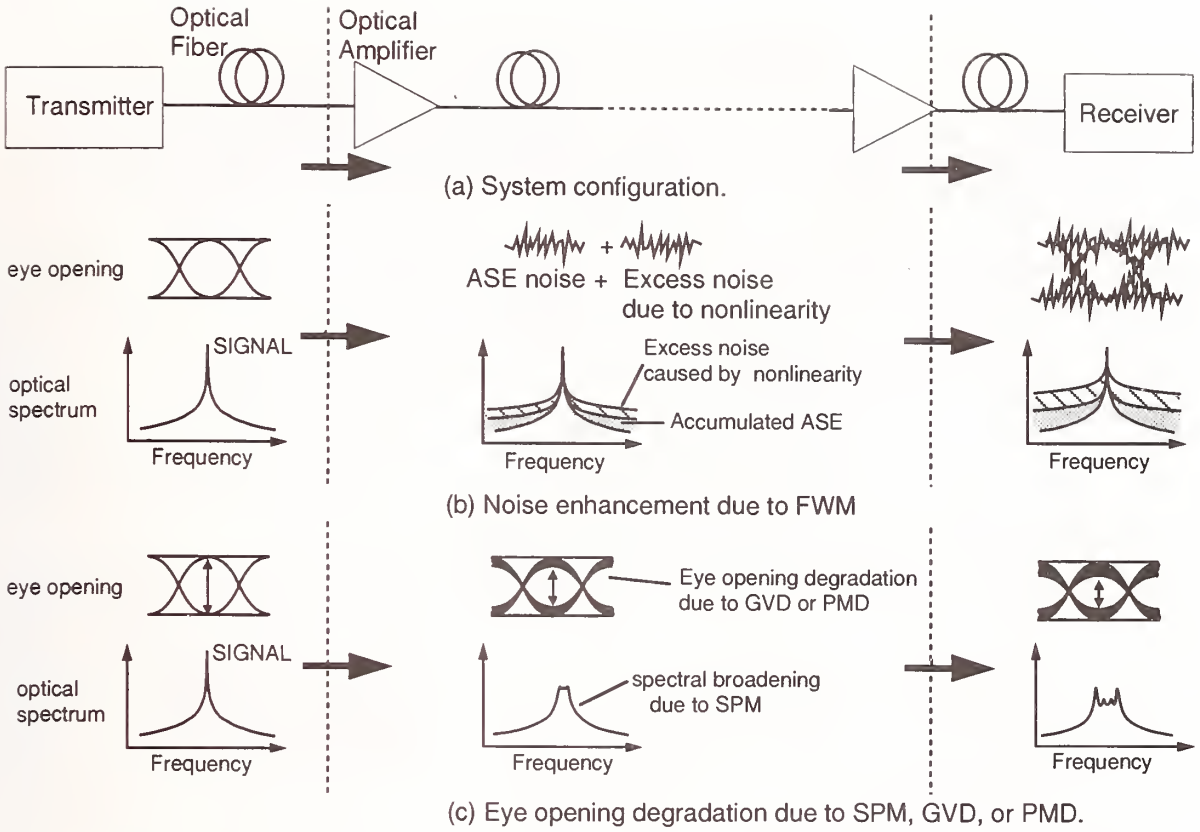

Fig. 1 Effects due to the fiber nonlinearity and PMD on long-distance transmission systems.

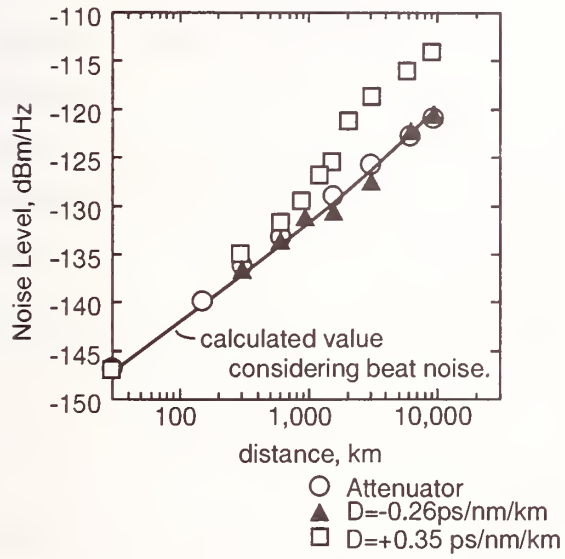

Fig.2 Measured intensity noise against the recirculating distance. (loop length = 30 km, amplifier output power = 6 dBm)

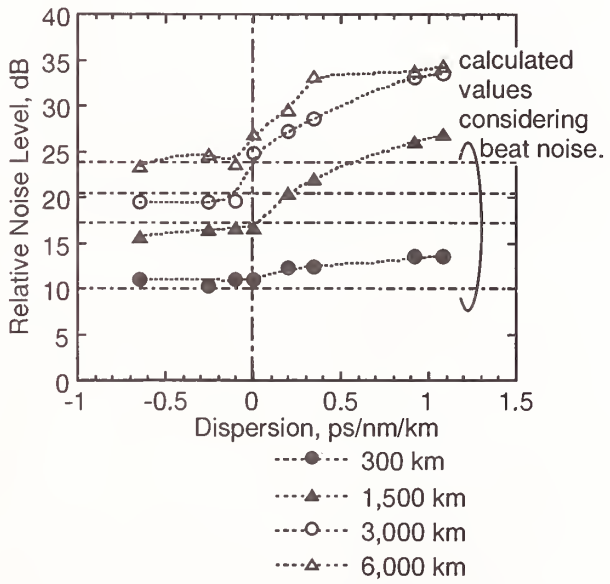

Fig. 3 Dispersion dependence of measured intensity noise relative to the spontaneous beat noise generated in one loop.
(Broken lines indicate the spontaneous beat noise calculated for each number of loops.)

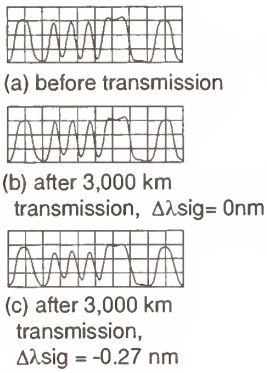

Fig.4 Observed waveform degradation due to SPM and GVD. (horizontal: 20 ps / div.)

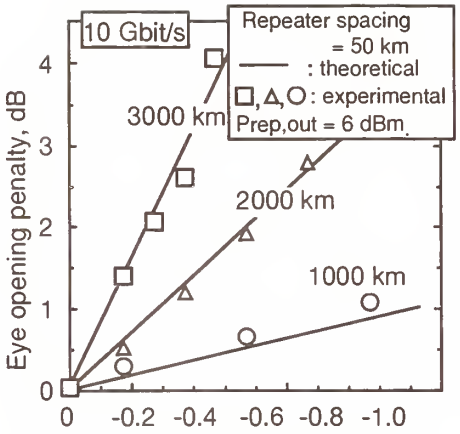

Fig. 5 Signal wavelength dependency of the eye opening penalty.

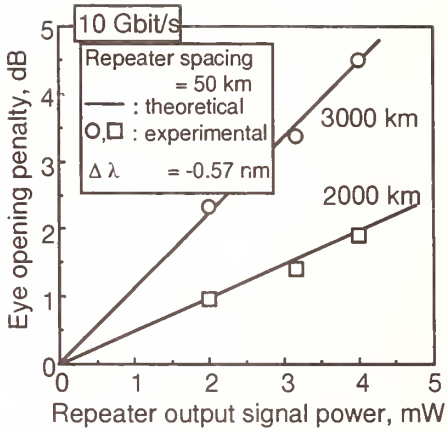

Fig. 6 Repeater output power dependency of eye opening penalty.

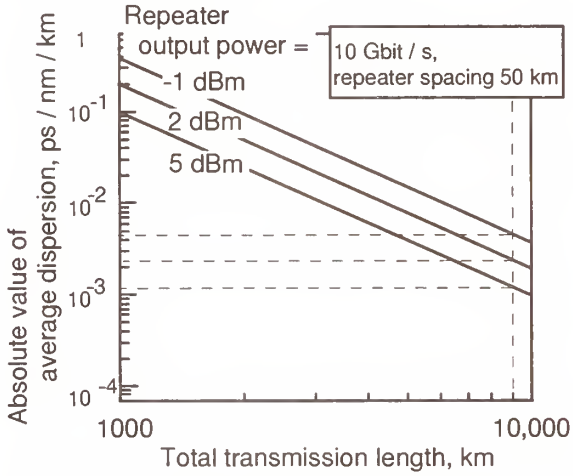

Fig. 7 Required average GVD value to suppress the eye opening penalty of less than 1 dB

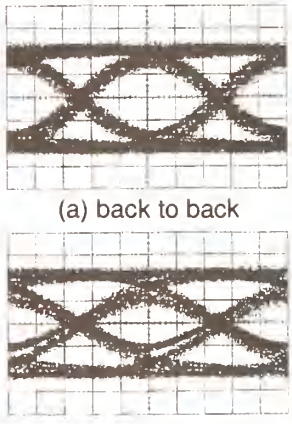

Fig. 8 Observed waveform degradation due to PMD (horizontal: 20 ps / div.)

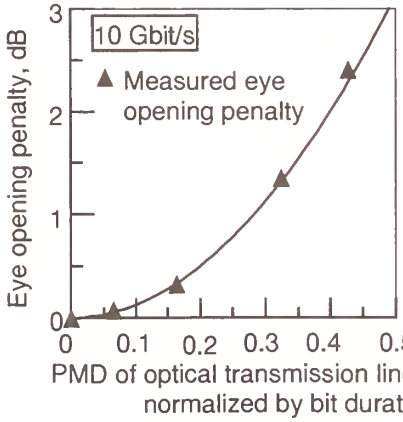

Fig. 9 Power penalty due to PMD
(Solid line indicates calculated results at C = 50)

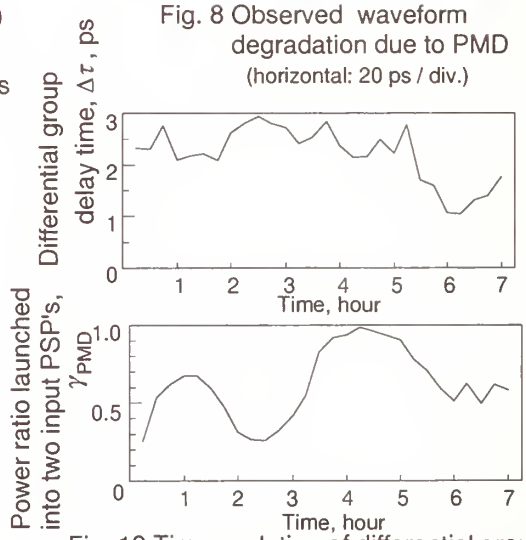

Fig. 10 Time evolution of differential group delay time $\Delta\tau$ and power ratio γ_{PMD} launched into two input principal states of polarization(Total fiber cable length = 119 km.)

Highly Repeatable Measurement of Nonlinear Refractive Index by Cross Phase Modulation Method using Depolarized Pump Light

Takatoshi Kato, Yoshiyuki Suetsugu, Masahiro Takagi, Eisuke Sasaoka
and Masayuki Nishimura
Yokohama Research Laboratories, Sumitomo Electric Industries, Ltd.
1 Taya-cho, Sakae-ku, Yokohama 244 JAPAN
Phone No.;+81-45-853-7171
Fax No.;+81-45-851-1557

High measurement repeatability within ±1% has been obtained using depolarized pump light in measurements of nonlinear refractive index by cross phase modulation (XPM) method. The standard deviation has been reduced to one sixth compared with the conventional XPM method. It has been determined that the nonlinear refractive index of dispersion shifted fiber at 1.55 μm was 3.3×10^{-20} [m^2/W] for linear polarization.

1. Introduction

In recent years, fiber nonlinearities[1] such as self-phase-modulation (SPM), cross-phase-modulation (XPM), or four wave mixing (FWM), have been drawing much attention in long-haul transmission systems. Several methods to measure nonlinear refractive index, n_2, have been reported based on those nonlinearities[2][3], however, measurement repeatability has remained unimproved. In this paper, method to measure n_2 with high repeatability is reported by the XPM method by depolarizing pump light to avoid uncertainties caused by polarization fluctuation.

2. Measurement of the Nonlinear Refractive Index by XPM Method

The phase shift Φ induced by fiber nonlinearities is given by

$$\Phi = \frac{2\pi L_{eff}}{\lambda} \frac{n_2}{A_{eff}} (P_{probe} + 2bP_{pump}) \qquad (1)$$

where L_{eff} is the effective fiber length, λ is the vacuum wavelength of the probe light, A_{eff} is the effective core area, P_{probe} is the probe power, P_{pump} is the pump power, b is the coefficient which depends on the polarization states of the probe and the pump lights. The first term is the effect of SPM and the second term is the effect of XPM.

A measurement system by the XPM method is shown in Fig. 1. In this system, probe signal power is set relatively weak so that n_2 index in test fibers is dominantly caused by amplified strong pump light through XPM and that the effect of SPM is negligible. When pump light is

modulated in its intensity, probe light is modulated in its phase through XPM. Therefore, n_2 can be determined by measuring frequency components induced by phase modulation with the self-delayed heterodyne detection technique while changing pump power.

In the conventional n_2 measurement by the XPM method, as well as the SPM method, repeatability was the major issue. One important point was the polarization dependence on the phase shift. The maximum phase shift is given at b=1 when the pump and the probe lights are linearly polarized and parallels each other. The minimum phase shift, on the other hand, takes the value at b=1/3 when they are linearly polarized and become orthogonal. However, because the polarization states are not maintained in non-polarization maintaining fibers, the observed maximum phase shift is smaller than the value at b=1, and the observed minimum phase shift is larger than the value at b=1/3. Therefore n_2 in non-polarization maintaining SM fibers had to be estimated from the average of the maximum and the minimum of the observed phase shifts. And the other point was the variation of the polarization states of those lights in fibers under test caused by changes in external conditions. Thus, variances was incurred by the above mentioned factors in the measurement of n_2 by the conventional XPM method.

3. Depolarized Optical Sources

In order to directly obtain the average phase shifts and to reduce the variances, the use of depolarized optical sources, instead of conventional LD, has been proposed as pump waves. Table 1 summarizes polarization extinction ratio in four types of pump sources tested this time. Type D was the conventional LD, type C was a broadband SLD (Super Luminescence Diode), and types B and A were a depolarized LD and a depolarized SLD, respectively. The depolarizer consisted of two polarization maintaining fibers fused with their principal axes rotated by 45 degrees. Polarization extinction ratio was determined by measuring the maximum and the minimum power levels transmitted through a polarizer placed at the output while the polarization states of these pump waves were changed by a polarization controller.

Table 1 Polarization Extinction Ratio for four types of pump sources.

Type	A	B	C	D*
Construction	SLD+depolarizer	LD+depolarizer	SLD	LD
Polarization Extinction Ratio [dB]	0.32	0.70	2.70	12.10

* conventional method

4. Measurement

In order to clearly know the influence of pump polarization extinction ratio, measurements were conducted on n_2 in a 7 km of polarization-maintaining dispersion shifted fiber (PM-DSF) with a refractive index difference $\Delta = 1.2\%$ and a birefringence of $B = 4.61 \times 10^{-4}$ to exclude uncertainties of the states of polarization. The maximum and the minimum phase shifts for four

types of pump waves were observed while input states of polarization were changed with polarization controllers. Fig. 2 shows the measured results as a function of polarization extinction ratio of the pump lights. As the extinction ratio was increased, the maximum and the minimum phase shifts approached to the ideal ones. And as the pump waves were depolarized to reduce the extinction ratio, the phase shifts came to converge at the value for random polarization, independent of the input polarization states. Therefore it was confirmed that the highly repeatable measurement became possible by sufficiently depolarizing the pump light to remove the uncertainties of polarization. From this result, a nonlinearity coefficient, n_2/A_{eff}, was obtained as 10.61×10^{-10} [1/W] corresponding to the average phase shift of 1.75[rad]. Since A_{eff} of this fiber was 31.5 [μm^2], n_2 of the PM-DSF was calculated as 3.34×10^{-20} [m^2/W].

Next n_2 was measured on a 10 km non-polarization-maintaining standard dispersion shifted fiber (DSF) with $\Delta = 1.0\%$ using the four types of pump sources. Because the states of polarization change in non-polarization-maintaining fibers, the variance of measurement results caused by imperfect degrees of depolarization is expected to be smaller than the case in PM fibers. Fig. 3 shows the average and the standard deviation of the measured n_2/A_{eff} obtained from five consecutive measurements on the same fiber while properly changing input polarization states in each measurement. Measurement conditions like probe power or maximum pump power, etc. were set nearly equal in all measurements. From Fig. 3, it was found that the average of n_2/A_{eff} obtained with the four types of pump sources were nearly the same and repeatability was improved by six times by using the depolarized SLD (±0.6% : [standard deviation]/[average]) compared with the conventional method using LD (±3.7%). Obtained n_2/A_{eff}, by using the depolarized SLD,was 6.39×10^{-10} [1/W] with the standard deviation of 0.037×10^{-10} [1/W]. Since A_{eff} of this fiber was 51.4 [μm^2], n_2 of the standard DSF was calculated as 3.28×10^{-20} [m^2/W]. The n_2 in the DSF was found smaller than that in PM-DSF because of the smaller refractive index.

5. Conclusion

High repeatability within ±1% was realized on the measurement of nonlinear refractive index, n_2 by XPM method. The use of depolarized SLD having the polarization extinction ratio of 0.32 dB enabled the improvement of the repeatability to be succeeded. The measured n_2 for linear polarization at 1.55 μm was 3.3×10^{-20} [m^2/W] in a standard dispersion shifted fiber.

Reference

[1] G. P. Agrawal, "Nonlinear fiber optics," Academic Press, 1989.
[2] A. Wada, T. O. Tsun and R. Yamauchi, Proceedings of ECOC'92, Berlin, Germany, p45, 1992.
[3] K. S. Kim and R. H. Stolen, Opt. Lett. **19**, 259, 1994.

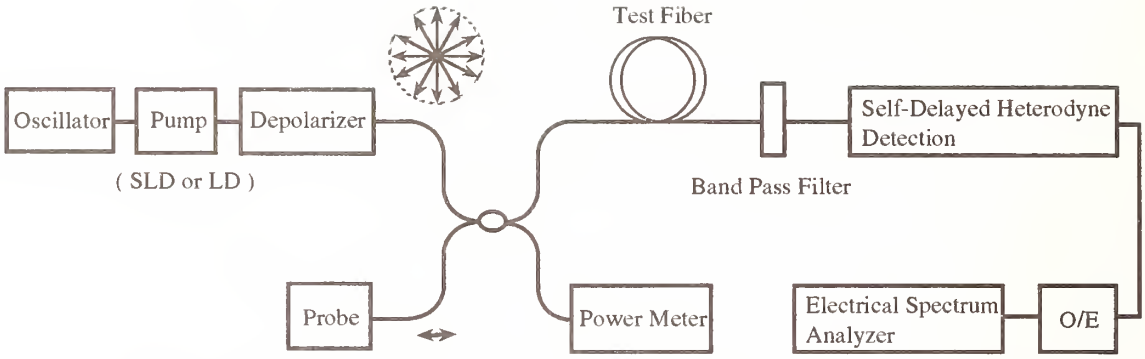

Fig. 1 Proposed measurement system of nonlinear refractive index by the XPM method using depolarized pump waves

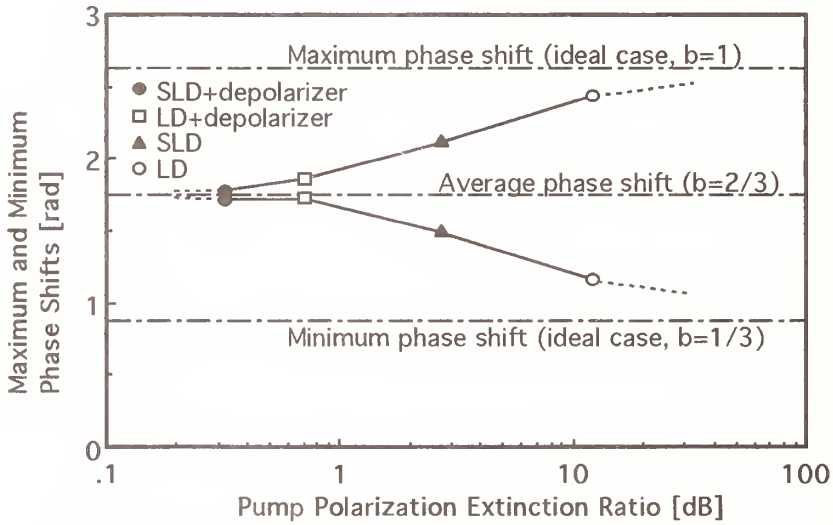

Fig. 2 Maximum and minimum phase shifts for four types of pump waves in PM-DSF

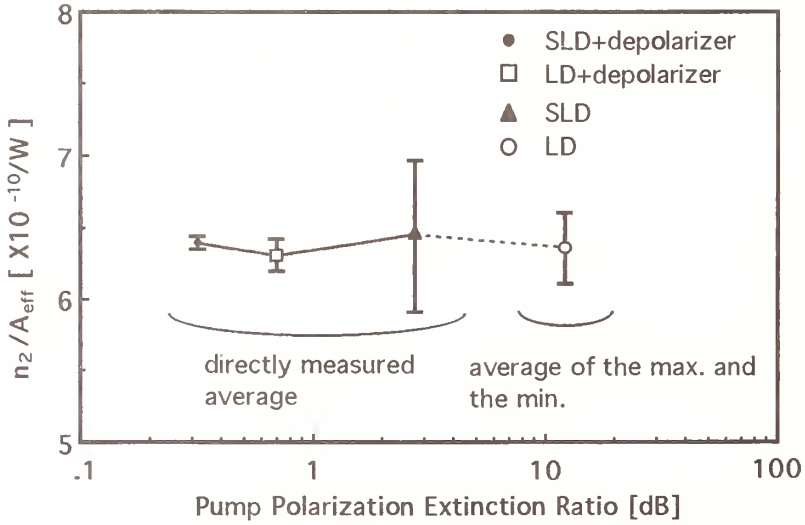

Fig. 3 Average and standard deviation of n_2/A_{eff} for four types pump waves in standard DSF

Automated Fiber Nonlinear Coefficient Measurements using Self-Phase Modulation Method

Yoshinori NAMIHIRA, Yuichi TANAKA (*), and Masahito MURE (*),

KDD R&D Laboratories,
2-1-15, Ohara, Kamifukuoka, Saitama 356 JAPAN
Phone : +81-429-66-7801, Fax : +81-429-66-7516
(*) **Oyokoden, Lab. Co., Ltd.**
3-1-23, Niizominami, Toda, Saitama 335 JAPAN
Phone : +81-48-445-6911, Fax : +81-48-445-6901

Abstract :

Automated nonlinear coefficient measurement for optical fibers using self-phase modulation (SPM) method has been developed for the first time. Nonlinear Kerr refractive index n2 for various dispersion shifted fibers (DSFs) is found to be around 2.23 x 10^{-20} m^2/W (± 5 %) for random polarization states at 1.55 μm. A comparison of the new automated measuring SPM method and the conventional SPM method is also presented.

Introduction :

Optical nonlinearities limit the maximum power transmitted through optical fibers and they have become a serious limitation in optically amplified ultralong transmission spans such as the transoceanic optical fiber submarine cable systems [1]. The magnitude of the nonlinearity in optical fiber depends on the nonlinear coefficient of the fiber doping materials, the power in the optical fibers and the mode confinement.

Recently, the nonlinear coefficient (n_2/A_{eff}; n_2 is the nonlinear Kerr refaractive index, A_{eff} is the nonlinear effective area) [2,3] of optical fibers has been measured by the self-phase modulation (SPM) method using a 514.5 nm Argon laser in a short fiber (~116m) [3], by the SPM method using a 1319 nm high power mode-locked Nd : YAG Laser in short optical fibers (~250 m) [4,5], by the cross phase modulation (XPM) method using a 1553 nm DFB laser in the long (~20 km) optical fibers [6], by the self-compensated interferometer (SCI) method using a 1064 nm Nd : YAG laser in Er-doped fibers (EDFs) [7], and by the four wave mixing (FWM) method using two 1555 nm DFB lasers [8].

In this paper, the automated fiber nonlinear coefficient measurements using the SPM method at 1.55 μm for various dispersion shifted fibers (DSFs) are first presented.

Experiment :

The experimental setup for automated fiber nonlinear coefficient measurement using the SPM method at 1.55 μm is shown in Fig.1. The picosecond transform-limited optical pulse was generated using a tunable optical band pass filter and a DFB laser using the gain switching

technique [9] with a 100 MHz repetition rate. The input optical pulse width (FWHM) $\Delta\tau$ was measured by a streak camera with time resolution of 1 ps and it was around 34 ps [10]. The output spectra from the DSF at different powers displayed on an oscilloscope as shown in Fig.2 [10]. The input frequency spectrum was around 13 GHz, which was measured by a fiber type Fabry-Perot interferometer. Accordingly, the product of the pulse width $\Delta\tau$ and the frequency spectral width $\Delta\nu$ is about $\Delta\tau\,\Delta\nu \cong 0.442$, which means that the pulse is nearly a transform-limited Gaussian pulse [9,10]. In Fig.2, the frequency spectra are labeled by the maximum phase shift ϕ_{max} which is proportional to the peak power P_0 [10]. The output frequency spectrum at $\phi_{max} = 5.5\,\pi$ has a slightly asymmetric pulse shape. The main reason is considered to be due to pulse broadening from the chromatic dispersion and polarisation effects such as polarisation mode dispersion.

The maximum phase shift ϕ_{max} is given by [2,3] ;

$$\phi_{max} = \frac{2\pi}{\lambda}\left(\frac{n_2}{A_{eff}}\right) L_{eff} P_0 \qquad (1)$$

where, L_{eff} and λ are the effective fiber length and wavelength in vacuum. In the conventional manual method, the nonlinear coefficient (n_2/A_{eff}) can be obtained from the number of peaks M in the SPM-broardened spectrum and is given approximately by the following relation $\phi_{max} \cong (M - 1/2)\pi$ [2,3]. In the new automated system, the fiber nonlinear coefficient (n2/Aeff) is obtained automatically from the relationship between output optical power and peak power trace as shown in Fig.3. The maximum phase shift (ϕ_{max}) as a function of peak powers is shown in Fig.4.

Results & Discussion :

The nonlinear measurement results of (n_2/A_{eff}) and the estimated value n_2 are summarized in Table 1. In Table 1, the fibers DSFs-1 ~ 4 are commercial DSFs from various fiber manufactures. All the DSFs have Germanium doped core and silica cladding.

The nonlinear Kerr refractive index n_2 can be estimated from the (n_2/A_{eff}) by multiplying the A_{eff}. The A_{eff} is given by [2,3]

$$A_{eff} = 2\pi\left[\int_0^\infty |E(r)|^2\, r\,dr\right]^2 \Big/ \int_0^\infty |E(r)|^4\, r\,dr \qquad (2)$$

The A_{eff} can be obtained by the computer analysis from the measured refractive index profiles of the optical fibers [2,3,5,10,11]. However, recently the A_{eff} is approximately expressed as $A_{eff} \cong 0.944(\pi/4)$ MFD^2 (Namihira's relation) [11].

From Table 1, it was found that the averaged value of n2 of the conventional manual measurement and automated measurement were 2.28 x 10 $^{-20}$ m^2/W and 2.23 x 10 $^{-20}$ m^2/W, respectively. The 2.23 x

From Table 1, it was found that the averaged value of n2 of the conventional manual measurement and automated measurement were 2.28 x 10^{-20} m^2/W and 2.23 x 10^{-20} m^2/W, respectively. The 2.23 x 10^{-20} m^2/W value of n_2 is in good agreement with that of 2.25 x 10^{-20} m^2/W value obtained by four wave mixing (FWM) method [8], and also which lies within 2.1 - 2.6 x 10^{-20} m^2/W range of recently reported results of n_2 values [3,4].

Conclusion :

An automated fiber nonlinear coefficient measurement system has been successfully developed. The nonlinear Kerr refractive index n2 for DSFs was around 2.23 x 10^{-20} m^2/W (± 5 %) for random polarization states at 1.55 μm. The value of n2 was in good agreement with that of the 2.1 - 2.6 x 10^{-20} m^2/W range of recently published results.

Acknowledgment :

The authors would like to thank Dr. Y. Urano, Dr. T. Yamamoto, Dr. K. Sakai, Dr. S. Akiba of KDD R&D Labs., and T. Yasumatsu and I. Kasahara of Oyokoden Lab. Co. Ltd., for their encouragement. We wish to thank A. Miyata of Univ. of Electro-Communications, and N. Tanahashi of Nihon Univ. for their experimental support.

References :

[1] D. Marcuse et al. :JLT,vol. 9, LT-9, pp.121-128, 1991.
[2] G. P. Agrawal :"Nonlinear Fiber Optics", Academic Press, 1989.
[3] R. H. Stolen et al.: Phys. Rev. A14, pp.1448-1453, 1978.
[4] R. H. Stolenet al.,: NIST, Boulder, USA, pp.71-75, 1992.
[5] K. S. Kim et al., : Optics Lett., vol.19, no.14, pp.257-259, 1994.
[6] A. Wadaet al.,: ECOC'92, Berlin, Germany, p.42, 1992.
[7] J. E. Meier et al.,:OFMC'93, Sept.,Torino, Italy, pp.125-128, 1993.
[8] L. Prigentet al., :. IEEE, PTL, vol.5, no. 9, pp.1092-1095, 1993.
[9] M. Nakazawa et al.,: Optics Lett., vol.15, no.12, pp.715-717, 1990.
[10] Y. Namihira et al.,: OEC'94, 14 B2-2, July, Makuhari, Japan, 1994.
[11] Y. Namihira :Electron. Lett., vol.30, no.3, pp.262-264, 1994.

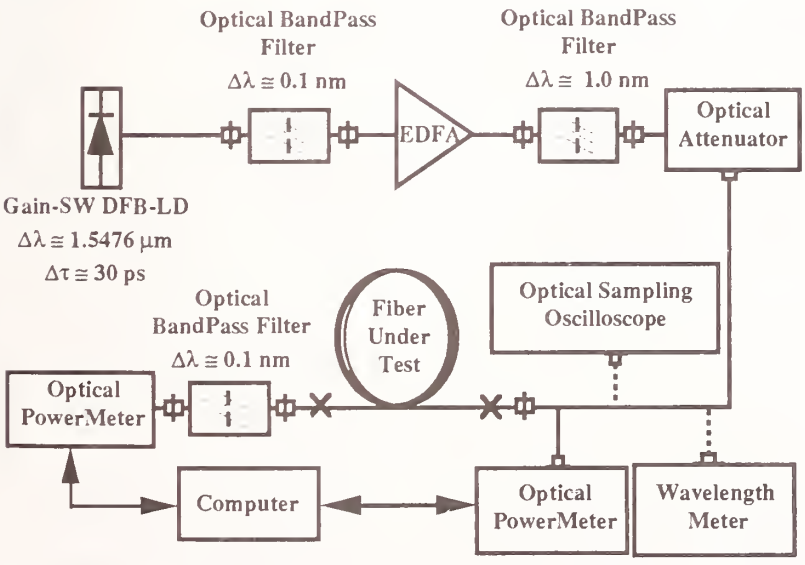

Fig.1 Automated optical fiber nonlinear coefficient measuring system using SPM method at 1.55 μm

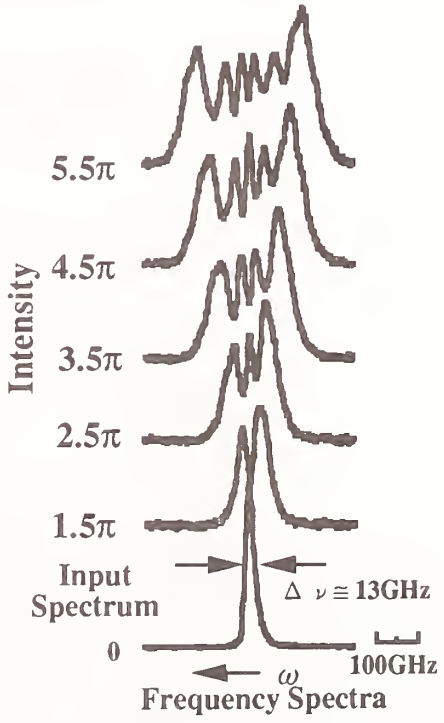

Fig.2 Examples of frequency spectra

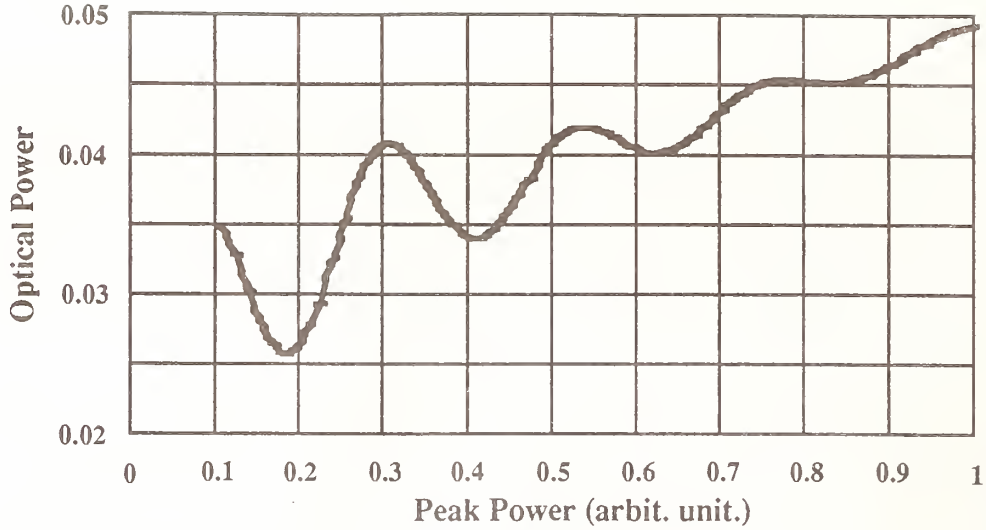

Fig.3 Example of automated SPM nonlinear coefficient measurement result

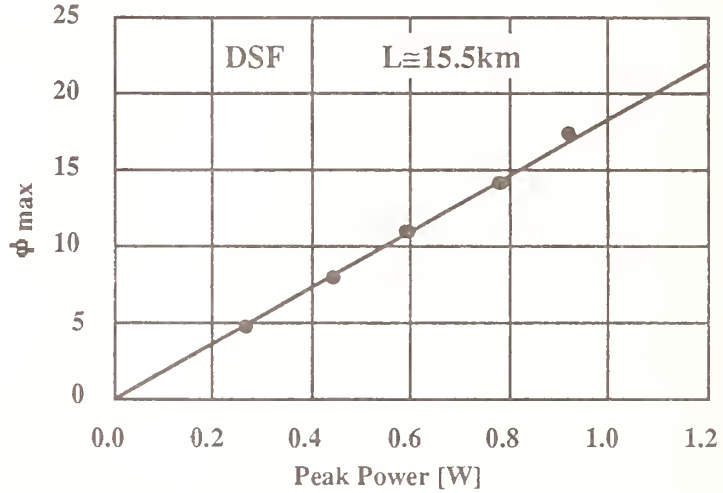

Fig.4 Maximum phase shift (ϕ max) as a function of peak powers.

Table 1 Comparison of nonlinear coefficient measurements from a manual system with the automated system

Fibers	Manual System		Automated System	
	n_2/A_{eff} [$\times 10^{-10}$/W]	n_2 [$\times 10^{-20}$ m^2/W]	n_2/A_{eff} [$\times 10^{-10}$/W]	n_2 [$\times 10^{-20}$ m^2/W]
DSF-1	4.561	2.398	4.268	2.259
DSF-2	4.240	2.245	4.102	2.167
DSF-3	5.280	2.468	5.280	2.468
DSF-4	3.804	2.000	3.880	2.030
Average	4.471	2.278	4.383	2.231

High-accuracy Brillouin Gain Spectrum Measurements of Single-Mode Fibers

Luc THEVENAZ, Marc NIKLES, Philippe ROBERT

EPFL Swiss Federal Institute of Technology, Metrology Lab.
CH-1015 Lausanne, SWITZERLAND

The importance of the measurements of the Brillouin gain spectrum has been growing in the past few years owing to its potential use for monitoring strains experienced by optical fibers [1] and for distributed temperature sensing [2]. It is classically measured by launching a highly coherent lightwave into a test fiber and by observing the amplification of a weak probe signal propagating in the backward direction [3]. The optical frequency of the probe signal must be stable and tunable to properly scan the Brillouin gain spectrum. This spectrum lies 12-13 GHz below the pump frequency at a wavelength of 1300 nm and has a Lorenzian line shape with a few tens of MHz FWHM. Generally two different laser sources are used to generate pump and probe signals, although a method using a single laser source, based on spoontaneous Brillouin scattered light analysis has been demonstrated [4]. Frequency resolution better than 1 MHz is difficult to achieve using all these methods, so that highly accurate measurements are not available so far. Especially only rough estimates for the FWHM linewidth (40-70 MHz) and the peak gain (1.5-2.5×10^{-11} m/W) have been reported to date [3, 4, 5].

In this contribution, we present a novel method using a single laser source for BGS measurements and the pump-probe technique. It makes possible reference measurements owing to its ideal inherent frequency stability and excellent SNR. Systematic measurements of fibers having various core-cladding index differences were performed, leaving accurate values for Brillouin gain parameters. A general behavior was observed and relations between Brillouin gain spectrum parameters and fiber core-cladding index difference are confirmed [4].

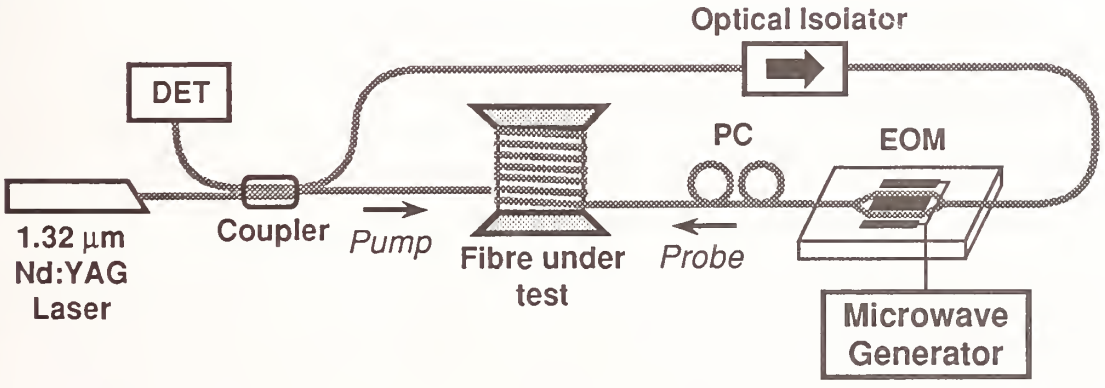

Fig. 1. Experimental setup for Brillouin gain spectrum measurements

The experimental setup is schematically shown in Fig. 1 [6]. Pump and probe signals originate in the same 1.32 µm Nd:YAG laser and are launched into the test fiber in opposite directions using a coupler. The isolator blocks the pump light, so that only the probe signal illuminates the detector. The test signal

is set at the proper frequency by modulating the laser light using an ultrawideband electro-optic modulator driven by a synthetised signal generator. This creates two sidebands in the optical spectrum that are separated from the pump frequency by the modulation frequency. When this frequency corresponds to the Stokes shift, Brillouin interaction may occur. The lower sideband experiences gain and grows exponentially as it propagates along the fiber under test, whereas the upper sideband is depleted and decays exponentially. The sum of this two effects yields an hyperbolic cosine relationship between amplification and gain coefficient.

$$I(L) = 2\, I_o \cosh\{ g_B(\nu)\, I_p\, L_{eff}\}$$

where I_o is the test signal input intensity, g_B is the Brillouin gain coefficient, I_p is the pump intensity and L_{eff} is the usual effective fiber length for the nonlinear interactions. This relationship is only strictly valid under the assumption that any effect on the pump signal (gain or depletion) is negligible.

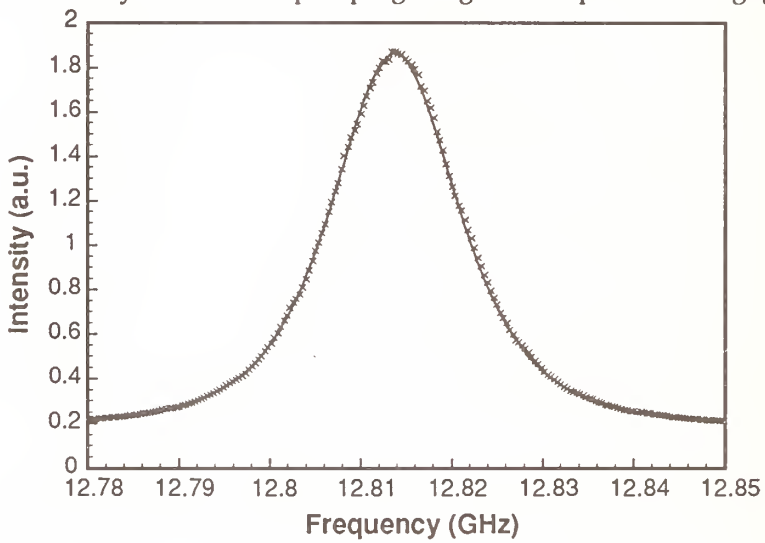

Fig. 2. Measured Brillouin amplification spectrum of a standard single mode fiber (Δn=5·10^{-3}, core diameter 9μm). Solid line is the numerical fit of the theoretical curve (hyperbolic cosine of a Lorentzian function).

A typical Brillouin gain spectrum measured using this method is shown in Fig. 2. The measured gain curve $g_B(\nu)$ perfectly fits a Lorentzian function and the Brillouin parameters can therefore be acurately determined. The length of the different measured fibers was in the 100m-600m range and were wound by hand to avoid any tension. Regular mechanical winding induces stresses that were observed to bias the measurements by causing an inhomogeneous broadening of the gain curve. Care was also taken to decrease the test signal amplitude until no effect on the gain curve are measured, meaning a negligible pump depletion.

Table I summarizes the measurements performed on theses fibers. The Brillouin Stokes shifts range from 11.5 GHz to 12.8 GHz and a clear relationship is observed between Stokes shift and core-cladding index differences, as shown in Fig. 3., confirming previously reported results [4]. An interesting feature is the excellent agreement between the extrapolated value for Δn=0 and the Stokes shift calculated for bulk silica.

Another relationship was found between Stokes shift ν_B and Brillouin gain line width, as shown in Fig. 4. The extrapolated value for Δn=0 is close to the bulk silica value, but the agreement is not perfect. This may be due to excess phonon damping occurring in the fiber waveguide, though the confidence level of the measurements made in bulk silica is not known. These measurements provide with a high

Core-cladding Δn ($\times 10^{-3}$)	Brillouin shift (GHz)	Linewidth (MHz)	Spot size µm	Peak Gain g_o m/W	Power Gain $go/Aeff$ $m^{-1}\ W^{-1}$
Bulk Silica	13.1000	23.0			
4.5	12.8527	34.5	5.04		
5.0	12.7960	35.7	4.64	$1.59\ 10^{-11}$	0.23
5.0	12.8088	35.4	4.82	$2.02\ 10^{-11}$	0.28
8.0	12.7191	34.5			
10.5	12.3886	40.6			
14.0	12.3309	42.5	2.96	$1.42\ 10^{-11}$	0.52
30.0	11.5094	52.4	1.84	$1.91\ 10^{-11}$	1.79

Table I. Summary of measurements performed on different fibers, together with aome fibers characteristics and calculated gain. Values for bulk silica are extrapolated from reported measurements.

confidence level a 35 MHz value for the Brillouin FWHM linewidth of standard telecommunication fibers (Δn=5·10^{-3}) at 1.32 µm.

Finally the Brillouin gain coefficient g_o was calculated from the maximum of the BGS after measurement of pump power and spot size ω_o. The effective cross section A_{eff} was determined using the classical formula $A_{eff}=\pi\omega_o^2$. A quite important fluctuation in the gain evaluation (1.4-2 10^{11} m/W) is observed but there is no clear correlation between gain value and core doping. This confirms the assumption that Brillouin interaction predominantly takes place within the core, so that the effective cross section A_{eff} must be weighted by the overlap integral between mode field distribution and core index profile [4]. Actually the highest gain is obtained for a fiber with no dip and a very uniform core index distribution, and lowest gain for a triangular profile. Care was taken to carefully adjust pump and probe

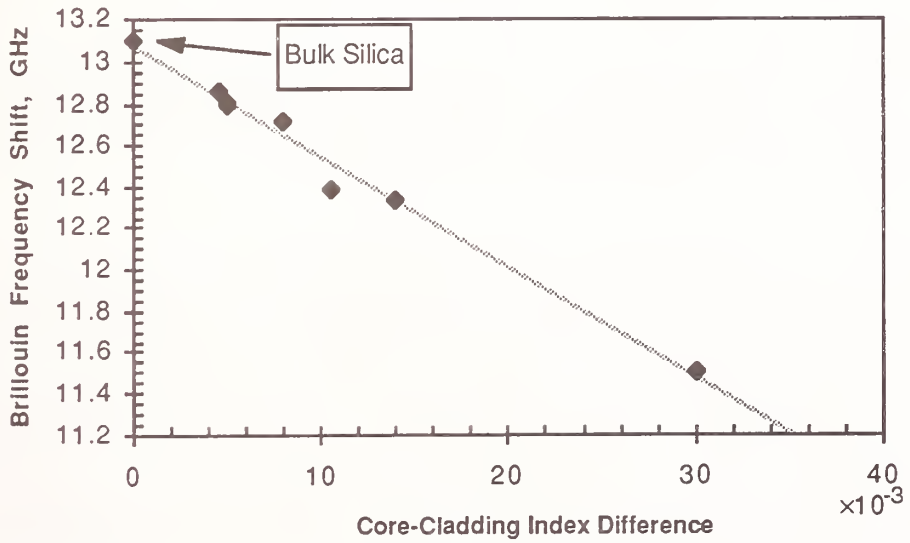

Fig. 3. Relationship between the frequency of the Stokes shift and the core-cladding index differences

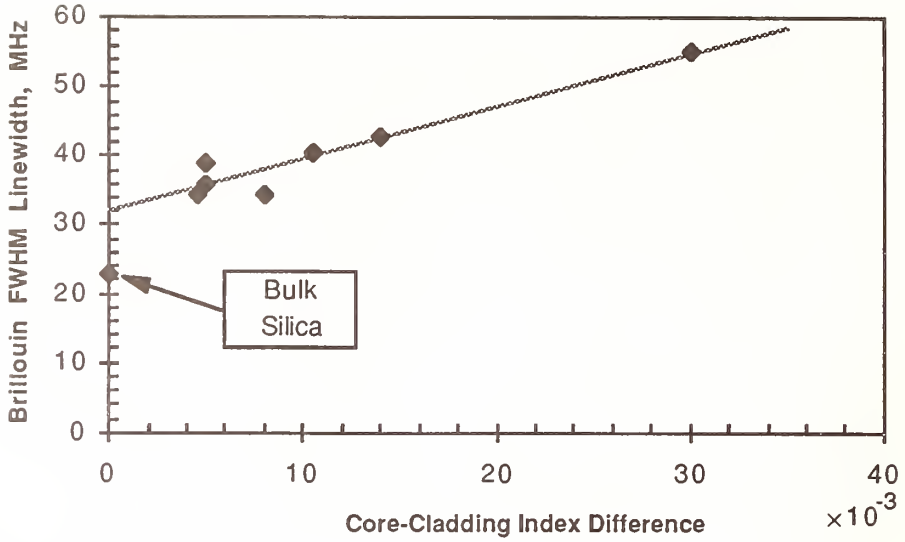

Fig. 4. Relationship between Brillouin gain linewidth and the core-cladding index difference.

polarizations, so that polarization scrambling effects are made negligible. This was checked by observing the absence of amplification in the orthogonal state of polarization.

The difficulty to exactly determine the effective cross section A_{eff} makes the power gain coefficient g_0/A_{eff}, shown in Table I, more suitable for fiber characterisation. Overall amplification can be calculated directly from pump power and comparative measurements are possible without further calculations using additional parameters (spot size, index profile).

In conclusion highly accurate measurements of the Brillouin gain curve were performed in fibers with very different guiding characteristics. These measurements explain the differences observed between fibers and bulk silica and the scattered value reported by different authors. They also confirmed that the core doping decreases the acoustic velocity - and thus the Stokes shift - and the phonon lifetime, causing a broader linewidth, and has a negligible effect on the gain coefficient.

Acknowledgments

The authors would like to thank the Swiss PTT, Câbles Cortaillod S.A. and PSEL fund for their kind support and Cabloptic S.A. to have, in addition to its support, supplied the different optical fibers. A patent is pending for this measuring technique.

References

[1] T. Horigushi, T. Kurashima and M. Tateda, IEEE Phot. Tech. Lett., vol. 2 (1990), no. 5, pp. 352-354.

[2] X. Bao, D. J. Webb and D. A. Jackson, Opt. Lett., Vol. 18 (1993), no. 7, pp. 552-554.

[3] N. Shibata, K. Okamoto and Y. Azuma,, J. Opt. Soc. Am. B, Vol. 6 (1989), no. 6, pp. 1167-1173.

[4] R.W. Tkach, A.R. Chraplyvy, R.M. Derosier, Electron. Lett. Vol. 22 (1986)., no. 19, pp 1011-1013.

[5] T.O. Tsun, A, Wada, T. Sakai, R. Yamauchi, Electron. Lett. Vol. 28 (1992)., no. 3, pp 247-249.

[6] M. Niklès, L. Thévenaz and P. Robert, Proc. Nonlinear Guided-Wave Phenomena (Cambridge 1993), OSA publications, paper MD 5

Guided Acoustic-Wave Brillouin Scattering as an Ultrasensitive Probe of Optical Fiber Geometry

Benjamin I. Greene
AT&T Bell Laboratories, 600 Mountain Ave, Murray Hill, NJ 07974

Peter N. Saeta
NIST/JILA, Campus Box 440, University of Colorado, Boulder, CO 80309-0440

Abstract

Guided acoustic-wave Brillouin scattering measurements were performed on a variety of different 20-cm lengths of optical fibers. The detailed line shapes of the lowest lying resonance at *ca.* 22 MHz were observed to vary significantly from sample to sample. We have attributed these variations to 0.01 - 0.1 μm distributed deviations from a perfect cylindrical geometry.

Introduction

Pioneering work by two groups in the mid 1980's predicted and experimentally verified the phenomenon of GAWBS (guided acoustic-wave Brillouin scattering) in optical fibers.[1-3] The effect has its origin in radial acoustic oscillations which are bounded as a consequence of cylindrical fiber geometry. With expectations based upon other high-Q resonance phenomena,[4] we set out to explore the possibility that the GAWBS line shape could be a very sensitive probe of deviations from ideal geometric form. Below we present high-resolution spectral data on the lowest lying GAWBS resonance from optical fiber samples. We have observed significant variations in these line shapes, and speculate how variations in the size or shape of fibers could be manifested in the data.

Experimental

GAWBS spectroscopy was performed as originally described by Shelby *et al.* [2,3] Briefly, we use a heterodyne technique, relying on the acoustically driven index fluctuations at the core to shift (add sidebands to) the fundamental laser frequency. The sidebands are mixed, via the nonlinear response of a photodiode, with the laser fundamental, and the difference frequency is detected with a microwave spectrum analyzer. Data were taken in the depolarized configuration primarily for convenience. In this configuration only those acoustic modes resulting in macroscopic birefringence (*i.e.*, non-radially symmetric modes) are observed.

Results

Several fibers were studied, including many commercial products and some "research" fibers. All samples were required to be single mode at our laser wavelength (900 nm), excluding from study, therefore, standard production telecommunication fiber. The fiber type from which most data were collected, including individual samples which gave the narrowest low frequency resonances, was Corning "Flexcore 1060." Two examples of the lowest-frequency resonance taken on different samples from the same 100-m Flexcore spool are shown in Fig. 1. The most common spectral shape, one that occurred in approximately 80% of the Flexcore samples, was characterized by a single (or nearly single) peak roughly 25-kHz wide, and a broad sideband or shoulder extending by as much as 80 kHz. This band shape is intermediate between those shown in the figure. Considerably less probable were either a single clean peak with a FWHM as small as 11 kHz, or an overlapping superposition of several spectral features having a composite width in excess of 120 kHz. Spectra of a Newport Research Corporation "NRC-820" fiber were taken (not shown) which consistently gave relatively broad (~60-kHz) single-peaked spectral signatures.

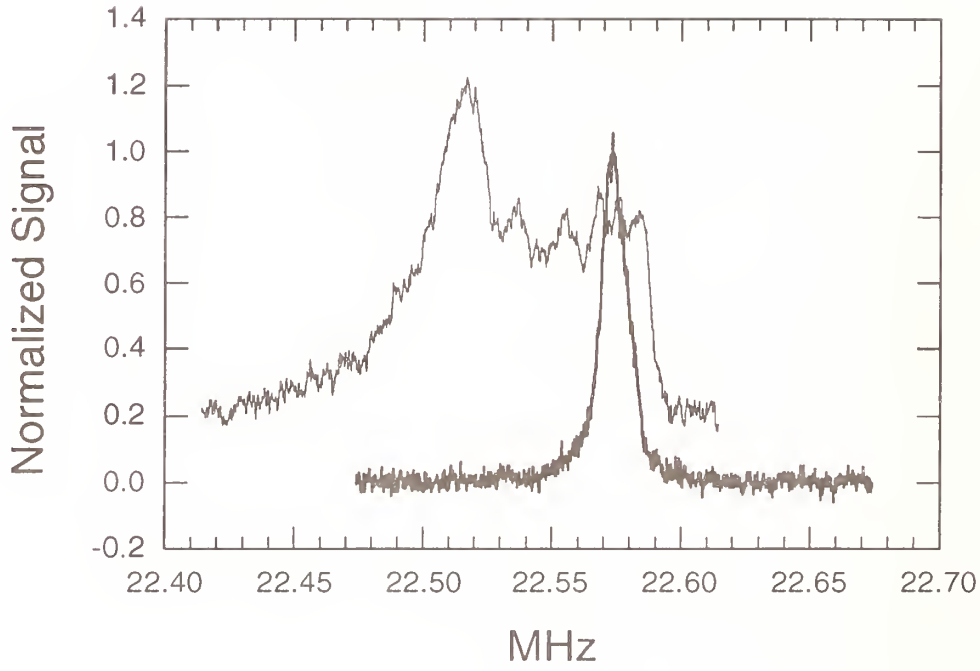

Figure 1 GAWBS signals from two samples from the same spool of Corning "Flexcore 1060". The narrow resonance has a FWHM of 11 kHz.

Additionally, lowest-order GAWBS resonances of "research drawn fibers" were observed to frequently exhibit distinct multiple peaks with individual widths on the order of 10 to 15 kHz.

Discussion

A discussion of phenomenological linewidths must first establish those factors entering into the homogenous width. For the current case, we suggest two significant homogeneous broadening mechanisms: material damping and transmission loss at the air-glass boundary. The literature contains several measurements of acoustic loss in silica, the most relevant to our frequency range by Fraser, Krause, and Meitzler.[5] These authors report a value of the absorption coefficient (α) for the transverse acoustic wave at 22 MHz of 2.12×10^{-2} dB/cm. Relating the resonant linewidth (Δ, FWHM) to α (the base-e absorption coefficient) as $\Delta = \alpha\, v / \pi$, where v is the velocity of sound, predicts a homogeneous width nearly 20 times narrower than that actually observed.[6] We note that optical fibers are not pure silica rods, but more accurately contain a core of doped silica. For our samples, the cores are roughly 5–8 μm in diameter and consist of germanosilicate glass, doped at not more than 5 mole-% germanium. Although we could not find published acoustic loss data on germanosilicate glass, unpublished data for 10 mole-% samples indicate these materials to be only a factor of 3 more attenuating at 20 MHz than pure silica.[7] Taken together with the fact that the core constitutes only a few percent of the acoustic path, it seems impossible to attribute the observed 11-kHz width (Fig. 1) to acoustic absorption alone.

Incomplete reflection is another loss mechanism. The core-cladding reflective loss is estimated with the aid of density and velocity data to be minuscule ($R = 10^{-6}$).[7] The air-cladding loss, however, appears to be significant ($T = 0.2\%$, $R = 99.8\%$). Converting this to an effective α

yields a value of 0.16 cm^{-1} (arrived at by assuming a 0.2% loss per traverse across the fiber 125-μm diameter), resulting in a 20-kHz component to the linewidth. This appears to indicate that in the narrowest cases, our linewidths are determined by transmission loss at the silica-air boundary. This conjecture could be verified by performing measurements *in vacuo*, where the acoustic reflection at the outer boundary should become unity. We did not attempt this measurement.

We now discuss possible causes of broader and more complex line shapes. Fluctuations in fiber diameter, deviations from perfect circularity of the cross section, and compositional variations affecting the velocity of sound could all broaden low-frequency GAWBS resonances. The easiest to appraise of these with respect to effects on the GAWBS linewidth are variations in diameter. Diameter fluctuations would simply shift the resonant peak position by the same fractional extent as the dimensional variation. For instance, a 0.1-μm change in size for a 125.0-μm-diameter fiber would shift the GAWBS resonance at 22 MHz by 17.6 kHz (see Fig. 1). Diameter fluctuations distributed along the sample could therefore result in broadened or distorted line shapes, depending in detail on the exact distribution of diameters.

Deviations from perfect circularity of the fiber cross section could also perturb GAWBS resonances. Depolarized GAWBS is produced by vibrational modes depending on azimuthal angle ϕ as either $\cos 2\phi$ or $\sin 2\phi$.[2,8] In a perfect circular fiber the two modes are degenerate. Slight distortions of the cross section from circularity perturb the vibrational modes and, in general, lift the two-fold degeneracy of the modes producing depolarized GAWBS light. This problem can, in principle, be solved in perturbation theory by treating the distortion as a small perturbation of the solution for the perfect circular case. We have not carried out such a procedure. However, the simpler problem of the vibrational modes of a nearly circular membrane is discussed by Nayfeh.[9] In that case, a distortion of the circumference of the form $\sin 2m\phi$ or $\cos 2m\phi$ lifts the degeneracy between the $\sin m\phi$ and $\cos m\phi$ modes (*i.e.*, of half the period). Furthermore, if ε is the relative amplitude of the distortion to the radius, the two eigenfrequencies are shifted by $\pm\varepsilon\omega$, where ω is the eigenfrequency in the absence of distortion. Just as for variations in the size of the fiber, the relative frequency shift is equal to the relative amplitude of the variation. Assuming that a similar result holds for the vibrations in the fiber cross section, a splitting between the depolarized GAWBS modes would arise from perturbations of the form $\cos 4\phi$ and $\sin 4\phi$ in the fiber cross section. These correspond to a slight "squaring" of the circle.

Geometric distortions in optical fibers have been documented and studied by analysis of backscattered light arising from a laser beam that is incident at right angles to the fiber axis.[10,11] These investigations leave little doubt that microscopic geometric deviations can exist in optical fibers. Finally, interferometric micrographs indicate that both radially and longitudinally periodic fluctuations in refractive index, of order 5×10^{-4}, can exist in preforms and drawn optical fibers.[12] The details of these latter effects are somewhat specific to the fabrication technique (MOCVD or VAD). The index, density, or compositional fluctuations are observed to be periodic on a scale small compared to acoustic wavelengths. Furthermore, observed modulations appear to be radially symmetric. Therefore, their impact on the GAWBS linewidth would be expected to be minimal.

Work on bulk samples correlating the effects of thermal processing on the acoustic properties of vitreous SiO_2 has been presented.[13,14] In the context of fiber process technology, one might envision pathological cases where non-radially symmetric compositional inhomogeneities could contribute to the inhomogeneous GAWBS linewidth. Lacking any specific data along these lines, we believe that the geometric variations discussed above are the most likely explanation for our current data.

Conclusion

In conclusion, we have investigated in detail the line shape of the lowest GAWBS resonance in nominal 125-μm-diameter optical fibers. Spectra typically displayed significant amounts of

inhomogeneous broadening. We attribute these effects to distributed variations in the fibers' outer dimensions. For measurements performed in air, we estimate a homogeneous GAWBS linewidth at 22 MHz of ~10 kHz, and ascribe this width to incomplete acoustic reflection at the fiber-air boundary. This technique is therefore expected to be sensitive to radial geometric distortions on the 0.01-μm length scale. Our measurements indicate that 0.01 to 0.1-μm deviations from perfect cylindrical geometry are statistically very common in commercial optical fibers.

Acknowledgment

The authors wish to thank J. T. Krause for sharing unpublished acoustic attenuation data on silicate glasses with us, and D. J. DiGiovanni for providing samples of limited-production research fibers.

References

[1] P. J. Thomas, N. L. Rowell, H. M. van Driel, and G. I. Stegeman, Phys. Rev. B **19**, 4986 (1979).

[2] R. M. Shelby, M. D. Levenson, and P. W. Bayer, Phys. Rev. B **31**, 5244 (1985).

[3] R. M. Shelby, M. D. Levenson, and P. W. Bayer, Phys. Rev. Lett. **54**, 939 (1985).

[4] S. C. Hill and R. E. Benner, J. Opt. Soc. Am. B **3**, 1509 (1986).

[5] D. B. Fraser, J. T. Krause, and A. H. Meitzler, Appl. Phys. Lett. **11**, 308 (1967).

[6] G. E. Durand and A. S. Pine, J. Quantum Electron. **QE-4**, 523 (1968).

[7] J. T. Krause, *unpublished data.*

[8] R. N. Thurston, J. Acoust. Soc. Am. **64**, 1 (1978).

[9] A. H. Nayfeh, *Introduction to Perturbation Techniques* (Wiley, New York, 1981).

[10] H. M. Presby, Appl. Opt. **15**, 492 (1976).

[11] H. M. Presby, Appl. Opt. **16**, 695 (1977).

[12] T. Izawa and S. Sudo, *Optical Fibers: Materials and Fabrication* (D. Reidel, Kluwer Academic Publishers Group, Norwell, Massachusetts, 1987).

[13] J. T. Krause, J. Appl. Phys. **42**, 3035 (1971).

[14] D. B. Fraser, J. Appl. Phys. **39**, 5868 (1968).

AUTHOR INDEX

• U.S. GOVERNMENT PRINTING OFFICE: 1994-300-568/03034

The National Institute of Standards and Technology was established in 1988 by Congress to "assist industry in the development of technology . . . needed to improve product quality, to modernize manufacturing processes, to ensure product reliability . . . and to facilitate rapid commercialization . . . of products based on new scientific discoveries."

NIST, originally founded as the National Bureau of Standards in 1901, works to strengthen U.S. industry's competitiveness; advance science and engineering; and improve public health, safety, and the environment. One of the agency's basic functions is to develop, maintain, and retain custody of the national standards of measurement, and provide the means and methods for comparing standards used in science, engineering, manufacturing, commerce, industry, and education with the standards adopted or recognized by the Federal Government.

As an agency of the U.S. Commerce Department's Technology Administration, NIST conducts basic and applied research in the physical sciences and engineering and performs related services. The Institute does generic and precompetitive work on new and advanced technologies. NIST's research facilities are located at Gaithersburg, MD 20899, and at Boulder, CO 80303. Major technical operating units and their principal activities are listed below. For more information contact the Public Inquiries Desk, 301-975-3058.

Technology Services
- Manufacturing Technology Centers Program
- Standards Services
- Technology Commercialization
- Measurement Services
- Technology Evaluation and Assessment
- Information Services

Electronics and Electrical Engineering Laboratory
- Microelectronics
- Law Enforcement Standards
- Electricity
- Semiconductor Electronics
- Electromagnetic Fields[1]
- Electromagnetic Technology[1]

Chemical Science and Technology Laboratory
- Biotechnology
- Chemical Engineering[1]
- Chemical Kinetics and Thermodynamics
- Inorganic Analytical Research
- Organic Analytical Research
- Process Measurements
- Surface and Microanalysis Science
- Thermophysics[2]

Physics Laboratory
- Electron and Optical Physics
- Atomic Physics
- Molecular Physics
- Radiometric Physics
- Quantum Metrology
- Ionizing Radiation
- Time and Frequency[1]
- Quantum Physics[1]

Manufacturing Engineering Laboratory
- Precision Engineering
- Automated Production Technology
- Robot Systems
- Factory Automation
- Fabrication Technology

Materials Science and Engineering Laboratory
- Intelligent Processing of Materials
- Ceramics
- Materials Reliability[1]
- Polymers
- Metallurgy
- Reactor Radiation

Building and Fire Research Laboratory
- Structures
- Building Materials
- Building Environment
- Fire Science and Engineering
- Fire Measurement and Research

Computer Systems Laboratory
- Information Systems Engineering
- Systems and Software Technology
- Computer Security
- Systems and Network Architecture
- Advanced Systems

Computing and Applied Mathematics Laboratory
- Applied and Computational Mathematics[2]
- Statistical Engineering[2]
- Scientific Computing Environments[2]
- Computer Services[2]
- Computer Systems and Communications[2]
- Information Systems

---

[1] At Boulder, CO 80303.
[2] Some elements at Boulder, CO 80303.

U.S. Department of Commerce
Technology Administration
National Institute of Standards and Technology
325 Broadway
Boulder, Colorado 80303-3328

OFFICIAL BUSINESS
PENALTY FOR PRIVATE USE, $300